Investigations on Solar Wind-Magnetosphere-Ionosphere coupling during storms and supersubstorms

A thesis submitted to the

Indian Institute of Space Science and Technology

Valiamala P.O., Thiruvananthapuram - 695 547. Kerala, India.

For the Ph.D (Science) degree in Physics

Submitted by

Sritam Hajra

Under the joint supervision of

Dr. Nirvikar Dashora
Scientist/Engineer-SF
NARL, Gadanki

Dr. J. Solomon. Evan
Associate Professor
IIST, Thiruvananthapuram

Research work carried out at

National Atmospheric Research Laboratory

Department of Space Government of India, Gadanki, India – 517 112

Dedicated to the brave souls all around the world who, despite facing discrimination on any basis, continue to persevere with unwavering honesty, courage and love that transcends all boundaries.

DECLARATION

I hereby declare that the thesis entitled "**Investigations on Solar Wind-Magnetosphere-Ionosphere coupling during storms and supersubstorms**" represents my own original research conducted under the supervision of Dr. Nirvikar Dashora (Scientist/Engineer-SF, NARL, Gadanki) and Dr. J. Solomon Ivan (Associate Professor, IIST, Thiruvananthapuram). This work is entirely original and has not been submitted for any other degree at this or any other university. In keeping with the ethical practice of reporting scientific information, due acknowledgments have been made wherever the findings of others have been cited.

Sritam Hajra

(Research fellow, NARL

& Ph.D. Registration at IIST)

CERTIFICATE

This is to certify that the thesis, entitled "**Investigations on Solar Wind-Magnetosphere-Ionosphere coupling during storms and supersubstorms**" submitted by Mr. Sritam Hajra to the Indian Institute of Space Science and Technology, Thiruvananthapuram is a bona-fide record of the candidate's original research work conducted under our guidance and supervision towards the award of the degree of a Doctor of Philosophy in Physics from the Indian Institute of Space Science and Technology, Thiruvananthapuram. This work has not been previously submitted for the award of any degree, diploma, fellowship, or similar title in any other institution or university.

Dr. Nirvikar Dashora
Scientist/Engineer-SF &
Head, Ionospheric and Space Physics Group
NARL, Gadanki

Dr. J. Solomon. Evan
Associate Professor
Department of Physics
IIST, Thiruvananthapuram

Acknowledgments

Activities, regardless of their magnitude, are never achieved by a single individual, but rather are the culmination of the collaborative efforts of those involved, be it directly or indirectly. The completion of this thesis has been a significant and formidable feat for me, and as such, I am profoundly grateful for the unwavering support, patience, and guidance of the individuals listed below, without whose contributions this work would have remained beyond my reach.

I like to begin by expressing my gratitude to my thesis supervisor, Dr. Nirvikar Dashora, for his support throughout the course of my research work. His invaluable guidance, mentorship, suggestions, and motivation have left an indelible mark on this thesis, and I am profoundly grateful for all his efforts. His mentorship has imparted invaluable lessons and expertise to me, benefiting me greatly in both academic and personal aspects of life. He has granted me abundant freedom to delve into my own exploration and discover the researcher within me, and, that thing is probably the best thing I could have been gifted with. In addition, I also want to thank his family members for all the care and affection they have extended towards me during my Ph.D. journey.

Furthermore, I wish to extend my sincere gratitude to my IIST supervisor, Prof. J. Solomon Ivan, for his continuous guidance and support during my Ph.D. tenure. Specially, I owe him my deep sense of gratitude for his compassionate responses on several occasions of my interactions during this period. I consider myself fortunate to have had the opportunity to benefit from his mentorship and forever grateful to him.

I am humbled to express my profound gratitude to Dr. Amit Kumar Patra, the Director of National Atmospheric Research Laboratory (NARL). His constant encouragement, advice, and insightful suggestions during academic reviews have been invaluable to the progress of my research work. His unwavering support and kind approvals to provide the laboratory, canteen, and hostel facilities have helped me immensely during my Ph.D. journey.

I also extend my gratitude to Prof. V. K. Dadhwal, the former Director of IIST, and Prof. S. Unnikrishnan Nair, the current Director of IIST for their constant encouragement and invaluable contributions in completing the procedural matters with regard to Ph.D.

I am filled with immense gratitude towards the Academic Committee of NARL for their continuous support, suggestions, and guidance throughout my academic journey. Their timely actions in all others matters related to my research and social activities have been nothing short of invaluable. In particular, I would like to express my heartfelt thanks to Dr. T.V.C. Sharma, Dr. M. Venkat Ratnam, Dr. S. Sridharan, Dr. T.N. Rao, Dr. Ramkumar, Dr. Amit Kesarkar, Dr. Chaitanya D. Jain, Dr. N.V. Rao, Dr. Vikash Singh, and Mr. Ravindra Devakate, who has played a pivotal role in shaping me into the researcher and person I am today. Moreover, I would also like to extend my sincere appreciation to all the members of the Doctoral Committee of IIST and professors from the Department of Physics, namely Dr. Tarun K. Pant, Prof. Sudheesh Chetill, Prof. Sudarshan Kartick, Prof Umesh R. Kadhane, and Prof. S. Murugesh for their constant support, encouragement and suggestions with regard to my Ph.D. thesis and doctoral committee reviews. Their timely reviews of my progress and valuable suggestions have been instrumental in ensuring the smooth progress of my research work. Especially, I am highly indebted to Dr. Tarun Kumar Pant for his invaluable insights, expert comments and suggestions, and unflagging support. I am truly grateful for their hearty commitment to my academic success.

I would like to express my sincere gratitude to NARL and the Department of Space for providing me with a scholarship throughout my Ph.D. tenure. This financial support has enabled me to focus on my research and pursue my academic goals with dedication and commitment. I am thankful to all the Web-based resources, data servers/facilities, and providers, which have been inevitable behind all the research I have carried out during my Ph.D. journey. I am thankful to the staff of Library, CMD and CDMG of NARL for their continuous support in the academic and co-curricular affairs during my Ph.D. tenure I am also grateful to the COSPAR committee for awarding me a grant to attend the 44th COSPAR scientific assembly held in Athens from 16-24 July 2022. I would like to extend my heartfelt thanks to Prof. Mirko Piersanti, Prof. B. T. Tsurutani, Prof. Jan Latsovika, Prof. A Jafronosky, Prof. Fagundez, and Prof. Dibyendu Chakrabarty for providing me with valuable suggestions and engaging in fruitful discussions during the COSPAR assembly. Additionally, I wish to express my gratitude to NSSS, SCOSTEP, URSI- RCRS, and ISWC for giving me the opportunity to attend conferences and symposiums.

I am grateful to Dr. V.K.D. Srinivasu, Mr. Himanshu S. Sethi, Dr. P.B.S. Harsha and Dr. Sunanda for their generous help in various lab activities and Ms. Vineetha for the moral

support at GNSS lab. I would also like to express my gratitude and appreciation to Mr. Sk Samin Kader for his invaluable support in the lab and hostel.

Friends play a crucial role in all aspects of life, and I am grateful for the support and contributions of Dr. Arpita Munshi, Dr.Meenakshi S, Dr. Soujan Ghosh, and Mr. Deepak Singh Bisht. They stood by me through both the highs and lows of this journey, and their kindness and concern helped me overcome obstacles and move forward. I also want to extend my gratitude to my friends and colleagues Dileep, Debojit, Kavita, Jitesh, Babu Pawan Kumar, Akshit, Reetambhara, Dr. Kasturi, Dr. Suman, Manoj, Mohan Babu, Venu, Varsha M Ravindran, Dr. Sarath, Bipin, Abhijeet, Brajesh, Jayashree, Dr. Aashiq, Hindu Arimili, Apsara, Vaishnavi, Vikas, Adarsh, Amal, Arnob, Riya, Alex, Kritika, Aditya, Dr. Gopika, Renju, Santhosh, Ujas, Krushi, Devender, Late Balaji garu, Yugandhar garu and Shahbazz, who treated me as their brother throughout this journey. I would like to express my gratitude to all my fellow Research Scholars, scientists, and employees of NARL, from every research group, for their contribution to my life. I extend my deep gratitude to the BENGAL TIGERS football team, and the HAVELI family for being my constant motivation and support.

Last but certainly not the least; I am deeply indebted to my father, Mr. Srihari Hajra, my mother, Mrs. Supriti Hajra, and sisters, Ms. Sayantani Hajra and Ms. Subhashree Hajra, who have been my constant source of inspiration throughout this journey. I express my deep gratitude to my grandfather Late Mr. Madan Mohan Bag and my grandmothers Late Mrs. Menoka Hajra and Mrs. Kalpana Rani Bag for being a constant source of motivation throughout my academic journey. I am also grateful to my extended family members for their love and support. I want to express my heartfelt gratitude to Ms. Anwesha Bhattacharya, whose unwavering encouragement, unconditional support, familiar affection, and constant motivation helped me achieve this significant milestone. They all stood by me through thick and thin, in good times and bad, offering their selfless love, affection, and care to help me overcome every obstacle.

Finally, yet most importantly, I want to thank the Almighty for the power, wisdom, and perseverance bestowed upon me during the course of this work and throughout my life. Without this divine guidance and grace, I could not have accomplished this feat.

- Sritam Hajra

Abstract

This thesis aims to quantitatively analyse the effects of solar wind-magnetosphere-ionosphere (SW-M-I) coupling on the near-Earth space environment and enhance the current understanding of both large and small-scale coupling processes and mechanisms in the SW-M-I system during extreme transient events of supersubstorm and geomagnetic storms. At the first, robust quantitative analyses with regard to the SW-M-I coupling during all the three supersubstorm events (i.e. May 2011, March 2012, and September 2017) of solar cycle 24 are carried out. The observations from the L1-point and network of magnetometer and radars are included in comparative assessments and investigations of different coupling functions and the most significant parameters known to define the SW-M-I coupling. The in situ observations from the MMS, Cluster, and THEMIS missions are additionally used to investigate the ion and electron scale coupling during the geomagnetic storm of 31 December 2015.

The thesis consists of six chapters, out of which the first chapter gives the introduction, motivation, and aim of the thesis, and the second chapter gives the details of the observations and methodology. Chapters three, four, and five provide details of results obtained under three aimed objectives. The sixth chapter provides a summary and future directions. Overall, the thesis work has led to three publications in peer-reviewed international journals.

The main results showcase the quantification of the solar wind drivers, energy sources, and sinks in the magnetosphere-ionosphere system during both short and long periods, along with the percentage share of the major energy sinks in the magnetosphere-ionosphere system during the growth and recovery phases during supersubstorms, and intriguing trends of substorms of different intensities. The major results of another study on the latitude-dependent H and D-component responses during the Storm Sudden Commencement (SSC) and the latitude-dependent anomalies and similarities during the main phases, indicate the complex interplay of different spatially and temporally varying current systems in the magnetosphere-ionosphere system. The investigations on the kinetic scale coupling bring about a few very interesting results regarding the carriers of the field-aligned currents and different ideal and non-ideal terms of the total electric fields. The in situ observations of different plasma and field parameters at the magnetopause and magnetotail have provided a broad overview of the multi-scale dynamics of the two reconnection regions in near-earth space.

Contents

Acknowledgements i

Abstract iv

Contents v

List of Figures x

List of Tables xix

1. Introduction 1

1.1 Motivation behind the research 2

1.2 The Sun and the origin of the space weather 4

1.2.1 Solar structure and activity 4

1.2.2 Emissions from the Sun 6

1.2.2.1 The solar wind 6

1.2.2.2 Solar flares 7

1.2.2.3 Coronal Mass Ejections (CME) 7

1.2.3 Classification of the solar wind disturbances 8

1.2.3.1 Quasi-stationary structures in the background flow of the solar wind 8

1.2.3.2 The disturbed plasma streams 9

1.2.3.3 The shock waves 11

1.3 Earth's magnetosphere and Solar wind-magnetosphere coupling 11

1.3.1 Formation and structure of earth's magnetosphere 11

1.3.1.1 The geomagnetic field and magnetospheric cavity 11

1.3.1.2 Major magnetospheric regions 12

1.3.2 Solar wind-magnetosphere coupling 16

1.3.2.1 The Dungey model and convection 16

1.3.2.2 Different coupling mechanisms 17

1.3.2.3 Magnetospheric current systems 21

1.3.3 Geomagnetic storms and substorms 24
1.3.3.1 Geomagnetic storms 24
1.3.3.2 Geomagnetic substorms 26
1.4 Earth's ionosphere and Magnetosphere-Ionosphere coupling 29
1.4.1 The Earth's ionosphere 30
1.4.2 Ionospheric current systems 31
1.4.3 Magnetosphere-ionosphere coupling 32
1.4.3.1 FAC and PCPD 32
1.4.3.2 Auroral electrojet and DP2 34
1.4.3.3 Joule heating and Auroral particle precipitation 35
1.4.3.4 Disturbed-time electric fields 36
1.5 Geomagnetic responses 37
1.5.1 Components of the geomagnetic field 37
1.5.2 Geomagnetic indices 38
1.5.3 Geomagnetically induced currents 40
1.6 Aim and Scope of the Thesis 40

2. Data Analyses and Methodology 45
2.1 Introduction 46
2.2 Observations of interplanetary parameters and geomagnetic indices 46
2.3 Identification of solar wind drivers 46
2.4 Estimations of parameters related to energy sources, coupling, sinks, and partitioning 48
2.4.1 Available solar wind power 48
2.4.2 Solar wind-magnetosphere coupling 49
2.4.3 Magnetosphere-ionosphere coupling 51
2.4.4 Power dissipation through ring current 51
2.4.5 Power dissipation through Joule heating 53

2.4.6 Power dissipation through auroral particle precipitation 54
2.4.7 Other energy sink and net energy sink 55
2.4.8 Energy transfer efficiency and ratio 56
2.5 Observations from magnetospheric satellites 56
2.5.1 In-situ observations 56
2.5.1.1 Observations from the MMS 57
2.5.1.2 Observations from the THEMIS 59
2.5.1.3 Observations from the Cluster 60
2.5.2 Estimation of Kinetic scale coupling parameters 61
2.5.2.1 Estimation of FAC 62
2.5.2.2 Estimation of electric field and power 63
2.6 Ionospheric observations 65
2.6.1 Observations from the SuperDARN 65
2.6.2 Observations from the DMSP-SUSSI 65
2.7 Observations from global magnetometer networks 66
2.7.1 Observations from INTERMAGNET network 66
2.7.2 Observations from SUPERMAG network 67

3. SW-M-I Coupling During Supersubstorms of Solar Cycle 24: Energy Flow 69
3.1 Introduction 70
3.2 Observation and methodology 72
3.2.1 Duration of the phases of the suspersubstorms 72
3.2.2 Procedure of estimations 73
3.3 Results 74
3.3.1 Solar wind drivers 74
3.3.2 Interplanetary parameters and geomagnetic indices 76
3.3.3 Coupling and energy transfer 78
3.3.4 Energy partitioning in the magnetosphere-ionosphere system 81

3.3.5 Dependence of energy partitioning on intensity of substorms 87
3.4 Discussion 89
3.5 Summary and conclusions 94

4. SW-M-I Coupling During Supersubstorms of Solar Cycle 24: Geomagnetic Responses 97
4.1 Introduction 98
4.2 Observations and methodology 100
4.3 Results 101
4.3.1 Variations in the interplanetary parameters and geomagnetic indices 101
4.3.2 Global impact of the SSC 104
4.3.2.1 Variations in the H-component 105
4.3.2.2 Variations in the D-component 107
4.3.3 Response of H-components during the supersubstorm period 109
4.3.3.1 Response from co-latitude band of 70^o-90^o 109
4.3.3.2 Response from co-latitude band of 15^o-70^o 111
4.3.3.3 Response from co-latitude band of 0^o-15^o 113
4.3.4 Response of D-components during the supersubstorm period 115
4.3.5 Signatures of the GIC during supersubstorms 117
4.4 Discussion 119
4.5 Summary and Conclusion 129

5. SW-M Coupling at the Kinetic Electron Scales During a Geomagnetic Storm 131
5.1 Introduction 132
5.2 Observations and methods 134
5.2.1 Estimation of Field Aligned Currents 135
5.2.2 Estimation of electric field components and power 136

5.2.3 Spacecraft orbits in the geospace 136

5.3 Results 138

5.3.1 Solar wind conditions and geomagnetic perturbations 138

5.3.2 MMS-magnetopause encounter at 2310-2330 UT on 31 December 2015 140

5.3.3 MMS-magnetopause encounter at 0735-0755 UT on 1 January 2016 146

5.3.4 Cluster-magnetopause encounter at 1145-1205 UT on 1 January 2016 149

5.3.5 THEMIS-A approach of the magnetotail at 1110-1130 UT on 1 January 2016 151

5.3.6 Simultaneous observations from the MMS-1, Cluster-4, THEMIS-C, and THEMIS-A (2300 UT on 31 December 2015 – 0700 UT on 1 January 2016) 153

5.4 Discussion 157

5.5 Summary and Conclusions 163

6. Summary and Future Directions 165

6.1 Summary of the thesis 166

6.2 Summary of new findings 167

6.3 Future scope 170

Appendix-A 172

Appendix-B 177

Appendix-C 185

References 188

List of Peer-Reviewed Publications 219

List of Conference papers 220

List of Figures

1.1 A schematic graphic showing the layers of the sun. [Credit: NASA/Goddard (https://www.nasa.gov/mission_pages/sunEarth/science/Sunlayers.html)]

1.2 The observations from the SDO (Solar Dynamic Observatory) are used to represent the solar activity cycle in terms of the occurrence of sunspots in the left images which correspond to December 2019 (low activity) and July 2014 (high activity). The images on the right show a mosaic prepared using SDO observations of the sun in X-ray during 1996-2020, displaying solar cycles 23 and 24.

1.3 A very large CME is captured on 2 December 2002 with the Large Angle and Spectrometric Coronagraph (an instrument that blocks the solar disk to reveal the much dimmer corona) on board solar and Heliospheric Observatory (SOHO) mission. [Credit: Encyclopaedia Britannica (https://www.britannica.com/science/coronal-mass-ejection)]

1.4 Schematic of (a) an Interplanetary Coronal Mass Ejection (ICME) and the associated shock and sheath. The ICME shown here features the flux rope or magnetic cloud structure (Figure adapted from Richardson and Cane., 2011 (modified from Cane, 2000 and Zurbuchen and Richardson, 2006)). (b) A CIR containing FAST and SLOW streams. Also, CIRs are bounded by fast forward–fast reverse shock pair (DFS and DRS) in the near-Earth orbit (Figure adapted from Kilpua et al., 2017). (c) RARE, FAST, SLOW, Forward, and Reverse shock waves (Figure adapted from Owens and Forsyth (2013).

1.5 A schematic diagram showing the Earth's magnetosphere and different plasma regions inside it. [Credit: Wikipedia]

1.6 Examples of different astrophysical and laboratory plasmas where magnetic reconnection occurs (adapted from Hesse and Cassak, 2020, for the purpose of illustration). The panels are arranged in a clock-wise fashion surrounding a pictorial representation of magnetic reconnection in the middle panel. A caption is provided below each panel (a-j) which is self-explanatory.

1.7 A cartoon representing kinetic scale magnetic reconnection is presented in the above figure. The faded red and sky-blue coloured rectangular regions represent an EDR and an IDR respectively. (Figure courtesy: NASA-GSFC (https://mms.gsfc.nasa.gov/science.html)

1.8 A schematic diagram showing the major current systems in the Earth's magnetosphere. (Modified from Kivelson and Russel.,1995)

1.9 A schematics representation of different phases of a geomagnetic storm (Figure adapted from Tsurutani et al. 2006) associated with ICME structures in the solar wind.

1.10 A schematic diagram representing the Substorm sequence in the noon-midnight meridian plane (Figure adapted from Hones, 1979). Sequentially, (1) the substorm growth phase starts, and the tail stretches and thins; (2) magnetic reconnection happens in the near tail region; (3-8) this leads to the development of a near-Earth neutral line, followed by the growth and ejection of a plasmoid; (7-9) the plasmoid departs and leaves a thin "post plasmoid plasma sheet" behind. (9-10) during the recovery phase, the near-tail plasma sheet gets refilled and the tailward retreat of the neutral happens.

1.11 A schematic of the substorm current wedge (Figure adapted from McPherron et al., 1973), showing the diversion of the cross-tail current into the ionosphere during geomagnetic substorms. Each pointed line represents the current flow and its direction. (https://www.issibern.ch/teams/scw/Proposal.html).

1.12 A schematic overview of ionosphere-thermosphere processes and their interaction with the magnetosphere and the solar wind, leading to the generation of various current systems (Figure adapted from Sarris et al., 2019)

1.13 A schematic diagram of magnetosphere-ionosphere coupling via field-aligned Region 1 and 2 and Pederson and Hall currents in the ionosphere (Figure adapted from Le et al., 2010).

1.14 A schematic flow chart of aim and scope of the research plan for the present thesis. On the left column, a flow of the coupling processes which are aimed to study is given and the regions of research interest are annotated as text box with arrows on a cartoon depicting an artistic view of the sun-earth connection.

2.1 An artistic depiction of the MMS spacecraft encountering the Earth's magnetosphere (Figure credit: Wikipedia (https://en.wikipedia.org/wiki/Magnetospheric_Multiscale_Mission))

2.2 A schematic view of an MMS spacecraft with the payloads is shown. (Figure Courtesy: https://mms-fields.unh.edu/mms_payload.shtml)

2.3 A schematic view of a THEMIS spacecraft with the payloads is shown. (Figure credit: https://www.nasa.gov/mission_pages/themis/spacecraft/index.html)

2.4 A schematic view of the Curlometer method applied on tetrahedral spacecraft formation to determine FACs. The R1-R4 represent the spacecraft positions in the 3-D and jxyz

represent the current vectors perpendicular to the respective facet of the tetrahedral (see Dunlop et al. 2002, for details).

2.5 Map of the locations of 45 magnetometer stations from the INTERMAGNET network that are used in this thesis

3.1 A comparative distribution of occurrence of supersubstorms of solar cycle 24 is given against the average occurrence during solar cycles 21, 22 and 23.

3.2 Presence of different solar wind structures is shown for the supersubstorms of solar cycle 24 in the first 3 columnar panels from left (panels a, d and g). The corresponding variations in the SYM-H (panels b, e and h) and the SML (panels c,f and i) indices for a duration of 4 days are given in the middle and bottom rows. Vertical dashed lines mark the start (Ts) and end (Te) of a supersubstorm. The rightmost columnar panel (j) shows the mean distribution of presence of different solar wind structures during 17 supersubstorms of solar cycle 23. The acronyms are referred to in text description in section 2.1 following Yermolaev et al. (2009).

3.3 The top three panels in each column give variations in the solar wind plasma parameters the IMF-Bz (Bz), speed (V) and pressure (P), and the bottom three panels give the AE, SYM-H, and SML indices, respectively. Columns from left to right show results for 2011, 2012, and 2017 events, respectively. A vertical dotted line in right two columns shows the time of the sudden commencement. The supersubstorm durations are shaded in yellow colour.

3.4 Panels from top in all columns give variations in the IMF-By/Bz and IEF-Ey/E_R (solar wind); R and $\frac{d\varphi_{MP}}{dt}$ (solar wind-magnetosphere coupling); PCPD, PCI and FAC (magnetosphere-ionosphere coupling) and, the SML indices respectively. The columnar panels are arranged respectively for 2011, 2012, and 2017 events. Vertical dashed lines show the time of occurrence of SSC for the 2012 and 2017 events and yellow shades represent the supersubstorm durations, in respective years.

3.5 The variations in the estimated power terms are given in 6 top panels, respectively in columnar panels from left to right for the 2011, 2012, and 2017 events. Panels from the top to bottom respectively give the available solar wind power (U_{sw}) (a, h, and o); the magnetospheric input power (ε) (b, i, and p); power through the ring current (U_r) (c, j, and q); the Joule heating (U_j)(d, k, and r) and the auroral particle precipitation sink (U_a)(

e, l, and s); total dissipated power (U_t) (f, m, and t); the SML index (g, n and u). The vertical yellow shades show the supersubstorm durations.

3.6 The respective power terms shown in Figure 5 are integrated for different intervals and given in panels from top i.e. supersubstorm (SSS) period, 4 days, 1 month, 6 months and 1 year, respectively, till bottom. The energy curves are given in different colours provided in a legend at the top. The columnar panels represent different time intervals selected from years 2011, 2012 and 2017, respectively. The vertical yellow shades show the supersubstorm durations in top three rows of panels.

3.7 Top two panels (a) show pie-chart distribution depicting the percentage share of different energy sinks during the expansion phase and recovery phase of the supersubstorms. Pie-charts from left to right respectively show the results for supersubstorm events of 2011, 2012, and 2017 (SSS1 and SSS2). Bottom panel (b) gives a bar-chart for the average energy dissipation during the four supersubstorms through the three major sinks and other minor sinks. Legend in the bottom panel gives respective colours used to represent different sinks.

3.8 Comparative energetics of the four supersubstorms of 2011 (orange), 2012 (yellow), '2017-SSS1' (violet), and '2017-SSS2' (green) to an average Akasofu-type substorm (blue) and an average moderate geomagnetic storm (red) is given in panels (a-e). The comparison is provided in terms of (a) available solar wind energy (b) input energy and sink-energy (c) input efficiency (d) coupling efficiency, and (e) energy distribution of the major energy sinks.

3.9 The abscissa gives SML index in all panels. Panels a-g respectively show scatter plots of available solar wind energy (E_{sw}), magnetospheric input energy (E_ϵ), total energy sink (E_t), Joule heating sink (E_j), auroral precipitation sink (E_a) and ring current sink (E_r). Panels i-k in the bottom row show respectively show the efficiencies e1, e2 and e3. First 3 columnar panels from left show a linear least square fit to the scatter points and fourth columnar panel in each row (i.e. d, h and l) shows the slope of the fit-lines from the first 3 panels.

4.1 Map of the locations of 45 magnetometer stations that are used in the present study. The full name and code of the respective stations as provided by the INTERMAGNET website are given aside from the triangle marker. A list of all the stations is provided as a table in the supporting information (SI-1)

4.2 Variations in the interplanetary parameters for four days of duration covering the supersubstorm events are given in the top four rows, and the bottom three rows give the variations in the SYM-H, AE, and SML indices, respectively. Columns from left to right show results for the 2011, 2012, and 2017 events, respectively. A vertical dotted line shows the SSC during the events of 2012 and 2017 and the durations of the supersubstorms are highlighted by brown shaded boxes in the respective panels.

4.3 Variations in the H-component at the time of SSC are shown from a group of stations from the northern hemisphere (NH) and southern hemisphere (SH), respectively in the left two and right two columnar panels for the events of 2012 (panels a to f) and 2017 (panels from g to l). Panels from the top in each column correspond to a co-latitude range of 0^o-45^o, 45^o-65^o, 65^o-90^o, respectively. Each curve corresponds to the observations from a station whose code name with geomagnetic latitude is given in the legends. Legends for stations from the NH (SH) are shown on the left (right). The vertical dotted line in each columnar panel shows the time of the SSC.

4.4 Variations in the D-component at the time of SSC are shown from a group of stations from the northern hemisphere (NH) and southern hemisphere (SH), respectively in the left two and right two columnar panels for the events of 2012 (panels a to f) and 2017 (panels from g to l). Panels from the top in each column correspond to a latitude range of 0^o-45^o, 45^o-65^o, 65^o-90^o, respectively. Each curve corresponds to the observations from a station whose code name with geomagnetic latitude is given in the legends. Legends for stations from the NH (SH) are shown on the left (right). The vertical dotted line in each columnar panel shows the time of the SSC.

4.5 The H-component variations as observed from the latitude band of 70^o-90^o for the northern and southern hemispheres are respectively shown in the upper and lower rows. Each panel begins with a quiet day followed by 2 days of variations covering each of the supersubstorm events, respectively for 2011, 2012, and 2017 from left to right columnar panels. The code name and geomagnetic latitude of each station are given on the rightmost side. The observation from a station DMC for the 2011 and 2012 events is not available. Different colors of the curves are used to indicate the difference in patterns of the variations.

4.6 The H-component variations from the latitude band of 15^o-70^o from the northern (top six rows) and southern (bottom four rows) hemispheres are given including observations on a quiet day (yellow shaded box at the beginning of each column). The columnar panels give results for the events of 2011, 2012, and 2017 respectively from left to right,

wherein the respective supersubstorm durations are shaded by vertical brown boxes. The geomagnetic latitudes of the respective magnetometer stations are given on the rightmost side of each row. The sudden reversals in the H-component variations are depicted by brown curves in different panels and a black arrow in each panel represents local noon.

4.7 The variations in H-component as observed over the co-latitudes between 0o to 15o from the northern (top five rows) and southern (bottom four rows) hemispheres, respectively, beginning with the variations on a quiet day (shaded by yellow boxes) for each event are given. All panels are plotted against UT, whereas, the axis tick marks in each panel correspond to local midnight and local noon with a black arrow depicting the local noon time at the respective station. The tick marks given on the bottom abscissa depict 0000 UT and 1200 UT for reference to all the panels. Blank panels represent an absence of the observations from Dalat and Saint Helena stations in the corresponding rows during the May 2011 and March 2012 events.

4.8 Observations of the D-component from a particular station are given in each row respectively in the columnar panels for the events of 2011, 2012, and 2017 from left to right. The vertical arrangement of panels is made to display the variations from pole-to-pole following a notation for hemispheres given on the left. The station code names with geomagnetic latitudes are given at the right of each row. The curves in red, blue, and violet respectively refer to the high latitude, the sub-auroral/mid-latitude, and, the low-latitude stations. All panels are plotted against UT, whereas, the axis tick marks in each panel correspond to local midnight and local noon with a black arrow depicting the local noon time at the respective station. The tick marks given on the bottom abscissa depict 0000 UT and 1200 UT for reference to all the panels.

4.9 The maximum and minimum dB/dt values as observed over 44 magnetometer stations are given according to the geomagnetic latitude of the stations. The peak values corresponding to the supersubstorm event of 2011, 2012, and 2017 are given by red, blue, and green markers, respectively.

4.10 The variations in the dB/dt for four days surrounding the supersubstorm period are given in columnar panels from left to right, respectively for the 2011, 2012, and 2017 events. The top three rows show variations from the northern hemisphere and the bottom two rows from the southern hemisphere for the respective stations.

4.11 Panels (a) and (b) receptively give the variations in the SML and SYM-H indices during 21-24 January 2005. Brown-shaded regions in these panels highlight observations on 21

January 2005 which are blown-out in panel (c), which gives the variations in H-component as observed by 29 stations from the northern and southern hemispheres. The station code with geomagnetic latitude for each curve in panel (c) is given on the right side and two heavy red curves depict the poleward beginning of the phase reversal in the H-component variations.

4.12 The latitudinal and longitudinal extensions of the DP2 current system as observed by SuperDARN radars during the 2011 event are presented. The variations in the DP2 just before the start of the expansion phase are given in the left panels and at the peak of the main phase in the right panels respectively, for the northern (upper panels) and southern (lower panels) hemispheres. Various label and notations have their usual meanings according to Cousins et al. (2013).

5.1 (a) Orbits of the MMS-1, Cluster-4, THEMIS-C, and THEMIS-A are shown for a month from 5 December 2015 to 5 January 2016 as given in the legend. The arcs of the orbits during the storm from 23:00 UT on 31 December 2015 to 13:00 UT on 1 January 2016 are highlighted by thick lines. Earth (black sphere) is located at the center of the GSE reference frame. The Sun is located towards positive abscissa as indicated by an arrow. The respective meeting with the magnetopause crossing of the MMS-1 is given in (b) and (c) and of the Cluster in (d). The orbital locations of THEMIS-A in the PSBL in the magnetotail are given in (e). Two black parabolic curves in panels (b-e) show the location of the bow-shock and magnetopause which cross the equatorial plane.

5.2 Panels (a), (b), (c), (g), (h), (i), and (j) show variations in the solar wind plasma parameters IMF-Bz, speed (V), temperature (T), electric field (E), magnetic field (B), plasma density (ρ) and ram pressure (P). Panels (d), (e), and (f) show PCN, AE, and SYM-H indices respectively during 31 December 2015 and 1 January 2016. Panel (k) depicts plasma beta (β) and panel (l) gives the epsilon parameter (ϵ).

5.3 Variations of Dng, $\sqrt{Q}$, $AG^{1/3}$ and $(A\phi_e)/2$ during 23:14:45-23:18:55 on 31 December 2015 are shown in the figure 5.3. These parameters are derived from the in-situ observations of MMS-1. Similar variations are noted in the case of MMS-2, 3 and 4, but not shown here.

5.4 Variations in the different ambient measurements from the MMS-1 spacecraft are given for a 20-minute duration between 2310-2330 UT on 31 December 2015. Left panels a-d show the variations in the ambient magnetic field (B), electric field (E), the bulk velocity of ions (Vi), and bulk velocity of electrons (Ve) with the x, y, and z components

in red, blue and green, respectively. Panels e-f show the parallel (brown curve) and perpendicular (sky blue curve) components of the ion and electron temperatures (Ti and Te), respectively. Panel g shows the ion (magenta) and electron (black) density of the plasma (N) and panel h shows plasma beta (β). Right panels give the energy-time spectrogram of different components. Panels i-m show the spectrograms for ions (Ei) (omnidirectional), electrons (Ee) (omnidirectional), parallel electrons (Ep), anti-parallel electrons (Ea) and net energy flux (dE_{FLUX}), respectively. Panels n-p show the pitch angle distribution of the energy flux for the low-energy electrons (PL), mid-energy electrons (PM), and high-energy electrons (PH), respectively.

5.5 Variations in the estimated electric field and current components from the MMS-1 spacecraft are given for a 20-minute duration between 2310-2330 UT on 31 December 2015. Panels (a), (b), (c), (d), and (e) give variations of the second term of the ideal (Ev), Hall (Eh), inertial (Ea), pressure gradient (Ep) and total electric field (Et), respectively. The X, Y, and Z components are shown respectively by red, blue, and green curves. Panel (f) provides variations in the divergence of the total electric field. Panel (gf) shows components of total current; and panels (hg) and (ih) provide variations in the FAC estimated by the Curlometer method, by the plasma method, respectively. Panel (ji) gives variations in the FAC carried by electrons (black) and ions (magenta) from the Curlometer method and panel (kj) provides power (W), representing the amount of electromagnetic energy density converted into plasma energy density.

5.6 Same as figure 5.4, but for the 20-minute duration between 0735-0755 UT on 1 January 2016, referred to here as the second encounter.

5.7 Same as figure 5.5 but for the 20-minute duration between 0735-0755 UT on 1 January 2016, referred to here as the second encounter.

5.8 Variations in the different measurements and estimations from the Cluster-4 spacecraft are given for the 20-minute duration between 1145-1205 UT on 1 January 2016. Panels a and b exhibit variations in the bulk velocity of ions (Vi) and bulk velocity of electrons (Ve) with the x, y, and z components in red, blue, and green, respectively. Panels c and d show the parallel (brown curve) and perpendicular (sky blue curve) components of the ion and electron temperatures (Ti and Te), respectively. Panel e shows the ion (magenta) and electron (black) density of the plasma (N). Panels (f)-(j) give variations of the ambient magnetic field (B), first (E) and second term (Ev) of the ideal electric field, Hall electric field (Eh) and total electric field (Et), respectively with the x, y and z components. Panel (k) shows components of the total current flowing in the region;

panels l and m give variations in the total FAC estimated by the plasma method and FAC carried by electrons (black) and ions (magenta) respectively. Panel (n) provides power (W) and panel h shows plasma beta (β).

5.9 Same as figure 5.8 but for THEMIS-A spacecraft and for the 20-minute duration between 1110-1130 UT on 1 January 2016.

5.10 The columnar panels show the variations in the different ambient measurements, respectively from the THEMIS-C, MMS-1, Cluster-4, and THEMIS-A spacecraft for the 8-hour duration between 2300 UT on 31 December 2015 and 0700 UT on 1 January 2016. Top panels (a, g, m, and s) show variations in ion (magenta) and electron (black) density (N). The panels in the second (b, h, n, and t), third (c, i, o, and u), and fourth (d, j, p, and v) rows from the top show magnetic field (B), ion velocity (Vi) and electron velocity (Ve) respectively with the x, y and z components in red, blue and green. The fifth (e, k, q, and w) and sixth (f, l, r, and x) rows represent ion temperature (Ti) and electron temperature (Te) with parallel (brown) and perpendicular (sky blue) components. The specific regions in the geospace traversed by respective satellites are marked on top of the columns, where, M(D/N) denotes magnetosphere (day/night).

5.11 Rows from the top show the variations in the energy flux (top two rows), electric field terms (the third to sixth row from top), current density, and power estimated, respectively. The columnar panels respectively show observations from THEMIS-C, MMS-1, and THEMIS-A spacecraft for the 8-hour duration. The rest of the annotations and symbols are the same as given in Figure 5.4, Figure 5.5, and Figure 5.10.

5.12 Same as figure 5.10 but for the maximum (green) and average (violet) values of observations from the THEMIS-C, MMS-1, and THEMIS-A spacecraft. The variations in maximum and average values of net magnetic field (B), total electric field (E), ion temperature (Ti), electron temperature (Te) (in the left column); ion density (Ni), electron density (Ne), ion velocity (Vi), electron velocity (Ve) (in the middle column); and current density (J), current density by plasma method (Jp), plasma beta (β), and power (W) (in the right column), respectively.

List of Tables

2.1 Criteria to define streams of the solar wind plasma to be classified into different types (Yermolaev et. al. 2009).

2.2 Characteristics of the solar wind parameters and their types (see Adekoya and Chukwuma, 2018 for details) (ρ=proton density; all other symbols are as given in Table 2.1).

2.3 Eleven types of models estimating Ring current decay time (τ)

3.1 The columns from left provide the concerned duration to obtain an average, available solar energy (Esw), magnetospheric input energy (Eε), total dissipated energy (Et), and the energy dissipated over the three major sinks (Ej, Er, Ea), the corresponding coupling efficiencies are given by e1, e2, and e3, respectively. The estimates are given as averages for different types of short and long periods.

4.1 Temporal occurrence chart depicting start and end epochs with the day and month of the respective phases of the supersubstorms and geomagnetic storm events. The lowest values of the SML and SYM-H indices in each case are also provided. The day and month of the epochs are given in "dd/mm" format.

5.1 Instruments on-board satellites providing different plasma and field parameters

CHAPTER 1

Introduction

"The beginning is the most impotant part of the work"

-Plato

1.1 Motivation behind the research

The desire to explore space is driven by a multifaceted motivation. At its core, the quest to explore the universe arises from a deep-seated curiosity about the unknown and an unquenchable thirst for knowledge. We, the researchers seek to unlock the mysteries of the cosmos, to gain insights into the origin, evolution, and future of life on Earth, and to uncover the secrets of the stars. Beyond the pursuit of scientific discovery, space research has also yielded practical applications that have benefited humanity, such as the development of cutting-edge technologies and materials, improved communication systems, and breakthroughs in life science (Ruyters et al. 2021). Furthermore, space exploration holds the promise of addressing pressing global challenges, including climate change, natural disasters, and resource depletion (Rao, 2001; Tobiska 2004). The significance of space research for developing nations like India was signified by Dr. Vikram Sarabhai after the launch of Russia's Sputnik satellite in 1957 when he underlined the relevance of space activities in developing nations and said that there was no ambiguity of purpose. He is quoted "The space program shall be adopted to play a meaningful role nationally, and in the community of nations, India must be second to none in the application of advanced technologies to the real problems of man and society" (Swaminathan, 2020). Subsequently, the Indian National Committee for Space Research (INCOSPAR) was set up in 1962, and thus Dr. Sarabhai is remembered as the father of the Indian Space Program. In essence, the motivation behind space research is a symbiosis of scientific curiosity and a desire to leverage the knowledge gained to improve the world around us.

The strong magnetospheric cavity of the Earth has played a very significant role in the origin and sustenance of life on the Earth besides the other elements supporting life. The magnetosphere provides a live connection to the upper atmosphere (ionosphere) of the Earth through a complex interplay of physical processes and hence, the impacts of the space weather on our planet can be understood by exploring the coupled magnetosphere-ionosphere system (Kamide and Baumjohann. 2012). The interaction between the solar wind and the Earth's magnetosphere is the primary factor determining the quantity of mass and energy that enters the magnetosphere, consequently influencing its internal dynamics. In addition, the connection between the magnetosphere and polar ionosphere through the Field Aligned Currents regulates the exchange of mass, energy, and momentum from the magnetosphere to the ionosphere. This coupling significantly affects the behaviour of the ionosphere. Hence, understanding the specific regions and mechanisms facilitating this transfer and connection has remained a focal

point of research and exploration for scientists. As of now, there is no universally accepted model for this phenomenon, leading to ongoing debates and discussions. This very issue served as the primary motivation for undertaking this thesis.

The prediction and mitigation of the severe effects of extreme space weather events on satellite communication and navigation systems (Cid et al., 2014), power grids, and other technological infrastructure (Kappenman 2005, Tsurutani et al., 2020; Coster et al., 2021) is needed for a thriving modern society. A recent failure of injection of newly launched satellites into desired orbits (Lockwood et al. 2023) has raised serious concerns about the growing impact of space weather on Human activity in space. We find that understanding the origin of such events on the Sun, tracking them through interplanetary space and till the L1-point of near-Earth observations could lead to better classification of a possible "cause and effect" which has been lacking for individual events. Therefore, in the recent past, the study of specific regions and mechanisms facilitating such a wholesome solar wind-magnetosphere-ionosphere coupling via transfer and magnetic reconnection has remained a focal point of research and exploration for scientists (Poudel et al. 2018; Lockwood et al., 2019; Borovsky, 2021). As of now, there is no universally accepted model for the coupling phenomenon at different boundaries of dynamically changing interfaces, leading to ongoing debates and discussions (Oliviera and Samsonov, 2018; Wang et al., 2020; Moretto et al., 2021). This very issue served as the primary motivation for undertaking this thesis. Moreover, our research has broader implications for our comprehensive understanding of the universal role of stellar magnetic fields in shaping it.

As noted above, the magnetosphere-ionosphere system is dynamically coupled with the solar activity. Sun exhibits a few extreme events during each solar cycle which manifest as major geomagnetic storms. The corresponding dynamical changes in the ionosphere-thermosphere directly connect with modern societal applications on the ground and for human endeavours in space.

Hence, this thesis aims to understand the impact of the varying solar forcing, and its dynamical coupling with the magnetosphere-ionosphere system, including its effects on technological infrastructure and other aspects of our planet during some extreme events. Thus, research on this specific subject pervades a vast area of science, ranging from the study of the Sun to the impacts of space weather on Earth.

1.2 The Sun and the origin of space weather

The solar system is comprised of the sun, the solar planets and their satellites (moons). The sun being a middle-aged star accounts for about 99.8% of the total mass of the solar system. In the cosmic or galactic medium, the solar emissions create a spatial boundary around the solar system generally referred to as the heliosphere. The commonality of the plasma physics of the solar system family has enabled the amalgamation of solar physics, cosmic ray physics, solar wind physics, magnetospheric physics, ionospheric physics, and more into Heliophysics (Schrijver et al. 2016). Space weather refers to the spatio-temporal variations of different plasma and field parameters governed by the Sun and their dynamic interaction in the space surrounding a planet such as the Earth (Baker, 1998; Hanslmeier, 2010). The Space Weather of Earth originates from the emission sources in the Sun, and their evolutionary development in interplanetary space which eventually dynamically couple with the Earth's magnetosphere, and the ionosphere system. The science of 'space weather' is a very interesting area of research and is still unexplored with respect to many aspects (Koskinen et al., 2017; Morley, 2020, special issue of Space Weather, 2019).

1.2.1 Solar structure and activity

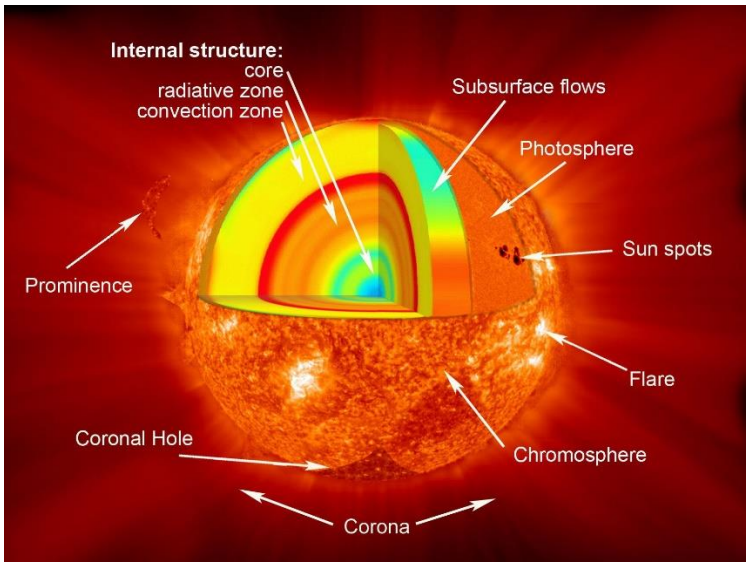

Figure 1.1: A schematic graphic showing the layers of the sun. [Credit: NASA/Goddard (https://www.nasa.gov/mission_pages/sunEarth/science/Sunlayers.html)]

The layers of the Sun: The structure of the sun can largely be divided into two layers- the inner layer and the outer layer. The inner layer is the energy-generating layer, which can be further classified into three main regions- the **convection zone**, the **radiation zone**, and

the **core** (Mullan, 2010). The outer layer, which forms the atmosphere of the sun, is classified into four major layers namely **photosphere**, **chromosphere**, **transition region,** and **corona** (Stix, 2004; Antia et al., 2003).

The temperature of the photosphere is referred to at ~6000 K, which is mostly referred to as the "black body curve" of the solar irradiance spectrum. The temperature dramatically rises to millions of degrees K in the Corona which is mostly responsible for corpuscular emissions (solar wind and mass ejections) from the sun. Several phenomena of the Sun still are not well understood and the coronal temperature and mass emissions are one of them.

The Sunspots and the solar cycle: Sunspots are those areas on the sun's photosphere where the temperature is lower and the magnetic field is stronger than the surroundings (Solanki, 2003). In the visible range of the electromagnetic spectrum, a sunspot appears as a dark region in contrast to the bright disc of the sun's photosphere. The total number of sunspots manifests a periodicity of ~11 years (Schwab cycle), known as the Solar activity cycle (Antia et al., 2003; Kusano, 2022). The Solar internal dynamo exhibits a major periodicity of ~22 years, which is known as the Hale cycle in solar magnetic activity (McIntosh et al., 2023). Additionally, solar activity has been noted (directly and indirectly) over several major scales of variabilities including 80-88 years (Gleissberg cycle), ~210 years, and ~2400 years over longer durations (Biswas et al., 2022).

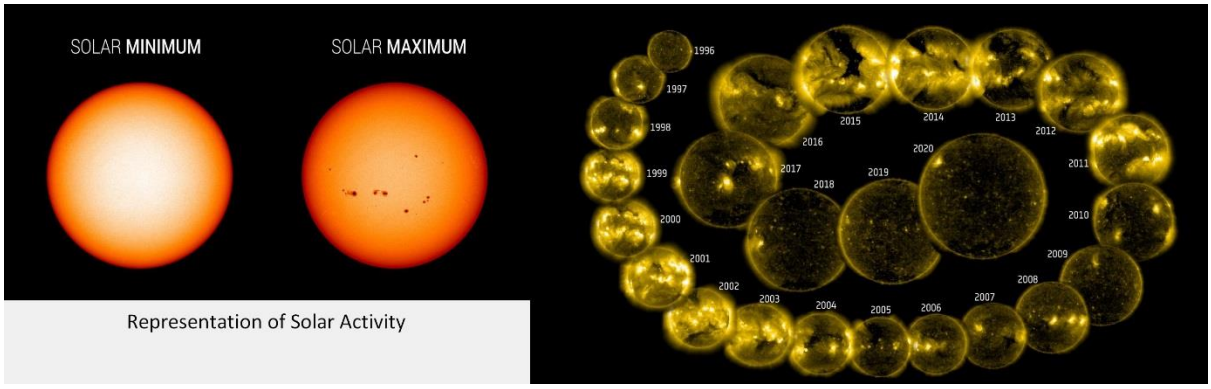

Figure 1.2: The observations from the SDO (Solar Dynamic Observatory) are used to represent the solar activity cycle in terms of the occurrence of sunspots in the left images which correspond to December 2019 (low activity) and July 2014 (high activity). The images on the right show a mosaic prepared using SDO observations of the sun in X-ray during 1996-2020, displaying solar cycles 23 and 24.

A recent review paper by Usoskin (2017) lucidly explains the transition of solar activity from the grand minimum to the regular solar cycles including various direct and proxy indices obtained from several kinds of observations. Long-term (a few hundred and thousand years) modulations in solar activity are known to affect the overall climate of the earth.

1.2.2 Emissions from the Sun

1.2.2.1 The Solar Wind

The solar wind is created by the continual stream of plasma i.e. a collection of protons, electrons, and other lighter-charged particles from the corona (Antia et al., 2003; Kusano, 2023). Due to the very high temperature at the origin, the thermal velocities become larger than the escape velocity eventually resulting in supersonic outflow. In terms of magnetohydrodynamics, the solar wind carries a magnetic field as frozen-in-field, owing to its very high conductivity. The solar magnetic field lines are carried into interplanetary space as Archimedean spirals (Parker, 1965) by the radial motion of the solar wind and is called the interplanetary magnetic field (IMF).

Coronal holes are a significant source of high-speed solar wind streams (Tu et al., 2005) and typically have speeds of around 700-800 km/s (Cranmer, 2009). In addition to these fast streams, there are also denser low-speed streams (300-400 km/s) (McComas et al., 2007) that originate from the equatorial coronal streamer belt, which is located in the closed regions near the equator. When high-speed solar wind streams from coronal holes come into contact with these slower streams, they can create a solar wind structure known as a corotating interaction region (CIR), which is characterized by enhanced density and magnetic field (Tsurutani et al., 1995).

The solar disturbance transients, which can affect the Earth, can be put together in a group of solar eruptive events of shorter time scales between a few seconds to days. A recent review article by Zhang et al. (2021) provides a detailed overview of several key studies, which advanced our understanding of these events, as well as listing many important review papers on this subject. A brief description of these events is provided below as part of the classification of solar eruptive phenomena.

1.2.2.2 Solar flare

A solar flare is a sudden and intense localized eruption of electromagnetic radiation in the Sun's atmosphere, caused by the rapid release of magnetic energy associated with complex magnetic field topology (Svestka et al., 1992). Solar flares are classified according to their peak flux (W/m^2) of soft X-rays with wavelengths of 0.1 to 0.8 nanometers (1 to 8 angstroms), as estimated by the GOES spacecraft in geosynchronous orbit. Flares last approximately from a few tens of seconds to several hours. The disturbances induced at the Earth by solar flares consist of the additional ionization at lower ionospheric regions produced by the intensified EUV and X-ray emissions which can cause significant radio blackouts and other geomagnetic effects collectively known as 'sfe' (Mitra, 1974; Tsurutani et al., 2009; Curto, 2020).

1.2.2.3 Coronal Mass Ejections (CME)

Coronal Mass Ejections (CMEs) are massive bursts of plasma and magnetic fields that are emitted from the Sun's corona and travel through interplanetary space (Gopalswamy, 2016).

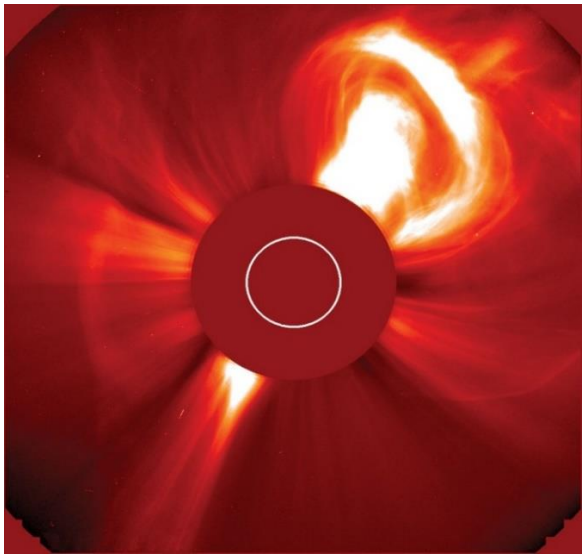

Figure 1.3: A very large CME is captured on 2 December 2002 with the Large Angle and Spectrometric Coronagraph (an instrument that blocks the solar disk to reveal the much dimmer corona) on board solar and Heliospheric Observatory (SOHO) mission. [Credit: Encyclopaedia Britannica (https://www.britannica.com/science/coronal-mass-ejection)]

It is important to note that Solar flares that are significant in size are frequently accompanied by CMEs (Harrison, 1995; Hundhausen et al., 1984, Liu et al. 2014). The cause of CME eruptions remains uncertain, but one theory suggests that the Sun releases magnetic

fields to decrease its energy. The Sun's coronal magnetic field becomes increasingly twisted and entangled, and it takes energy to maintain these structures (Priest and Wood, 1991). When the complexity reaches a certain threshold, it becomes more advantageous for the Sun to eject a portion of the magnetic field, resulting in a CME (Howard, 2011).

Interplanetary coronal mass ejections (ICMEs) are the CMEs that leave the Sun's Corona and travel through space. As they move away from the Sun, they can interact with other solar wind structures and gain energy and momentum (Gopalswamy et al., 2000). Subramanian and Vourlidas (2009) have emphasized that the flux carried by a typical CME toward the start of its journey is somewhat larger than what it carries when it reaches the Earth in the form of a magnetic cloud (MC). ICMEs are more complex than CMEs, with a more turbulent structure and a wider range of speeds and densities. The literature suggests that CMEs that are fast, associated with strong flares, and originate from a favourable location, i.e., in close proximity to the central meridian and at low or middle latitudes, have the highest potential to cause intense geomagnetic storms (Vourlidas et al., 2019) by generating strong ram pressure at the Earth's magnetosphere (Gosling et al., 1991; Srivastava and Venkatakrishnan., 2004; Zhang et al., 2007). Solar cycle 24 witnessed the anomalous expansion of CMEs, which can be attributed to the decrease in ambient pressure, and which led to weaker magnetic fields in the ICMEs, causing relatively subdued magnetic storms during the cycle making it the weakest in the space age (Gopalswamy et al., 2014).

1.2.3 Classification of Solar Wind disturbances

Solar wind disturbances can arise from both large-scale disruptions on the Sun and disturbances originating in interplanetary space (Yermolaev et al. 2019; Adekoya and Chukwuma, 2018). The sources in the solar wind that drive the geomagnetic storm and substorm processes can be classified according to their origin at the Sun or in the interplanetary medium. Broadly, the solar wind drivers can be classified into three major types (Yermolaev et al., 2019) - (a) the **quasi-stationary structures in the background flow** of the solar wind, (b) the **disturbed plasma streams**, and (c) the **shock waves**. A detailed description of the major solar wind sources or drivers of all types is given below.

1.2.3.1 Quasi-stationary structures in the background flow of the solar wind

Heliospheric Current Sheet (HCS): The magnetic field of the Sun covers all the planets, and the biggest thing is the "current sheet" (Hoeksema et al., 1983). It is like a big surface where

the direction of the sun's magnetic field changes from positive to negative. It causes the flapping of the sheet due to the tilt of the magnetic axis, creating regions of an opposite magnetic field called sectors (Smith, 2001). As the Earth moves around the sun, it sometimes goes through the current sheet, and when the solar magnetic field points south, it cancels out Earth's magnetic field, allowing solar wind energy to penetrate the local space and cause geomagnetic storms.

FAST and SLOW streams: There is no clear boundary between the slow and fast streams of the solar wind, just as there is no clear distinction in the topology of the coronal magnetic field between regions with the low divergence of magnetic field lines and regions with open field lines (Feldman et al., 2005; Richardson and Cane, 2012). Therefore, the line between the slow and fast streams is drawn arbitrarily. In general, plasma with velocities below ~450 km/s was considered SLOW, while plasma with velocities equal to or greater than 450 km/s was classified as FAST (Yermolaev et al., 2019) which in some studies is referred to be greater than ~600 m/s. It is worth noting that the slow plasma stream is denser and colder than the hot and rarefied high-velocity fast stream.

1.2.3.2 The disturbed plasma streams

Magnetic Cloud and EJECTA: Magnetic Clouds (MC) and EJECTA have rope-like magnetic fields, with magnetic pressure dominating over thermal pressure ($\beta << 1$) (Burlaga et al. 1981). While MCs are a subclass of EJECTA, they have a stronger and more regular magnetic field, which according to recent studies are found to bear varying magnetic structures near Earth compared to their point of origin at the Sun (Gopalswamy et al., 1998). Observational differences in MCs and EJECTA can be attributed to both the intensity of the CME on the Sun and the intricacies of the underlying magnetic rope axis (Schwenn, 2006). In general, MC, which is associated with the most severe geomagnetic storms, is classified as the strongest EJECTA.

SHEATH and CIR: In general, when a large-scale plasma volume with a frozen-in magnetic field overtakes a slower plasma volume, a compression region is formed at their boundary (Hajra and Sunny, 2022 and references therein). This compression region has higher values of plasma density, temperature, and magnetic field strength, with $\beta > 1$. Similar scenarios occur in the solar wind in two cases: (1) when a faster MC/EJECTA moves in a slower solar wind, a

compression region called SHEATH forms before it, and an interplanetary shock wave can be formed on the leading edge of SHEATH under certain conditions. (2) A fast solar wind stream can act as a piston, creating a Corotating Interaction Region (CIR) when there is a large enough velocity gradient (dV/dt). Although the general principle of formation is the same for SHEATH and CIR, they differ in the form of pistons that form them and in some observational characteristics (Tsurutani et al. 1988; Richardson et al. 2002).

RARE: In the solar wind, the opposite scenario can also occur when a fast plasma volume moves away from a slow volume to create a region of plasma density (N) less than 1 cm^{-3}. This creates a rarefaction region (RARE) that has limited geoeffectiveness (Yermolaev et al. 2019).

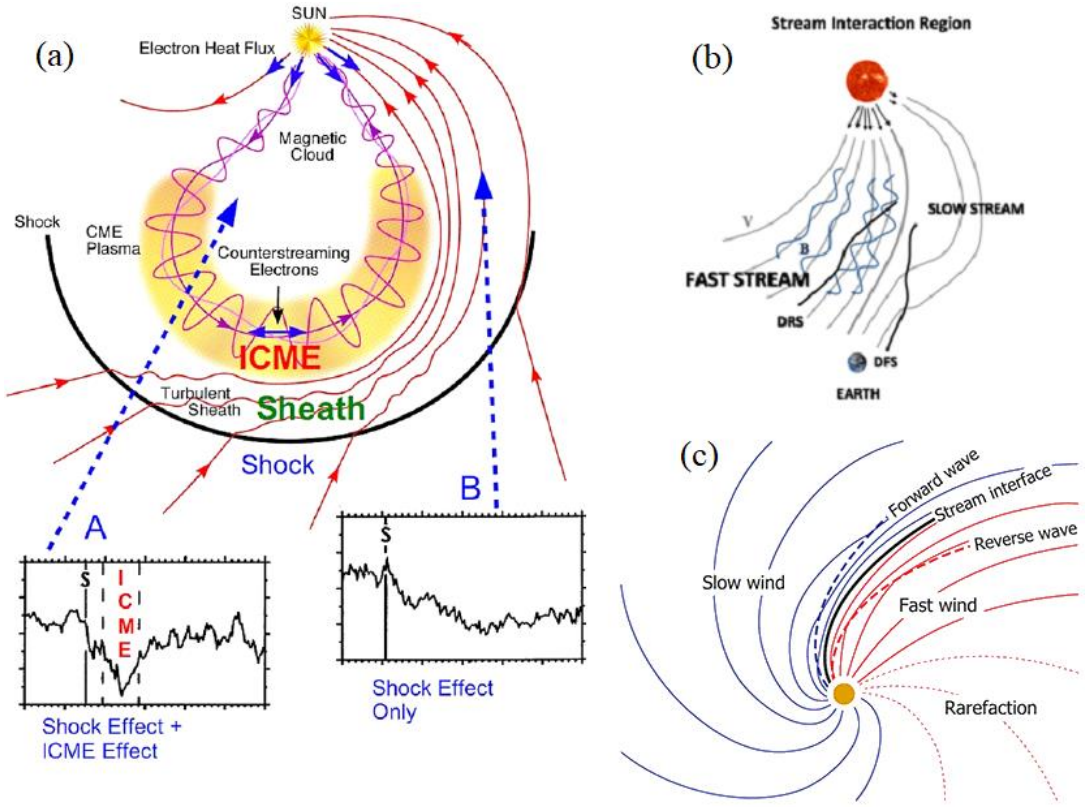

Figure 1.4: Schematic of (a) an Interplanetary Coronal Mass Ejection (ICME) and the associated shock and sheath. The ICME shown here features the flux rope or magnetic cloud structure (Figure adapted from Richardson and Cane., 2011 (modified from Cane, 2000 and Zurbuchen and Richardson, 2006)). (b) A CIR containing FAST and SLOW streams. Also, CIRs are bounded by fast forward–fast reverse shock pair (DFS and DRS) in the near-Earth orbit (Figure adapted from Kilpua et al., 2017). (c) RARE, FAST, SLOW, Forward, and Reverse shock waves (Figure adapted from Owens and Forsyth (2013).

1.2.3.3 The shock waves

Forward and Backward shock waves (IS and ISA): Sometimes, with large-scale structures, small-scale events such as the forward (IS) and backward (ISA) interplanetary shock waves also become important. Typically, the observation time for a shock wave front is around one minute, and it is difficult to identify these boundaries in most cases (Yermolaev et al. 2019). In most cases, interplanetary shock waves serve as natural boundaries of large-scale SHEATH and CIR.

1.3 Earth's magnetosphere and Solar wind-magnetosphere coupling

1.3.1 Formation and structure of Earth's magnetosphere

The Earth's magnetosphere is a region of space that surrounds our planet (Keith and Heikkila, 2020). This invisible force field acts as a shield, preventing harmful solar and cosmic particle radiation from penetrating our atmosphere and eroding it away (Gold., 1959; Spreiter et al., 1966; Russel., 1972). This magnetic environment has played a critical role in the habitability of our planet, allowing life to develop and thrive under the protection of the magnetosphere. Of all the rocky planets in our solar system, the Earth has the strongest magnetosphere.

1.3.1.1 The geomagnetic field and magnetospheric cavity

The Earth's magnetic field is best known to be generated by the motion of molten ferromagnetic materials like Iron and Nickel in its outer core (Merrill and McElhinny., 1983; Panovska et al., 2019). This process, known as the geodynamo, involves the generation of electrical currents from the motion of the liquid iron. The motion of the liquid iron is driven by a combination of factors, including the Earth's rotation and thermal convection (Merrill and McElhinny., 1983; Olsen et al., 2010).

The changes in the geomagnetic field can be broadly categorized into two different timescales. The **Secular or long-term variations** and the **Transient or short-term variations**. It is important to note that the transient variations are caused by currents generated in the magnetosphere-ionosphere system during geomagnetic storms and substorms (Gonzalez et al., 1994), while the secular variations occur over a long period of tens of years to millions of years

(Stewart, 1861; Cox et al. 1964; Courtillot et al., 1988). The best candidate model of the geomagnetic field in the present era is given by the international geomagnetic reference field (IGRF).

The magnetospheric cavity of the Earth is basically formed by the dynamic interaction of the Earth's magnetic field and the ever-forcing solar wind, which is permeated by an interplanetary magnetic field. This interaction deforms the Earth's dipolar magnetic field, creating a bow-shock structure on the dayside and a comet-like tail on the night side (Keith and Heikkila, 2020).

1.3.1.2 Major magnetospheric regions

Basic composition: Compositionally, the plasma within the magnetosphere consists primarily of electrons and protons, which originate from both the solar wind and the terrestrial ionosphere (Johnson, 1979).

However, the plasma is not uniformly distributed throughout the magnetosphere but rather is separated into two distinct regions known as the inner and the outer magnetosphere. The inner magnetosphere is commonly referred to as the co-rotating region of the magnetic field lines with the Earth, whereas, the outer magnetosphere is exposed directly to the interplanetary space with open and closed field line structures (Keith and Heikkila, 2020).

From the point of view of varying plasma and field properties, different regions of the Earth's magnetosphere can be defined (Eastwood et al., 2015) as given below in brief.

Bow shock: The supersonic and Alfvenic solar wind forms a steady bow shock upstream of an obstacle such as a planetary magnetosphere, the shock near the Earth's equatorial plane (Axford and Hines, 1961; Axford, 1962). The interaction of supersonic magnetized solar wind plasma with the Earth's magnetic field forms the magnetosphere and a fast magnetosonic wave, the bow shock, which then acts to divert the solar wind flow around the obstacle (Keith and Heikkila, 2020). The location and shape of shocks have been studied for over 40 years using various approaches, such as direct observations of spacecraft crossings. The boundary layer between the magnetosphere and the shocked solar wind (plasma downstream of the shock) is called the magnetopause. The configuration of both the magnetopause and the bow shock is very dynamic and depends on both the solar wind and magnetospheric properties (Merka and Szabo 2004). The bow shock position and shape are controlled by the obstacle size and shape,

upstream Mach numbers, and IMF orientation (Fairfield, 1971; Farris and Russell, 1994; Lu et al., 2019).

Magnetosheath: As the solar wind approaches the Earth's magnetosphere, most of its particles are deflected around it, creating an area known as the magnetosheath (Eastman et al., 1976; Lucek et al., 2005). Within this region, a mix of shocked solar wind and particles that have escaped the magnetosphere is found, with ion temperature generally exceeding electron temperature. The plasma properties of the magnetosheath are shaped by the density, velocity, and plasma beta of the upstream solar wind.

Magnetopause: The magnetopause (Chapman and Ferraro, 1933), which is the outermost boundary of the magnetosphere, acts as a barrier separating the primarily terrestrial geomagnetic field and plasma from the solar wind plasma (Schulz, 1995). The precise location of the magnetopause is determined by the equilibrium between the magnetic pressure within the magnetosphere and the dynamic pressure exerted by the solar wind. The pressure balance equation is given by -

$$\rho_{sw} v_{sw}^2 = \frac{B_{ms}^2}{2\mu}$$

where ρ is solar wind density V is the solar wind velocity and B is the magnetic field the subscripts sw and ms refer to solar wind and magnetosphere respectively. The magnetopause stretches to approximately 10 Earth radii (R_E) in the sunward direction along the Sun-Earth line, marking the outermost boundary of the magnetosphere. The solar wind dynamic and thermal pressure and the orientation of the dipole and the three components of the IMF control the shape and location of the magnetopause (Sibeck et al. 1991; Petrinec and Russell 1995; Merka and Szabo 2004).

Polar cusp: Located near the Earth's geomagnetic field poles, the polar cusps are funnel-shaped regions where the solar wind particles can directly enter the Earth's ionosphere (Frank, 1971; Russel, 2000). These regions are of particular interest as they provide an important entry point for the solar wind to interact with the Earth's magnetic field and ionosphere.

Magnetotail: The solar wind also stretches the terrestrial magnetic field in the anti-solar direction, forming a long, comet-like tail known as the magnetotail that can extend up to 100 Earth radii (R_E) in length. This region is shaped by the interaction between the solar wind and the Earth's magnetic field and is an essential component of the magnetosphere (Petrinec and

Russell, 1993; 1996). The magnetotail plays a significant role in the solar wind-magnetosphere-ionosphere coupling and formation of substorms (Russell, 1972; Akasofu, 2012).

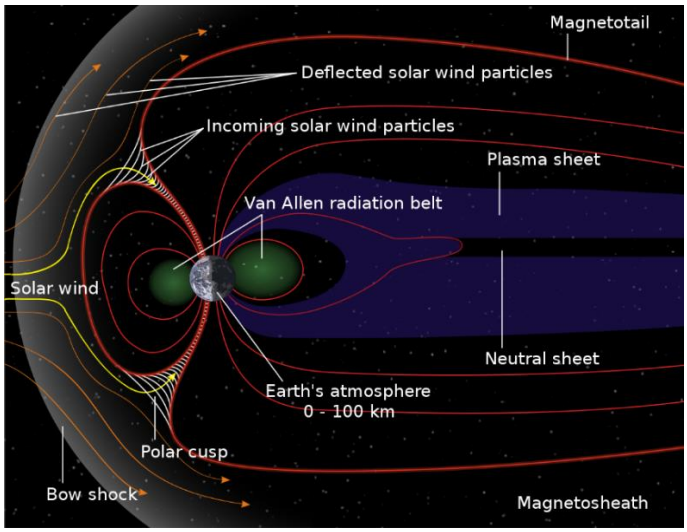

Figure 1.5: A schematic diagram showing the Earth's magnetosphere and different plasma regions inside it. [Credit: Wikipedia]

Plasmasphere: The plasmasphere is a region surrounding the Earth where the density of the plasma is higher than the ambient density. It is composed of cold and dense plasma that originates in the topside ionosphere (Carpenter and Park 1973; Goldstein, 2006). The density of the plasma exceeds 10^3 cm^{-3} and gradually decreases with the distance from the Earth. The ions in the plasmasphere typically have a temperature of 1-2 eV, which increases with the distance from the Earth. Plasmaspheric plumes and ion outflow produced during geomagnetic storms significantly contribute to the total ion outflow from the Earth's magnetosphere (Yamauchi, M. 2019; Dandouras, 2021).

Plasmapause: The plasmapause is a region in the plasmasphere where the density of the plasma drops sharply by an order of magnitude (Carpenter and Park 1973; Goldstein, 2006). The plasmapause separates the dense and cold plasma of the plasmasphere from the less dense and hot plasma of the outer radiation belt. The plasmapause is important as through this the transport of energetic particles between the inner and outer magnetosphere occurs.

Van Allen Radiation Belts: The Van Allen Radiation Belts, which were discovered by Van Allen in 1958, are the regions in the Earth's magnetosphere that are filled with high-energy charged particles, trapped by the geomagnetic field (Mann et al., 2016). There are two main belts: the inner belt and the outer belt, separated by a gap called the slot region, wherein, the energy of the particles varies from a few kilo-electron volts to several mega-electron volts

(known as 'killer electrons) (see the review by Li and Hudson, 2019 for details). The motion of the particles in this radiation belt is influenced by the Earth's magnetic field and by the interactions with other particles and with waves in the magnetosphere (Green and Kivelson, 2004).

Plasma sheet: The plasmasheet is a relatively thick region of hot and dense plasma that is located at the center of the magnetotail, extending about 4-8 R_E in thickness (DeForest and McIlwain., 1971; Hill, 1974). Here, the magnetic field pressure is dominated by the plasma pressure. The plasmasheet is a site of intense particle acceleration, where particles can reach energies of several mega electron volts. It also plays an important role in the dynamics of the magnetotail, as it is the source of the plasma that fills the tail lobes and the plasma sheet boundary layer. In addition, this region is a host of various important phenomena associated with magnetotail dynamics like the current sheet known as Neutral sheet current, dipolarization fronts, the flow of plasma bubbles and plasmoids, etc (Runov et al., 2011; Baumjohann and Treumann., 2012); Frühauff and Glassmeier., 2017).

Tail lobes: The tail lobes are regions outside the plasma sheet in the Earth's magnetotail that are bounded by the magnetopause at the front and the plasma sheet at the back (Cowley, 1980, 2000). Basically, these are plasma-free regions adjacent to the plasma sheet in the magnetosphere, characterized by a density of less than 0.01 cm^{-3}. The plasma in the tail lobes is typically cold and tenuous, and the magnetic field pressure dominates over the plasma pressure. The tail lobes extend from the end of the plasma sheet to the boundary of the magnetosphere, and they can stretch up to several tens of Earth radii (Baumjohann, 2002) to reach very near to the moon's orbit (Poppe et al., 2012; Cao et al., 2020).

Plasma sheet boundary layer (PSBL): The plasma sheet boundary layer is the transition region between the hot, dense plasma of the plasma sheet and the colder, less dense plasma of the magnetotail lobes (Eastman et al., 1984). The thickness of the plasma sheet boundary layer is typically a few thousand kilometers. During times of strong geomagnetic activity, the plasma sheet boundary layer can become highly unstable, leading to the release of huge amounts of energy and particles in the form of substorms. This region is very important from the aspect of nightside magnetic reconnection, which happens mostly in this region, leading to the release of energy and the acceleration of particles (Wellenzohn et al., 2021).

Neutral Sheet: The neutral sheet is a narrow plasma region that forms in the Earth's magnetotail where the magnetic fields of the Earth and the solar wind merge (Russell, 1973).

Basically, it is the boundary between the inward magnetic field of the northern tail lobe and the outward magnetic field of the southern tail lobe. Within the neutral sheet, magnetic fields from both sources are directed oppositely and cancel each other out. A detailed text by Keith and Heikkila (2020) provides a current understanding of recent advancements in the magnetospheric regions and their respective dynamical properties.

1.3.2 Solar wind-magnetosphere coupling

Solar wind-magnetosphere (SW-M) coupling refers to the physical interactions between the plasma and magnetic fields of the solar wind and those of the Earth's magnetosphere (Axford and Hines, 1961; Dungey, 1961; Akasofu., 1981). A brief overview of the coupling mechanism at large scale and ion/electron scales followed by a description of various current systems is given below.

1.3.2.1 The Dungey model and convection

The classical Dungey model, also known as the "open magnetosphere" model, proposed by Dungey (1961), is a theoretical model used to describe the behaviour of Earth's magnetosphere in response to the impinging magnetohydrodynamic solar wind. According to the Dungey model, when the z-component of the IMF (IMF-Bz) turns southward, it reconnects with the northward geomagnetic field through a process known as magnetic reconnection in the magnetopause. Conversely, during northward IMF-Bz conditions, the magnetosphere remains compressed due to the dynamic pressure of the solar wind, and the solar energy can enter through other mechanisms like viscous interactions (Cowley and Stenley, 2015).

These particles move the magnetotail where the nightside reconnection occurs following a convective cycle (Heikkila, 1990). Then, some of the particles undergo gradient and curvature drifts to relocate them in different parts of the magnetosphere to form different plasma regions; others gyrate along the magnetic field lines to reach the Earth’s ionosphere. The rate of reconnection during the cycle depends on the strength and the orientation of the interplanetary magnetic field, and the plasma conditions at the site of reconnection (Milan 2007, Seki et al. 2015). The duration of the reconnection cycle varies between planets, but on Earth, it takes around one hour.

1.3.2.2 Different coupling mechanisms

The coupling between the solar wind and Earth's magnetosphere-ionosphere system is a complex process that involves various mechanisms such as (i) magnetic reconnection (ii) viscous interaction (iii) cross-field diffusion and (iv) pressure fluctuations, etc. These processes result in the transfer of mass, momentum, and energy from the solar wind to Earth's magnetosphere-ionosphere system, leading to various space weather phenomena. Notably, the solar wind-magnetosphere-ionosphere system involves interactions at different spatial and temporal scales. Broadly, they can be segregated into two categories- large-scale and small-scale coupling. Large-scale coupling refers to the interactions between the solar wind and the Earth's magnetic field over long distances i.e. over tens to hundreds of thousands of kilometers, and timescales of hours to days. In contrast, kinetic-scale coupling involves the interactions of individual particles, such as electrons and ions, in the magnetosphere and ionosphere over much smaller scales, i.e. over several centimeters or meters in the timescale of seconds. Kinetic-scale processes are characterized by plasma waves, particle acceleration, and collisionless shocks. A brief description of the processes is given below which is important in the context of solar wind-magnetosphere-ionosphere coupling.

Magnetic reconnection: Magnetic reconnection is a fundamental process that occurs in plasmas containing magnetic fields, wherein, the field lines can become twisted and tangled, and through magnetic reconnection, the magnetic field lines break and reconnect into a different configuration and topology, releasing energy in the process (Hesse, 1988; Biskamp, 1996; Yamada, 2010, Fu et al., 2015; Burch et al., 2016; Torbert et al., 2018). Magnetic reconnection is a key mechanism for the conversion of magnetic energy into kinetic energy and thermal energy, and it is thought to play a critical role in a wide range of astrophysical phenomena, including solar flares, coronal mass ejections, and magnetospheric substorms. In these events, magnetic reconnection can cause the sudden release of large amounts of energy in the form of high-energy particles, radiation, plasma jets, etc. (see Figure 1.6).

Magnetic reconnection is also important in laboratory experiments with plasma, such as magnetic confinement fusion, where it can cause the loss of plasma confinement and hinder the success of the fusion process. In general, this is a very important phenomenon occurring in different astrophysical and laboratory plasmas like the solar flares, CMEs, prominence eruptions, coronal jets, Earth’s magnetosphere, X-ray flares in pulsar wind nebulae, active

galactic nuclei jets, edge of heliospheres, other planetary magnetospheres, laboratory fusion experiments, etc (Hesse and Cassak., 2020). Understanding the fundamental physics of magnetic reconnection is an open and crucial area of research in astrophysics, plasma physics, and star-planetary coupling processes in the space plasma.

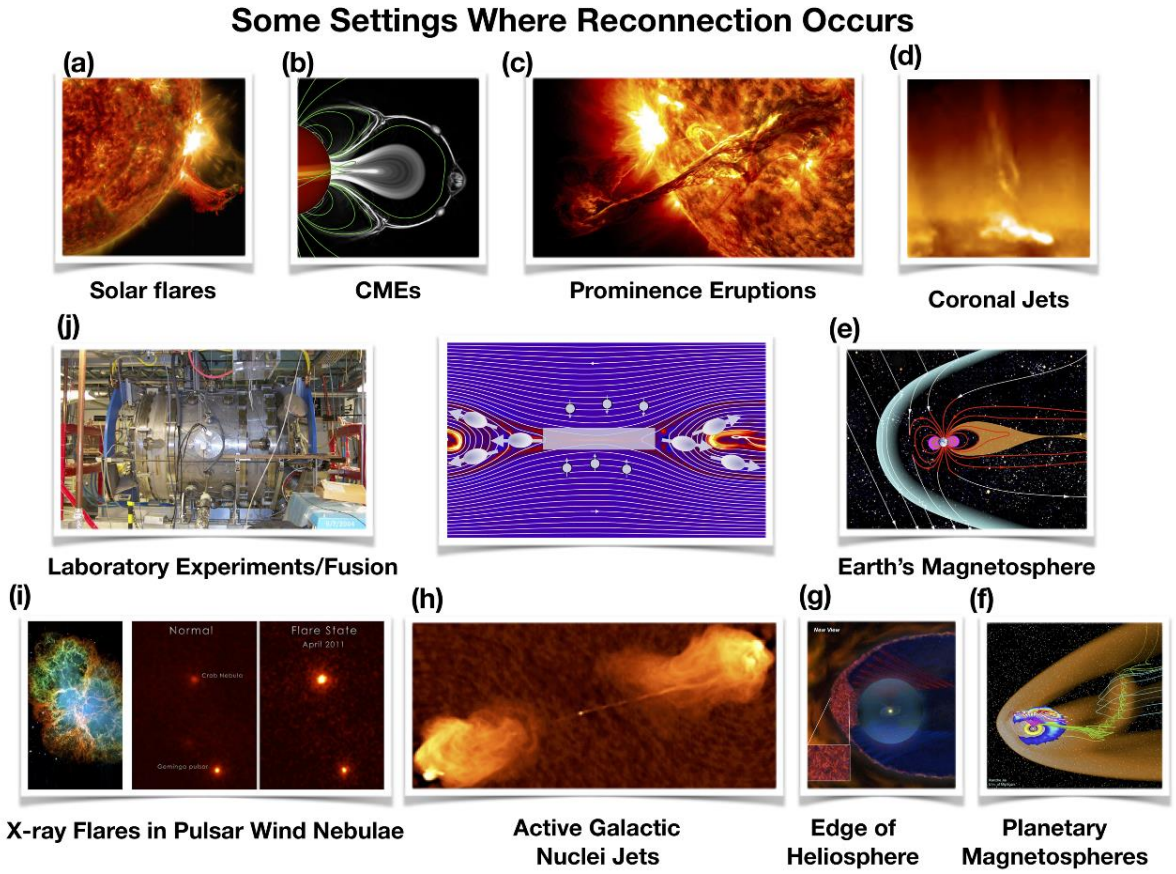

Figure 1.6: Examples of different astrophysical and laboratory plasmas where magnetic reconnection occurs (adapted from Hesse and Cassak, 2020, for illustration). The panels are arranged in a clock-wise fashion surrounding a pictorial representation of magnetic reconnection in the middle panel. A caption is provided below each panel (a-j) which is self-explanatory.

Viscous interactions: Viscous interactions refer to the transfer of momentum and energy between different plasma populations through viscous processes, such as collisions and frictional interactions (Axford and Hines., 1961; Axford, 1964; Tsurutani and Gonzalez., 1995; Borovsky, 2021). In plasmas, viscosity arises due to the interactions between particles and the presence of electric and magnetic fields. These interactions lead to momentum and energy transfer between different plasma populations, resulting in the dissipation of energy and the heating of the plasma (D'Amicis et al., 2020). In astrophysical systems, viscous interactions

can occur in a variety of contexts, such as in the accretion disks around black holes or in the interstellar medium. Sometimes, when the solar wind impinges on the Earth's magnetosphere, viscous interactions lead to the transfer of energy and momentum between different populations of particles, such as between protons and electrons or between different ion species. This can influence the properties of the solar wind, such as its speed and density, and can also affect the dynamics of the Earth's magnetosphere. In laboratory plasmas, viscous effects can be studied through experiments that involve the interaction between different plasma populations or the interaction between plasmas and material surfaces.

Cross-field diffusion: Cross-field diffusion is a process in which particles or energy are transported across a magnetic field in a plasma through random or turbulent motions (Tsurutani et al. 1981; Khotyaintsev et al., 2019). In plasma, cross-field diffusion can occur through a variety of processes, such as collisional diffusion, anomalous diffusion, or wave-particle interactions. Collisional diffusion occurs when particles collide with each other and exchange momentum and energy, leading to their diffusion across the magnetic field. Anomalous diffusion, on the other hand, arises due to the presence of turbulence or fluctuations in the plasma that cause particles to experience random motions and move across the magnetic field. Wave-particle interactions can also lead to cross-field diffusion, as particles can interact with waves and be scattered across the magnetic field.

Pressure fluctuation: Pressure fluctuations in the solar wind can play a key role in the coupling between the solar wind and the Earth's magnetosphere (Kepko et al., 2002). When the periodic density structures in the solar wind encounter the Earth's magnetosphere, they can lead to the generation of waves and instabilities in the magnetosphere, which can cause the magnetosphere to expand or contract (Viall et al., 2021 and references therein). In addition, pressure fluctuations in the solar wind can also cause changes in the magnetic field of the Earth, leading to magnetic reconnection events and the release of energy into the magnetosphere.

Coupling in the kinetic scale: Fundamentally the initial coupling between the solar wind and magnetosphere begins at a very short kinetic scale inside a very small region (Torbert et al., 2018). The manifestation of this short-scale transfer of energy and momentum is observed on larger scales as discussed above. The kinetic scale coupling processes basically refer to the individual motions and behavior of the particles at microscopic levels. These interactions are governed by the principles of kinetic plasma physics, which include the effects of particle acceleration, wave-particle interactions, and turbulence and are commonly known as magnetic

reconnection (Chen et al. 2008; Fu et al. 2015a, 2015b; Burch and Phan 2016; Macek et al., 2019a, 2019b). Thus, magnetic reconnection is a dominant solar wind-magnetosphere coupling process that occurs at small ion and electron kinetic scales and influences larger-scale processes. Magnetic reconnection occurs on the dayside magnetopause (Burch et al., 2016) and nightside magnetotail (Torbert et al., 2018), with the plasma sheet boundary layer (PSBL) between the plasma sheet and tail lobe playing a critical role in nightside reconnection and transfer (Cheng et al. 2016; Chen et al. 2019). These coupling processes transfer a significant amount of mass, momentum, and energy to the magnetosphere-ionosphere system from the reconnection site, with field-aligned currents (FACs) and electric fields supporting the transfer of energy from the reconnection regions to the ionosphere (Baumjohann and Treumann 2012; Petrukovich et al. 2014).

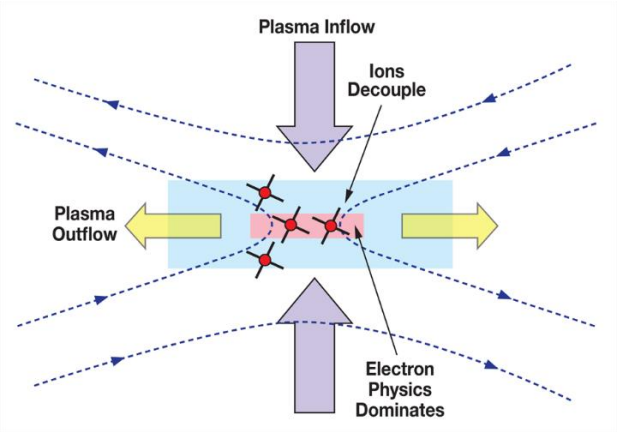

Figure 1.7: A cartoon representing kinetic scale magnetic reconnection is presented in the above figure. The faded red and sky-blue coloured rectangular regions represent an EDR and an IDR respectively. (Figure courtesy: NASA-GSFC (https://mms.gsfc.nasa.gov/science.html)

The two very important small kinetic-scale regions where magnetic reconnection occurs are known as the electron and ion diffusion regions. The **electron diffusion region (EDR)** is described as a region in which the magnetic field lines break and the plasma undergoes a rapid acceleration, leading to the separation of the magnetic field lines (Fu et al., 2015, 2016; Burch et al., 2016; Torbert et al., 2018). Briefly, a reconnection EDR is generally characterized by a steep gradient in the plasma acceleration and energy, a change in magnetic field line topology, and a rise in ideal and non-ideal electric fields. The **ion diffusion region (IDR)** is described as a relatively larger region with respect to dimension and scale by the above-mentioned studies, where the ions get separated from the magnetic field lines and the newly reconnected magnetic field lines separate from each other. The basic structure and

functions of the EDR and IDR in the magnetic reconnection process have remained a subject of intense research (Priest and Forbes, 2007; Hesse et al., 2011) and this subject is growing even as we write this thesis. Hesse et al. (2011) indicated the use of the MMS (magnetospheric multiscale mission) of NASA to uncover the then unresolved scientific questions. Lu et al (2022) have provided a lucid review of the magnetic reconnection at the magnetosheath, magnetopause, and magnetotail region including the recent studies and development on this subject using MMS observations. There are still many questions to be resolved concerning the quantification of the energy and structure of the EDR and IDR as well as the development of a general theory of magnetic reconnection (Pontin and Priest, 2022).

1.3.2.3 Magnetospheric current systems

The interaction between the Earth's magnetic field and the solar wind leads to the formation of the 'open' magnetosphere system and the generation of electric currents. The magnetospheric current systems can undergo dramatic changes in response to the transient solar wind conditions. Hence, the major current systems in the magnetosphere exhibit suddenly enhanced variability during such events. In the context of the research studies carried out during this thesis, a brief overview of some significant current systems is given below.

Magnetopause current: The magnetopause current or the Chapman-Ferraro current arises due to the diversion of ions and electrons in opposite directions that are perpendicular to the magnetic field at the magnetopause (Chapman and Ferraro, 1931; Berchem and Russell, 1982). Such an arrangement generates an electric field caused by the varying gyro-radii of these particles, leading to a separation of charges. The ions infiltrating deeper into the magnetopause contribute to an accumulation of negative charges in the external zone (Ganushkina et al., 2018).

Tail Current: The tail current is a flow of charged particles that occurs in the Earth's magnetotail, a region located on the nightside of the Earth's magnetosphere (Cowley, 2000). It is caused by the stretching and twisting of the magnetic field lines as they are pulled away from the Earth by the solar wind. The resulting electric field accelerates charged particles, creating a current that flows back toward the Earth. The tail current flowing along the elongated nightside magnetosphere accompanies the closure of the magnetopause current through the tail surface (Ganushkina et al., 2018). The tail current plays a crucial role in the dynamics of the magnetotail and can result in various phenomena such as substorms.

Neutral sheet current: At the center of the magnetotail, the central plasmasheet contains a horizontal current sheet, also known as the neutral sheet current, which is an important component of magnetotail dynamics (Baumjohann and Treumann, 2012).

Ring current: The ring current is a broad toroidal kind of band of charged particles that encircle the Earth in varying densities between 2 and 9 R_E around the equatorial plane (Frank 1967, Tsyganenko 1995, Ganushkina et al. 2018). Currents are carried by charged particles wherein the ions drift westward in the main part of the ring current while the electrons move eastward, resulting in a net westward current (See Figure 1.8). During the geomagnetic storms, the ring current becomes stronger and moves closer to Earth. (Kozyra and Liemohn., 2003; Keika et al., 2013; Ganushkina et al., 2010). The storm time development of westward (ring) current gradually generates a magnetic field that opposes the quiet time ambient magnetic field resulting in a decrease in the magnetic field strength over the equatorial and low latitudes.

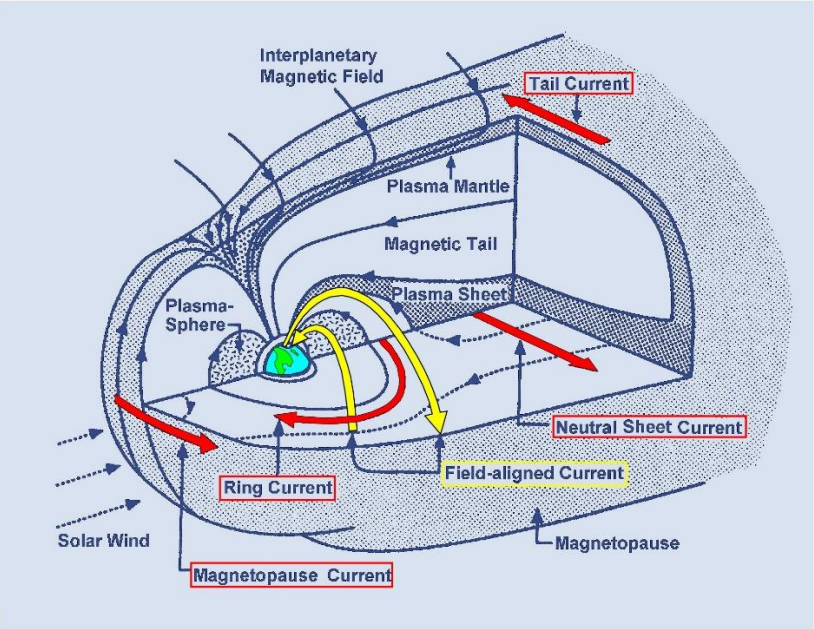

Figure 1.8: A schematic diagram showing the major current systems in the Earth's magnetosphere. (Modified from Kivelson and Russel.,1995).

The ring current is mainly composed of ions, with protons being the most abundant, but alpha particles and oxygen ions are also present in smaller quantities. The predominant carriers of energy in the ring current are ions, with a majority being protons. Nonetheless, alpha particles, a specific type of ion abundant in the solar wind, are also observed in the composition of the ring current. Furthermore, traces of O^+ oxygen ions are also found which generally come from the ionosphere according to many researchers. This diverse ion composition implies that

particles in the ring current likely originate from multiple sources from both the magnetospheric and ionospheric ends.

The ring current is known to have a strong local time-dependent amplitude, which results in an azimuthally asymmetric ring current. The **partial ring current** refers to the portion of the ring current that extends only partially around the Earth, rather than fully encircling it (Lühr et al., 2017), and forms the asymmetric ring current. This occurs when there is a non-uniform distribution of energetic particles within the ring current, which has been shown to occur due to substorms (Fukushima et al. 1973, Rostoker et al., 1997) during an ongoing geomagnetic storm (discussed in a later section). The ring current can be measured by the variations in the H-component of the ground magnetometer records during the geomagnetic storms, which is defined as the disturbance storm time (Dst) index. In a later section, we describe the Dst index in detail.

Field aligned currents (FAC): Field-aligned currents, also known as Birkland currents, are electric currents that flow parallel to the magnetic field lines in the Earth's magnetosphere but the continuity is facilitated through polar ionospheric regions (Iijima and Potemra, 1976a; 1978; 1982,). The flow of field-aligned currents facilitates the transfer of energy and momentum between the magnetosphere (Cummings and Dessler, 1967) and ionosphere (Baumjohann 1982), which leads to significant disturbances during geomagnetic storms and substorms (Hasegawa and Sato, 1979). Iijima and Potemra (1976a; 1976b) have described three major FAC systems namely the R0 (cusp current), R1 (Region-1), and R2 (Region-2) currents.

The cusp current, known as R0 FAC (Haraguchi et al. 2004; Milan et al. 2017), is associated with east-west flows in the dayside polar cap caused by magnetic tension forces on newly reconnected field lines. Whereas, the Region 1 and Region 2 currents connect the polar ionosphere to the magnetopause and inner magnetosphere. Milan et al (2017) have referred to this circuit as (MP-R1-I-R2-PRC-R2-I-R1-MP, where MP, PRC, and I refer to the magnetopause, partial ring current, and ionosphere, respectively) as the convection circuit, wherein the R2 FAC is known to be associated with the partial ring current. Further details on the FAC are given in subsection 1.4.3.1 in the context of the magnetosphere-ionosphere coupling.

1.3.3 Geomagnetic storms and substorms

1.3.3.1 Geomagnetic storms

The dynamic interaction between the solar wind and the Earth's magnetosphere leads to energy transfer to the magnetosphere-ionosphere system over several days, during which the geomagnetic field exhibits drastic variations including several changes in the size and shape of the magnetosphere. Thus, such durations qualify to be called a storm in the geomagnetic field. A systematic approach to identifying the storms, their phases, and classification according to the intensity of the storms has developed over decades (Perreault and Akasofu., 1978; Gonzalez et al., 1994; Lakhina and Tsurutani., 2016). Commonly, a geomagnetic storm is referred to by the level of depression in the Dst index (Iyemori and Rao, 1976), or similar other indices (Kp/ap/AA), which originate from the ground magnetic field perturbations. A classification provided by Gonzalez et al. (1994) is well-accepted in the community to refer to a Geomagnetic storm as moderate, intense, or super storm based on the level of the Dst index. Similarly, a statistical analysis of several geomagnetic storms has resulted in a broad classification of characteristics of Dst index variations (Kamide et al. 1998), which are associated with different durations and processes of the Solar wind-magnetosphere coupling. Accordingly, the temporal progression of a geomagnetic storm (see figure 1.9) is found to occur in phases corresponding to the storm sudden commencement (SSC), initial phase (IP), main phase (MP), and the recovery phase (RP) (Ebihara, 2019 and references therein).

(a) Storm sudden commencement (SSC): When the supersonic solar wind collides with the magnetopause, it compresses the dayside magnetosphere, rapidly increasing the magnetopause current. This induces a magnetic field that adds to the Earth's magnetic field, causing a sudden increase in the horizontal component of the geomagnetic field, known as storm sudden commencement (Chapman and Ferraro 1931; Milan et al., 2017). This typically has a rise time of a few minutes, corresponding to the propagation time of MHD waves from the magnetosphere to the observation point. However, not all storms exhibit SSC.

(b) Initial phase: The initial phase occurs after the SSC and is characterized by a relatively stable disturbance in the H component of the geomagnetic field. This phase is due to the sustained compression of the solar wind and is determined by the magnetopause current. Its duration can be calculated by subtracting the onset of the main phase from the sudden commencement. However, not all storms exhibit an initial phase.

(c) Main phase: When a magnetic storm occurs, the most important phase is known as the main phase. This phase is initiated by a decrease in the H component of the magnetic field, which falls below its normal pre-storm value. This decline is caused by the enhancement of the westward flowing ring current (Gonzalez et al., 1994). During the main phase, which can last from a few hours to a few days, the magnetic field experiences significant fluctuations and disturbances. Understanding the main phase of a magnetic storm is crucial for predicting and mitigating its potential impact on Earth and space-based technologies.

(d) Recovery phase: Following the main phase of a magnetic storm, the magnetic field gradually relaxes back to its pre-storm level, marking the beginning of the recovery phase. This process is initiated by the weakening or disappearance of the southward component of the Interplanetary Magnetic Field (IMF), which causes the decay of the ring current and a gradual return of the horizontal component of the magnetic field to its normal value (Gonzalez et al., 1994; Tsurutani and Gonzalez 1997; Kamide et al., 1998; Schunk and Nagy., 2000). The recovery phase occurs in several stages, as the reconnection rate reduces and the injection of new particles into the ring current decreases, moving the convection boundary outward. As depleted flux tubes within this expanded boundary are filled with cold ionospheric plasma, the overlap of this cold plasma with the energetic ring current ions increases the ring current loss rate due to charge exchange and pitch angle scattering. These interactions gradually decay the ring current over several hours to days.

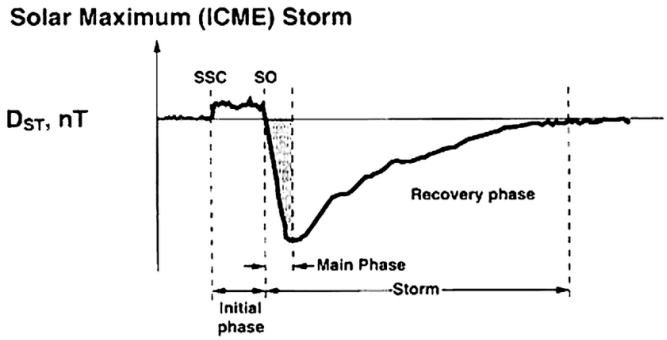

Figure 1.9: A schematic representation of different phases of a geomagnetic storm (Figure adapted from Tsurutani et al. 2006) associated with ICME structures in the solar wind.

Multi-step development of geomagnetic storms has also been reported (Wu et al. 2016; Keika et al., 2018a, 2018b, 2022), which is caused due to consecutive multi-hit of magnetic cloud and multi-step development of ring currents in the magnetosphere. The recent studies by Gopalswamy (2015), Liemohn et al. (2010), Jin et al. (2017), Green et al. (2018), and Webb

and Nitta (2018) add more to the existing knowledge and understanding of how solar wind and coronal mass ejections (CMEs) originate and traverse through interplanetary space and eventually affect the magnetosphere-ionosphere coupling and development of geomagnetic storms and substorms through more complex and intricate theoretical treatments and multi-scale observational evidence.

1.3.3.2 Geomagnetic substorms

The present understanding of substorms processes and associated phenomena is based upon decades of observational evidences and theoretical developments (Akasofu, 1981; Gonzalez et al., 1994). Accordingly, the substorms are classified as either isolated events or events associated with geomagnetic storms (Gonzalez et al., 1994; Kamide et al., 1998). A significant advancement in the storm-substorm relation was made by Kamide (1992) by clarifying the main phase of a geomagnetic storm can occur without any substorm and substorm can occur with or without a geomagnetic storm. Following Rostoker et al. (1980) and Hoffman et al. (2010), a generalized description of a substorm can be given by "transient process initiated on the nightside of the earth in which a significant amount of energy derived from the solar wind-magnetosphere interaction is deposited in the auroral ionosphere and magnetosphere". A consistent theoretical and observational understanding evolved during the Chapman conference in 1997 (Siscoe 1997), wherein, leading studies by Iyemori and Rao (1996); McPherron (1997); Wolf et al (1997), and Siscoe and Petschek (1997) eventually explicated the long-standing questions on the storm-substorm relationships. The observations and theoretical simulations, both converged on one specific manifestation that the main phase of a geomagnetic storm is not primarily driven by substorms but by the magnetospheric convection, and that the substorms during the main phase of a storm can also positively contribute to the development of ring current. However, Akasofu (2003) further stressed upon development of an integrated framework on the paradigm of the storm-substorm relationship, which must consider all the observational facts reported so far and build a theoretical understanding, that could explain the corresponding variations. In this context, Sharma et al. (2003) have provided an inclusive idea based on the formation and composition of the ring current (ionospheric O^+ ions) during the main phase of a geomagnetic storm. Further significant advances in the substorm onset (triggering) and driving conditions are made using SuperMag network observations by Newell and Gjerloev (2011), and Newell and Liou (2011). Studies on the

storm-substorm relationship are continued to date, for example, McPherron (May 2023), has revisited the subject through a robust statistical analysis.

In general, the process of a substorm can be described by three phases: the growth phase, expansion phase, and recovery phase (See Figure 1.10). As noted above, each phase has its origin in the processes involved for example the **growth phase** results from stretching of the magnetic field lines and thinning of the magnetotail which could eventually energize the magnetospheric plasma.

In the **expansion phase**, the stretched magnetic field lines become unstable and break apart, releasing energy and plasma into the magnetotail region (Akasofu, 2017). This results in a flow of plasma and electric currents Earthward along the magnetotail, which eventually forms the **substorm current wedge**. Finally, the magnetic field lines relax, and the plasma flow returns to its normal state during the **recovery phase**. The substorm current wedge dissipates and the magnetosphere returns to its pre-substorm state.

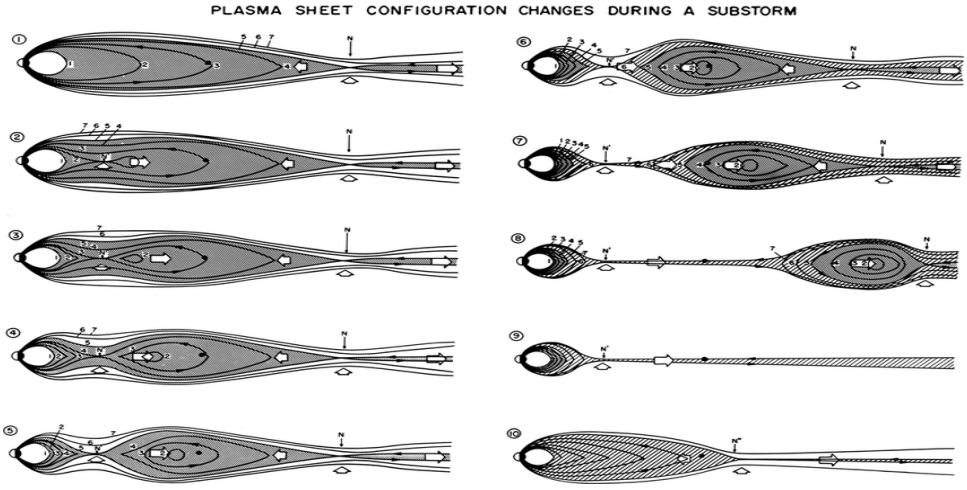

Figure 1.10: A schematic diagram representing the Substorm sequence in the noon-midnight meridian plane (Figure adapted from Hones, 1979). Sequentially, (1) the substorm growth phase starts, and the tail stretches and thins; (2) magnetic reconnection happens in the near tail region; (3-8) this leads to the development of a near-Earth neutral line, followed by the growth and ejection of a plasmoid; (7-9) the plasmoid departs and leaves a thin "post plasmoid plasma sheet" behind. (9-10) during the recovery phase, the near-tail plasma sheet gets refilled and the tailward retreat of the neutral happens.

During a geomagnetic substorm, auroral activity in the auroral ovals is significantly intensified, along with a significant increase in ionospheric current flow during the substorm's expansion phase. There are two main ways in which this current is amplified. Firstly, the

auroral electrojet is enhanced due to the increased convection, which commences during the growth phase of the substorm. Secondly, the substorm electrojet or **substorm current wedge** is responsible for the additional current flow, and it is linked to the discharge of magnetic energy in the magnetotail (Kepko et al., 2015). The current in the substorm current wedge or substorm electrojet flows westward in the midnight sector, and it is connected to cross-tail currents through field-aligned currents. The development of the substorm current wedge is an outcome of the reconnection process that takes place in the near-Earth magnetotail.

During the growth phase of the substorm, the magnetic flux in the tail lobes rises, and the cross-tail sheet becomes thinner due to the increased pressure from the lobes. Once a part of the current sheet reaches an appropriate threshold, reconnection begins spontaneously near the center of the current sheet. This process disrupts the cross-tail current, and a portion of the current is diverted towards the ionosphere along magnetic field lines in the form of the substorm current wedge. Approximately an hour after the substorm onset, the ionospheric current flow and the auroral activity begin to decrease, and the substorm recovery phase starts. This phase lasts for a few hours, and it ends when the magnetosphere returns to a quiet state. Subsequent studies by Keika et al. (2018a; 2018b; 2022) reported several cases of intra-magnetospheric energization, and generations of charged particles followed by plasma flow and demonstrated the multi-step development of geomagnetic storm or substorm. Koskinen (2011) has given a lucid explanation of the storm-substorm processes including the formation of the substorm current wedge showing the diversion of the cross-tail current into the ionosphere

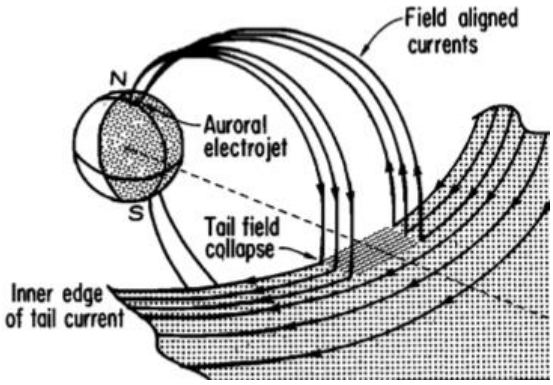

Figure 1.11: A schematic of the substorm current wedge (Figure adapted from McPherron et al., 1973), showing the diversion of the cross-tail current into the ionosphere during geomagnetic substorms. Each pointed line represents the current flow and its direction. (https://www.issibern.ch/teams/scw/Proposal.html).

Supersubstorms: As noted in the above subsections, the response of the magnetosphere to the transient solar events produces different classes of geomagnetic storms, with the most intense geomagnetic storm referred to as "super storms". On the other side, the substorms can occur in association with or without geomagnetic storms. In the category of the substorms, the extreme events are referred to as "Sueprsubstorms". As per the criteria defined by Tsurutani et al. (2015), extremely intense substorms with Supermag lower index (SML) ≤ −2500 nT are identified as supersubstorms. Owing to the intense magnetospheric response, Supersubstorms may also have a substantial impact on satellites, communication and navigation systems, power grid, technological devices, international space stations, etc. It is known that the most intense currents in the ionosphere happen during substorms, which can occur repeatedly throughout magnetic storms, as well as outside of them. When the substorm currents exceed amplitudes of 10^6 A, they induce currents in conductors on the ground, which can cause overheating and, in some cases, failure of transformers (Pulkkinen et al., 2012; Schrijver and Mitchell, 2013). The supersubstorms have been reported in some of the previous studies in recent past (Hajra et al., 2018; Adhikari et al., 2017), however, a complete understanding of the processes that could trigger the supersubstorms have not been established yet. This thesis is an effort to understand such extreme space weather events with a comprehensive understanding of the sources of the supersubstorm including solar wind-magnetosphere-ionosphere coupling and consequences. Details of the identified gap areas and the aim of the thesis in this context are given in the last section of this chapter.

1.4 Earth's ionosphere and Magnetosphere-Ionosphere coupling

The Earth's (neutral) atmosphere can be divided into several layers, each with distinct characteristics and boundaries. Primarily, the atmospheric profile can be divided into a few layers based on the vertical temperature variations (see detail in Wallace and Hobbs, 2006). These layers are called as troposphere (up to ~17 km over the tropics), stratosphere (~17-50 km), and mesosphere (~50-90 km) according to the temperature profile of the atmosphere.

The atmospheric (gaseous) composition is found in the same proportion up to the turbopause altitude (~100 km) due to well-mixing, however, it changes according to the diffusive separation in the upper atmosphere, known as thermosphere (up to ~1000 km). Eventually, the vertical expansion of the atmosphere extends up to an altitude of about 10,000 km, known as the exosphere, which gradually transforms into a very-very thin atmosphere (almost a space vacuum).

1.4.1 The Earth's ionosphere

The Earth's ionized part of the atmosphere is known as the "ionosphere" where free electrons and ions can significantly impact radio wave propagation. The ions and electrons are produced by the process of photoionization, which is an altitude-dependent process and thus creates a sufficient number of electron density that increases upwards from ~50 km to ~200 km. Above the altitude of ~200 km, gradually the photoionization yield decreases but the transport processes dominated by diffusion extend the ionospheric presence up to ~1000 km (Rishbeth and Garriot, 1969).

During the daytime, solar X-ray and extreme ultraviolet radiation are the primary ionization sources, and the ionization rate depends on the intensity of the ionizing radiation, atmospheric density, composition, and ionization cross sections of atmospheric constituents at a given altitude. The three main atmospheric constituents, N_2, O_2, and O, are ionized by incoming solar radiation, producing primary ions such as N_2^+, O_2^+, N^+, O^+, and NO^+, each of these species maintains a different vertical profile Various physical, chemical, and dynamical processes result in the redistribution of this ionization, forming distinct ionization peaks and layers (regions) denoted by the symbols D (~60-90 km), E (~90-120 km) F1 (~140-210 km), and F2 (above 210 km) (see excellent texts by Rishbeth and Garriot, 1969; Rees, 1989; Schunk and Nagy, 2004). An additional layer, F3, is also known to exist, primarily over the equatorial and low latitudes owing to the vertical ExB drift-dominated transport (Balan and Bailey, 1995; Venkatesh et al. 2020 and references therein).

The layers below ~220 km are formed as a product of photoionization which naturally become extinct beyond the sunset, thus creating a large difference between the day and night time ionospheric profiles. During the daytime, the **F-layer (region)** splits into two distinct layers- **F1 and F2-layer (region)** under the effect of varying rates of production, recombination, and diffusion varying with altitude. However, during the night time, only the F2 layer, which is produced majorly through vertical diffusion and transport processes, carries a significant amount of ionization with longer lifetimes owing to the lower recombination rate at those altitudes (Rishbeth and Garriot, 1969; Rees, 1989) The ambient electron density profile shows gradual changes under the effect of the solar activity cycle (~11 years). Apart from the local time and the solar activity-related variations, the electron density profile also varies with changes in season and latitude. Additionally, the forcing from solar transient events like solar flares and geomagnetic storms can drastically change the electron density profile.

1.4.2 Ionospheric current systems

Ionospheric current systems refer to the various electric current systems that flow within the ionosphere. The ionospheric currents are driven by a variety of factors, under the mutual interaction of the atmosphere and the Earth's magnetic field (dynamo) and the solar wind-magnetosphere coupling, etc. Major current systems that are pertinent to this thesis include the Sq (solar quiet), equatorial and auroral electrojets, and the field aligned currents (FACs), are briefly described below.

Sq current (Solar quiet current): The tidal motions in the atmosphere are generated by differential solar heating (Schuster and Lamb, 1889). The pressure gradient eventually causes tidal winds in the atmosphere. The heating of the atmospheric column varies with the altitude, and thus, the tidal modes produced in the lower atmosphere in combination with the local thermospheric modes, result in the thermospheric winds (Forbes and Lindzen, 1976; Onwumechikli, 1997; Pedatella 2011). In a simplistic representation of the atmospheric dynamo (Forbes, 2007), the horizontal motions of neutrals at the E-region altitudes produce ion currents across the magnetic field lines. This motion primarily forms the solar quiet or Sq current system (See a lucid review by Yamazaki and Maute, 2017 and references therein). The inhibition of current continuity at the solar terminator results in a primary eastward electric field over the equatorial and low latitudes on the dayside. Eventually, a complex interplay of the primary electric field in the presence of anisotropic ionospheric conductivity produces a latitude and local time-dependent current system (See Figure 1.12).

Equatorial electrojet (EEJ): The equatorial electrojet (EEJ) is a very special current system found flowing eastward in a narrow belt around the dip equator (Thick arrow over the dip equator in Figure 1.12) during the daytime (see details in Forbes, 1981; Reddy, 1989; Kelley, 2009; Onwumechikli, 1997). The main reason behind the generation of the equatorial electrojet in the eastward direction is the generation of Cowling conductivity (σ_C), which is generally much greater than Hall (σ_H) and Pederson ((σ_P) conductivities. In the E-region of the ionosphere, $\sigma_H >> \sigma_P$, hence, eventually yields a very high value of Cowling conductivity represented as- $\sigma c = \left[\sigma p + \frac{\sigma H^2}{\sigma p}\right]$. The variabilities of the EEJ system during geomagnetically disturbed periods are highly dependent on the intensity of the geomagnetic storm and couplings in the solar wind- magnetosphere-ionosphere system (Dashora et al., 2009; 2019; Yamazaki and Kosch, 2015; Yamazaki and Maute, 2017).

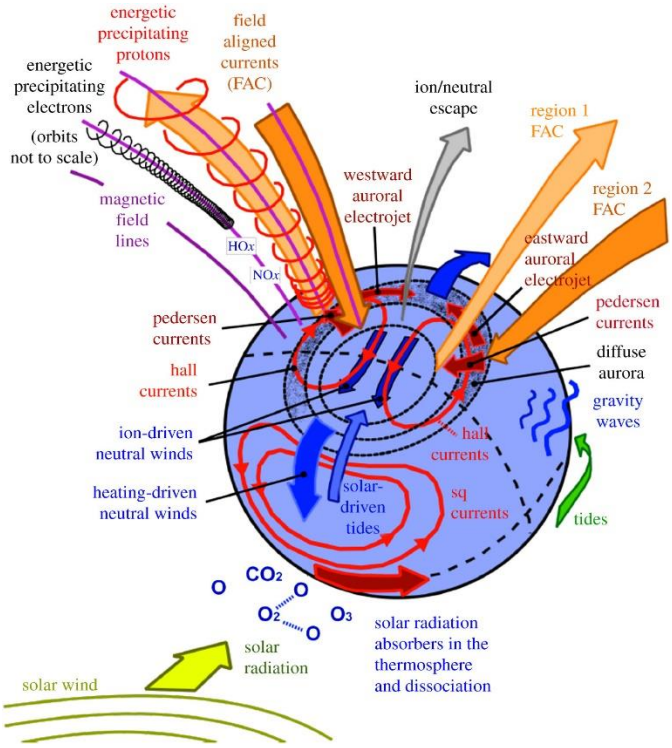

Figure 1.12: A schematic overview of ionosphere-thermosphere processes and their interaction with the magnetosphere and the solar wind, leading to the generation of various current systems (Figure adapted from Sarris et al., 2019)

1.4.3 Magnetosphere-ionosphere coupling

The transfer of mass, energy, and momentum between the magnetosphere and ionosphere through various physical processes is referred to as magnetosphere-ionosphere coupling. These processes include different kinds of electric fields, electric currents, particle precipitation, heating as well as wave-particle interactions, and turbulence.

1.4.3.1 FACs and PCPD

Field Aligned Currents (FACs): In one of the subsections above (section 1.3.2.3), the FACs are introduced as part of the magnetospheric current systems. However, the FACs play a major role in magnetosphere-ionosphere coupling (Ganushkina et al., 2015; 2018; Adhikari et al. 2018), by facilitating the dynamic connection from the reconnection sites located at the magnetopause and magnetotail (substorm-related dynamics) to the polar ionosphere (Siscoe et al. 1991) have explained the coupling mechanism convection driven voltage generator. The Region-1 FACs originated at the low latitude flanks of magnetopause (Ebihara and Tanaka,

2022 and references therein), and flow into the polar ionosphere along the reconnected (open) magnetic field lines from the dawn side. Thus, Region-1 FAC is the source of the ionospheric DP2 current system over the auroral region (detail below in a subsection), and, the current conservation leads the Region-1 current to flow out of the ionosphere from the dusk side (Iijima and Potemra, 1976a). The Region-1 current flows in the poleward part of the auroral region, whereas, the Region-2 FACs flow in the equatorward part of it with the opposite polarity to that of Region-1 FACs (See Figure 1.13). In the last two decades, the understanding of the FACs has enhanced multi-fold from a simple statistical mapping (Iijima and Potemra, 1976a) to a much more complex pattern owing to the recently available precise and multi-point spacecraft observations and inversion techniques. For example, the advances made in this context can be given in chronological order as Weimer (2001), Papitashvili et al. (2002), Anderson et al., (2014), and Edwards et al. (2020) and references therein. The sequences of development of the Birkland currents or the FACs, show the physical coupling processes that begin with the southward excursion of the IMF in the main phase, followed by the reconnection at the magnetopause and the anti-sunward convection of the open field lines. The local time-dependent development of the R1 and R2 currents in the day and night side (Anderson et al. 2014) further determines the penetration electric field from high to low latitudes.

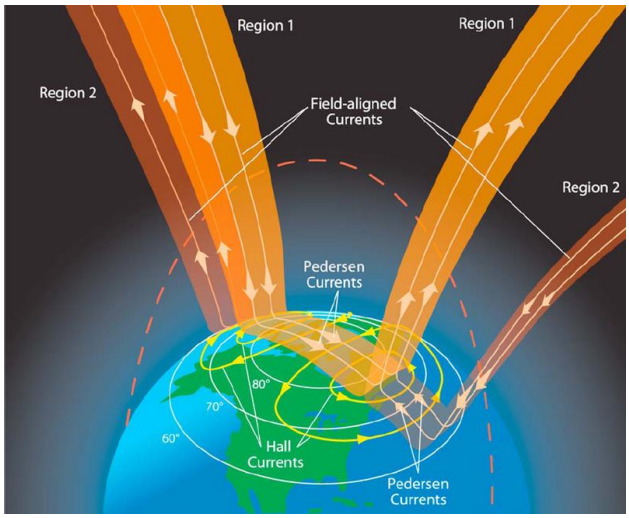

Figure 1.13: A schematic diagram of magnetosphere-ionosphere coupling via field-aligned Region 1 and 2 and Pederson and Hall currents in the ionosphere (Figure adapted from Le et al., 2010)

PCPD (polar cap potential drop): The amount of magnetic flux and plasma flowing through the magnetosphere, in other words, the magnetospheric convection, can be measured through the PCPD. As noted above, the reconnection in the dayside drives the convection, so an

equivalent electric field ($E=-V_{SW}$ x IMF-Bz) can be considered mapping to the high-latitude ionosphere. The electric field thus can be expressed as the divergence of the potential across the polar cap known as PCPD (Φ_{PC}). (Reiff et al., 1981; Ahn et al,. 1983; Boyle et al., 1997, Adhikari et al. 2018). The difference in the potential between the dawn cell (where the electric field reaches a maximum) and the dusk cell (where the electric field attains a minimum) is referred to as the cross polar cap potential (CPCP) (Liu et al., 2019) or polar cap potential drop (PCPD). The PCPD has long been used as an index to determine the solar-wind-magnetosphere-ionosphere coupling, however, at the same time it is recognized that the Φ_{PC} exhibits saturation limit for increasing degree of convection at large values of IMF (Ridley, 2002; Shephard, 2007). Recent studies on the estimation of PCPD show an efficient estimation using the SuperDARN radar and machine learning (Liu et al., 2019). Here, it shall be mentioned that there exists another measure of magnetic activity in the polar cap, which is known as the PC index (Troshichev et al., 2006). PC index which can be determined by using the magnetometer observations from the polar latitudes and the merging electric field (see details in section 1.5.2).

1.4.3.2 Auroral electrojet and DP2

Auroral electrojet: The auroral oval exhibits a strong and persistent horizontal electric current system at about E region altitudes during enhanced magnetospheric convection and particle precipitation. This current system is known as auroral electrojet (Bostrom, 1964; Devis and Sugiura, 1966). The auroral electrojet is composed of two distinct, yet coupled, loops of current, known as the eastward and westward auroral electrojet. A review on auroral electrojet by Feldstein et al. (1997) shows the formation and expansion of the structure of both the eastward and westward electrojets during geomagnetic storms, which largely depend upon the local time. Our understanding of the auroral electrojet and its variability has grown from the ground network of magnetometers like SuperMag (Newell and Gjerlov, 2011) and the SuperDARN radars. The AE index, its development and manifestation of the geomagnetic activity, along with the equatorward expansion of the polar disturbances, all are associated with the ever-changing structure and variability of the auroral electrojet system. An equivalent current can be derived from ground magnetic perturbations (Kelley, 2009) which can be fine-tuned using high latitude ionospheric conductivity, which varies in space and time with the intensity of the geomagnetic storms and substorms. The structure and expansion of the auroral electrojet system during increased magnetic activity and their association with R1/R2 FACs

are studied by Feldestien et al. (2006) using a chain of magnetometer, through the CHAMP satellite observations and Space Weather Modelling Framework (SWMF) comparison (See for details Wang et al. 2008).

DP2 Fluctuations: The DP2 (Disturbance Polar two) fluctuations in the horizontal component of magnetic field (H) have historically been defined by Nishida (1966; 1968) with an equivalent current system consisting of two vortices over the polar cap. Kikuchi et al. (1996) have explained that the DP2 fluctuations are caused by a Hall current system (auroral electrojet) at auroral latitudes and by a Pedersen current enhanced by the Cowling effect at the dip equator, both of which are controlled by the convection electric field. The geomagnetic disturbances, typically, during geomagnetic storms and substorms can produce varying DP2 signatures around the globe (Kikuchi et al., 2008; Amory- Mazaudier et al., 2017). The convection electric field associated with the DP2 can instantaneously penetrate to the equatorial and low latitudes (Kikuchi and Araki, 1979) and hence the DP2 fluctuations show a global imprint and consequences.

1.4.3.3 Joule heating and Auroral particle precipitation

Joule heating in the ionosphere is primarily a result of the Ohmic interaction between the ionospheric plasma and the electric fields generated by the Earth's magnetosphere. (Akasofu, 1981). When charged particles in the ionosphere move through these electric fields, they experience a force that causes them to move. As the ionospheric plasma has a finite resistance, the flow of electric current leads to the generation of heat, which manifests as Joule heating. This process can lead to significant heating of the ionospheric plasma and neutrals, causing an increase in temperature. Joule heating is an important energy transfer mechanism in the ionosphere, with significant effects on its structure and dynamics (Rodger, 2001 and references therein; Østgaard et al., 2002). The estimation of Joule heating has been known to depend upon the method and experimental technique (Guo et al., 2012; Zhu et al., 2018). The theoretical and experimental methods of calculation of the energy dissipation through Joule heating such as AMIE, have been improved by various studies (Rastätter et al., 2016; Richmond, 2010; Weimer, 2005 and references therein).

The auroral particle precipitation is a term associated with high energy magnetospheric particles bombarding the high latitude region. Particles with mirror points below 100 km altitude are prone to deposit their energy through ionization, aurora, and heating as a result of encountering a higher concentration of neutral particles at this altitude (Cole,

1962, 1971; Rees, 1975; Østgaard et al., 2002). Several studies have estimated that the dissipation of power resulting from auroral particle precipitations has a linear correlation with the AE index (Ahn et al., 1983; Akasofu, 1981; Lu et al., 1998; Richmond et al., 1990; Spiro et al., 1982).

Both the phenomena, the Joule heating, and the auroral particle precipitation have shown significant variability from event to event. Previous studies have given descriptions of many attempts to quantify these two terms following different methodologies (see Chapter 2 for details). This thesis makes a concerted effort to estimate the energies associated with these phenomena (see Chapter 3 for details).

1.4.3.4 Disturbed-time electric fields

Prompt Penetration Electric field (**PPEF):** The high-latitude convection electric field (as noted above in association with the DP2 fluctuations) can penetrate to equatorial and low latitudes (Kikuchi and Araki, 1979; Kelley et al., 1979; Kikuchi 1996 and references therein) which is now commonly known as the Prompt Penetration Electric field (PPEF). Mathematically, the convection electric field can be represented as E_c=-V_c x B. The associated convection electric potential (Φ_C) is given as Ec= - $\nabla\Phi_C$. The PPEF, according to the present understanding, is associated with a condition that can cause an imbalance between the R1 (poleward current system) and R2 (equatorward current system) (Peymirat et al., 2002 and references therein). The dawn-to-dusk polarity of the electric field associated with the dayside magnetospheric convection (i.e. stable southward excursion of IMF-Bz and enhanced R1 FACs) manifests as the eastward electric field. After some time (an hour or so), when the R2 FACs develop in response to the above initiation of convection, an electric field of opposite polarity (westward) dominates the one that is associated with the R1. During substorms and the sudden rise of the asymmetric ring current, the dusk-to-dawn electric field (westward in the daytime) of reverse polarity (i.e. associated with the R2) grows significantly and penetrates all over (Radley and Leimohn, 2002). The perturbation in the H-component under the effect of PPEF depends upon the latitude (distribution of conductivity) and is enhanced over the dip equator due to enhanced Cowling conductivity. Dramatic changes in the electrodynamics have been observed under different kinds of PPEF during intense geomagnetic storms (Dashora et al. 2019 and references therein).

Disturbance Dynamo Electric field (DDEFs): The Disturbance Dynamo Electric field (DDEF) relates to the delayed effect of the ionosphere-thermosphere response to the high

latitude forcing during geomagnetic storms. The intense geomagnetic storms produce widespread, sustained Joule heating over the high-latitude, which in turn launch the pressure impulses or TADs (Hocke and Schlegel, 1996; Bauske and Prolss, 1997) away from the polar ionosphere. These perturbation equatorward meridional flows at the F-region and lower altitudes arrive at the mid-latitude in a few hours and under the effect of Coriolis force are directed westward. Such a situation brings an oppositely directed dynamo, producing, perturbed equatorward and westward electric fields known as disturbance dynamo electric fields (DDEF), which drive the mid and low-latitude electrodynamics for tens of hours to days. Blanc and Richmond (1980) have performed exhaustive simulations, which provide a substantial foundation for the observed long-lasting effects of the DDEF over mid-to-low latitude and up to the dip equator (Abdu et al., 1995; Fejer et al., 1986). A recent review of the DDEF mechanisms and manifestations by Fejer et al (2017 and references therein) provides details and is a good read for the community. In general, the effects of DDEF are prevalent during the recovery phase of the geomagnetic storm. The Disturbance Dynamo causes global magnetic perturbations that are frequently represented as D_{dyn} (Amory- Mazaudier et al., 2017; Rout et al. 2019) as follows-

$$D_{dyn} = \Delta H - S_R - SYMH$$

wherein ΔH, S_R, and SYMH are overall fluctuations in the horizontal geomagnetic field above the crustal magnetic field, magnetic field fluctuations due to quiet time ionospheric dynamo, and magnetic field induced by the ring current, respectively.

1.5 Geomagnetic responses

Long-term observations of the Earth's magnetic field have shown that it undergoes major changes over time, which can be classified into two broad categories: secular (climatic) and transient (few minutes to days) variations. The works in this thesis are focused on studying the transient variations during geomagnetic storms and substorms.

1.5.1 Components of the geomagnetic field

The geomagnetic field is generally represented in the XYZ or HDZ coordinate systems (Campbell, 2003). In the XYZ system, the variations of the main field along the geographic north-south, east-west, and vertical up-down are represented along the X, Y, and Z-directions respectively. On the other hand, in the HDZ system, the variations of the main field along the geomagnetic north-south, east-west, and vertical up-down are represented along the H, D, and

Z-directions respectively. The magnetospheric and ionospheric currents at different time intervals in the magnetosphere-ionosphere system cause a resultant effect on the Earth's surface which is observed as a net perturbation in the **H-component** (Villante and Piersanti 2009 and references therein). On the other hand, the **D-component** during geomagnetic storms, especially during the time of SSC, exhibits significant perturbations (See for example Rastogi 1999; 2005; Piersanti and Villante, 2016).

1.5.2 Geomagnetic indices

Geomagnetic indices are widely used to monitor these transient variations and characterize the dynamic state of the magnetosphere-ionosphere system. Several indices of geomagnetic activity have been introduced to assess the degree of geomagnetic activity at various latitudes and time intervals. Some of the relevant geomagnetic indices to the present thesis are discussed below.

AE and associated indices: The Auroral Electrojet (AE) index was initially introduced by Sugiura and Davis (1966) as a metric for measuring global electrojet activity in the auroral zone. It is calculated as the total deviation from quiet day values of the (H-component from selected observatories (typically 10-13) along the auroral zone in the northern hemisphere. The upper envelope of the H component disturbances observed at these observatories is called the AU index, which is a measure of the maximum intensity of the eastward electrojet. The lower envelope of H disturbances, the AL index, provides an idea of the maximum intensity of the westward electrojet. The difference (AU-AL), defines the AE index, and the mean value of AU and AL, i.e., (AU + AL)/2, defines the AO index.

Since the eastward and westward electrojets are generated by different physical phenomena and are quite different, it is questionable whether the AE index gives a proper and meaningful representation of the spatio-temporal variabilities (Kamide and Rostoker, 2004).

SME and SML index: The SME (Super Magnetic Electrojet) and SML (Super Magnetic Electrojet Lower) indices, as a replacement for AE/AL indices are constructed from denser ground magnetometer data gathered by the SuperMAG network. This network includes more than 100 magnetometers operated by various national and organizational agencies, covering both high, mid, and low latitude stations, in addition to the standard AE and AL magnetometer sites (Gjerloev., 2009, 2012; Newell and Gjerloev, 2011a, 2011b). This feature proves crucial, as particularly during the magnetic storm and substorm intervals, the auroral current systems

exhibit drastic structural changes including deeper equatorward movements compared to the nominal auroral zone. The SML index is used in this thesis to identify and characterize the Supersubstorm events of solar cycle 24 (See Chapters 3 and 4 for details).

Kp index: The planetary K-index, known as the Kp index is computed by using H-component records from 13 sub-auroral observatories distributed in longitude across the northern (11 observatories) and southern (2 observatories) hemispheres are used (Bartels et al., 1939; Matzka et al., 2021). This index is quasi-logarithmic, ranging from 0 to 9 depending on the level of geomagnetic activity. A Kp value of 0 indicates an extremely quiet magnetospheric condition, while a value of 9 suggests highly disturbed times.

Polar Cap index (PC-I): The PC-index (Troshichev et al., 2006 and references therein) is a magnetic activity index for the Polar Cap region. It is designed to monitor the magnetic activity in the Polar Cap generated by various solar wind parameters, such as the IMF-Bz, the IMF-By, and the solar wind velocity in connection with the observed perturbations in the ground magnetic field. To obtain the PC-index, observational data from a single station located close to the magnetic pole in each hemisphere is used (Thule (77.47° N, 290.77° E) for the northern hemisphere (known as PCN) and Vostok (78.4645° S, 106.8339° E) for the southern hemisphere (known as PCS).

Dst index: The Dst (disturbance storm time) index, is used to evaluate the intensity of geomagnetic storms (Gonzalez et al. 1994). The depressions in the H-component caused by the ring current during geomagnetic storms can be detected by ground magnetometers at low and mid-latitude stations (Sugiura., 1964; Nose et al., 2015). Geomagnetic storms are classified based on the minimum Dst value and can range from weak to intense (Perreault and Akasofu., 1978). Though there are debates and discussions in the community regarding the hard and fast limits of the ranges of minimum Dst value, the storms are majorly classified as (a) **moderate (≤-50 nT)**, (b) **Intense (≤-100 nT)**, and (c) **super intense (< -250 nT)** or **super storms** (Gongalez et al, 1994; Vichare et al., 2005; Eicher et al., 2010).

Symmetric and asymmetric (SYM-H and ASY-H) indices:

To provide a detailed account of geomagnetic disturbance fields in the low and mid-latitudes with a high temporal resolution of 1 minute, two indices have been developed: a longitudinally symmetric (SYM) and a longitudinally asymmetric (ASY) disturbance index (Iyemori and Rao, 1996), each for both the H and D components (SYM-H, ASY-H, SYM-D, ASY-D). The symmetric disturbance field in H, known as SYM-H, is similar to the hourly Dst

index (Sugiura and Poros 1971), but with a higher temporal resolution of 1 minute and estimated using different station sets and coordinate systems.

1.5.3 Geomagnetically induced currents

Geomagnetically induced currents (GICs) are electrical currents generated on the Earth's surface induced by rapid fluctuations in the geomagnetic field due to space weather events, such as geomagnetic storms and substorms (Pirjola, 2000; Pulkkinen et al., 2017). The quick-changing magnetic fields generally induce GICs through electromagnetic induction. The spatially and temporally varying current systems in space induce geo-electric fields in the ground through the application of Faraday's law of magnetic induction (Carter et al. 2015). GIC generally operates within a frequency range of 0.01-0.0001 Hz, hence it can be considered as a quasi-DC current. In general, GIC poses a risk directly to transformers (Albertson et al., 1973, 1974). However, during these periods, the presence of severely distorted exciting currents contained significant levels of harmonics, posing a threat to the safe operation of other equipment and the entire power system (Boteler et al., 1998). Overall, these currents can interfere with the normal functioning of extended electrical conductor systems like electric transmission grids, railroad tracks, and underground pipelines. In extreme cases, GICs can cause blackouts, making them a significant concern for the power grid and other infrastructure systems (Kappenman, 2005; Pulkkinen et al., 2005; Gaunt and Coetzee, 2007). The impact of GICs on space weather is a growing concern. This has resulted in increased attention from international policymakers, scientists, industry leaders, and the public, who are seeking solutions to address this issue (Pulkkinen et al., 2017).

1.6 Aim and Scope of the Thesis

In the above sections, several research studies are cited in the context to the historical development and state-of-the-art knowledge on each topic. It shall be noted that each topic and sub-area under the solar wind-magnetosphere-ionosphere coupling presents some challenging and unresolved problems, although an overview of several processes is understood quite well.

A motivation for this thesis work also originates from the past space weather research studies conducted at NARL. Particularly the studies by Suresh and Dashora (2016) and Dashora et al. (2019) have embarked upon some peculiar observations of ionospheric responses during intense and super geomagnetic storms. The discussions on their results have led us to find the sources of the equatorial and low latitude perturbations at high latitudes, which in turn

sought a clearer understanding beginning from the drivers of the perturbations in the solar wind structures, the magnetospheric processes and the high latitude processes as part of the complex system. The strong foundation of the present understanding of the sun-earth connection and space weather, fortunately, leads us to some very specific gap areas, open questions, and unresolved issues. In this context, it has been noted that the extreme events of intense geomagnetic storms and supersubstorms provide much better and potential opportunities to search efficient pathways of energy and momentum transfer from the solar transient perturbations to the magnetosphere and ionosphere.

Hence, this thesis aims to comprehensively understand the solar extreme transient events like "Supersubstorms" and, focuses on obtaining quantitative relationships of the dominant pathways of energy and momentum transfer from the solar wind to the magnetosphere and, from the magnetosphere to the global magnetic perturbations. For this purpose, a literature survey is carried out encompassing several research articles in the vast domain of solar wind-magnetosphere-ionosphere coupling. It is found that the coupling functions which determine the quality of interface between the solar wind perturbations and magnetosphere as well as between the magnetosphere-ionosphere, have been estimated only for individual case studies of the storms and substorms.

In particular, such studies are rarely found wherein energy flow from the solar wind to the magnetosphere and in the ionosphere is analyzed robustly with a wide coverage of the sources in the solar wind, its coupling with the magnetosphere, merging electric field, FACs and the coupling scenarios and relationship with ionospheric sink and proportion of energy flow in different sinks. In addition to this, the body of literature reporting the coupling during space weather events mostly constituted evidence from observations of solar cycle 23 and the previous solar cycles. Considering the fact that the solar cycle 24 has behaved very differently than some of the previous solar cycles (of the space age), it is consciously decided to select the observations of "Supersubstorm" events of solar cycle 24. This decision is also in conjunction with the present understanding that the solar wind-magnetosphere coupling consists of the large scales (convection and dynamo processes) and the short scales (e.g. electron/ion kinetic scales).

Therefore, at first, an analysis is performed to decipher the difference between the occurrence climatology of the Supersubstorms of solar cycle 24 and in the solar cycles 21-23. With satisfactory evidence that the solar cycle 24 has exhibited the lowest number of supersubstorms (no supersubstorm during the peak of the solar activity) in the above

comparison (See Chapter 3 for details), a methodology is developed to trace the sources of the Supersubstorms in the solar wind (using observations at L1-point) and compare several coupling functions including the epsilon parameter and Borovsky functions, etc. for quantifying the dynamics interaction between the solar wind and the magnetosphere. Further in this methodology, the magnetosphere-ionosphere coupling parameters and indices like the PCPD, PC indices, and the FACs are included. Then, the available solar wind power, power at the input to the magnetosphere, and the power associated with the energy dissipation in the form of Ring current (magnetospheric sink), Joule heating, and Auroral particle precipitation (ionospheric sinks) are included in the computations. Also, detailed comparative and statistical analyses are designed to properly designate the coupling and energy transfer of the Supersubstorms in comparison to the geomagnetic storms and nominal (isolated) substorms along with a large number of substorms. Further, considering that the intense magnetospheric and ionospheric currents and associated disturbances, perturb the geomagnetic field, and also drive the geomagnetically induced currents (GICs), are less understood in the light of the effect of the extreme transient events. So, the global effect of the Supersubstorm events on the geomagnetic field (H and D components) and the GICs is also aimed to complete the study of the solar-wind-magnetosphere-ionosphere coupling during extreme events of Supersubstorms. In addition to the above aims, it is highlighted in para above that the short-scale coupling processes during magnetic reconnection like the kinetic electron scale (~hundred-meter scale) and the ion scales (~a few kilometer scales) need to be investigated for better understanding. This additional objective shall complete the overall framework of the solar wind-magnetosphere-ionosphere (SW-M-I) coupling. Hence, the following objectives are framed for this thesis in the above-mentioned background.

1. Study of the Solar-wind Magnetosphere and Magnetosphere-Ionosphere Coupling during supersubstorms of solar cycle 24 in the context of the identification of sources in the Solar wind, energy transfer, and sink processes.
2. Study of the global impact of the Supersubstorm events on the geomagnetic field (H and D components) and in the GICs in the context of deciphering the magnetospheric and ionospheric contributions of the geomagnetic storm and Supersubstorm origin.
3. Study of dynamics and flow of energy during magnetic reconnection process during geomagnetic storm and substorm events.

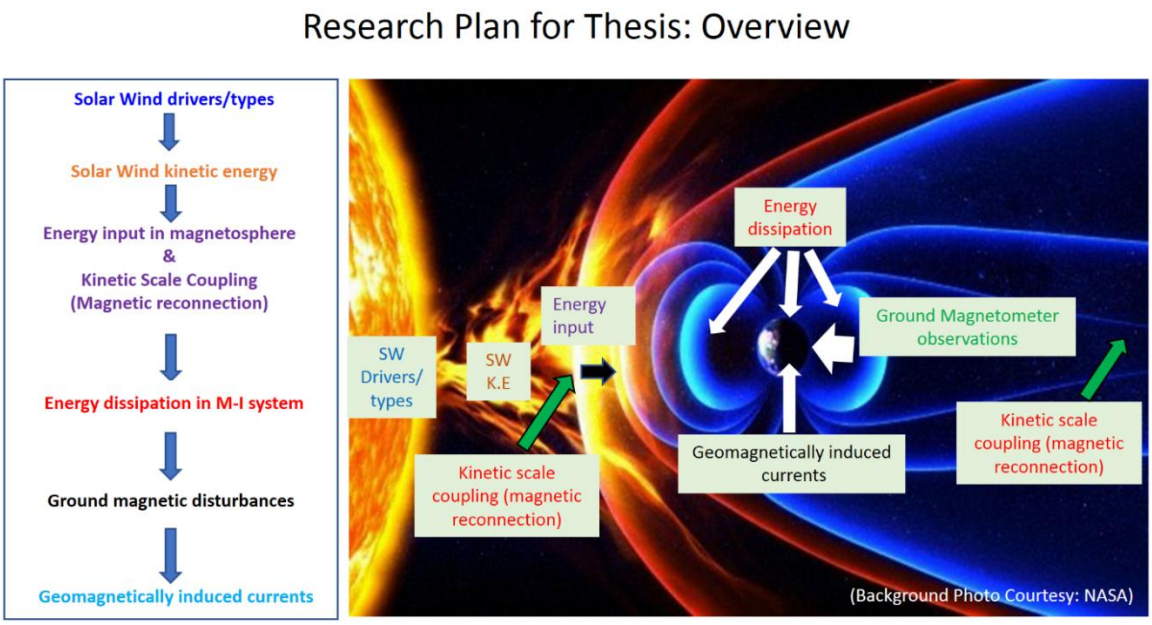

Figure 1.14: A schematic flow chart of the aim and scope of the research plan for the present thesis. On the left column, a flow of the coupling processes that are aimed to study is given, and the regions of research interest are annotated as a text box with arrows on a cartoon depicting an artistic view of the sun-earth connection

Hence, in light of the above objectives, the scope of the present thesis is to examine the intricate interactions between the solar wind, magnetosphere, and ionosphere during geomagnetic storms and substorms, with a focus on extreme events like moderate-intense storms and supersubstorms (see Figure 1.14). The primary focus will be on identifying and characterizing the key physical processes that contribute to the coupling between the solar wind, magnetosphere, and ionosphere during these events. Geomagnetic storms and substorms are crucial space weather phenomena that can significantly impact delicate technological systems such as satellites, power grids, communication networks, and international space stations. Therefore, it is essential to investigate the mechanisms of their origin, evolution, and impacts on the magnetosphere-ionosphere system. Hence, the research studies of this thesis are open to perform a robust and comprehensive analysis of all the Supersubstorms during Solar cycle-24, which was the weakest in the space age. Analyzing the coupling processes in the magnetosphere-ionosphere system during a series of storms may have important implications for predicting and mitigating the effects of space weather on technological systems.

Researchers have proposed various methodologies to estimate the solar wind-magnetosphere and magnetosphere-ionosphere coupling processes, but validating them is a crucial task. It is important to note that these methodologies are suitable for describing coupling

processes during specific conditions of the solar wind-magnetosphere-ionosphere system. Connecting studies from the sun to coupling mechanisms, magnetosphere responses, and magnetometer responses to GICs is a challenging task, and only a few studies have accomplished this. Additionally, studying the morphological structures of the H and D components during geomagnetically disturbed periods is important for understanding the ever-changing geomagnetic field, which is a critical part of sustaining life on Earth. Thus the scope of the thesis covers the above-mentioned specific tasks to arrive a conclusive and appropriate evidence.

Apart from the large-scale processes, the kinetic-scale processes of coupling are also a gap area in this field of research, especially magnetic reconnection, which is a controlled nuclear fusion occurring in the Earth's magnetopause and magnetotail. This is still a burning area of research. With the launch of magnetospheric satellites like MMS by NASA, and ongoing observations from the ESA-Cluster, and NASA-THEMIS spacecrafts, it is now possible to describe and understand the kinetic-scale processes occurring inside the reconnection regions. To study the physical processes that cause magnetic reconnection, determining structures and dynamics inside the electron diffusion region (EDR) with sufficiently high-resolution plasma and field measurements is necessary, beyond the capabilities of previous spacecraft missions that have encountered the EDR. This thesis aims to address the gap area mentioned above.

The thesis is organized into Six chapters beginning with this Introduction chapter as Chapter 1. Chapter 2 is written to describe different observations and data sets including the details of the state-of-the-art methods and formulae to analyse these observations. Chapter 3, Chapter 4, and Chapter 5 are dedicated to giving detailed descriptions of the studies performed for this thesis respectively under the above-mentioned three objectives. Finally, Chapter 6 provides an overall Summary of all the new results obtained during the course of all the above studies. This chapter also provides future scope and applications of the new results in achieving a better understanding of the solar wind-magnetosphere-ionosphere coupling with a few particular well-defined objectives. The chapters follow three Appendices, A, B, and C, which are integral parts of the studies described respectively in Chapters 3, 4, and 5. An exhaustive list of all the references cited in Chapter 1 through Chapter 6 is compiled and arranged in alphabetical order with all the bibliographic information. Finally, a list of peer-reviewed publications and a list of conference papers presented, as an outcome of the thesis work are given.

CHAPTER 2

Data Analyses and Methodology

"To measure is to know. If you cannot measure it, you cannot improve it."

-Lord Kelvin

2.1 Introduction

The aim of this thesis is to investigate the complex interplay between the solar wind, magnetosphere, and ionosphere during geomagnetic storms and substorms. To perform a robust and vivid analysis of all the phenomena associated with all these parts separately, a variety of data sources and methodologies are employed. In this chapter, we attempted to probe the solar wind-magnetosphere-ionosphere system systematically one after another with the help of a range of ground-based and space-based instruments, including magnetometers, RADARs, and satellites. In some other cases, several estimations propounded in previous works of literature are employed to understand the responses of the solar wind-magnetosphere-ionosphere system during extreme space weather events.

2.2 Observations of interplanetary parameters and geomagnetic indices

All the observations related to the solar wind and interplanetary parameters are obtained from the Advanced Composition Explorer (ACE) spacecraft located at the L1 point in the interplanetary space between the Earth and the sun. The X, Y, and Z components of the ambient electric field (E), magnetic field (B), and the plasma parameters like the pressure (P), velocity (v), proton density (ρ), temperature (T), plasma beta (β), etc are directly extracted from NASA/GSFC's OMNI data set through OMNIWeb (https://omniweb.gsfc.nasa.gov/form/omni_min.html) at a cadence of 1 min (Papitashvili & King, 2020). The data related to the geomagnetic indices like AE, SYM-H, and PC are directly obtained from NASA-OMNIWeb (https://omniweb.gsfc.nasa.gov/). The SML/SME indices are obtained from the website of SUPERMAG (https://supermag.jhuapl.edu/indices/). As described in section 1.5.2, all these indices are derived from the H-component observations from different bands of strategically placed magnetometers.

The initial point of analysis for Chapters 3, 4, and 5 is based on the observations pertaining to interplanetary parameters and geomagnetic indices. These observations serve as a foundation for further investigations conducted in those chapters.

2.3 Identification of solar wind drivers

As discussed in section 1.2.1 the solar wind drivers are segregated according to several physical parameters. To quantify and categorize them, several schemes have been proposed by

researchers. Below, we will present two such schemes used to identify the solar wind drivers during a geomagnetic storm.

Table 2.1. Criteria to define streams of the solar wind plasma to be classified into different types (Yermolaev et. al. 2009). (SW=solar wind; P=pressure; N=proton density; V=SW bulk velocity; T=SW temperature; Texp=SW expected temperature; β = plasma beta parameter; k=Boltzmann constant; DN = Increments (gradients) of density; DB = Increment in magnetic field magnitude; DV6 = Increment in velocity on an interval of 6 hours)

Sl. No	SW type	P	N	V	B	T/Texp	NkT	β	DV6	DN	DB
	Unit	nPa	/cm^3	km/s	nT		J/cm^3		km/s	/cm^3	nT
1	HCS	5	>7	<500				>0.7			
2	SLOW	3	>3	<450				<1			
3	FAST	3	<20	>450				<1			
4	CIR/ SHEATH	5	>3		>5	>1	>0.007	>1			
5	EJECTA	4	<10			<0.5	<0.01	<0.5			
6	MC	5	<10		>10	<0.5	<0.01	<0.5			
7	RARE	4	<1	<500		<1	<0.01				
8	IS								>50	>2	>2
9	ISA								<-50	<-2	<-2

To validate the scheme provided by Yermoalev et al. (2019) and gain confidence in the sources of the perturbations in solar wind during geomagnetic storms, another classification of solar wind drivers given by Adekoya and Chukwuma (2018) is also considered. This classification mainly focuses on disturbed plasma streams and their intricate and complex drivers, as listed in Table 2.2 below.

All the estimations regarding the solar wind drivers are made using observations from NASA-OMNIWeb (https://omniweb.gsfc.nasa.gov/). These methods are used to quantify the solar wind drivers and associated analysis presented in Chapter 3.

Table 2.2. Characteristics of the solar wind parameters and their types (see Adekoya and Chukwuma, 2018 for details) (ρ=proton density; all other symbols are as given in Table 2.1).

SW type	Bz	T	ρ	V	β
MC	≥10	≤4,00,000	≤10	≥450	≤0.8
S+MC	≥10	≤4,00,000	≤10	≤450	≤0.8
S	≥10	≤4,00,000	>10	Unspecified	≤0.8
S+E	≥10	Unspecified	>10	Unspecified	>0.8
E	<10	>4,50,000	>11	>450	>0.8

2.4 Estimations of parameters related to energy sources, coupling, sinks, and partitioning

The past studies on the solar wind-magnetosphere-ionosphere coupling have led to the advanced formulations to determine the solar wind kinetic energy that is available for the earth's magnetosphere, the actual input energy, and the dissipated energy through different channels in the magnetosphere-ionosphere system (e.g. Burton et al. 1975; Perrault and Akasofu 1978; Kan and Lee 1979; Akasofu 1981; Iijima and Potemra 1982; Nishida, 1983; Gonzalez 1993; Valdivia et al. 1996; Mac-Mahon and Gonzalez 1997; O'Brien and McPherron 2000; Ostgaard et al., 2002; Borovosky 2008; Li et al. 2012; Guo et al., 2012; Tenfjord and Østgaard 2013 and references therein, Adhikari et al. 2019). The rate of change of energy defines the available and dissipated power for a given interval of the geomagnetic storm or substorm. A literature survey is performed to obtain the latest validated formulae for the estimation of the power at different phases of the solar wind-magnetosphere-ionosphere interactions. The estimation of all the power and energy terms for this study is performed with 1-hour cadence observations through OmniWeb (https://omniweb.gsfc.nasa.gov/). The estimations and models demonstrated in this section are used to carry out the analyses presented in Chapter 3.

2.4.1 Available solar wind power

The cross-section of the earth's magnetospheric cavity provides us with the transferrable kinetic energy flux of the solar wind. There were efforts in many previous literatures to quantify it (Spreiter et al., 1966; Holzer and Slavin, 1979; Sibeck et al., 1991; Monreal-MacMahon; Gonzalez, 1997; Shue et al., 1997; Shue and Chao, 2013; Hajra et al., 2014; Adhikari 2019).

The magnetic and thermal energies in the solar wind are generally neglected because they are usually 1 or 2 orders of magnitude smaller than the kinetic energy (Tenfjord and Østgaard, 2013). Conventionally, Weiss et al. (1992) suggested using magnetospheric cross-section area (A) ~30 R_E^2, where R_E is the radius of the Earth. However, Mac-Mahon and Gonzalez (1997) found a reduced cross-section under dynamic solar wind pressure and compression of the magnetosphere. In this thesis, the available kinetic energy flux of solar wind power is estimated by

$$U_{sw}(\text{watt}) = \left(\frac{1}{2}\right)\rho v^3 A \qquad \text{(equation 1)}$$

where ρ (kg/m^3) is the mass density and v (km/s) is the bulk velocity of the solar wind. A (m^2) is the cross-sectional area of the dayside magnetopause assuming a cylindrical symmetric configuration (GSM coordinate system). We have used $A = \pi \times (r_0 \times 2^{\alpha})^2$; from Li et al. (2012); where r_0 represents the standoff distance at the subsolar point and α represents the level of tail flaring (Shue et al. 1998).

2.4.2 Solar wind-magnetosphere coupling

The Epsilon parameter: The large-scale solar wind magnetospheric coupling parameter has been estimated empirically because there is no direct method available. Historically, Perrault and Akasofu (1978) and Akasofu (1981) have provided an empirical transfer function known as the epsilon parameter. Later on, many studies have found that the constant value of the linear dimension of the effective area of interaction (l_0=7R_E) between the magnetosphere and the solar wind used in their formula has remained a source of error in the computations. However, some of the studies like Nishida (1983), Mac-Mahon and Gonzalez (1997), Lu et al. (1998), Vichare et al. (2005), and Li et al. (2011) have attempted to improve the estimation of l_0. They proposed to use the Chapman-Ferraro magnetopause distance (L_{CF}) as l_0. L_{CF} has been obtained from the pressure balance equation between kinetic solar wind plasma pressure and pressure of the geomagnetic field and can be given by $L_{CF}\,(\text{m}) = (\frac{B_0^2}{4\pi\rho v^2})(R_E)$, where B_0 is the earth's magnetic field strength, in general, $\sim 3\times 10^{-5}$ T. Recent studies like Tenfjord and Østgaard (2013) have proposed the use of the dynamic effective area of interaction and the stress tensors to estimate the Solar wind input power. Apart from this, the solar wind energy transfer mechanism due to cross-field diffusion by resonant wave-particle interactions at the dayside magnetopause during intense northward IMF has also been proposed (Shi et al., 2007 and

references therein). However, this is unlikely to be the main coupling process for the present study and hence is not considered.

In the present study, we have used the formula for the epsilon parameter with $l_0 = L_{CF}$ (Li et al. 2012) given by

$$\epsilon\ (\text{watt}) = \frac{4\pi v B^2 \sin^4\left(\frac{\theta}{2}\right) l_0^2}{\mu_0} \qquad \text{(equation 2)}$$

where v, B, ϴ, and l_0 are the solar wind velocity, total interplanetary magnetic field (IMF), magnetospheric clock angle, and the linear dimension of the effective area of interaction between the magnetosphere and the solar wind, respectively.

The Borovsky parameter: Borovsky (2008) propounded the solar wind-magnetosphere coupling rate (R), which has been derived from the first principles, given below.

$$R\ (\text{km nT/sec}) = \frac{0.8\pi^{0.5}\sin(\frac{\theta}{2})\rho_0 v_0^2(1+0.5M_{MS}^{-2})}{\sqrt{((1+\beta_S)(C\rho_0+(1+\beta_S)^{-1/2}\rho_M)((1+\beta_S)^{1/2}+1)))}} \qquad \text{(equation 3)}$$

where $\beta_S = 3.2 \times 10^{-2} M_A^{1.92}$ is the plasma beta value of the magnetosheath plasma near the nose; $C = (\left(\frac{1}{4}\right)^6 + \frac{1}{1+1.38\ln(M_A)^6})^{-\frac{1}{6}}$ is the compression ratio of the bow shock; $C_{MS} = (v_A^2 + \frac{5P}{3\rho})^{1/2}$ is magnetosonic speed; $M_A = (\rho_0\mu_0)^{1/2}\ v_0/B_0$ and $M_{MS} = v_0/C_{MS}$ are the Alfvenic and Magnetosonic Mach numbers respectively; ρ_0 and v_0 are the upstream solar wind mass density and bulk velocity respectively. Here, ρ_M is the dayside magnetospheric mass density, however, Borovsky et al. (2008) proposed this value to be zero.

The Newell parameter: Newell et al (2007) proposed a nearly universal coupling function deduced from about 10 magnetospheric state variables. The coupling function represents the rate of magnetic flux opened at the magnetopause which is given by

$$\frac{d\varphi_{MP}}{dt} = v^{\frac{4}{3}} B_T^{\frac{2}{3}} (\sin(\frac{\theta_c}{2}))^{\frac{8}{3}} \qquad \text{(equation 4)}$$

The reconnection electric field: Another important parameter in the context of the coupling is the reconnection electric field (E_R) (Kan and Lee, 1979), given by $E_R = V_{SW} B_{yz}\ [\sin^2\frac{\theta}{2}]$ (mV/m), where, V_{sw} is the velocity of the solar wind, $\theta = \tan^{-1}\frac{B_y}{B_Z}$ and $B_{yz}(nT) = \sqrt{{B_y}^2 + {B_z}^2}$ respectively are the clock angle and component of the IMF in the Y-Z plane and the northward and southward components are respectively given by 0^0 and 180^0 values of the θ.

2.4.3 Magnetosphere-ionosphere coupling

As mentioned in section 1.5.2, the magnetosphere-ionosphere coupling can be defined using the polar cap potential drop (PCPD) and field aligned currents (FAC), as detailed in past studies. For example, Boyle et al. (1997) have provided an empirical relationship to derive PCPD ($\emptyset_B$) which is given by -

$$\emptyset_B(\text{kV}) = 10^{-4}v_{SW}^2 + 11.7\text{Bsin}^3(\tfrac{\theta}{2}) \qquad \text{(equation 5)}$$

However, the calculation of large-scale FAC was performed using the following formula given by Iijima and Potemra (1982)

$$\text{FAC}\ (\mu Am^{-2}) = 0.328\left[n^{(\frac{1}{2})}V_{sw}B_T\sin\left(\tfrac{\theta}{2}\right)\right]^{1/2} + 1.4 \qquad \text{(equation 6)}$$

where $B_T = [{B_y}^2 + {B_z}^2]^2$ and n (cm^{-3}) is solar wind number density.

2.4.4 Power dissipation through ring current

A dominant energy sink in the magnetosphere is formed through the ring current. The Dst index has been customarily used as a proxy for the intensity of the ring current. However, a few corrections have been needed for the calculation of the Dst index considering other magnetospheric current systems like the magnetopause current, cross-tail current, and ground-induced current which are reviewed by Maltsev (2004).

In the recent literature, a corrected Dst formula is used, beginning with the formula given by Burton et al. (1975). They have corrected for the magnetopause current by $Dst^* = Dst - bP_d^{\frac{1}{2}} + c$; where Dst^* is the pressure corrected Dst term, P_d is solar wind the dynamic pressure. The coefficients b and c have been given by O'Brien and McPherron (2000) and Li et al. (2012), respectively, and are used in the present study with b=7.26 (nT $nPa^{(-1/2)}$) and c=11 (nT). Finally, following Turner et al. (2001), a corrected Dst index (Dst^{**}) is estimated by scaling down the Dst^* by 54% to remove the contributions from cross-tail currents and ground-induced currents.

The dissipated power through ring current is calculated in this thesis by using the formula given by Li et al. (2012) denoted by U_r

$$U_r\ (\text{gigawatt}) = -4\times 10^4\left(\frac{\partial Dst^{**}}{\partial t} - \frac{Dst^{**}}{\tau}\right) \qquad \text{(equation 7)}$$

Where, τ denotes the ring current decay time, which has been expressed in different static and dynamic formulations in the previous studies. Before arriving at a final formula of τ,

the eleven most used models of τ are examined (see Table 2.3 below). Four models are found to agree well with each other (in the study of substorms presented in Chapter 3) which have been given by Burton et al. (1975) (τ=7.7 h), Valdivia et al. (1996) (τ=12.5/(1-0.0012Dst) h), O'Brien and McPherron (2000) ($\tau=2.4e^{[\frac{9.74}{4.69+VB_z}]}$ h) and Xu and Du (2010) ($\tau=\frac{1}{[0.1+3\times10^{-4}\times\epsilon\ (\text{gigawatt})]}$ h); where h=hours. In this thesis, the τ model of O'Brien and McPherron (2000) is mostly used for the estimation of dissipated power through ring current (U_r).

Table 2.3: Eleven types of models estimating Ring current decay time (τ)

	Model	Decay time τ (h)	Reference
1.	DP-1967	τ: 5 (Dst≥-50); 7 (-20>Dst≥-30); 10 (-30>Dst≥-40); 24 (-40>Dst≥-50); 10 (<50)	Davis and Parthasarathy [1967]
2.	BM-1975	7.7	Burton et al. [1975]
3.	PA-1978	τ: 20 (ϵ <500); 1 (ϵ >500)	Perrault and Akasofu. [1978]
4.	A-1981	τ: 20 (ϵ <100); 6 (ϵ <500); 3 (ϵ <1000); 1 (ϵ <5000); 0.3 (ϵ <10000); 0.2 (ϵ >10000)	Akasofu [1981]
5.	G-1989	τ: 4 (Dst≥-50); 0.5 (-50>Dst≥-120); 0.25 (Dst<-120)	Gonzalez et al. [1989]

6.	G-1993	τ | Dst (nT) 4 | Dst≥-50 2 | -50>Dst≥-100 1 | -100>Dst≥-200 0.5 | -200>Dst≥-300 0.25 | <300	Gonzalez [1993]
7.	VS-1996	12.5/(1-0.0012Dst)	Valdivia et al. [1996]
8.	L-1998	τ | Dst (nT) 4 | <-30 8 | -50≤ Dst<-30 20 | ≥-50	Lu et al. [1998]
9.	OM-2000	$2.4e^{[\frac{9.74}{4.69+VB_z}]}$	O'Brien and McPherron [2000]
10.	ML-2008	$(\frac{\alpha}{Dst})^{3/2}$	MacMahon and Llop-Romero [2008]
11.	XD-2010	$\frac{1}{(0.1+3\times10^{-4}\times\epsilon\,(\mathrm{GW}))}$	Xu and Du [2010]

A comparative plot of dynamical variations of the ring current calculated from the 11 selected ring current models is given in Appendix-A, supporting information (SI-3).

2.4.5 Power dissipation through Joule heating

The previous studies demonstrate that the direct measurements of ionospheric electric fields and conductivities using rocket-born instruments (Evans et al., 1977) or the incoherent scatter radars (Wickwar et al., 1975) can only provide Joule heating integrated over a small area. As both the currents and electric fields in the magnetosphere-ionosphere coupling region can be monitored using geomagnetic perturbations, geomagnetic proxies such as AE and PC indices have been used as a first approximation measure of the global Joule heating (Akasofu, 1981). Also, the global Joule heating has been found closely related to the indices that give auroral evolutions and disturbances with the availability of larger data sets from radars and magnetic measurements (Ahn et al., 1983; Baumjohann and Kamide, 1984) and the assimilative mapping of ionospheric electrodynamics (AMIE) procedure (Richmond et al., 1990; Lu et al., 1998). It is also now well accepted that the auroral electrojet indices show

seasonal variations (Russell and McPherron, 1973; Kamide and Akasofu, 1983; Lu et al., 1995), such that the activity maximizes during equinox and minimizes during the solstice. The estimation of Joule heating has been known to depend upon the method and experimental technique (Guo et al., 2012). The theoretical and experimental methods of calculation of energy dissipation through Joule heating have been improved by various studies (Weimer et al., 2005; Richmond, 2010; Vanhamäki et al., 2012; Rastätter et al. 2016 and references therein).

The energy partitioning studies have mostly used empirical estimates of the power dissipation through Joule heating based upon AE and different expressions have been given for solstices ($U_j(\text{gigawatt}) = 0.54AE + 1.8$) by Ahn et al (1989) and Richmond et al., (1990). Ahn et al. (1983) have given the following equation for both hemispheres during equinoxes. These expressions have been used extensively in many studies (Palmroth et al. 2005; Li et al. 2012).

$$U_j(\text{gigawatt}) = 0.46AE \qquad \text{(equation 8)}$$

Another method proposed by Knipp et al. (2004) using the PC index with the Sym-H/Dst indices has been used in previous studies like Turner et al. (2009); and Hajra and Tsurutani (2018). This method provides a different formula in the context of seasonal background at high latitudes, which is an important aspect of north-south asymmetry. The formulae are given as follows and are used in the present study to estimate the dissipated power by global Joule heating (U_j), where PC is the polar cap index (Troshichev and Janzhura, 2012).

$$U_j(\text{gigawatt}) = 13.36PC + 5.08PC^2 + 0.47Dst + .0011Dst^2 \text{ (winter: 21 Oct} - \text{20 Feb)}$$
$$U_j(\text{gigawatt}) = 29.27PC + 8.18PC^2 - 0.04Dst + .0126Dst^2 \text{ (summer: 21 April-20 Aug)}$$
$$U_j(\text{gigawatt}) = 29.14PC + 2.54PC^2 + 0.21Dst + .0023Dst^2 \text{ (equinox: 21 Feb-20 April)}$$

(equation 9)

In this thesis, we have compared one set of formulae of Joule heating associated with AE indices (Ahn et al. 1983; Ahn et al. 1989; Richmond et al.1990) with another set of formulae associated with PC indices (Knipp et al. 2004).

2.4.6 Power dissipation through auroral particle precipitation

The power dissipation by the auroral particle precipitations had been estimated by several studies (Cole, 1962, 1971; Rees, 1975) and is found to be linearly related to the AE index (Akasofu, 1981; Spiro et al., 1982; Ahn et al., 1983; Richmond et al., 1990; Lu et al., 1998). Østgaard et al. (2002) used X-ray and UV emissions to derive the dissipation through auroral

particles from 0.1 to 100 keV electron energies in the northern hemisphere. Considering both the hemispheres, they gave an estimation of auroral dissipation rate (U_a) given by

$$U_a\,(\text{gigawatt}) = 2 \times (4.4\sqrt{AL} - 7.6) \qquad \text{(equation 10)}$$

Li et al. (2012) have also used this formula and the same is used in most of the cases in this thesis.

By comparing this result with the previously used parameterized methodologies based on AE or AL, Tenfjord and Ostgaard (2013) found that most of those methods underestimate U_a significantly which may be due to the reason that those old parameterized methods were developed by using data that only cover electron energies up to 20–30 keV. Hence, instead of a linear relation reported before, they argued that a non-linear relation is more appropriate. They also rewrote the above equation using the SUMERMAG lower (SML) index using the same methodology.

$$U_a\,(\text{gigawatt}) = 2 \times (4.1\sqrt{SML} - 9) \qquad \text{(equation 11)}$$

We have compared the results from both the above formulas, which provide similar variation in U_a.

2.4.7 Other energy sinks and net energy sink

Eventually, the power dissipation through major sinks in the ionospheric regions $U_i = U_j + U_a$ and the total power dissipation U_t through major magnetospheric and ionospheric sinks is equal to the sum of U_i and U_r i.e. $U_t = U_j + U_a + U_r$. It shall be noted that the input and dissipated power of different channels are integrated with respect to time, to obtain the respective input and dissipated energies. However, during extreme events, the energy can also dissipate through other minor channels such as **plasmoid ejections**, **post-plasmoid plasma sheet heating**, **relativistic electron precipitation and heating**, **formation of substorm current wedge**, **charge inflow-outflow-exchange mechanism**, etc.

The energy dissipated through plasmoid ejection and post-plasmoid plasma sheet retains a considerable share of the energy budget (Slavin et al., 1993, Ieda et al. 1998; Koskinen and Taskanen, 2002), however, the computation of the same has not been directly possible yet. However, the total energy dissipation through plasmoid ejection and direct loss through post-plasmoid plasma sheet heating have been considered together to be ~ 10^{15} J (Li et al. 2012). About the energy flux of relativistic electrons due to precipitation and heating, Lu et al. (1998) have found that about 1% of the epsilon parameter is dissipated in this process. Likewise, the consumption of energy in the formation of the substorm current wedge also contributes as a minor sink (Belehaki et al. 1995). Baker et al. (1997) argued about ≤1% of the magnetospheric

dissipation happens through the minor sinks such as substorm current wedge formation, auroral kilo-metric radiation, ultra-low frequency (ULF) magnetic field oscillations, charge inflow and outflow, dayside losses, etc.

In some works in this thesis, the total energy dissipation through plasmoid ejection and direct loss through post-plasmoid plasma sheet heating has been considered together to be ~ 10^{15} J. Also, about 1% and ≤1% of the total input energy considered to be dissipated through the relativistic electrons and other minor sinks, respectively.

2.4.8 Energy transfer efficiency and ratio

As noted above, the respective energies, namely available solar wind energy, input energy, and total sink energy are obtained by integrating the calculated power for the duration of the supersubstorm events. The energy transfer process across the solar wind-magnetosphere-ionosphere system can be defined from two coupling efficiencies following Li et al. (2012). Using the energies calculated by integrating the respective power terms, the efficiencies **e1** (input efficiency), **e2** (dissipation efficiency) and **e3** (ratio of sink energies) can be defined as $\mathbf{e1} = \frac{\text{input energy}}{\text{available solar wind energy}}$; $\mathbf{e2} = \frac{\text{total sink energy}}{\text{input energy}}$ and $\mathbf{e3} = \frac{\text{magnetospheric sink energy}}{\text{ionospheric sink energy}}$.

2.5 Observations from magnetospheric satellites

2.5.1 In-situ observations

Since the beginning of the Space age (October 4, 1957), demarked by the launch of the Soviet Union's Sputnik 1 satellite, there have been many different types of satellites launched into space for a variety of purposes such as communication, navigation, probing the weather and climate, observation of the solar-terrestrial elements, and probing the astrophysical bodies, etc. In the last few decades, several magnetospheric satellites such as Cluster (2000), IMAGE (2005), TWINS (2006), THEMIS (2007), Ørsted (2010), VAP (2014), MMS (2015), ERG (2016), etc have been launched by the space agencies from different countries of the world to probe the large and small scale dynamics of the magnetosphere. For the scope of this thesis, we have taken observations from MMS, THEMIS, and Cluster, which can be directly obtained from NASA-SPDF (https://cdaweb.gsfc.nasa.gov/). Most of the following descriptions are obtained from the mission websites and technical papers.

2.5.1.1 Observations from the MMS

NASA (The National Aeronautics and Space Administration) launched the Magnetospheric Multiscale (MMS) Mission on March 13, 2015, which involves four identical spacecraft that fly in a tetrahedral formation to study the Earth's magnetosphere (see "https://lasp.colorado.edu/mms/sdc/public/" for details on the MMS mission and payloads). The mission aims to collect data on the microphysics of various processes associated with astrophysical plasmas, including magnetic reconnection, turbulence, and energetic particle acceleration. The sensors inside MMS provide unprecedented high-resolution in-situ observations, which are very useful to study small ion, and electron scale processes inside Earth's magnetosphere.

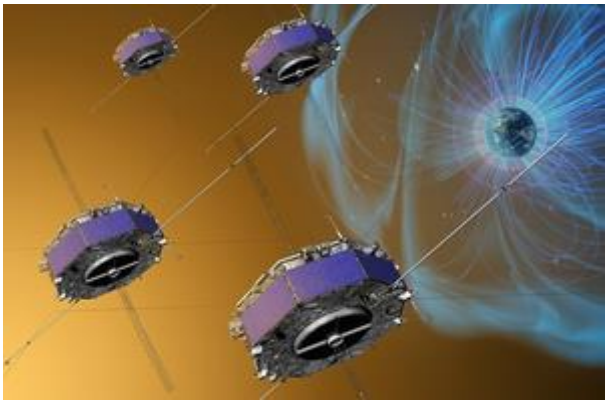

Figure 2.1: An artistic depiction of the four MMS spacecrafts encountering the Earth's magnetosphere (credit: https://en.wikipedia.org/wiki/Magnetospheric_Multiscale_Mission)

Payloads and sensors: The sensors inside each spacecraft carry out several experiments. Those are classified into three suites- the Hot Plasma Suite, the Energetic Particles Detector Suite, and the Fields Suite. The **Hot Plasma Suite** takes in-situ observations related to plasma particle counts, directions, and energies during magnetic reconnection. It consists of two instruments namely the Fast Plasma Investigation (FPI) and Hot Plasma Composition Analyzer (HPCA). The **Energetic Particles Detector Suite** is for detecting particles having energy ranges far exceeding those detected by the Hot Plasma Suite. It consists of two instruments namely the Fly's Eye Energetic Particle Sensor (FEEPS) and Energetic Ion Spectrometer (EIS). The **Fields Suite** provides measurements of magnetic and electric fields and consists of six instruments, namely, Analog Fluxgate magnetometer (AFG), Digital Fluxgate magnetometer (DFG), Electron Drift Instrument (EDI), Spin-plane Double Probe (SDP), Axial Double Probe (ADP) and Search Coil Magnetometer (SCM).

In this thesis, we have used observations from FGM, FPI, EDI, SDP, and ADP. A short description of the payloads and associated sensors are given below with respective lead publication. The MMS website hosted at Colorado University also provides details of the mission, payloads, and data sets (https://lasp.colorado.edu/mms/sdc/public/).

- FGM: The FGM (Torbert et al., 2016) consists of an Analog Fluxgate Magnetometers (AFG) and a Digital Fluxgate Magnetometer (DFG). These provide redundant observations of the magnetic field and associated structures in the diffusion region.
- FPI: The FPI (Pollock et al., 2016) includes two sets of sensors, the Dual Ion Sensors and Dual Electron Sensors, which are capable of measuring ion and electron flux distributions in three dimensions. These measurements cover an energy range of approximately 10 eV to 30 keV and have an energy resolution of 20%. The sensors can provide electron measurements with a time resolution of 30 ms and ion measurements with a time resolution of 150 ms.
- EDI: The EDI (Lindqvist et al., 2016) measures the electric and magnetic fields by analyzing the drift of electrons with an energy of approximately 1 kilo-electronvolt emitted from the Gun Detector Unit (GDU). To transmit and receive data, each GDU uses a designated beam that is coded and exchanged with the other EDI-GDU.

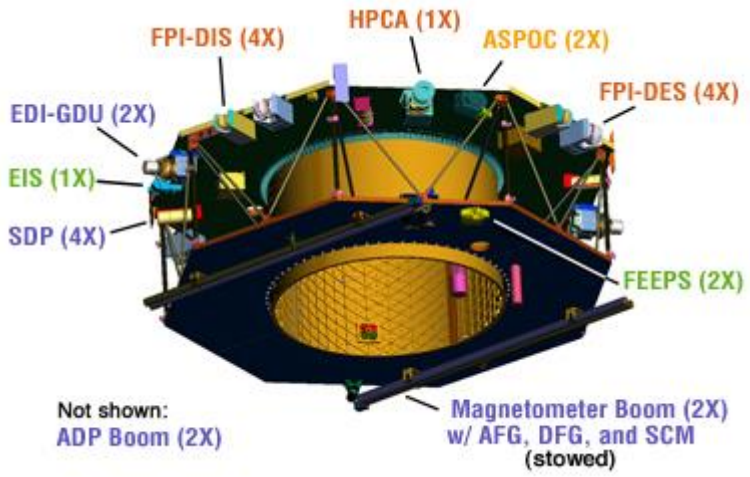

Figure 2.2: A schematic view of an MMS spacecraft with the payloads is shown. (Figure Courtesy: https://mms-fields.unh.edu/mms_payload.shtml).

EDP: To measure the electric fields two sets of double probe sensors are used (Lindqvist et al., 2016). The Spin-plane Double Probe (SDP) consists of four wire booms

measuring 48 meters in length and spherical sensors at their ends. The other set is the Axial Double Probe (ADP), which has two 10-meter antennas deployed axially close to the spacecraft spin axis. Together, the SDP and ADP provide accurate 3-Dimenbtional electric field measurements in a range from DC to 100 kHz. The SDP has an accuracy of 0.5 mV/m, while the ADP has an accuracy of 1 mV/m. Together with the Axial double probe instrument (ADP) and the Electron Drift Instrument (EDI), SDP consists of 4 biased spherical probes extended on 60 m long wire booms 90◦ apart in the spin plane, giving a 120 m baseline for each of the two spin-plane electric field components.

2.5.1.2 Observations from the THEMIS

The Time History of Events and Macroscale Interactions during Substorms (THEMIS) mission was initiated by NASA in February 2007, consisting of a group of five satellites namely THEMIS-A, B, C, D, and E. The main objective of this mission was to explore the mechanism of energy release, flow, and transfer in the magnetosphere-ionosphere system during substorms, and the dynamics associated with the change in the net magnetic field during the intensification of aurorae near the poles of the Earth.

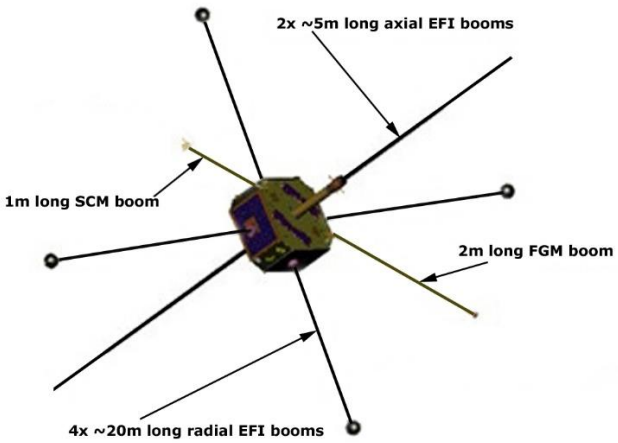

Figure 2.3: A schematic view of a THEMIS spacecraft with the payloads is shown. (Figure credit: https://www.nasa.gov/mission_pages/themis/spacecraft/index.html)

While three of the satellites revolve around the Earth within the magnetosphere, the other two have been strategically transferred to the Moon's orbit, and have been renamed as ARTEMIS (Acceleration, Reconnection, Turbulence and Electrodynamics of the Moon's Interaction with the Sun). THEMIS-B was later named ARTEMIS-P1, and THEMIS-C became ARTEMIS-P2. Each satellite consists of five identical instruments, namely, the **Electric Field**

Instruments (EFI), the **Electrostatic Analyzer (ESA),** the **Fluxgate magnetometer (FGM)**, the **Search-coil magnetometer (SCM)**, and the **Solid State Telescope (SST)**. In this thesis, the observations from the EFI, ESA, and FGM are taken and analyzed.

A short description of these three payloads is given below-

- EFI: The EFI (Bonnell et al., 2008) sensor is capable of measuring electric fields across a broad spectrum of frequencies, ranging from 8 kHz to 400 kHz. Its primary objective is to gather data on the electric fields present in the ever-changing magnetosphere of the Earth, to detect plasma flows and electromagnetic waves that are linked to the onset of a substorm.
- ESA: The ESA (McFadden et al., 2008) captures the particle distribution function which indicates the number of electrons and ions detected with specific energy levels, from a given direction and at a particular time, typically ranging from around 3 electron volts to 30 kilo-electron volts. The primary objective of the ESA is to track and identify high-speed flows through the magnetotail, as well as pressure pulses, by measuring thermal electrons and ions which are primarily responsible for creating spectacular auroras. This helps in determining the density, velocity, and temperature of the ambient plasma which ultimately aids in identifying the onset of a substorm.
- FGM- FGM (Auster et al., 2008) measures the background magnetic field and any low frequency (~ up to 64 Hz) fluctuations superimposed upon it to identify and time the abrupt reconfigurations of the magnetosphere during substorm onset. The instrument will be used to identify and time the abrupt reconfigurations of the magnetospheric magnetic field that occur at substorm onset.

2.5.1.3 Observations from the Cluster

The European Space Agency (ESA) with some participation from NASA envisaged, designed, and launched the Cluster (Escoubet et al., 2001). This spacecraft aimed to observe the dynamics of the Earth's magnetosphere for almost two solar cycles. The mission comprises four identical spacecraft arranged in a tetrahedral formation. Following the loss of the original Cluster spacecraft during a launch accident in 1996, the whole project was redeveloped again and four Cluster II spacecrafts were successfully launched in July-August 2000. Cluster has been conducting fruitful scientific operations in space for more than 22 years, and, as of March 2023, the mission has been extended until September 2024.

The sensors present inside each spacecraft are- Active Spacecraft Potential Control experiment (ASPOC), Cluster Ion Spectroscopy experiment (CIS), Digital Wave Processing instrument (DWP), Electron Drift Instrument (EDI), Electric Field and Wave experiment (EFW), Fluxgate Magnetometer (FGM), Plasma Electron and Current Experiment (PEACE), Research with Adaptive Particle Imaging Detectors (RAPID), Spatio-Temporal Analysis of Field Fluctuation experiment (STAFF), Wide Band Data receiver (WBD) and Waves of High Frequency and Sounder for Probing of Density by Relaxation (WHISPER**). Out of these, the observations from the EFW, FGM, CIS, and PEACE are taken and analyzed**. A short description of these four sensors is given below-

- EFW: The EFW (Escoubet et al., 2001) gives the magnitude and direction of the ambient electric field. To measure the electric field, EDI inside the EFW launches two beams of electrons from each spacecraft, which then travel in orbits of at least 10 km before returning to receivers on the opposite side of the spacecraft. By analyzing the direction of the fired beams and the time it takes for the electrons to travel and return, the strength of the electric and magnetic fields surrounding the Cluster spacecraft is estimated, which helps us to quantify the electric field vector, potential, electron density, and temperature.
- FGM: FGM (Riedler et al., 1997) is an instrument that consists of two magnetometers used to detect and measure the magnetic fields. To prevent any interference from the spacecraft, FGM is mounted on a five-meter-long boom. It can record magnetic field measurements up to 67 times per second.
- CIS: CIS (Reme et al., 1997) investigates and examines the composition, mass, and distribution of particles (basically ions) it encounters. It consists of two different instruments, a Hot Ion Analyser (HIA) and a Composition and Distribution Function analyzer (CODIF), along with a highly advanced instrument control and data processing system that allows for extensive onboard data analysis.
- PEACE: As the CIS investigates ions, the PEACE (Riedler et al., 1997) looks at the 3-D distribution of electrons in the plasma. It also examines their energy ranges, counts them, and measures the magnitude and direction of their flow.

2.5.2 Estimation of kinetic scale coupling parameters

Quantifying the kinetic scale coupling parameters is necessary to understand the electron and ion-scale processes (like magnetic reconnection) happening inside electron and

ion-scale regions like EDR and IDRs in Earth's magnetosphere. The observations from this section are used in Chapter 4 to study the dynamics of the reconnection regions during the 31 December 2015 geomagnetic storm.

2.5.2.1 Estimation of FAC

In general, the FACs can be calculated using the Curlometer method (Dunlop et al., 2002) and the plasma method (Cheng et al. 2016). The Curlometer method uses the geometry of the face of the tetrahedron to apply Ampere's law and derives the current density normal to the face (see Dunlop et al., 2021 and references therein). This technique has been widely used in many prior studies (Shi et al. 2010; Phan et al. 2016; Cheng et al. 2016; Nakamura et al. 2018) to calculate the FACs.

The formula for the Curlometer technique is based upon Ampere's law as derived by Dunlop et al. (2002) (see figure 2.4).

$$j_{||(\mathbf{B})} = \frac{j.B}{|B|} = \frac{\left(\frac{\nabla \times B}{\mu_0}\right).B}{|B|} \qquad \text{(equation 12)}$$

Where j is the current density (nA/m^2), μ_0 is the magnetic permeability ($4\pi \times 10^{-7}$ H/m), B is the magnetic field in the barycentre (nT), and $j_{||(\mathbf{B})}$ (nA/m^2) is the FAC density parallel to the magnetic field calculated using the Curlometer method.

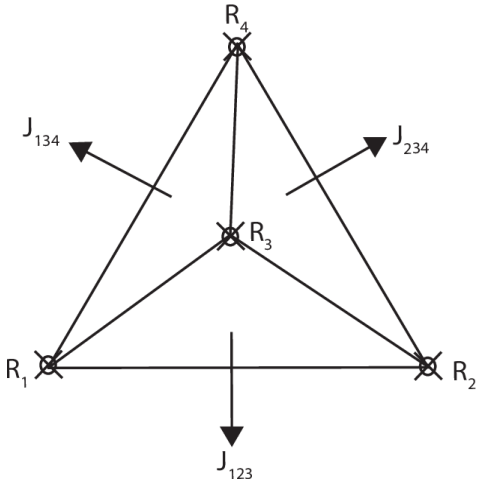

Figure 2.4: A schematic view of the Curlometer method applied on tetrahedral spacecraft formation to determine FACs. The R1-R4 represent the spacecraft positions in the 3-D and j_{xyz} represents the current vectors perpendicular to the respective facet of the tetrahedral (see Dunlop et al. 2002, for details).

The FACs are also estimated using the plasma method observations (Cheng et al. 2016; Chen et al. 2019), which can be given by

$$j_{||(plasma)} = ne(V_{||\mathbf{i}} - V_{||\mathbf{e}}) \quad \text{(equation 13)}$$

where $j_{||(plasma)}$ is the FAC density, n (/m^3) is the plasma number density with an assumption that the number of ions is equal to the number of electrons (i.e. $n_i = n_e$), e is the unit electric charge (Coulomb), and $V_{||\mathbf{i}}(V_{||\mathbf{e}})$ is the ion (electron) bulk velocity along the magnetic field. So, $j_{||(\mathbf{i})} = neV_{||\mathbf{i}}$ and $j_{||(\mathbf{e})} = neV_{||\mathbf{e}}$, respectively represent ion FAC and electron FAC.

2.5.2.2 Estimation of electric fields and power

The total electric field in a multi-fluid space like the magnetosphere can be expressed as a sum of five terms, which arise from the contributions of the ambient, reference frame-dependent, Hall, Inertial, and Pressure-gradient electric field (Torbert et al. 2016; Macek et al. 2019a; 2019b). The first and second terms are classical, whereas, the third, fourth, and fifth terms are non-ideal (Martin 2010). The summation of all these terms is equal to the dissipation created by an anomalous resistivity which can be presented as

$$E_t = E + V \times B + E_H + E_a + E_P = \eta j \quad \text{(equation 14)}$$

Where the first two terms i.e. ($E_0 = E + V \times B$) collectively represent the classical electric field seen in the rest frame by plasma moving with the velocity V (Macek et al. 2019a; 2019b).

The third (E_H), fourth (E_a), and fifth (E_p) terms are non-ideal terms that are important at the ion and electron scales in the kinetic regime (Spitzer 1956; Rossi & Olbert 1970). The third term represents the Hall electric field which is generally contributed by the motion of electrons in a highly variant magnetic field regime like a reconnection region (Macek et al. 2019a,b). The Hall electric field is produced because of the ion-electron decoupling. It is noteworthy to mention that E_H is important only at the ion scale. This term contributes the most to the total electric field when the plasma is in the ion diffusion region (Burch et al. 2016). The Hall term is calculated as

$$E_H = \frac{-j \times B}{(en)} = (V_e - V_i) \times B \quad \text{(equation 15)}$$

Where V_e and V_i are the electron and ion bulk velocity (m/s), respectively.

The fourth term (E_a) is nothing but the electric field resulting from the separation between the accelerated electrons and ions and is denoted as the inertial term. It is noteworthy

to mention that E_a is important only at the electron scale. Following Martin (2010) and Macek et al. (2019a), this term can be represented as

$$E_a = \frac{m_e}{e}\left[\frac{1}{n_e}\frac{\partial}{\partial t}(n_e V_e) - \frac{1}{n_i}\frac{\partial}{\partial t}(n_i V_i)\right] + \frac{m_e}{e}\left[\frac{1}{n_e}\nabla.\{n_e(V_e \cdot V_e)\} - \frac{1}{n_i}\nabla.\{n_i(V_i \cdot V_i)\}\right]$$

(equation 16)

where m_e (kg) is the mass of an electron and ∇ denotes the divergence of the respective tensor.

The fifth term (E_p) arises from the divergence of the pressure tensor (Gurnett & Bhattacharjee 2005) due to the thermal pressure of electrons relative to the ion background. Notably, in the electron diffusion region where the ions decouple from the magnetic field, electron physics becomes dominant. Remarkably, Ep is important both at ion and electron scales. So the electron pressure eventually producing the electric field term (Macek et al. 2019a) can be derived with the following expression.

$$E_P = \frac{1}{en_e}\nabla.P_e = \frac{m_e}{en_e}\nabla.[n_e < (V_e - U)(V_e - U) >] \quad \text{(equation 17)}$$

Where the thermal pressure tensor P_e is composed of $p_{\|e} = n_e k T_{\|e}$ (parallel) and $p_{\perp e} = n_e k T_{\perp e}$ (perpendicular). k is the Boltzmann constant; U is the mean bulk velocity (m/s); $T_{\|e}$ and $T_{\perp e}$ are the parallel and perpendicular electron temperature tensors, respectively. It is noteworthy to mention that the estimation of the fourth and fifth terms of the above-mentioned total electric field usually involves large uncertainties, due to the low resolution and high noise in the spacecraft measurements of particles.

It is important to mention that the estimation of the fourth and fifth terms can often be challenging due to the high level of uncertainty associated with spacecraft measurements of particles, which is primarily attributed to low resolution and high noise.

The electromagnetic energy associated with the electromagnetic fields is converted into the particle or plasma kinetic energy, the time rate of change of which can be represented in terms of the associated power expressed as $W = j.E$; where j and E respectively depict the vector fields representing current density and total electric field contributions to the generalized Ohm's law in that region (Burch et al., 2016; Fu et al., 2016). Estimation of power helps us to understand the energy dynamics in the probable reconnection regions.

2.6 Ionospheric observations

The observations discussed in this section (and Section 2.7) primarily serve the purpose of conducting qualitative and quantitative analyses related to the magnetospheric-ionospheric current systems, electric fields, and geomagnetic responses as presented in Chapter 4.

2.6.1 Observations from the SuperDARN

The Super Dual Auroral Radar Network (SuperDARN) consists of 36 high-frequency radars covering the mid and high latitudes of both hemispheres. These radars operate in the HF band ranging from 8.0 MHz (37m) to 22.0 MHz (14m). Typically, the radar operates in a standard mode where it scans through 16 beams, which are separated by approximately 3.24° in the azimuth direction. In a single full scan, the radar covers an area of approximately 1 million square kilometers, encompassing a range of over 3000 km and an azimuthal span of 52° (Greenwald et al., 1995; Chisham et al., 2007; Nishitani et al., 2019).

The SuperDARN convection maps with a cadence of 10 minutes were obtained from the website of SuperDARN through "http://vt.superdarn.org/tiki-index.php?page=Conv+map+overview" by selecting the date and time.

2.6.2 Observations from the DMSP-SSUSI

The Defence Meteorological Satellite Program (DMSP) orbits the Earth at an altitude of approximately 840 km. It is a sun-synchronous, polar-orbiting satellite with an orbiting period of ~101 minutes and provides global coverage twice per day (Hardy et al., 1984). The special sensor ultraviolet spectroscopic imager (SSUSI) instrument onboard the DMSP satellite is used to cross-track scanning by far-ultraviolet emissions. SSUSI consists of a far-ultraviolet scanning imaging spectrograph (SIS) which observes 5 spectral bins: HI Laymn α (121.6 mm), OI (130.4 nm), OI (135.6 nm), N2 Lyman-Brige-Hopfield Short (LBHS, 140-150 nm) and Long (LBHL, 165- 180 nm) in far ultraviolet (FUV) bands (Zhang and Paxton, 2008; Sotirelis et al., 2013; Zhou et al., 2020). DMSP satellite monitors different meteorological, oceanographic, and ionospheric features associated with solar-terrestrial physics. During the main phase of the geomagnetic storms and substorms, continuous impingement of charged particles occurs over the high latitudes followed by the equatorward expansion of the auroral

oval (Bounsanto 1999; Fedrizzi et al., 2008). DMSP-SSUSI probes the ionospheric conditions during disturbed periods thoroughly and provides the convection maps, which can be directly obtained from the DMSP-SSUSI website (https://ssusi.jhuapl.edu/).

2.7 Observations from global magnetometer networks

As discussed in Section 2.6, the observations discussed in this section, too, focus on probing the geomagnetic responses to perform an understanding regarding the electric fields and current systems in the magnetosphere and ionosphere, as presented in Chapter 4.

2.7.1 Observations from the INTERMAGNET network

The International Real-time Magnetic Observatory Network (INTERMAGNET) is a global consortium of organizations operating ground-based magnetometers, comprising more than 100 magnetic observatories spread across over 50 nations (Kerridge, 2001; Rasson, 2007). The utilization of INTERMAGNET data is broad, encompassing a range of applications associated with the Earth's interior, the atmosphere, and the space weather. The INTERMAGNET observations are used in formulating many important tools frequently used in space weather research like the geomagnetic indices (Dst, SYM-H, and Kp) and framing different models like the World Magnetic Model (WMM), and the International Geomagnetic Reference Field (IGRF).

The geomagnetic observations of both 1-second and 1-minute resolutions can be obtained from the latitudinal and longitudinal chains of magnetometers available at the INTERMAGNET website (https://www.intermagnet.org/data-donnee/download-eng.php) (see Love and Chulliat, 2013 for the description of the data set). Figure 2.5 shows a map of the locations/stations selected for this thesis.

The X, Y, Z, H, and D-component observations from the ground magnetometer network located throughout the globe (as shown in Figure 2.5) are taken at a 1-minute cadence. The X, Y, and Z represent magnetic field components in the X, Y, and Z directions in the Cartesian coordinate system. The H-component has been calculated using the mathematical equation $H=\sqrt{X^2+Y^2+Z^2}$, and the D-component is computed using the associated equation $D= H.\tan\varphi$, where $\varphi=\frac{Y}{X}$

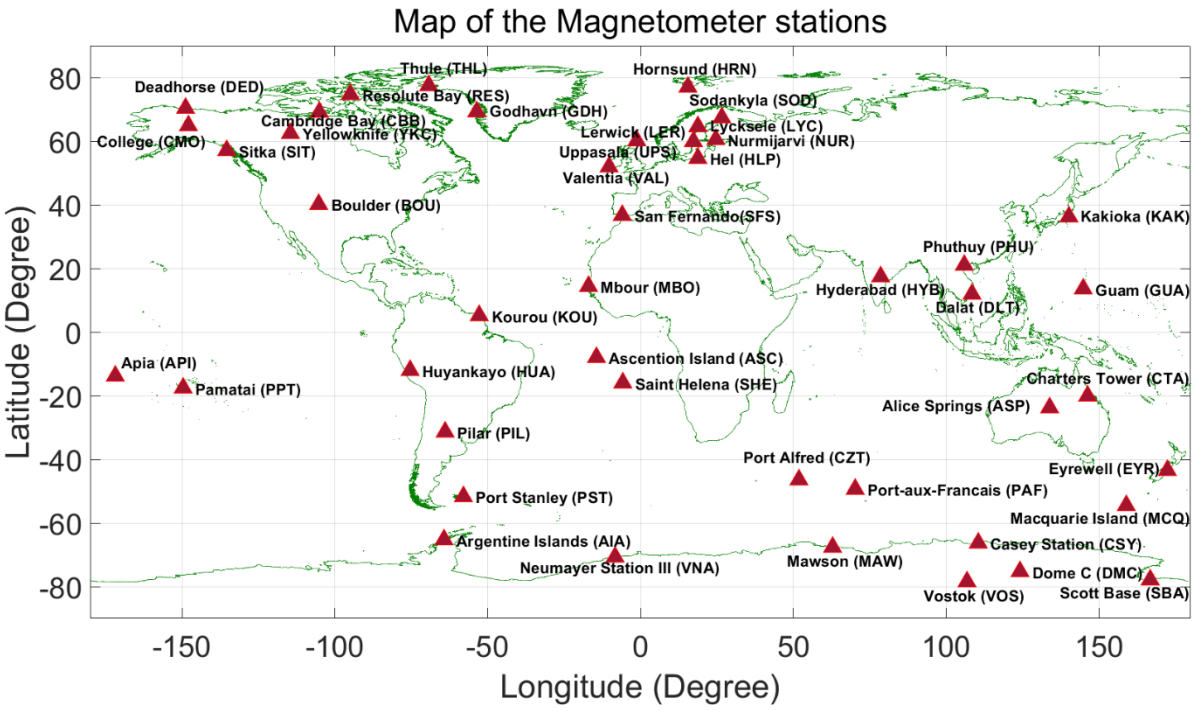

Figure 2.5: Map of the locations of 45 magnetometer stations that are used in this thesis. The full name and code of the respective stations as provided by the INTERMAGNET website are given aside from the triangle marker. A list of all the stations is provided as a table in the supporting information (SI-1) in Appendix B.

The necessary baseline corrections are done by the estimation of the quiet time base level (H_Q) as an average of the H-component observations between 02:00 and 04:00 hours local time of each station. For this purpose, the three quietest days before the storm are taken from the list of the international quiet days published at the website https://www-app3.gfz-potsdam.de/kp_index/quietdst/qd201019.html. The base level (H_q, $for\ the\ H-component$) is then subtracted from the storm time variations (H_q) to obtain the base-corrected daily H-component ($\Delta H_d = H_d - H_q$), where d and q denote the disturbed and the quiet time variations. A similar baseline correction is carried out for the D-Component observations. In addition, following Carter et al. (2016), the effect of the GICs is assessed using the dB/dt (nT/min) estimation from 1-minute sampled global H-component observations.

2.7.2 Observation from the SUPERMAG network

SuperMAG is a global collaboration of organizations and national agencies that use over 300 ground-based magnetometers to provide validated 3-D vector magnetic field perturbations acquired by ground-based magnetometers (Gjerloev, 2009, 2012). The network comprises stations that offer both absolute measurements (such as those from Intermagnet

Observatories) and relative measurements. The service focuses on the variations due to electric currents in the magnetosphere-ionosphere system, and therefore, it eliminates the dominant and slowly changing main field of the Earth. It provides data at 1-minute and 1-second temporal resolutions, which can be obtained from the SUPERMAG website (https://supermag.jhuapl.edu/info/).

The SML index is based upon the observations by the magnetometers located in a belt of 40^{o}-80^{o} N latitudes (see for details- Newell and Gjerlov 2011). The data set of the SML index is obtained from the website of the SuperMag (https://supermag.jhuapl.edu/indices/).

CHAPTER 3

SW-M-I Coupling During Supersubstorms of Solar Cycle 24: Energy Flow

"Everything is energy and that's all there is to it."

-Albert Einstein

3.1 Introduction

The energy transfer from the solar wind to the magnetosphere of the Earth happens through different pathways (Tsurutani and Meng, 1972; Gonzalez et al., 1994; Echer et al., 2008). The magnetospheric cavity experiences geomagnetic storm and substorm events (Gonzalez et al., 1994), wherein, the solar-wind-magnetosphere-ionosphere coupling manifests through a large number of physical processes (Axford and Hines, 1961; Akasofu, 1964; Akasofu, 1981; Rostoker et al., 1980; Baker 1996; Liou et al., 2001; Østgaard et al., 2005). The geomagnetic storms are associated with substorms, however, isolated substorms are also known to occur through the magnetospheric processes without an immediate or explicit forcing from the sun (Nishida and Kamide, 1983; Liou et al. 2013; Vorobjev et al. 2016). Additionally, there may be cases when the magnetosphere is in a pre-substorm state, and a change in the interplanetary parameters may eventually favour the generation of a substorm (Guo et al. 2012; Sandholt et al. 2014 and references therein).

Substorms of varying magnitudes have been customarily identified by using the AL (auroral lower component) index along with the gross night side activity by using the AE (auroral electrojets) index. The denser SuperMAG network of magnetometers has made it possible to define a new pair of indices called the SME (super magnetic electrojets) index and SML (lower component of SME) index (Newell and Gjerlov 2011a, 2011b), which can better identify the spatio-temporal occurrence of the substorms. Using the SML data, Tsurutani et al. (2015) have found that substorms can occur as extreme events, and a threshold of SML<-2500 nT has been used to declare them as supersubstorms. Subsequently, Hajra et al. (2016) analyzed more than 70 geomagnetic storms with a superposed epoch analysis and found that supersubstorms may not have a strong relationship with the associated geomagnetic storm and that seasonal variations show ionospheric dominance during such events. The solar wind sources that drive the extreme substorm events have been studied by Hajra et al. (2016), Adhikari et al. (2017), and Despirak et al. (2019), and it has been shown that the supersubstorms are sourced majorly from magnetic clouds and the interplanetary sheath fields. These studies have also reported that the majority of the supersubstorms occur during the initial or main phase of the geomagnetic storms. Nishimura et al. (2020) have highlighted the dominance of nightside drivers and magnetotail during supersubstorms. They found enhancements in auroral brightening, TEC (total electron content), and neutral wind during the supersubstorms, which were higher than average substorm levels of any other type. Further, Despirak et al. (2020) have analysed the supersubstorm event of 7-8 September 2017 and reported that the westward

electrojet expanded over all longitudes in the auroral region possibly due to the production of the daytime magnetic bay at polar latitudes.

However, the recent studies on the supersubstorms have not emphasized the quantification of the sources and sinks of the solar wind energy through detailed analysis of the solar wind-magnetosphere-ionosphere coupling, which is significant to understand the impacts in geo-space. A closer look at the supersubstorm events, that have occurred during the past four solar cycles emphasizes anomalous characteristics of occurrence during solar cycle 24. Figure 3.1 gives a comparative distribution of the total, month-wise and year-wise occurrences of supersubstorms from 1971 to 2019 obtained using the SuperMag data set of substorms (Newell and Gjerlov, 2011a) and the threshold of SML<-2500 nT.

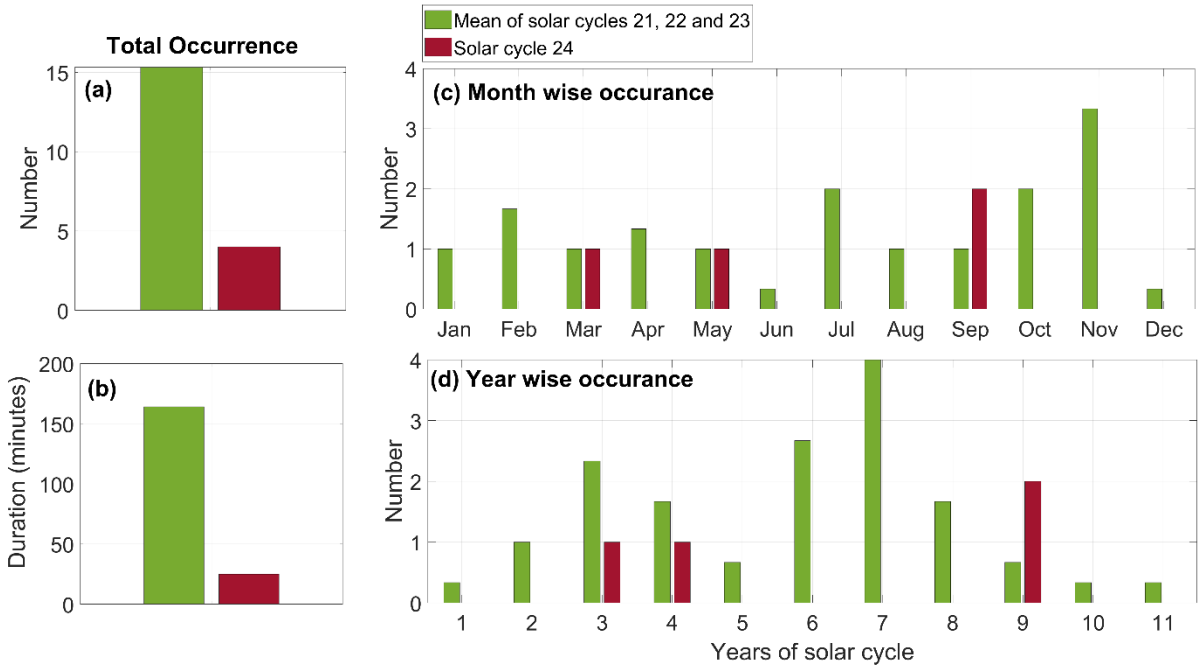

Figure 3.1. Comparative distribution of the occurrence of supersubstorms of solar cycle 24 is given against the average occurrence during solar cycles 21, 22, and 23. Panels (a) and (b) respectively provide the number of supersubstorms and the total duration of SML<-2500 nT and panels (c) and (d) give the month-wise, and year-wise distributions, respectively, in each case.

It is found that against the average of the previous -three solar cycles, the total number of supersubstorms in the solar cycle 24 is much less along with the lowest total duration. The monthly occurrence partly matches the average, but, the occurrence during 11 years of a mean solar cycle anomalously shows no supersubstorm during solar high activity years of solar cycle

24. It is pertinent to emphasize that a study on comparative analysis of the geomagnetic storms by Hajra (2021) has reported reduced average magnitudes of the interplanetary and coupling parameters during the solar cycle 24 compared to the previous cycles. The weakest magnitude of the solar cycle 24 may be associated with an overall reduction in energy coupling resulting in the reduced number of supersubstorms. However, we shall investigate this aspect in greater detail using the recent formulations to estimate the solar wind and the interplanetary conditions, the coupling through the Epsilon parameter, Borovsky parameter (Borovsky, 2008), field aligned current, polar cap potential drop along with the power dissipated through ring current, auroral precipitation and Joule heating.

The study presented in this chapter is focused on comprehensive and detailed case studies of the geomagnetic events of May 2011, March 2012, and September 2017, which are associated with the supersubstorms, to demonstrate the probable origin, the solar wind-magnetosphere coupling, magnetosphere-ionosphere coupling, and energy partitioning (sources and sinks). The study is further substantiated by analyses of the energetics and partitioning of 101 substorms of varying intensities during 1998-2018. The following sections give observations and methods, results and discussion, and a summary of new findings.

3.2 Observation and methodology

Since a detailed methodology with formulae to estimate the coupling parameters and other indices are already described in Chapter 2, in this section the definition of phases of supersubstorms is given, followed by a very brief overview of different estimations and primary models employed to quantify different energy terms and indices.

3.2.1 Duration of the phases of the suspersubstorms

Conventionally, the substorms are expressed in terms of the growth phase, expansion phase, and recovery phase. Of these three phases, the expansion and the recovery phases are the most important with respect to energy dissipation in the magnetosphere-ionosphere system. We have followed the definitions given by Li et al. (2012) for substorms to calculate the exact durations of the respective phases of the supersubstorms considering the value of minimum depression and its time epoch as reference. So, t_1=instant of time when $\frac{1}{5}^{th}$ of the minimum depression is attained before the minimum); t_m=instant of time of minimum depression and t_2= instant of time when $\frac{1}{5}^{th}$ of minimum depression is attained after the minimum. Then, it is obvious that the duration of the expansion phase = t_m-t_1, recovery phase=t_2-t_m, and total

substorm= t_2-t_1. In this study, the variation in the SML index is considered to determine the respective phases of the supersubstorms.

3.2.2 Procedure of estimation

A detailed description of the key methodologies, observations, and estimations utilized for the analyses presented in this chapter has already been covered in Chapter 2. Here, a brief overview of the relevant computations is given for completeness of the results.

The dataset of the SML index is obtained from the website of the SuperMag (http://supermag.jhuapl.edu/indices/). The observations of the solar wind, interplanetary parameters, and geomagnetic indices are obtained from the NASA-OMNIWeb database (https://omniweb.gsfc.nasa.gov/form/omni_min.html) at a cadence of 1 minute. The estimation of all the power and energy terms for the study in this Chapter is performed with 1-hour cadence observations. Chapter 2.2 can be referred for all the details on the methods and estimations in this context. For the identification of the types of solar wind structures during the supersubstorms the set of criteria (threshold values) provided by Yermolaev et al. (2009) is used in the study presented in this chapter (see Table 2.1 for details). Chapter 2.3 presents more details about the methodology.

The available kinetic energy flux of the solar wind power is estimated following equation-1 of Chapter 2. The input power is calculated by estimating the Epsilon parameter (Chapter 2, equation 2). The other terms associated with solar wind-magnetosphere coupling are the Borovsky parameter (Chapter 2, equation 3), and Newell parameter (Chapter 2, equation 4). The magnetosphere-ionosphere coupling parameters are estimated as the PCPD (Chapter 2, equation 5) and FAC (Chapter 2, equation 6). The power dissipated through ring current, Joule heating, and auroral precipitation is estimated using equations 7, 9, and 10 respectively.
The input and dissipated power of different channels are integrated with respect to time, to obtain the respective input and dissipated energies. The energy dissipated through other minor channels is also considered here. However, they are found to be negligible with respect to the major energy sinks. The details of this are presented in Chapter 2.4.7.

The efficiencies e1 (input efficiency), e2 (dissipation efficiency), and e3 (ratio of sink energies) are computed using the formula given in Chapter 2.4.8. All the computations are carried out using computer programs specifically written to obtain the time series of variations in the required parameter. Since different data sets are obtained in different formats and units

of indices, a careful examination is performed to bring them all into the units described in the methods given in Chapter 2.

3.3 Results

The analyses of the geomagnetic events of May 2011, March 2012, and September 2017 are performed in terms of the solar wind sources, energetics associated with sources, and sinks in the solar wind-magnetosphere-ionosphere system. It shall be noted that during the geomagnetic storms of May 2011 and March 2012, one supersubstorm occurred whereas September 2017 storms exhibited two supersubstorms. The cause-to-effect relationship for each event is highlighted and discussed. The following subsections provide the main results of this study.

3.3.1 Solar wind drivers

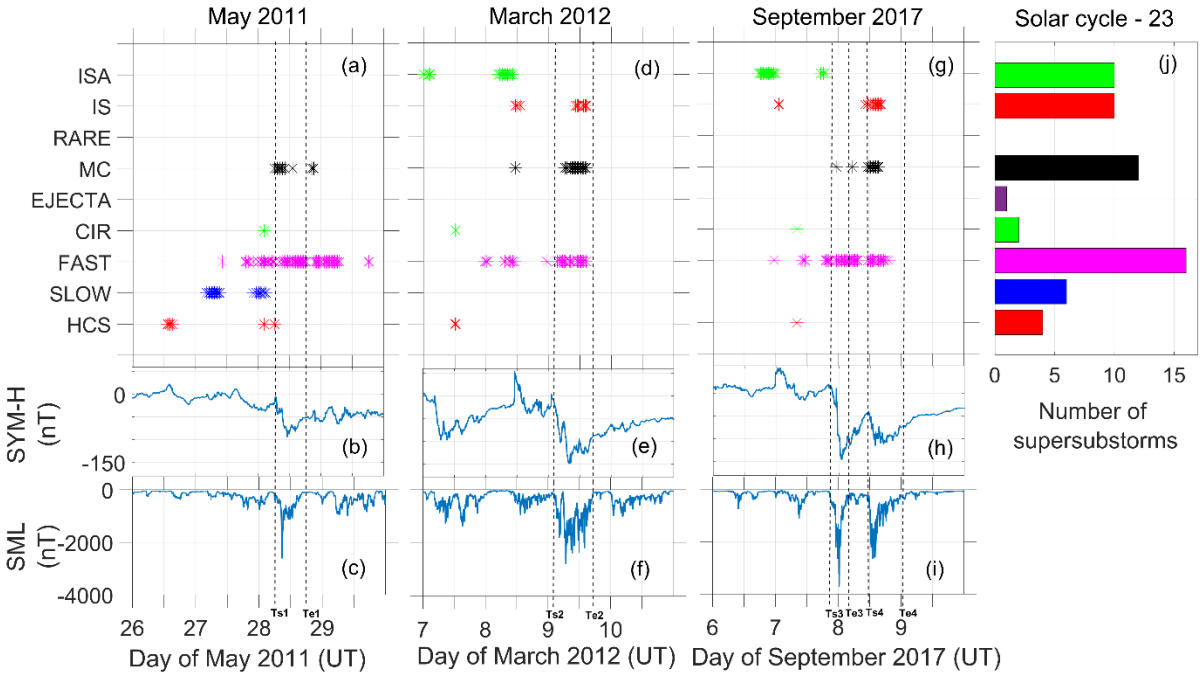

Figure 3.2. The presence of different solar wind structures is shown for the supersubstorms of solar cycle 24 in the first 3 columnar panels from left (panels a, d, and g). The corresponding variations in the SYM-H (panels b, e, and h) and the SML (panels c, f, and i) indices for 4 days are given in the middle and bottom rows. Vertical dashed lines mark the start (Ts) and end (Te) of a supersubstorm. The rightmost columnar panel (j) shows the mean distribution of the presence of different solar wind structures during 17 supersubstorms of solar cycle 23. The acronyms are referred to in the text description in section 2.1 following Yermolaev et al. (2009).

The solar wind sources that could have possibly caused the supersubstorm events have been mostly attributed to the interplanetary CMEs in past studies. Results from the study presented in this chapter of the geomagnetic storms associated with the supersubstorms are given in Figure 3.2. The presence of different solar wind streams for the solar cycle 24 is given event-wise (first 3 columnar panels from the left) and for the solar cycle 23 are as mean distributions (right-most columnar panel) for an immediate comparison. The supersubstorms have occurred on 28 May 2011, 9 March 2012, and 7-8 September 2017. The corresponding variations in the SYM-H index show their association with a geomagnetic storm. It is found from Figure 3.2 that the magnetic cloud preceded by the FAST background stream is commonly present as a source during the main phases of all 4 events of solar cycle 24.

Specifically, during the March 2012 and September 2017 events, a brief presence of the forward (shown as IS) and backward (shown as ISA) interplanetary shock waves well before the initial phases of the supersubstorms is observed, which is not found during the 2011 event. Instead, the slow-moving plasma preceding the 2011 event was observed on 27 May, a day before the initiation of the supersubstorm. Particularly, the event of 2017 exhibited two supersubstorms, with the lowest SML index at 0024 UT and 1308 UT on 8 September 2017. A couple of the supersubstorms (SSS) are termed '2017-SSS1' and '2017-SSS2', both of which are found to be separately associated with a stream of FAST background stream with the magnetic cloud. During the supersubstorm of March 2012, a SLOW background stream with a Heliospheric current sheet appeared along with a brief period of corotating interaction region well before the initial phase of the geomagnetic storm. This is followed by multiple hits of magnetic clouds with FAST background stream, which acted as the driver of the main phase of the storm and possibly also triggered the supersubstorm on 9 March 2012. The recovery phase of the supersubstorm is highlighted by the presence of a corotating interaction region in the background of the SLOW stream.

A direct comparison of the solar wind streams present during the supersubstorm events of the solar cycle 23 is given in panel (j) of Figure 3.2. This illustrates that the major drivers of the supersubstorm events during solar cycle 23 have been the FAST stream and multiple hits of the magnetic clouds along with the forward (IS) and backward (ISA) shock waves. So, the supersubstorms of the solar cycle 24 mostly agree with the mean distribution of solar cycle 23, albeit with the presence of the shock waves for a smaller period during the former. These results significantly infer that the presence of multiple hits by the magnetic cloud with FAST background stream could be a dominant and governing condition for the supersubstorms to

occur at any level of solar activity. This is reinforced by the fact that each of the events is associated with a moderate geomagnetic storm, as detailed below.

3.3.2 Interplanetary parameters and geomagnetic indices

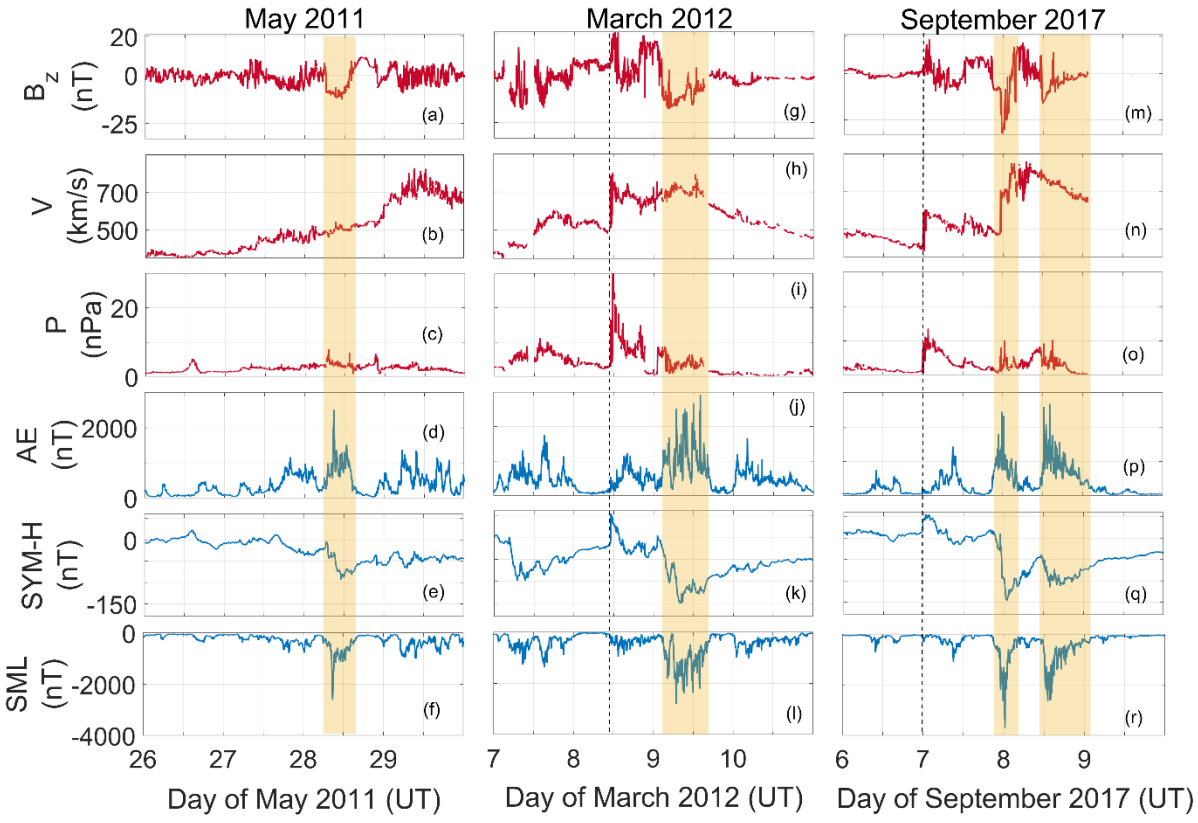

Figure 3.3. The top three panels in each column give variations in the solar wind plasma parameters the IMF-Bz (Bz), speed (V), and pressure (P), and the bottom three panels give the AE, SYM-H, and SML indices, respectively. Columns from left to right show results for 2011, 2012, and 2017 events, respectively. A vertical dotted line in the right two columns shows the time of the sudden commencement. The supersubstorm durations are shaded in yellow colour.

Figure 3.3 shows the variations in the interplanetary parameters as observed at the L1 point (top four panels) and in the geomagnetic indices (bottom 3 panels). The variations in the SYM-H and SML indices are repeated for reference. The supersubstorm durations are shaded in a yellow colour corresponding to the variations in the SML index. A close inspection of the variations in the solar wind parameters shows a large difference among the 4 supersubstorm events. Particularly, neither the solar wind pressure nor bulk velocity shows any abrupt increase before the expansion phase of the supersubstorm on 28 May 2011. A gradual rise in the velocity is observed from about 05 UT (dashed vertical line) on 27 May, which peaks on 29 May after the occurrence of the supersubstorm. Additionally, the variations in the SYM-H index from

26-29 May 2011 show the absence of the sudden commencement of the geomagnetic storm. However, the variation in SYM-H shows some intermittent negative excursions during 0500-1500 UT on 27 May, a bay-like decrement during 1500 UT on 27 May and ~0600 UT on 28 May which can be termed as the first-sub main phase, and, a negative excursion between ~0600-2355 UT on 28 May, which can be termed as the second sub-main phase of the moderate geomagnetic storm. Notably, an unusual extreme excursion in the SML index occurred during the second sub-main phase of the geomagnetic storm, leading to the occurrence of a supersubstorm on 28 May, which is also replicated in the AE index. We discuss the development of the multi-step storm and its possible association with the occurrence of a supersubstorm in section 3.4.

In contrast to the above storm, the storms of 2012 and 2017 show a sudden commencement respectively, at ~1200 UT on 8 March and 00 UT on 7 September. The commencement is accompanied by an abrupt rise in bulk velocity, and ram pressure (shown by a vertical dashed line). In the case of the 2012 event, two consecutive southward excursions in the IMF-Bz at 1200 UT on 8 March and 0215 UT on 9 March are noted which caused a two-step decrease in the SYM-H index. The presence of magnetic clouds at ~1100 UT on 8 March and ~0500 UT on 9 March (shown in Figure 3.2) seems to be associated with the couple of southward excursions in the IMF-Bz (Figure 3.3). Following similar arguments, it is found from Figure 3.3 that three consecutive southward excursions in IMF-Bz have occurred at ~0100 UT and ~2000 UT on 7 September, and at 1137 UT on 8 September 2017. Out of the above three southward excursions, only the latter two are found to be associated with intervals of magnetic clouds which occurred between ~2000 UT on 7 September and ~1400 UT on 8 September (shown in Figure 3.2). Therefore, a three-step decrease in SYM-H was observed on 7 and 9 September 2017 along with simultaneous excursions in the AE and SML indices. Intriguingly, two supersubstorm events are noted during this event namely '2017-SSS1' and '2017-SSS2', which occurred within about 12 hours. It is pertinent to highlight here that in comparison to the '2017-SSS1', the '2017-SSS2' is found to be associated with a lesser magnitude of minimum IMF-Bz and SYM-H indices and negligible variations in the solar wind ram pressure.

Thus, all four cases of the supersubstorm of 2011, 2012, and 2017 are found to exhibit multiple southward and northward excursions in IMF-Bz followed by a multi-step development of the associated geomagnetic storm, which eventually led to the occurrence of the supersubstorms in the later part of the main phases of the storms. It shall be noted here that the development of a multi-step storm is a very complex subject by itself and needs a careful

quantification of the involvement of several other aspects of multi-step coupling (see viz. Kamide et al., 1998; Keika et al. 2018; Verkhoglyadova et al. 2016). A detailed investigation is performed to obtain the pre-conditioning, the energy transfers, and partitioning, which can highlight the differences and commonalities of the responses during the supersubstorms. A discussion on the relationship among observed variations is given in section 3.4.

3.3.3 Coupling and energy transfer

We aim to quantify the solar wind energy available for the earth's magnetosphere, its conversion, and dissipation during the spatial and temporal evolution of the energy flow through the magnetosphere-ionosphere system. The solar wind-magnetosphere-ionosphere coupling consists of the merging of the interplanetary and geomagnetic field lines along with the electrodynamic interactions through the three-dimensional current system and the associated electric fields.

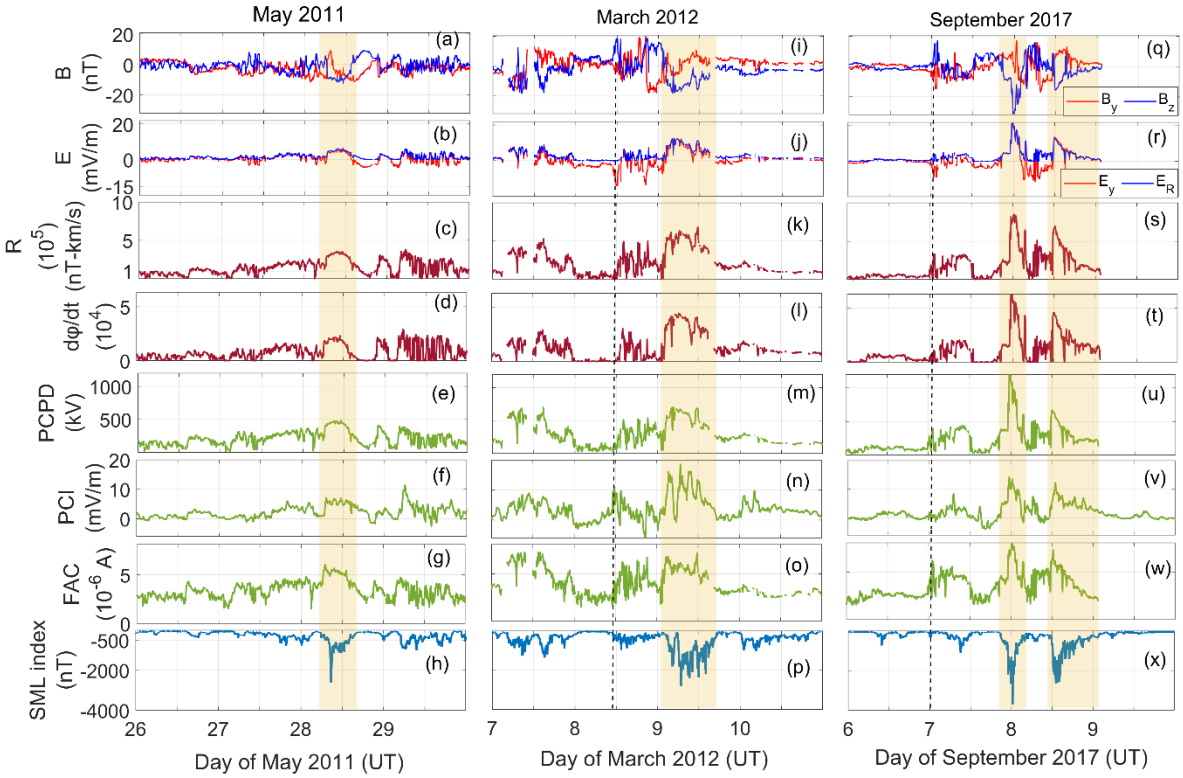

Figure 3.4. Panels from the top in all columns give variations in the IMF-By/Bz and IEF-Ey/E_R (solar wind); R and $\frac{d\varphi_{MP}}{dt}$ (solar wind-magnetosphere coupling); PCPD, PCI, and FAC (magnetosphere-ionosphere coupling) and, the SML indices respectively. The columnar panels are arranged respectively for the 2011, 2012, and 2017 events. Vertical dashed lines show the

time of occurrence of SSC for the 2012 and 2017 events and yellow shades represent the supersubstorm durations, in respective years.

The variations in the IMF-By/Bz, y-component of the interplanetary electric field (IEF-Ey), reconnection (or merging) electric field (E_R), the solar wind driver function (R), rate of merging at the magnetopause ($\frac{d\varphi_{MP}}{dt}$), the PCPD, the integrated FAC, and the PCI are given in Figure 3.4. The variations in the IMF-Bz and SML indices are reproduced in this figure for ready reference. With a sudden change in the coupling rate (R), the rate of magnetic flux opening at the magnetopause ($\frac{d\varphi_{MP}}{dt}$), the PCPD and FAC are found in synchronization with a sudden southward excursion in IMF-Bz and enhancement in E_R, and a sudden impulsive peak in the SML index is noted as a consequence of the coupling, during all the events of supersubstorms. The coupling parameters R and $\frac{d\varphi_{MP}}{dt}$ show one-to-one correspondence throughout 4 days during each of the events. The IEF-E_y, E_R, and PCPD exhibit almost similar variations for the respective duration of the supersubstorms. While, the PCI index mostly follows a correspondence with the variations in the other interplanetary parameters and with E_R and PCPD, specifically, a few exceptionally large fluctuations in PCI between 00 UT and 1200 UT on 9 March 2012 are not found to match with other coupling parameters. Additionally, the fluctuations in the PCI index are mapped as oscillatory variations in the SML index in the same duration on 9 March 2012. In the case of other supersubstorms, we did not observe such a departure in the PCI index from the other parameters and correspondence with the SML index, which is intriguing. Thus, in a nutshell, it is found from Figure 3.4 that the prolonged southward excursions of IMF-B_z and higher values of R led to sustainable perturbations over the polar region, which could eventually have triggered the supersubstorms. It is intriguing to find a large impulsive response of PCI during the SSC at about 12 UT on 8 March 2012 and in FAC at about 00 UT on 7 September 2017. Possibly, the northward IMF-B_Z associated with the sudden global magnetospheric compression could have produced large positive impulse-like variations (Troshichev and Janzhura, 2012) but this needs further investigations.

So far, the analysis of the events shows a few commonalities like multiple hits by magnetic clouds along with fast-moving solar wind background conditions, followed by episodic increments in the coupling parameters and a multi-step decrease in the SYM-H index. All these common factors exemplify a possible contribution to energy storage within the magnetosphere and a release when a threshold is encountered at a later stage of the event.

Figure 3.5 gives variations in the available solar wind power, the coupling parameters, and the major power dissipations along with total sink power during each event from top to bottom panels. The SML index is given for a ready reference in the bottom panels. The magnetospheric input power given by the ε is found 3 to 4 orders of magnitude lesser than the available solar wind power, U_{sw}. An interesting observation is that the peaks in the input power (ε) show a higher magnitude when the available solar wind power (U_{sw}) is found lower during a given event. Among the major sinks, the maximum dissipation of the SW power is found through joule heating (U_j) and the minimum through the ring current (U_r). The available solar wind power (U_{sw}), and the magnetospheric input power (ε) are found significantly lower during the 2011 event compared to the other two events and are found at the highest level during the '2017-SSS1' supersubstorm event. A similar pattern is seen in the variation of the power dissipated due to the ring current (U_r) among the events. However, the magnitude of powers dissipated through Joule heating and auroral particle precipitation is found comparable among the events, which could be due to the common volume affected at the ionospheric altitudes.

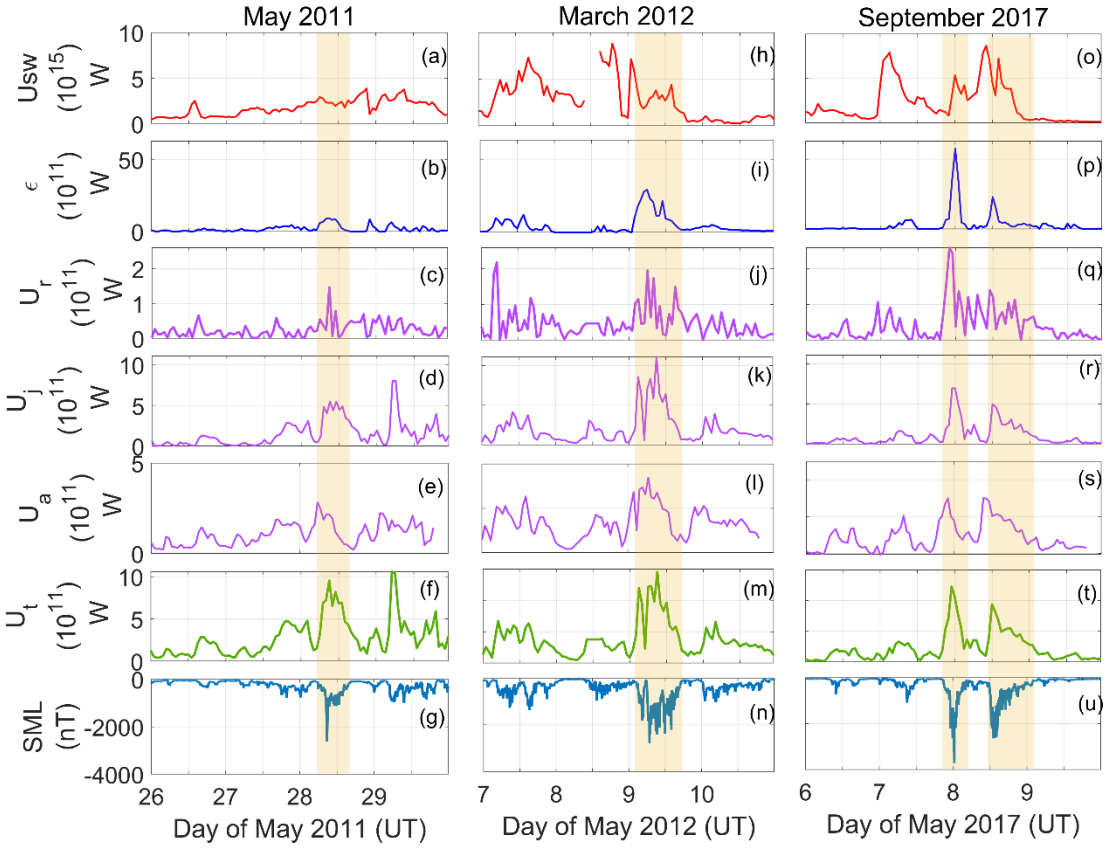

Figure 3.5. The variations in the estimated power terms are given in 6 top panels, respectively in columnar panels from left to right for the 2011, 2012, and 2017 events. Panels from the top to bottom respectively give the available solar wind power (U_{sw}) (a, h, and o); the

magnetospheric input power (ε) (b, i, and p); power through the ring current (U_r) (c, j, and q); the Joule heating (U_j)(d, k, and r) and the auroral particle precipitation sink (U_a)(e, l, and s); total dissipated power (U_t) (f, m, and t); the SML index (g, n, and u). The vertical yellow shades show the supersubstorm durations.

The variations in the total power dissipated (U_t) show comparable magnitudes, however, the input power shows different magnitudes at different phases of the events. Also, the peaks in the power dissipation terms are synchronized with the peaks of the input power, but, not with the available solar wind power, emphasizing the significance of the solar wind-magnetosphere coupling on the energy transfer. An anomalous post-supersubstorm feature is noticed as the maximum in Joule heating power dissipated during the 2011 event at about 06 UT on 29 May, which falls after the recovery phase of the supersubstorm and contributes significantly to the peak of the total dissipated power on the same day. However, a detailed analysis of this feature is beyond the scope of the study presented in this chapter.

3.3.4 Energy partitioning in magnetosphere-ionosphere system

The process of energy flow, transfer, and partitioning in the magnetosphere-ionosphere system is an important aspect of the substorm studies (Guo et al., 2012), more so, when storms of moderate intensity are associated with extreme substorms. The power (or rate of energy) terms given in Figure 3.5 above, are integrated to obtain the continuous energy curves. Figure 3.6 shows the energy curves for different time intervals beginning with the exact duration of the supersubstorms, 4-day (corresponding to previous figures), 1 month (30 days beginning from the day of the respective supersubstorm), 6 month (180 days beginning from the day of the respective supersubstorm) and 1 year (the year 2011, 2012 and 2017).

The top panel of Figure 3.6 shows that during the supersubstorm period (less than 12 hours duration), the magnetospheric input energy (blue) is found to be always more than the total dissipated energy (red) in the magnetosphere-ionosphere system. Also, during this period, the curves showing the energy dissipation through Joule remain (magenta) higher than the auroral precipitation (black), followed by the ring current (green). The second row of panels from the top shows the advent of the supersubstorm as a step-like increase in the input energy (blue), the magnitude of which depends upon the absolute amount of energy during the event and the integration time. The third row of panels from the top shows a gradual change in the energies, wherein, the total dissipated energy (red) supersedes the input energy (blue), respectively in about 12 hours (2011), 10 days (2012), and 8 days (2017). In addition, the

energy dissipation through auroral precipitation supersedes the Joule heating energy respectively in about ~27 days (2011), 20 days (2012), and 7 days (2017). However, when a longer period like 6 months (fourth row of panels from top) and 1 year (bottom panels) are considered, it is observed that the total energy dissipated (red) is always more than the magnetospheric input energy (blue) and a step-like increase is observed during the geomagnetic storm/substorm events in the respective intervals.

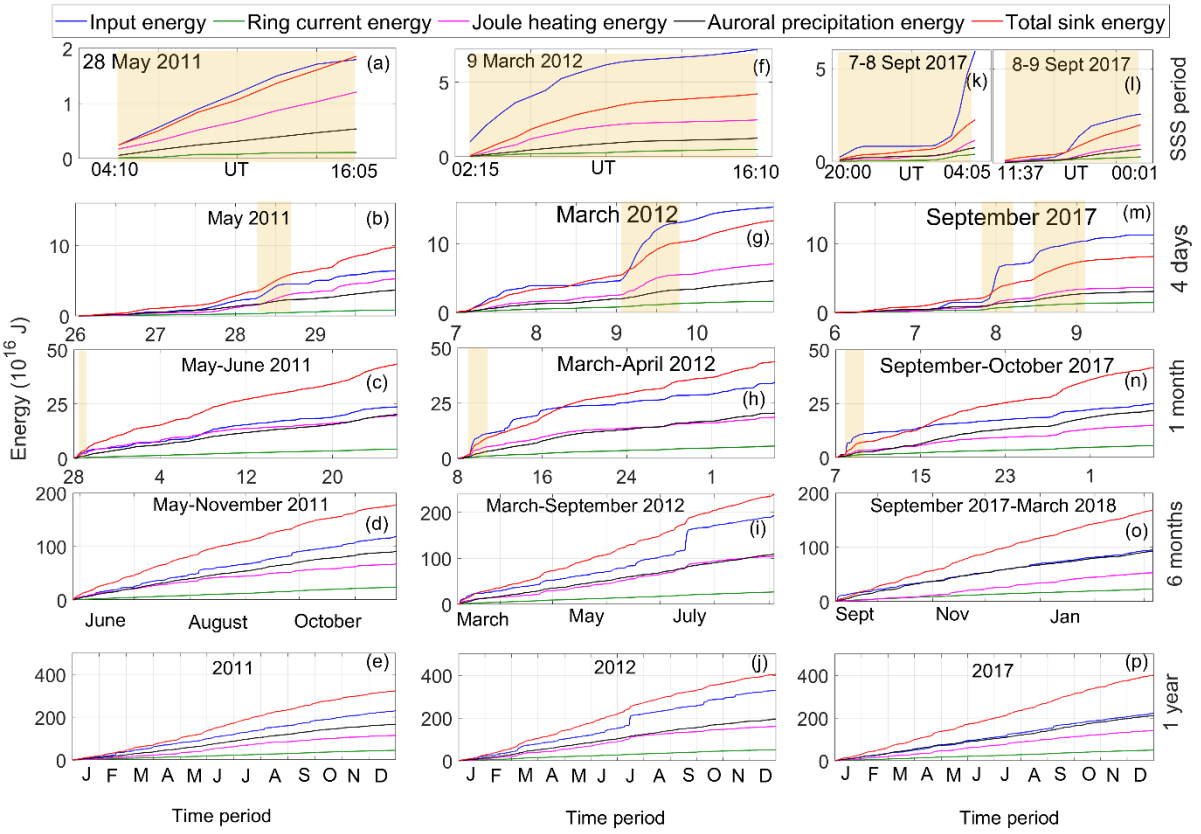

Figure 3.6. The respective power terms shown in Figure 3.5 are integrated for different intervals and given in panels from the top i.e. supersubstorm (SSS) period, 4 days, 1 month, 6 months, and 1 year, respectively, till bottom. The energy curves are given in different colours provided in a legend at the top. The columnar panels represent different time intervals selected from the years 2011, 2012, and 2017, respectively. The vertical yellow shades show the supersubstorm durations in the top three rows of panels.

A significant result obtained for the longer periods is that the dissipation through auroral precipitation is found to be the largest compared with the Joule heating and ring current, except for the substorm periods. The main cause behind this response could probably be the continuous high-energy particle precipitation in the auroral regions during both the geomagnetically quiet and the disturbed periods. The results also suggest that the mechanisms

of the evolution and decay of a storm or a supersubstorm event, through energy input, accretion, and dissipation, are unique and differ from one to another (Guo et al., 2012).

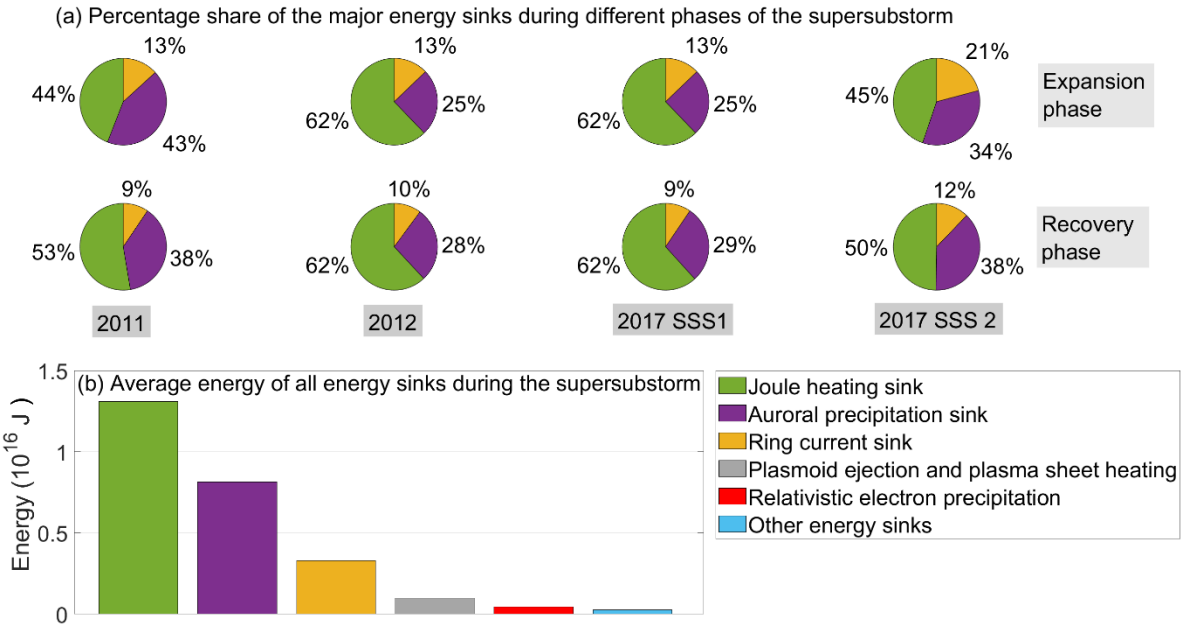

Figure 3.7. The top two panels (a) show a Pie-chart distribution depicting the percentage share of different energy sinks during the expansion phase and recovery phase of the supersubstorms. Pie charts from left to right respectively show the results for supersubstorm events of 2011, 2012, and 2017 (SSS1 and SSS2). Bottom panel (b) gives a bar chart for the average energy dissipation during the four supersubstorms through the three major sinks and other minor sinks. Legend in the bottom panel gives respective colours used to represent different sinks.

Further, during the shorter durations like the expansion and recovery phases of a supersubstorm, it is interesting to obtain the percentage energy distribution among different energy sinks. The respective phases are defined according to the durations given in section 2.2 and results are given in Figure 3.7. An important outcome of this comparison is that the percentage share of the energy dissipated through the Joule heating (ring current) is found lower or equal in the expansion (recovery) phase with respect to the recovery (expansion) phase of the supersubstorms. Thus, the share of a couple of sink energies changes during the different phases of the supersubstorms. This result can be explained by the dominant processes during the respective phases, which are produced by currents at the magnetospheric altitudes (i.e. the ring current) during the expansion phase and, at the ionospheric altitudes (i.e. Ohmic loss by the Joule heating) and the auroral particle precipitation during the recovery phase of the supersubstorms. Here, the contribution from the other minor energy sinks (which are generally

less than 1%) shall also be considered. Further, the average of energy sinks (panel 7b) obtained from the four supersubstorms shows that the energy dissipation majorly occurs through the joule heating, auroral precipitation, and ring current, whereas, other energy sinks contribute negligibly to the total sink energy.

Since a geomagnetic storm is associated with each of the supersubstorms presented in this study, a comparative energetics with an average isolated substorm and a geomagnetic storm (of minimum Dst >-150 nT) is needful to delineate the relative dominance of processes. The average energies corresponding to a nominal substorm are taken from Tenfjord and Østgaard (2013) and an average geomagnetic storm is taken from Li et al. (2012). The respective energies for the supersubstorms are taken as the last values of the curves given in the top panels of Figure 3.6. A comparative bar chart is given in Figure 3.8 to illustrate the comparison in five categories, respectively for the available solar wind energy, the input and sink energies, the input (e1) and dissipation (e2) efficiencies, and major sink energies.

It is found that the available solar wind energy (panel 8a) during the supersubstorms compares well with an average geomagnetic storm and is higher than a nominal substorm, except for the 2011 supersubstorm. The magnetospheric input energy and the total sink energy (panel 8b) remain one or two orders higher during the supersubstorms compared to a nominal substorm and, compared with an average geomagnetic storm. The input efficiency of the magnetosphere (e1) (panel 8c) is found to be higher during the supersubstorms in comparison to nominal substorms and an average geomagnetic storm. It is also observed that although the available solar wind energy was the highest during the second event of '2017-SSS2' (panel 8a), the corresponding magnetospheric input coupling efficiency (panel 8c) was the lowest followed by a lower level of sink energy (panel 8b). In the same contest, the 2012 supersubstorm is found to have the highest magnetospheric input energy (panel 8b) due to the highest coupling efficiency (panel 8c) amongst the supersubstorms despite lesser available solar wind energy (panel 8a). This illustrates the significance of the coupling efficiencies. Panel 8(d) also suggests that the dissipation efficiency (i.e. the magnetosphere-ionosphere coupling) is almost double during a nominal substorm compared with the supersubstorms and a storm.

Also, it is noted that the dissipation efficiency during supersubstorms is found lesser than a moderate geomagnetic storm. A comparative chart amongst the major energy sinks is given in panel 8(e). The energy dissipated through the Joule heating and auroral precipitation during the supersubstorms remains in between the respective energies of a nominal substorm and a storm of less intense or moderate level (of minimum Dst >-150 nT). However, in the case of the ring current, the dissipation during an average storm is found to be the highest

compared to the supersubstorm and a nominal substorm. It can be inferred from panel 8(e) that the distribution of the dissipation of energy during the supersubstorms corroborates better with a nominal substorm than an average storm. Notably, the supersubstorms presented here are associated with an average storm so the respective dissipations are found at higher scales.

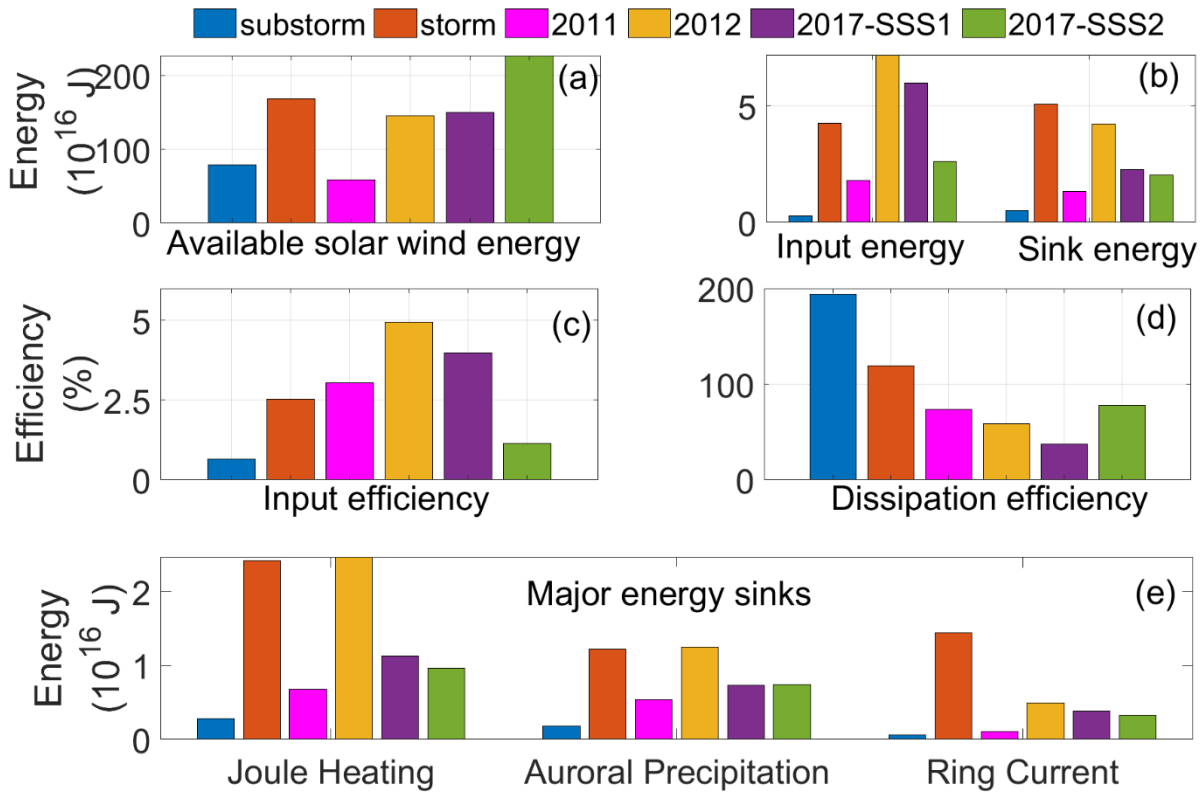

Figure 3.8. Comparative energetics of the four supersubstorms of 2011 (orange), 2012 (yellow), '2017-SSS1' (violet), and '2017-SSS2' (green) to an average Akasofu-type substorm (blue) and an average moderate geomagnetic storm (red) is given in panels (a-e). The comparison is provided in terms of (a) available solar wind energy (b) input energy and sink energy (c) input efficiency (d) coupling efficiency, and (e) energy distribution of the major energy sinks.

A quantitative estimate of the energy partitioning is given in Table 3.1, which is prepared from the analysis presented in Figures 3.6 and 3.8. Østgaard et al. (2002) have found an average input efficiency smaller or roughly ≈1% for the geomagnetic storms of solar cycle 23 during 1997-2010. Other studies like Lu et al. (1998) have found higher average input efficiency at 4.2% for geomagnetic storms, whereas, Vichare et al. (2005) have found it at 3.5%, especially for intense geomagnetic storms. Li et al. (2012) have provided separate input efficiencies at 2.8%, 6.2%, and 14.7% respectively for the moderate, intense, and super storms whereas, Tenfjord and Østgaard (2013) have given an average input efficiency of about 0.66%

for an average of isolated substorms. In the context of the previous studies, the present estimates of the input efficiency during the supersubstorm associated with a geomagnetic storm are found at ~3.05%, 4.95%, 3.98%, and 1.15%, respectively for the 2011, 2012, and 2017 events.

These results show that the average input efficiency during a supersubstorm of solar cycle 24 is found to be more than the levels of a nominal substorm and an average geomagnetic storm. Further, the dissipation efficiency (e2) obtained for the four supersubstorms is found at 73.95%, 58.56%, 37.72%, and 77.94 %, respectively. The e3, which is the ratio between the magnetospheric energy sink and ionospheric energy sink, the values of 9.04%, 13.85%, 20.60%, and 19.57% are obtained respectively for the four supersubstorms. A detailed quantitative tabulation from the study presented in this chapter is given in Table 3.1 below for an interested reader. A notable statistic from Table 3.1 is about the ratio of magnetospheric sink energy to the ionospheric sink energy (e3). The e3 is found to be at comparable levels for the substorms and the supersubstorms, but this becomes about 3 times higher during moderate geomagnetic storms. This indicates the dominance of ionospheric sinks during the supersubstorms and substorms.

Table 3.1. The columns from left provide the concerned duration to obtain an average, available solar energy (E_{sw}), magnetospheric input energy (E_ε), total dissipated energy (E_t), and the energy dissipated over the three major sinks (E_j, E_r, E_a), the corresponding coupling efficiencies are given by e1, e2, and e3, respectively. The estimates are given as averages for different types of short and long periods.

Duration	E_{sw} ($x10^{16}$ J)	E_ε ($x10^{16}$ J)	E_t ($x10^{16}$ J)	E_r ($x10^{16}$ J)	E_j ($x10^{16}$ J)	E_a ($x10^{16}$ J)	e1 (%)	e2 (%)	e3 (%)
Substorm	79.0	0.3	0.5	0.1	0.3	0.2	0.34	192.6	14.89
Storm	168.1	4.3	5.1	1.4	2.4	1.2	2.53	119.5	39.56
Supersubstorm	145.3	4.4	2.5	0.3	1.3	0.8	3.02	56.04	15.49
One month	4000	27.7	42.0	5.1	15.9	20.8	-	-	-
One year	41000	260.8	355.2	49.0	138.9	167.4	-	-	-

3.3.5 Dependence of energy partitioning on the intensity of substorms

A better statistical result is obtained through a detailed analysis of the energetics and energy partitioning of a solar wind-magnetosphere-ionosphere system during substorms of different intensities and levels. A statistical survey of 101 geomagnetic substorms that occurred between 1998 and 2018 with varying SML between -100 nT and -4100 nT is performed. These results (Figure 3.9) are prepared by using a complete day of observations on the day of the substorm considering different ways of substorm evolution, energy dissipation, and occurrence of multiple substorms in a very short time interval.

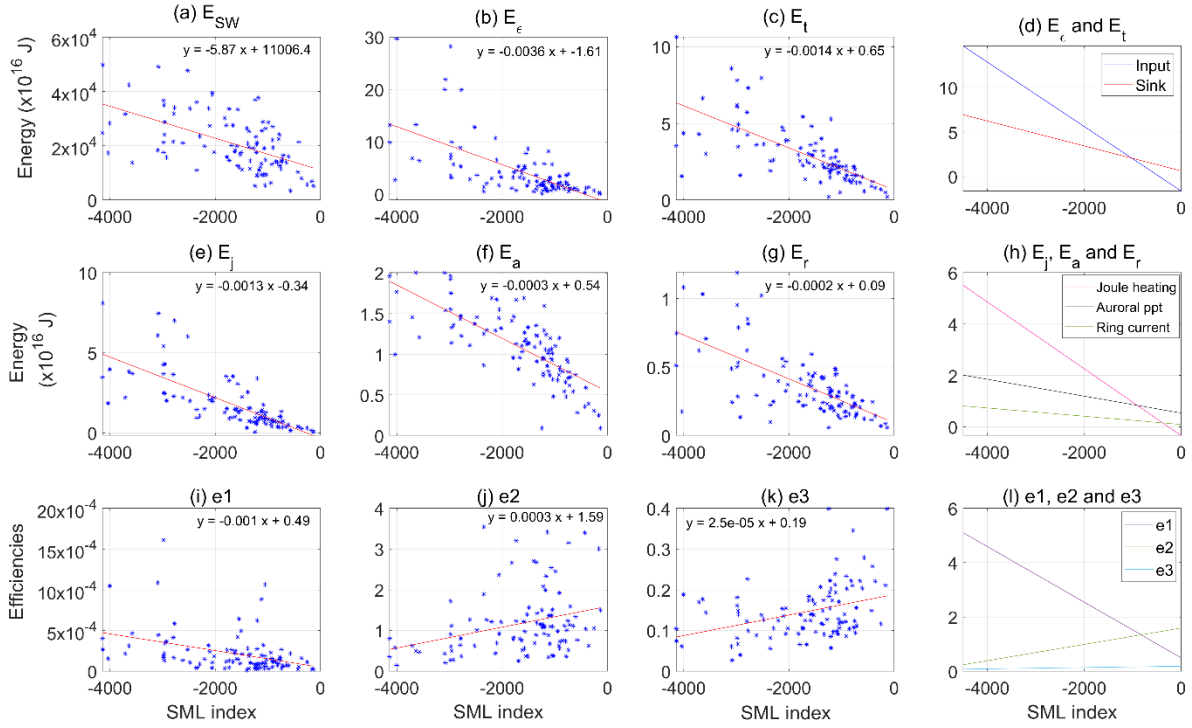

Figure 3.9: The abscissa gives the SML index in all panels. Panels a-g respectively show scatter plots of available solar wind energy (E_{sw}), magnetospheric input energy (E_ε), total energy sink (E_t), Joule heating sink (E_j), auroral precipitation sink (E_a) and ring current sink (E_r). Panels i-k in the bottom row show respectively the efficiencies e1, e2, and e3. The first 3 columnar panels from the left show a linear least square fit to the scatter points and the fourth columnar panel in each row (i.e. d, h, and l) shows the slope of the fit-lines from the first 3 panels.

The scatter plot of different energies against the SML index (Figure 3.9) shows some very interesting results. A large scatter in the values of the available solar wind energy (E_{sw}) is found in contrast to the relatively more linear and converged scatter in the magnetospheric

input energy (E_ϵ) and total energy sink (E_t) (panels a-c), but all three show an increasing trend with the increase of intensity of the substorms. Among the major energy sinks, the Joule heating sink (E_j) shows a faster proportionate increase with the increase in strength of the substorms followed by the auroral precipitation (E_a) and the ring current sink (E_r). The efficiency e1 follows almost linear proportionality but much more interestingly, e2 and e3 follow reverse proportionality with the SML index. It is found that the ratio of total energy dissipation with energy input (e2), as well as the ratio of dissipation through the magnetospheric sink (ring current) to the ionospheric sink (e3), are much more during moderate and less intense substorms than supersubstorms.

The panels in the fourth column (d, h, and l) of Figure 3.9 show the respective slope of the linear regression lines, representing the proportionalities of different energy and efficiency parameters with intensities of the substorms, given in each row. Panel (d) suggests that the rate of input energy (E_ϵ) is higher than the rate of total sink energy (E_t) against the rise in the SML index. Although, the absolute values of E_ϵ remain lesser than that of E_t for minor and moderate substorms (SML > -1000 nT), E_ϵ supersedes E_t gradually for intense and supersubstorms (up to SML< -1000 nT). Thus, the dominance of sink energy can be inferred during most of the substorms, which can be considered as isolated nightside events. Whereas, for the more intense substorms and supersubstorms the input energy at the dayside dominates. In addition, from panel (j), we can see that with the increase in the intensity of the substorms, e2 decreases. Hence, it can be said that for moderate and less intense substorms more energy dissipation happens with respect to the magnetospheric input energy. For the intense substorms and the supersubstorms, the input energy is generally much more, wherein a lesser proportion of this energy is dissipated in the magnetosphere-ionosphere system. Hence, it seems that a part of the input energy is accreted in the magnetosphere for this class of substorms. This could imply that for the occurrence of the supersubstorms, a bulk volume of the input energy is necessary. We surmise that in such cases, the occurrence of completely isolated supersubstorms may not be possible. These results on a different class of substorms suggest that the earth's magnetosphere reacts differently to different levels of substorms of different intensities. Interestingly, ratio-wise it is possible that a larger part of the magnetospheric energy input (or the energy accreted in the inner magnetosphere) can be dissipated during moderate or less intense substorms. Also, from panel (h) we observe that with the increase in the intensity of the substorms, the rate of increase in dissipation through Joule heating (E_j) is much more than that through auroral particle precipitation (E_a) and ring current (E_r). Hence with the increase in the intensity of the

substorms, e3 gains a negative slope i.e. the lesser share of energy is dissipated through the ring current, and the higher share of energy through the ionospheric energy sinks.

Briefly, our study quantitatively establishes an inference that the magnetosphere reacts and responds in a coupled manner, which depends upon the intensity of substorms. The evolution and decay of each substorm follow a series of processes beginning from the source of energy in the solar wind, the solar wind-magnetosphere-ionosphere coupling, and the energy sinks, which makes the study of these events interesting and fascinating. However, more investigations are needed to understand some of the mechanisms that can cause extreme substorms during moderate and multi-step geomagnetic storms.

3.4 Discussion

The present study gives an analytical and quantitative evaluation of the occurrence and energetics of the supersubstorms during solar cycle 24, which show anomalous characteristics with respect to the previous solar cycles (Figure 3.1). Out of the total of four supersubstorms, three are found to occur during two geomagnetic storms with SSC, whereas, one is found during a geomagnetic storm without SSC. The minimum Dst during the storm of March 2012 was -145 nT and of September 2017 is -145 nT, whereas, it remained about -80 nT for the storm of May 2011. The occurrences of supersubstorms have been mostly associated with geomagnetic storms of varying intensities (Hajra et al 2016), which corroborate the cases studied in this paper. All four supersubstorms have occurred either during the ascending or declining phase of the solar cycle 24.

The supersubstorms are extreme substorm events that are recently classified based on the lower bound of the auroral-electrojet-based index, like the SML (Tsurutani et al. 2015). The occurrence characteristics, morphology, and the associated auroral evolution as well as the probable cause of such extreme substorms have been subjects of the recent investigations by (Tsurutani et al. 2015; Hajra et al. 2016; 2018; Nishimura et al. 2018; Despirak et al. 2019; 2020). However, the supersubstorms of the solar cycle 24 have not been investigated from the viewpoint of the coupling characteristics and energy partitioning, which are in fact the salient features of the study presented in this chapter. Additionally, a robust methodology is followed to find the sources, the energy transfers and coupling, and the sinks for each supersubstorm.

One of the main results of this study shows that all four events associated with the supersubstorms have probable origin in the conditions wherein, the solar wind stream was moving at a fast speed coincident with multiple hits by the magnetic clouds (Figure 3.2). When

compared with the average solar wind drivers of the events associated with the supersubstorms of the solar cycle 23, almost similar results of the dominance of magnetic cloud with FAST background plasma are found during solar cycle 24. But, the presence of the forward and reverse shock waves as the drivers of the supersubstorms was significantly high during the former cycle. A prior arrival of other solar wind drivers like shock waves, slow-moving plasma, co-rotating interaction regions, and heliospheric current sheets for brief periods could probably set the preconditioning of the magnetosphere.

Hence, using a four-day interval, the solar wind-magnetosphere coupling parameters are examined and a quantitative estimate of the available and transferred power is obtained (Figures 3.4 and 3.5). , Multiple southward and northward excursions in IMF-Bz are observed before the commencement of the geomagnetic storms in all cases. This is subsequently followed by a multi-step development of the associated geomagnetic storm, which eventually leads to the occurrence of the supersubstorms in the later part of the respective main phases of the geomagnetic storms. Previous studies have emphasized that the development of a geomagnetic storm in multiple steps is possible under several scenarios including the structure of the solar disturbance, the interplanetary evolution of the event, and the solar wind-magnetosphere coupling, which are different for different events (Kamide et al. 1998; Verkhoglyadova et al. 2016, etc). In context to the occurrence of the supersubstorm cases presented in this study, the above observations could serve as evidence of the inner magnetospheric response to the long-duration energy accumulation in the magnetosphere even before and during the multi-step event, which eventually may release a trigger process. The energization of plasma consisted of multi-ion species that occur in the near-earth magnetotail and inner magnetosphere causing enhancements of ion pressure during extreme events. Keika et al. (2013; 2016) have deciphered multiple physical processes responsible for the energization which are generally associated with magnetic field reconfiguration (depolarization) and temporally impulsive transport of plasma (with energies of a few to a few hundred kiloelectron volts) from the plasma sheet and tail lobe in the form of narrow flow channels of energy. Subsequent studies by Keika et al. (2018a; 2018b; 2022) have investigated several cases of inner magnetospheric energization, the origin of ions and charged particles, and plasma flow and demonstrated the multi-step development of geomagnetic storms or substorms. They have shown, that a multi-step build-up of the geomagnetic storm in specific cases (Keika et al. 2018b) may lead to populating the plasma sheet during the earlier phases of the interplanetary disturbance, which, at later phases of the storms can get energized and may produce enhanced ring current and auroral activity, which support the occurrence of intense substorms. The

present results (Figures 3.3 and 3.4) show a multi-step development of each of the geomagnetic storms with evidential confirmation from the IMF-Bz and other coupling parameters like PCPD, FAC, R, and $\frac{d\varphi_{MP}}{dt}$. The intriguing observation of the double supersubstorm during 8-9 September 2017 also possibly has a relationship with the double southward excursion of IMF-Bz separated by 6-7 hours on 8-9 September. Keiling et al. (2022) have shown that the periodic mode of the substorms can be generated through an internally driven quasi-periodic reconnection. Other major studies in this context like Tsurutani et al. (2006) and Morley et al. (2009) have elucidated the occurrence of recurrent substorms. However, unfortunately, there is no study to date to specifically explain the mechanism of occurrence of subsequent supersubstorms or extremely intense substorms. As a plausible explanation of the second supersubstorm (SSS-2) of 9 September 2017, the short period northward and southward fluctuations of IMF-Bz (between the two supersubstorms) have pre-conditioned and a long duration southward excursion could have triggered the sudden huge energization of the magnetospheric plasma populations. However, since, the magnitude of the southward IMF-Bz on 9 September is found to be lesser, the intensity of the second supersubstorm is also found to be lower with respect to the previous one (i.e. on 8 September 2017). As the two supersubstorms of September 2017 happened within a time interval of 6-7 hours, these two could be considered recurrent supersubstorms against the pre-conditioning for a long 24-hour interval between 7-8 September 2017. Thus, with the present understanding, it may be feasible to state that all four supersubstorms have occurred largely due to the above-mentioned reasons. Further investigations are needed to establishthe possible pathways of a rare double supersubstorm event, like this one.

The results on the solar wind-magnetosphere-ionosphere coupling parameters (PCPD and FAC) and rates (R, $\frac{\mathrm{d}\varphi_{\mathrm{MP}}}{\mathrm{dt}}$) show (Figure 3.3) that stable southward excursion of IMF-Bz and higher values of R facilitated a trigger (onset) of the supersubstorms. This result is substantiated by the aforementioned discussion on multiple hits by the magnetic clouds (Figures 3.2 and 3.3) resulting in a multi-step build-up of the geomagnetic storm. The strength of the dawn-dusk electric field is represented by PCPD ($-\nabla\emptyset=E=-V\times B$) (Shepherd et al. 2007) which provides a quantitative estimate of the intensity and extent of plasma convection in the high-latitude ionosphere (Reiff et al., 1981). The coinciding peaks in the IMF-Bz, IEF-Ey, R, and $\frac{d\varphi_{MP}}{dt}$ channelize a synchronized transfer of the solar wind energy, which results in simultaneous peaks observed in the FAC (inside magnetosphere), PCPD, and PCI indices (at the polar ionosphere). The synchronous correspondence is found during all the events as shown in Figure

3.3, which substantiates the occurrence of the four supersubstorms during the ongoing geomagnetic storms. However, an intriguing oscillatory variation in the PCI index, which is also observed in the SML index during 00-12 UT on 9 March 2012 is not observed in all other parameters during other events as given in Figure 3.3. Possibly such a departure may indicate a difference between the local and global processes and the way the PC index is obtained in both conditions. Notably, all the coupling parameters and rates are found to peak during the highest SML perturbations as well as during the time of SSCs of the geomagnetic storms. The IMF-Bz and IEF-Ey are found to be the crucial field parameters behind the above-mentioned drastic increments in the expansion phase of the supersubstorms, however, such a relationship during SSC is not found.

A huge amount of energy enters into the earth's magnetosphere, especially, during extreme events and at the same time energy dissipation also happens rapidly. However, considering only the supersubstorm periods, the magnetospheric input energy is found to be always more than the energy dissipated. But while increasing the interval, the energy dissipated slowly supersedes the magnetospheric energy input and eventually for larger periods say for 15 days or more (Figure 3.6); the energy dissipated is always more than the total input energy (Tenfjord and Ostgaard, 2013). A possible explanation for the longer duration response could come through, one, the very slow accretion of input energy inside the magnetosphere due to weaker coupling, and two, the dissipation of the stored energy through intra-magnetospheric dynamical activities.

It is found that during the expansion and recovery phases of all the four supersubstorms, maximum energy is dissipated through Joule heating, followed by that through the auroral precipitation and ring current, which is consistent with the previous studies on substorms (Rodger et al. 2001 and reference therein). In addition, the direct Joule heating in the dayside ionosphere is possible through sudden ram compression which drives the FACs in the dayside outer magnetosphere (Zhou et al. 2003). The direct solar wind energy input through the polar cusp region is also a possible and feasible reason. However, when we proceed beyond the supersubstorm period and carry forward the estimation for a larger period like one month, six months, or even one year, the dissipation through the auroral precipitation supersedes the one from Joule heating and persists as the largest energy sink (Figure 3.6). This result is in contrast with some of the previous studies like (Tenjford and Ostgaard, 2013) who have also integrated the energies for one year and found that the Joule heating sink energy attains the maximum (for both the solar high and low activity durations). In this context, our results show that the period of one year sampled either at the ascending or declining phase of the solar activity exhibits the

auroral dissipation energy sink to be at the maximum among the energy sinks. A possible explanation behind this observation could be that the high energy particle precipitation is found to occur continuously both during the geomagnetic quiet and disturbed periods (Newell et al. 2009), albeit with different rates and values. The subject needs further investigation to obtain a clear understanding of the duration of energy accumulation and its solar cycle dependence. Additionally, it is found that the percentage share of the energy dissipated through the Joule heating (ring current) is lower or equal in the expansion (recovery) phase in comparison to the recovery (expansion) phase (Figure 3.7) of the supersubstorms. This is better explained by the dominance of the ring current at the magnetospheric altitudes during the expansion phase and, that of the dissipations at the ionospheric altitudes (i.e. Ohmic loss by the Joule heating and the auroral particle precipitation) during a recovery phase.

Our results also show that the input efficiency, total magnetospheric input energy, and sink energies are found at a level higher than a nominal 'Akasofu-type' substorm, but at a comparable level with an average geomagnetic storm (of minimum Dst >-150 nT). Nevertheless, it shall be noted that the energy distribution among sinks during the supersubstorms corroborates better with a nominal substorm than an average storm. Generally, a nominal substorm is considered exclusively to be a nightside phenomenon, and the input energy during a substorm (i.e. the epsilon parameter) provides an accumulated effect of dayside long-term coupling. Whereas, during a geomagnetic storm the sudden changes in the interplanetary parameters like the velocity and IMF dominate the input energy. Hence, in the case of the supersubstorms, which occurred during the solar cycle 24, an association of an ongoing moderate (of minimum Dst >-150 nT) geomagnetic storm has brought down the dissipation efficiencies (Figure 3.8). This conclusion is further vindicated by our results given in Table 3.1, which show an average behaviour of supersubstorm lying between the substorm and moderate storm levels for the input efficiency.

The rate of change of energy flow (i.e. the power transferred from the solar wind to the magnetosphere-ionosphere system) is found to maximize at different times in terms of the coupling power and the total dissipated power. These power terms are not necessarily synchronized with the peaks in the available solar wind power. This follows from the fact that solar energy can also enter into the magnetosphere through other channels like viscous interaction (Axford and Hines, 1961; Tsurutani and Gonzalez, 1995), cross-field diffusion by resonant wave-particle interactions at the dayside magnetopause (Sonnerup, 1980; Tsurutani et al., 1981), penetration of the neutral component of the solar wind (H atoms) and development of a variety of degree of ionisations (Gosling et al., 1980) and, the pressure fluctuation of the

solar wind leading to the generation of the Alfven waves (Dessler et al., 1961), etc. The energy coupling mechanisms are neither unique nor simplistic to directly unveil the underlying processes and additionally, they vary for different storm/substorm processes. The peak in the coupling power (i.e. the epsilon parameter) corroborates the observed peak in the total dissipated power during all three events of 2011, 2012, and 2017. This signifies the control of coupling between the solar wind and magnetosphere which subsequently also drives energy and plasma flow through different channels within the magnetosphere which is also vindicated by Figure 3.8.

Finally, this study has been expanded to confide with a statistical analysis using observations from 101 substorms of different intensities. Our results show greater sink energy during most of the substorms (processes on the nightside), whereas, greater magnetospheric input energy for the more intense substorms and supersubstorms (dayside processes). Also, for a shorter duration (i.e. one day), it is very interesting to note that the dissipation can be greater than the magnetospheric input for the moderate and less intense substorms (SML>-1000 nT), which is in contrast to the response of the intense substorms (SML<-1000 nT) and supersubstorms. It is also found that for intense or supersubstorms a part of the input energy is dissipated and the remaining energy is stored inside the magnetosphere. Eventually, it may be conjectured that the occurrence of the completely isolated supersubstorm may be very rare. It is found that with the increase in the intensity of the substorms, more part of the energy is dissipated through the ionospheric energy sinks. Among the energy sinks, the Joule heating sink is found to increase at a larger rate for an increase in the intensity of the substorms in comparison to the other major energy sinks. This suggests that the earth's magnetosphere reacts differently to the substorms of different intensities for a particular interval of time. Our results further qualify that with an increase in the intensity of the substorms, a lesser share of energy is dissipated through ring current, and a higher share of energy through the ionospheric energy sinks.

In a nutshell, our study quantitatively establishes an inference that the magnetosphere reacts and responds in a coupled manner, which depends upon the intensity of substorms. However, more investigations are needed to understand the mechanisms that can cause extreme substorms during moderate and multi-step geomagnetic storms.

3.5 Summary and conclusions

A summary of the salient features and new findings from this study is given below.

1. Multiple hits of the magnetic cloud associated with fast-moving background plasma are found to be the main solar wind sources to cause the supersubstorm events in solar cycle 24. A comparison with the supersubstorms of solar cycle 23 provides lesser dominance of shock waves during solar cycle 24 in the intervals preceding the supersubstorms.
2. The magnetosphere-ionosphere coupling parameters such as PCPD and FACs and the solar wind-magnetosphere coupling rate R and $\frac{d\varphi_{MP}}{dt}$ are found to peak during the highest SML perturbations as well as during the time of SSCs. The IMF-Bz and IEF-Ey are found to be the crucial field parameters behind the drastic increase in the expansion phase of the supersubstorms, however, such a relationship during SSC is not found.
3. For shorter intervals like periods of substorms and supersubstorms, the magnetospheric input energy dominates over the energy dissipated, whereas, for longer durations up to one year, the energy dissipated surpasses. In a similar fashion, the dissipation through Joule heating is found to be the dominant energy sink in shorter intervals but the dissipation through auroral precipitation takes over for longer periods.
4. During the supersubstorm periods, the ionospheric sink energy dissipated through the Joule heating attains a maximum, whereas, the dissipation through ring current remains at the lowest levels. It is found that ~79-91% of the energy is dissipated through ionospheric energy sinks during the supersubstorm periods.
5. The percentage share of dissipation through Joule heating is found more or equal in the recovery phase with respect to the expansion phase of the supersubstorms, and that of the ring current is found more in the expansion phase with respect to the recovery phase.
6. The input efficiencies are found at ~3.05%, 4.95%, 3.98%, and 1.15%, respectively for the supersubstorms of 28 May 2011, 9 March 2012, 7 September 2017, and 8 September 2017. In the case of the energy dissipation through the major energy sinks, our results show 73.95%, 58.56%, 37.72%, and 77.94 % efficiency during the above-mentioned events, respectively. Thus, the results signify the control of coupling on the transmission, conversion, and dissipation in the solar wind-magnetosphere-ionosphere system. Occasionally, the solar wind-magnetosphere coupling is found to bear higher importance than the available solar energy flux.
7. The dissipation efficiency (e2) and the ratio of the sink energies (e3) are found to be inversely proportional to the intensity of the substorms. The Joule heating sink energy is found to increase at a larger rate for an increase in the intensity of the substorms compared to other energy sinks. A survey of 101 substorms of different intensities shows

that the magnetosphere reacts differently to different levels of substorms. The energy partitioning in the magnetosphere-ionosphere system also responds in a contrasting fashion to different levels of substorms.

Finally, it is necessary to mention that further investigations are needed to examine the relative dominance of processes like the energy sources and sinks in generating the observed efficiencies for the extreme class of substorms. **The work presented in this chapter is published as a research article by Hajra et al. (2022).** Following these findings and interesting discussions on the solar wind drivers and the diverse coupling processes in the solar wind-magnetosphere-ionosphere system occurring during supersubstorms, we have carried out a comprehensive analysis of the resulting geomagnetic responses, which we will delve into in the upcoming chapter.

CHAPTER 4

SW-M-I Coupling During Supersubstorms of Solar Cycle 24: Geomagnetic Responses

"Electricity and magnetism are those forces of nature by which people who know nothing about electricity and magnetism can explain everything.

-Egon Friedell

4.1Introduction

Extreme space weather events can severely affect the low earth-orbiting satellites, satellite navigation links as well as ground-based power grids, and the performance of modern technological devices (Kappenman 2003; Schrijver et al. 2014; Tsurutani et al. 2015). The solar wind-magnetosphere-ionosphere coupling during major interplanetary disturbances leads to an episodic heavy energy impingement on the system and causes geomagnetic storms and substorms (Tsurutani and Meng 1972; Gonzalez et al. 1994). The sudden enhancement of the solar wind dynamic pressure associated with the solar wind transient structures like the solar wind discontinuities and the interplanetary shocks (Tsurutani et al., 2011; Oliviera and Samsonov 2018) can produce impulsive geomagnetic and ionospheric responses (Chi et al., 2001; Zou et al., 2017; Wang et al. 2018). Especially, the substorm events manifest as the main channels for the mass, energy, and momentum flow from the nightside magnetotail to the high latitude ionosphere (Akasofu 1964; Kamide 1991; Rostoker et al. 1980; Baker 1996; Liou et al. 2001; Østgaard et al. 2005; Ebihara 2019). The dynamical interaction of the dayside magnetopause with the solar transients can also produce a variety of magnetospheric perturbations at different scales (Oliviera and Reader, 2014; Yue et al. 2010). Particularly, the enhanced solar wind pressure produces the compression of the dayside magnetopause. This is manifested as a large step-like enhancement in the geomagnetic field intensity observed by the ground-based magnetometers (Chapman and Bartles 1940; Matsushita 1962; Kamide 1991; Rastogi, 1999; Villante and Piersanti 2011) known as the storm sudden commencement (SSC) or sudden impulse (SI) (Kikuchi and Araki, 1979). The morphology of SSC or SI has been investigated by Tamao (1964), Matsushita (1962), Sugiura (1971), Araki (1977), Kikuchi and Araki (1979) Araki (1994) and Yamada et al. (1997), which shows that different geomagnetic depressions are associated with different current systems in the magnetosphere and ionosphere (Fujita 2019 and references therein). Thus, the geomagnetic H-component response of the SSC is known to be composed of the main impulse (MI) preceded by a short-lived preliminary impulse (PI) during storms. Therefore, the geomagnetic depressions due to the SSC (D_{SSC}) can be given as $D_{SSC} = DL_{MI} + DP_{MI} + DP_{PI}$; where, DL and DP are the disturbances that originated at the low and polar latitudes, respectively due to the MI and PI. DP_{PI} is found to spread instantaneously in the TM_0 (transverse magnetic zero) mode associated with the prompt penetration electric field (PPEF) towards the equatorial latitudes (Araki, 1977; Kikuchi and Araki, 1979; Reddy et al. 1979). The preliminary impulse (PI) can manifest (depending upon the latitude and local time) as a preliminary positive impulse (PPI) mostly in the morning sector

or a negative preliminary reverse impulse (PRI) mostly in the afternoon sector (Rastogi, 1993; Sastri et al., 1993; Araki 1994; Yamada et al. 1997; Shinbori et al. 2009). Thereafter, the magnetospheric convection at high latitudes produces a global dawn-to-dusk convection electric field giving rise to the long-term enhancement in the H-component called a main impulse (MI) (Kikuchi et al. 2001).

A geomagnetic substorm can occur in isolation or association with a geomagnetic storm (Rostoker et al. 1980; Ebihara 2019). During the main phase of the substorms, a complex interplay between all these currents and shock signatures ultimately leads to enhancements or depressions of the geomagnetic field on different parts of the globe (Rastogi 1999; Piersanti and Villante 2016). The composite effect of the magnetospheric and the ionospheric currents observed at different time intervals can be resolved to obtain a resultant H-component perturbation (Villante and Piersanti 2009; Araki and Shinbori; 2016; Amory-Mazaudier et al. 2017; Ganushkina et al. 2018). In addition, the variations of the D-component (which provides geomagnetic east-west perturbations) during geomagnetic storms have also been investigated in many previous studies like Iyemori (1990), Tsunomura (1998), Rastogi (1999; 2005) Rastogi et al. (2001), Villante et al. (2007), Villante and Piersanti (2009; 2011) and Piersanti and Villante (2016). These studies have comprehensively shown that to understand the complex response of the magnetosphere-ionosphere system during solar transient forcing (especially in the case of the SSC), an analysis of the D-component variations is essential to decipher the ionospheric contribution to the total current. Further, the intense magnetospheric and ionospheric currents and associated disturbances in the geomagnetic field drive the geomagnetically induced currents (GICs), which can be vulnerable to power-grid systems and delicate technological appliances (Kappenman 2005). Some of the recent studies (for example, Carter et al. 2015) have attempted to decipher the variations in the GIC, based on the variations of the dB/dt (i.e. the time derivative of the total geomagnetic field intensity, B).

In general, a typical substorm is characterized by indices associated with auroral electrojets, like AE and AL (Davis and Suguira 1966); however, the SML (Super Magnetic Lower) index derived from the SuperMAG network of more than 300 magnetometers (Newell and Gjerlov, 2011) maps and characterizes the extreme auroral events better than the other indices. Tsurutani et al. (2015) have introduced a threshold of SML < -2500 nT (Super Magnetic Lower index) to define the extreme substorm events as supersubstorms. Different aspects of the supersubstorms have been reported in the literature such as the sources, occurrence characteristics, morphology, and the associated auroral evolution (Tsurutani et al. 2015; Hajra et al. 2016; Adhikari et al., 2017; Hajra and Tsurutani 2018; Despirak et al. 2019;

2020; 2021; Nishimura et al. 2020). Recently, Hajra et al. (2022) have reported a detailed analysis of the supersubstorms of solar cycle 24 including the originating solar wind structures, solar wind-magnetosphere-ionosphere coupling efficiencies, and the associated energy partitioning in the magnetosphere-ionosphere system. They have noted that the multiple hits by magnetic cloud structures have triggered the supersubstorms of the solar cycle 24 during the respective ongoing geomagnetic storms. The following sections give observations and methods, results, and a discussion with a summary of the new findings at the end.

4.2 Observations and Methodology

The durations of the phases of supersubstorms for this study are considered similar to as mentioned in Chapter 3.2.1. The observations of the solar wind, interplanetary parameters, and geomagnetic indices as extracted from NASA/GSFC's OMNI data set through OMNIWeb (https://omniweb.gsfc.nasa.gov/form/omni_min.html) at a cadence of 1 min (see Papitashvili & King, 2020) are used. The details about all these observations are given in Chapter 2.2.

The global high-resolution geomagnetic observations are obtained from the latitudinal and longitudinal chains of magnetometers available at the INTERMAGNET website (https://imag-data.bgs.ac.uk/GIN_V1/GINForms2) (see Love and Chulliat 2013 for the description of the data set). More details regarding the observations taken from the INTERMAGNET chain of magnetometers are provided in Chapter 2.7.1.

For the present study, we have divided the analysis of the observations into three sets. The first set includes 13 stations from the latitude band of 70^{o}-90^{o}; the second set includes 60 stations from the band of 15^{o}-70^{o}, and the third set includes 9 stations from the band of 0^{o}-15^{o}. However, for brevity and to avoid congestion in the presentation, we have selected a few stations from each set to give results. Thus, the results include observations from 11 stations from the first set, 16 stations from the second set, and 9 stations from the third set are given in this Chapter. It is important to mention here that number of magnetometer stations vary by region and time (not all magnetometers are functional at all times), especially during disturbed periods. Figure 2.4 shows a map of the locations/stations selected for the present study. A list of all the stations is provided as a table in the supporting information (SI-1) in Appendix B.

In addition, The SuperDARN (Super Dual Auroral Radar Network) convection maps with a cadence of 10 minutes for all the supersubstorm durations obtained from the website of SuperDARN through " https://kauai.ccmc.gsfc.nasa.gov/instantrun/superdarn/" by selecting the date and time. The details about the observations from SuperDARN are given in Chapter

2.6.1. Finally, the effect of the GICs is represented using the dB/dt (nT/min) estimation from 1-minute sampled global H-component observations. Details of GIC computation are given in Chapter 2.7.1.

4.3 Results

Following the definition of the supersubstorm, it is found that during the geomagnetic storms of May 2011 and March 2012, only one supersubstorm occurred whereas, during the geomagnetic storm of September 2017, two consecutive supersubstorms separated by an interval of 12 hours (Hajra et al. 2022) occurred. In addition, it is interesting to note that all three geomagnetic storms were less intense or moderate-level storms (of minimum Dst > −150 nT). A detailed analysis of the interplanetary parameters and H-component variations at the time of the SSC and during the supersubstorms is performed. Results are categorized for three different latitude bands as mentioned above in the following subsections.

4.3.1 Variations in the interplanetary parameters and geomagnetic indices

The variations in the x, y, and z-components of the interplanetary magnetic field (i.e. B_x, $B_{y,}$ and B_z), the bulk velocity of the solar wind (V), and the solar wind dynamic pressure (P) are given in the top four rows of Figure 4.2. The variations in the AE and SML indices show the phases of the auroral perturbations during the supersubstorms, whereas the SYM-H index is added to signify the associated geomagnetic storm phases. The supersubstorm durations for these cases are provided by Hajra et al. (2022) in a detailed manner and these durations are highlighted in all the results of the present study. A close inspection of the solar wind parameters shows that the global minima in the variations in the IMF-B_y are found before or during the supersubstorms. The phase variations in the IMF-B_y mostly match well with that of the IMF-B_z except for a few instances like around 23 UT on 8 March 2012 and 13 UT on 8 September 2017. The southward excursions of the IMF-B_z coincide with the occurrences of the supersubstorms which are indicated by the sudden rise/fall of the AE/SML indices, which is a well-known phenomenon. On the contrary, no specific pattern in the variations in the IMF-B_x is found.

As a common feature of most geomagnetic storms, the events of 2012 and 2017 show a noticeable occurrence of an SSC, but the event of 2011 begins without an SSC. Neither the solar wind pressure nor the bulk velocity showed any abrupt increase before the commencement of the main phase of the supersubstorm on 28 May 2011.

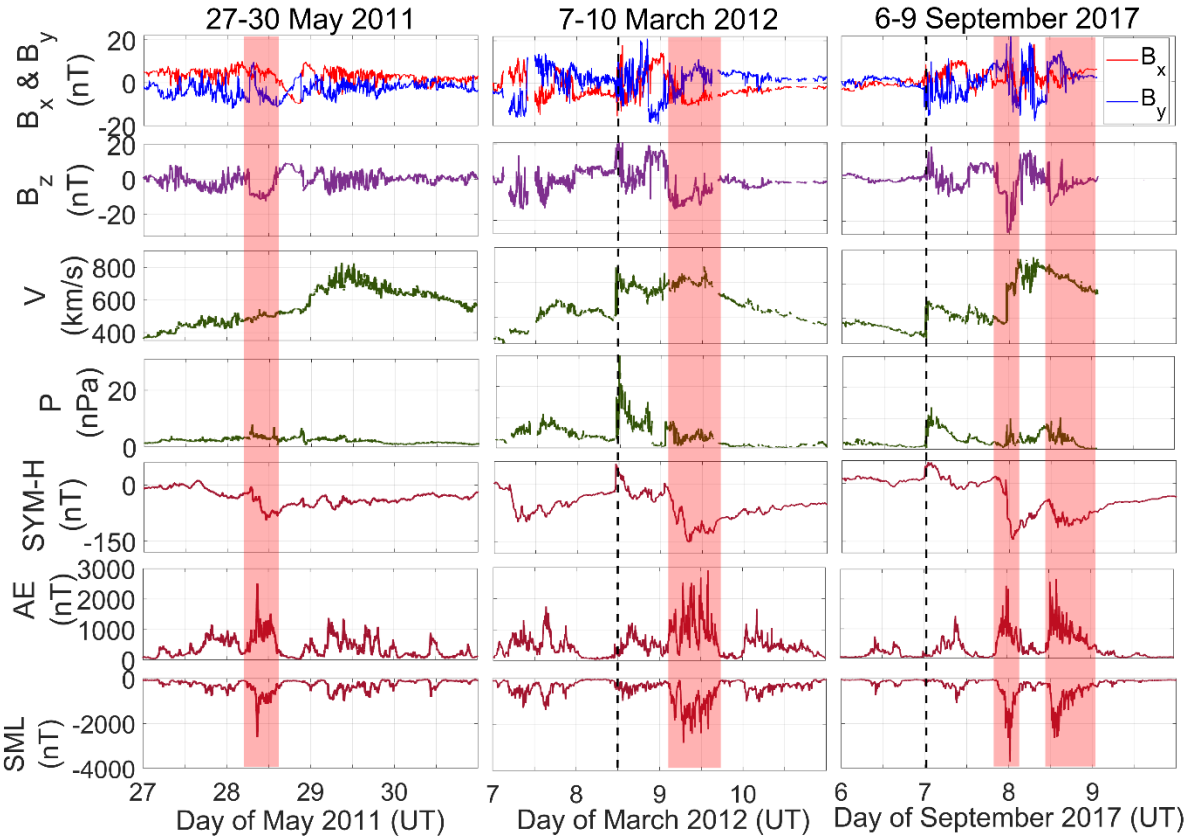

Figure 4.2. Variations in the interplanetary parameters for four days of duration covering the supersubstorm events are given in the top four rows, and the bottom three rows give the variations in the SYM-H, AE, and SML indices, respectively. Columns from left to right show results for the 2011, 2012, and 2017 events, respectively. A vertical dotted line shows the SSC during the events of 2012 and 2017 and the durations of the supersubstorms are highlighted by brown shaded boxes in the respective panels.

However, the solar wind bulk velocity shows a peak on 29 May, long after the occurrence of the supersubstorm. The variation in SYM-H shows bay-like decrement around1500 UT on 27 May and ~0600 UT on 28 May, termed as the first-sub main phase, and, a negative excursion between ~0600-2355 UT on 28 May, termed as the second-sub main phase. An unusual extreme excursion in the SML index on 28 May occurred during the second-sub main phase of the geomagnetic storm, which is also reflected in the AE index.

Table 4.1. Temporal occurrence chart depicting start and end epochs with day and month of the respective phases of the supersubstorms and geomagnetic storm events. The lowest values of the SML and SYM-H indices in each case are also provided. The day and month of the epochs are given in "dd/mm" format.

Events	Supersubstorm			Geomagnetic Storm		
Epoch of Phase	Start of the Expansion phase, UT (dd/mm)	Min. SML UT (dd/mm) (nT)	End of Recovery Phase, UT (dd/mm)	Time of SSC, UT (dd/mm)	Duration of Main phase, UT, (dd/mm)	Min. SYM-H (nT)
2011	0410 (28/05)	0847 (28/05) (-2615)	1605 (28/05)	NIL	1600 (27/05) to 1113 (28/05)	(-94)
2012	0215 (09/03)	0651 (09/03) (-2791)	1610 (09/03)	1104 (08/03)	1300 (08/03) to 0745 (09/03)	(-149)
2017-SSS1	2000 (07/09)	0024 (08/09) (-3712)	0405 (08/09)	2345 (06/09)	2130 (07/09) to 0105 (08/09)	(-146)
2017-SSS2	1137 (08/09)	1308 (08/09) (-2644)	0100 (09/09)			

In contrast to the 2011 event, the SSC during the 2012 and 2017 events is accompanied by an abrupt rise in the bulk velocity, temperature, and ram pressure (shown by a vertical dashed line in Figure 4.2). Hajra et al. (2022) have classified the probable drivers of these events and found an absence of both the forward interplanetary shockwave (IS) and the interplanetary reverse shockwave (ISA) during the 2011 event and the presence of the both during 2012 and 2017 events. This probably explains the non-occurrence of SSC during the 2011 event. The corresponding time and date of the SSCs are given in Table 4.1. A two-step decrement in the SYM-H index during the 2012 event is noted following the consecutive southward excursions in the IMF-Bz at 1200 UT on 8 March and 0215 UT on 9 March.

Similarly, three consecutive southward excursions in IMF-B_z are found to occur during 7-8 September 2017. So, a three-step decrease in SYM-H is observed during the 2017 event along with three simultaneous peak excursions in the AE and SML indices. Intriguingly, two supersubstorm events are noted during this event namely '2017-SSS1' and '2017-SSS2', which respectively occurred on 8 and 9 September within about 12 hours. It is pertinent to highlight here that in comparison to the '2017-SSS1', the '2017-SSS2' supersubstorm is found to be

associated with a lesser magnitude of minimum IMF-B_z and SYM-H index and negligible variations in the solar wind temperature and ram pressure. Hajra et al. (2022) found that the multiple hits by magnetic clouds associated with FAST background solar wind plasma possibly triggered these supersubstorms. Additionally, they showed that the coupling efficiencies and the energy balance eventually play a prominent role in triggering the supersubstorms. Table 4.1 gives a summary of the different phases and associated time epochs of the supersubstorms and geomagnetic storms during the three events.

Following a magnetic reconnection in the tail-side (Ohtani et al., 2022), a substorm onset location is often identified through a sequence of pre-onset and onset signatures using multi-instrument observations (Lyons et al. 2018; Orr et al. 2021; Nishimura et al. 2022). The substorms-related magnetospheric reconfiguration produces significant disturbances in the currents which can be identified by using the observations from the ground-based network of instruments like SuperMAG (e.g. Kaki et al. 2021; Orr et al. 2021) and SuperDARN (e.g. Lyons et al. 2022). The SuperMAG network of magnetometer can be used to derive global maps of the ground-level magnetic field perturbations in terms of horizontal component vectors (Waters et al. 2015). To locate the onset of the supersubstorms in the present study, the polar plots from the SuperMAG website at "https://supermag.jhuapl.edu/rBrowse" are obtained and used. A detailed polar structure of the supersubstorm onset locations is given in the supporting information as SI-7 in Appendix B. Accordingly, the geographic regions are visually marked and noted to be surrounded by 59^o-71^o N and 95^o-167^o W for the May 2011 event, 55^o-81^o N and 45^o-150^o W for the March 2012 event, 59^o-70^o N and 0^o-30^o E for the 2017-SSS1 event, and 61^o-72^o N and 75^o-150^o W for the 2017-SSS2 event. It is important to note that the above localization has its limitations due to the uneven distribution of magnetometers across the globe (Kaki et al. 2021). Nevertheless, this information may prove helpful for an interested reader to have a basic understanding of the location of the supersubstorms.

4.3.2 Global impact of the SSC

The occurrence of the SSC is noticeable during the events of 2012 and 2017 through Figure 4.2. Quiet time variations of the H, D, and Z-components of the geomagnetic field show an intriguing relationship (Rastogi and Stenning, 2002; Rastogi, 1999) over different latitudes and longitudes as well as during SSC (Shinbori et al., 2009). Hence, it is important to understand the latitudinal and longitudinal impact of the SSC, by using both the H-component (north-south perturbations) and D-component (east-west perturbations) variations. Villante and

Piersanti (2009) and Piersanti and Villante (2016) have found an emerging difference in geomagnetic response across a range of latitudes. Therefore, latitudinal variations are emphasized in the following section where we describe the results of the H and D components.

4.3.2.1 Variations in the H-component

Figure 4.3 shows the global H-component observations during the SSC for the 2012 and 2017 events. The results are segregated into two columns for each event, respectively for the northern (NH) and southern (SH) hemispheric stations. For the convenience of the study, columns are stacked into three rows of panels corresponding to a co-latitude band of 0^o-45^o, 45^o-65^o, and 65^o-90^o, respectively. Notably, three distinct types of latitudinal signatures of the SSCs in the H-component observations are found in Figure 4.3. A main impulse (MI) is followed by each of the short-lived signatures mentioned below.

a) The step-like increase between co-latitudes of 0^o to 45^o
b) The step-like increase followed by a sudden decrease (between co-latitudes of 45^o to 65^o)
c) Sudden decrease (between co-latitudes of 65^o to 90^o).

Some of the unique features e.g. the step-like increase as reported earlier by Shastri et al. (1993), Rastogi (1993), Yamada et al. (1997), and Kikuchi et al. (2001), are observed for the co-latitude band of 0^o-45^o during both the 2012 and 2017 events in both the hemispheres. The effect of the SSC as a step-like increase is observed at about 1104 UT and 2345 UT respectively during the 2012 and 2017 events. The impact of the SSC over all the stations in this low-to-mid latitude band is seen as a simultaneous rise irrespective of the local time (or longitude of the station) and the phase variations in the H-component.

However, the absolute amplitude of the H-component is found to exhibit significant local time and latitude dependence. The effect of local time can be inferred from the lower values of the H-component over Dalat (Figure 4.3a, red curve) in the northern hemisphere and Saint Helena (Figure 4.3d, blue curve) during the 2012 event. Similarly, during the 2017 event, the lower values of the H-component over Dalat (red curve) and Kakioka (black curve) in the northern hemisphere (Figure 4.3g), but comparatively higher values over Huyancayo (red curve) in the southern hemisphere (Figure 4.3j) are observed. These observations resemble the occurrence of a step-like preliminary positive impulse (PPI) followed by MI.

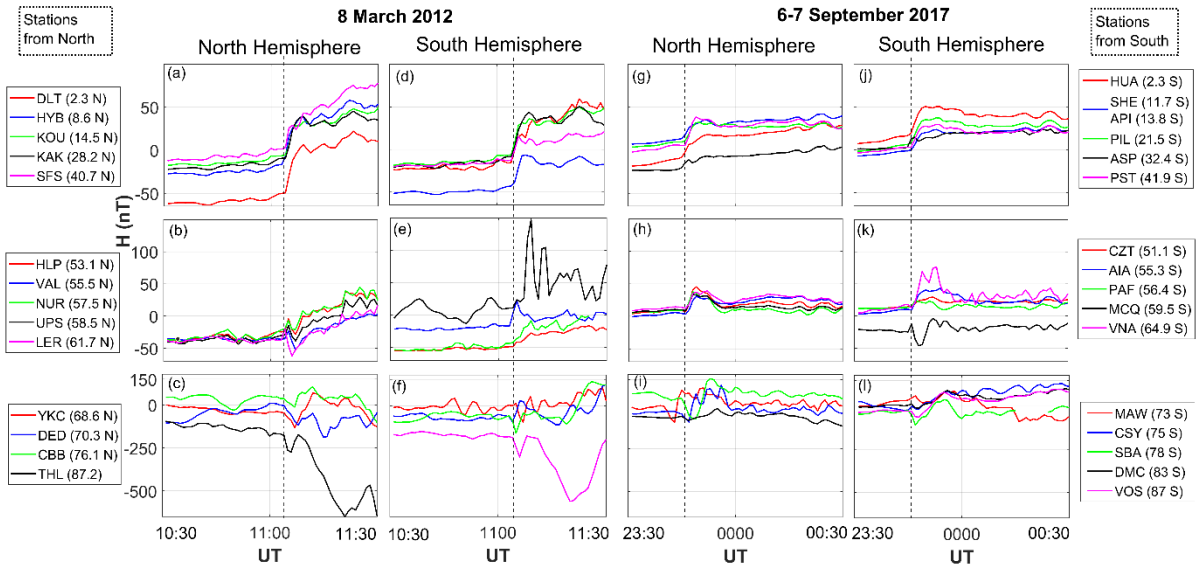

Figure 4.3. Variations in the H-component at the time of SSC are shown from a group of stations from the northern hemisphere (NH) and southern hemisphere (SH), respectively in the left two and right two columnar panels for the events of 2012 (panels a to f) and 2017 (panels from g to l). Panels from the top in each column correspond to a co-latitude range of 0°-45°, 45°-65°, and 65°-90°, respectively. Each curve corresponds to the observations from a station whose code name with geomagnetic latitude is given in the legends. Legends for stations from the NH (SH) are shown on the left (right). The vertical dotted line in each columnar panel shows the time of the SSC.

Observations from the middle to higher latitudes (45°-65°) show a sudden impulse-like rise followed by a sudden decrease in the H-component, which is found to last for about 3-15 minutes over different stations during the events of 2012 and 2017. These transient variations show a Gaussian- kind of structure before reaching a stationary state of MI and remain independent of the local time. The short-lived signatures take the shape of a Gaussian through a sudden increase followed by a sudden decrease in the H-component. So, the observations from the latitude band of 45°-65° resemble a Gaussian-kind of PPI followed by an MI. Anomalously, the variations in the H-component over Port Alfred (CZT) (Figure 4.3e, red curve) and Port-Aux-Francais (PAF) (Figure 4.3k, green curve) stations show very low amplitude Gaussian-kind of structures in the southern hemisphere. Additionally, during the 2017 event, the H-component variations over Macquarie Island (MCQ) station show a negative Gaussian-kind of structure (Figure 4.3k, black curve) which is in contrast to the variations over

other stations in this band of latitude. A strong asymmetry in the occurrence pattern of the PPI and MI in the latitude band of 45°-65° is noticeable between the northern and southern hemispheres.

However, the H-component variations from the band of the high to polar co-latitudes (65°-90°) show completely different signatures. In the case of 2012, a preliminary reverse impulse (PRI) (with a 3 to 5-minute period) followed by a mild presence of the MI with multiple undulations is seen over all the stations except over Thule (THL) (Figure 4.3c, black curve) in the northern hemisphere and Vostok (VOS) (figure 4.3f, pink curve) in the southern hemisphere. The variations over THL and VOS show the occurrence of the PRI followed by a strong negative appearance of the MI which undergoes a depression of about -600 nT and -500 nT, respectively within ~20 minutes of the SSC. Also, a minute advance in the occurrence of a sharp increase over CSY (Figure 4.3f, blue curve) before the dotted line in the case of March 2012 can be observed. Such an advance may be possible under the effect of local time over CSY compared to other stations. But, in the case of the 2017 event, the H-component variations show a signature of a PRI followed by a positive MI with multiple undulations over the northern and southern hemispheres over most of the stations. Intriguingly in the northern hemisphere (Figure 4.3i), the time of onset of the PRI is observed a few minutes before the time of SSC, and the earlier occurrences are found different over different stations. The onset of the PRI at Yellowknife (YKC) is found to occur about 5 minutes before the time of SSC at 2345 UT (vertical dotted line). Additional results on the response of SSC from the rest of the stations are given in supporting information as SI-2 in Appendix B, which provides a detailed global response from different latitudes.

In general, the net rise or fall in the amplitude of the H-component variations is found to be the highest for the high-latitude stations and decreases towards the mid and low latitudes during both events.

4.3.2.2 Variations in the D-component

Figure 4.4 shows the global D-component observations for 1-hour during the SSC for the 2012 and 2017 events. Alike the previous section, the results are segregated into two columns for each event, respectively for the northern (NH) and southern (SH) hemispheric stations. For the convenience of the study and having a logical comparison with the H-component perturbations, columns are stacked into three rows of panels corresponding to a co-latitude band of 0°-45°, 45°-65°, and 65°-90°, respectively.

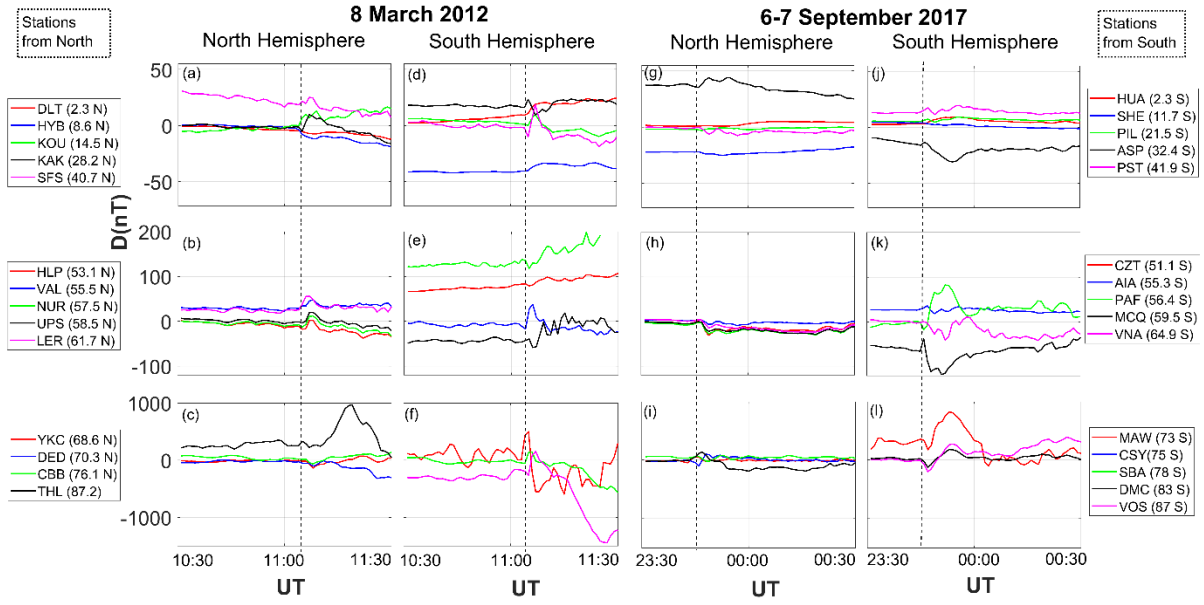

Figure 4.4. Variations in the D-component at the time of SSC are shown from a group of stations from the northern hemisphere (NH) and southern hemisphere (SH), respectively in the left two and right two columnar panels for the events of 2012 (panels a to f) and 2017 (panels from g to l). Panels from the top in each column correspond to a latitude range of 0º-45º, 45º-65º, and 65º-90º, respectively. Each curve corresponds to the observations from a station whose code name with geomagnetic latitude is given in the legends. Legends for stations from the NH (SH) are shown on the left (right). The vertical dotted line in each columnar panel shows the time of the SSC.

Unlike the H-component perturbations, the signatures in the D-component do not follow a specific latitudinal pattern, as reported earlier by Rastogi et al (2001) and other studies. Nevertheless, a transient positive or negative Gaussian-like sudden impulse is observed over most of the stations; while some of the low-latitude stations follow almost unperturbed variations at the time of SSC. The positive and negative Gaussians resemble the upward and downward FACs respectively, over high latitudes. The variations in the D-component show a higher order of asymmetries and variabilities among the stations. The non-uniformity in the perturbations of the D-component reflects the complex interplay of the SSC-related electric fields and currents in the ionosphere. One important pattern observed in the signatures of the D-component is an absence of the main impulse (as seen in the H-component variations) in most of the cases. An indistinct main impulse (MI) is observed over a few stations like KAK (panel a), ASP (panel d), and PAF and MCQ (panel e) during the 2012 event; DLT (panel g), HUA and PIL (panel j) and PAF (panel k) during the 2017 event. However, several cases of

non-uniform and transient PPI e.g. from stations KAK and KOU (panel a), HLP, VAL, NUR, UPS and LER (panel b), THL (panel c), PIL and PST (panel d), AIA (panel e), MAW and SBA (panel f) during the 2012 event; and KAK (panel g), THL (panel i), PST (panel j), PAF (panel k), MAW, DMC and VOS (panel i) during the 2017 event are observed. Similarly, several cases of PRI e.g. from stations YKC, DED, and CBB (panel c), ASP (panel d), MCQ (panel e), VOS (panel f) during the 2012 event; and HLP, VAL, NUR, UPS, and LER (panel H), CSY (panel i), ASP (panel j), MCQ and VNA (panel l) are observed. With these specific signatures, multiple undulations of small amplitude are also observed over some of the stations. Intriguingly, the time of onset of the perturbations does not match well either with the advent of the global SSC or with the step-like PRI/PPI patterns in the H-component. For example, during the 2012 event, the positive or negative Gaussian-like signatures are observed at about 4-5 minutes after the onset time of the global SSC (designated by the dashed line at 1100 UT on 8 March 2012). On the contrary, during the 2017 event, all the positive and negative Gaussians-like signatures are observed at about 4-5 minutes before the global SSC occurred (designated by the dashed line at 0000 UT on 7 September 2017). However, the onset epochs of the events as observed in the D-component perturbations are almost the same for almost all the stations. A close inspection also reveals a drastic structural difference between the two sets of signatures during the two events. For example, during the March 2012 event, more positive Gaussian signatures (and hence PPI) are found, whereas, during the 2017 event, mostly negative Gaussians (and hence PRI) are found in the D-component signatures. Additionally, the absolute fluctuations in the amplitude of the D-component are found to exhibit significant local time and latitude dependence.

4.3.3 Response of H-components during the supersubstorm period

4.3.3.1 Response from the co-latitude band of 70^{o}-90^{o}

The supersubstorms are known to produce spatial and temporal variations of the storm time auroral ionospheric currents, the magnitude of which can be different at different local times and latitudes. The high latitude H-component (Figure 4.5) variations show a similar pattern only for latitudes higher than ~75^{o} within a particular hemisphere. For example, the variations from all the stations in the northern (southern) hemisphere except over HRN (MAW) station show a close resemblance with each other.

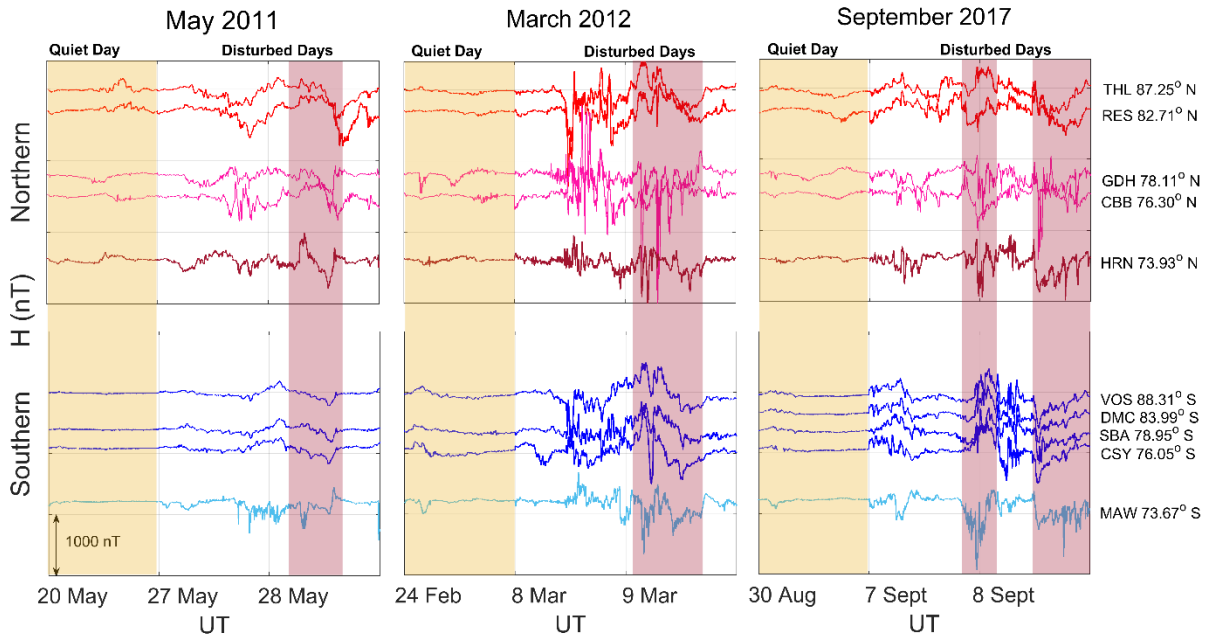

Figure 4.5: The H-component variations as observed from the latitude band of 70°-90° for the northern and southern hemispheres are respectively shown in the upper and lower rows. Each panel begins with a quiet day followed by 2 days of variations covering each of the supersubstorm events, respectively for 2011, 2012, and 2017 from left to right columnar panels. The code name and geomagnetic latitude of each station are given on the rightmost side. The observation from a station DMC for the 2011 and 2012 events is not available. Different colors of the curves are used to indicate the difference in patterns of the variations.

Drastically different types of phase changes are observed over HRN and MAW. A close examination of the patterns further shows better qualitative matches from stations of similar latitudes (like pairs of station THL-RES and GDH-CBB), although they are longitudinally far apart (see Table SI-1 in the supporting information in Appendix B). Also, there exists a strong asymmetry across the hemispheres over the high latitudes. This interhemispheric asymmetry is observed to a lesser extent during the 2011 event (summer) than during the 2012 and 2017 events (equinox). Hence, in the equinoctial periods, the asymmetry is found to be better distinguished. Further, in terms of magnitude, the largest perturbations are not found over the polar stations like CBB and HRN; but over the sub-polar regions (between ~70°-75° latitudes). Intriguingly, the largest perturbations are seen (-1825 nT) during the 2012 event, though the 2017 event was the largest in terms of the lowest magnitude of the SML. A detailed response from each station with the magnitude of the H-component variations from the latitude band of 70°-90° for four days covering each of the events is provided in the supporting information as SI-3 in Appendix B. In general, some episodic fluctuations in the H-component are found

before and after the period of each supersubstorm, which conform to the ongoing geomagnetic activity associated with the supersubstorms.

4.3.3.2 Response from the co-latitude band of 15º-70º

The H-component variations from the magnetometers located between 15º and 70º (in both hemispheres) are observed from 60 stations, however, for brevity, representative results from 16 magnetometers are only shown in Figure 4.6.

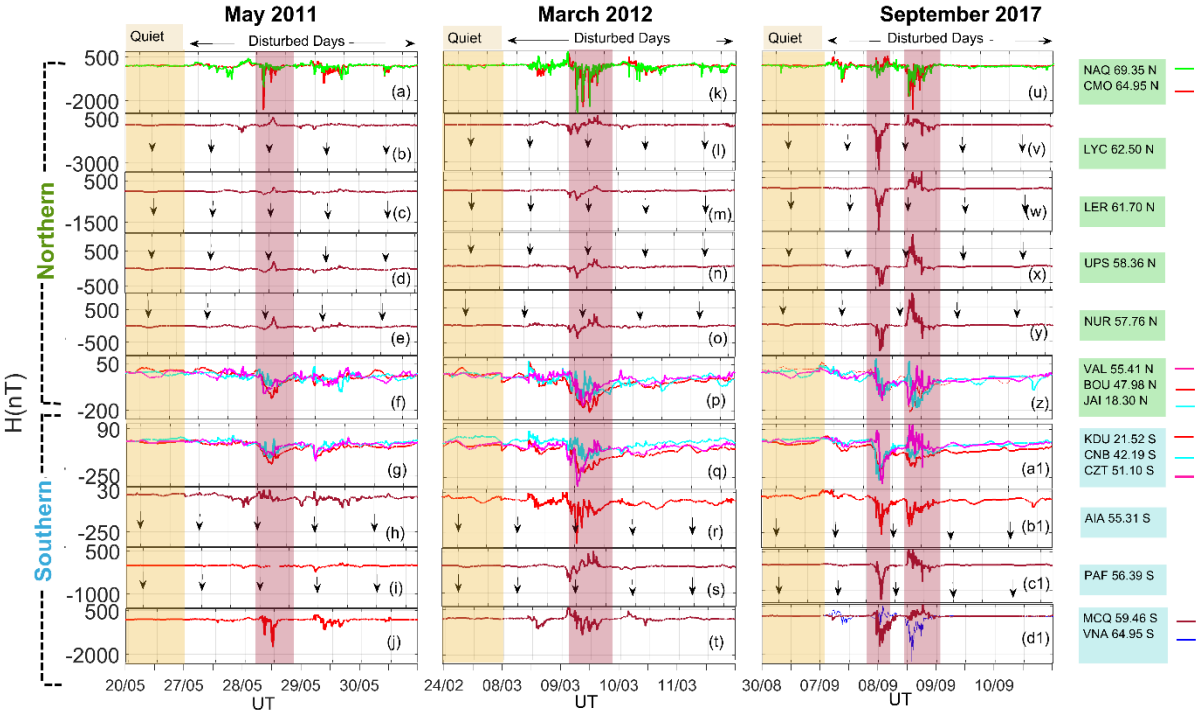

Figure 4.6. The H-component variations from the latitude band of 15º-70º from the northern (top six rows) and southern (bottom four rows) hemispheres are given including observations on a quiet day (yellow shaded box at the beginning of each column). The columnar panels give results for the events of 2011, 2012, and 2017 respectively from left to right, wherein the respective supersubstorm durations are shaded by vertical brown boxes. The geomagnetic latitudes of the respective magnetometer stations are given on the rightmost side of each row. The sudden reversals in the H-component variations are depicted by brown curves in different panels and a black arrow in each panel represents local noon.

The H-component variations from the co-latitude band of 15º-70º for four days for each event along with a reference quiet day are given in Figure 4.6. The panels are segregated

according to the patterns in the variations of the H-component during the supersubstorm events. Thus, we get well-matched variations for bands of 63^o -70^o, 56^o-63^o, and 15^o-55^o N. For example, the top row of Figure 4.6 (see Figure 4.6a, 4.6k, and 4.6u) shows peak depressions over NAQ and CMO during the supersubstorm period between 63^o N and 70^o N in the northern hemisphere with almost similar phase and amplitude variations. A similar pattern of deep depression is observed over VNA from the southern hemisphere during the 2017 event. Unfortunately, no observations from the southern hemisphere between 63^o S and 70^o S are available during the 2011 and 2012 events.

However, some salient and common features of the H-component variations from the co-latitude band between 56^o and 63^o are shown from the second to fifth rows from the top of Figure 4.6. Each row gives variations respectively from LYC (62.50^o N), LER (61.70^o N), UPS (58.36^o N), and NUR (57.76^o N) stations during all the three events of 2011, 2012, and 2017. The variations show a deep depression followed by a steep identical enhancement during the supersubstorm events (shaded by brown boxes in Figure 4.6). This enhancement in the H-component can also be termed as a reversal from an expected depression (global minima) which is observed elsewhere from all the stations between 63^o and 70^o N (top row) and between 15^o and 55^o N (sixth row from top).

It is interesting to note that the variations in the H-component from the co-latitude band of 15^o-55^o latitudes (sixth and seventh row from top) show almost identical patterns with respect to the phase and amplitude during the supersubstorm events. For the sake of convenience, the available observations from only three out of twenty stations from the 15^o-55^o co-latitude band are plotted. Similarly, the variations from the southern hemisphere show the pattern of a reversal over PAF (56.39^o S) and MCQ (59.46^o S) during the supersubstorms of 2012 and 2017 given by brown curves in the ninth and tenth row from the top, respectively.

However, the variations over AIA (55.31^o S), PAF (56.39^o S), and MCQ (59.46^o S) stations during different events (see panels 5i, 5j, 5r and 5b1) do not match with the variations from a similar latitude band (between 56^o and 63^o) either in the southern or northern hemisphere. The variations over the CZT (51.10^o S) station also show unusual phase reversals of smaller magnitude during the 2012 and 2017 events. The depressions in the SYM-H, SML, and AE indices (shown in Figure 4.1) are found to greatly vary in contrast with the phase reversal patterns (enhancements) during the supersubstorm periods shown by the curves in dark brown in Figure 4.6. Results of H-component variations from a few more stations, especially in the latitude band of 15^o-55^o and 63^o-70^o are provided in the supporting information as SI-4 in Appendix B to strengthen the above-mentioned statements.

4.3.3.3 Response from the co-latitude band of 0º-15º

It is known that the equatorial ionosphere exhibits a completely different set of current systems from that found in the other latitude bands, although, the dawn and dusk current systems are reported to be connected to the high latitudes. Nine magnetometer stations which are confined within 15°N and 15°S located at Dalat (DLT), Guam (GUA), Hyderabad (HYB), Phuthuy (PHU), Kourou (KOU), Huancayo (HUA), Ascension Island (ASC), Saint Helena (SHE) and Apia (API) are selected and corresponding observations are analyzed during the supersubstorm events. Figure 4.7 gives the H-component observations during the events with a respective quiet day variation from the northern (top five rows) and southern (bottom four rows) hemispheres.

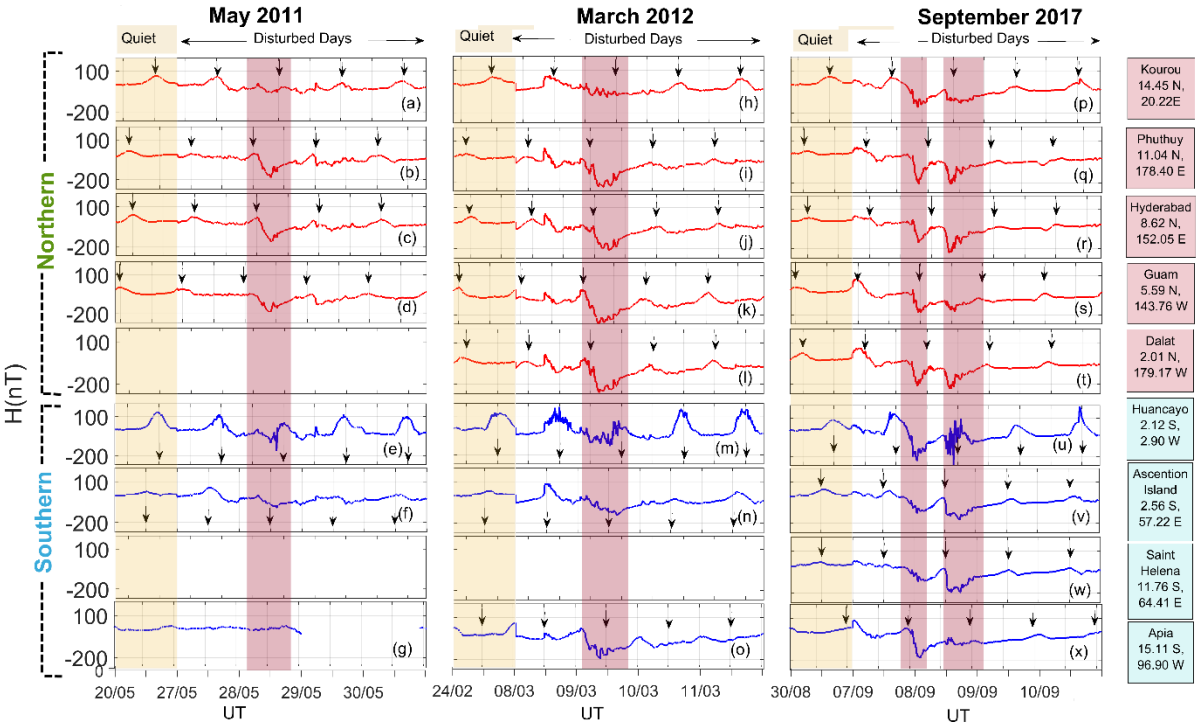

Figure 4.7: The variations in H-component as observed over the co-latitudes between 0º to 15º from the northern (top five rows) and southern (bottom four rows) hemispheres, respectively, beginning with the variations on a quiet day (shaded by yellow boxes) for each event are given. All panels are plotted against UT, whereas, the axis tick marks in each panel correspond to local midnight and local noon with a black arrow depicting the local noon time at the respective station. The tick marks given on the bottom abscissa depict 0000 UT and 1200 UT for reference to all the panels. Blank panels represent an absence of the observations from Dalat and Saint Helena stations in the corresponding rows during the May 2011 and March 2012 events.

The H-component variations from low latitudes show two completely different types of signatures depending upon the local noon. An obvious qualitative similarity in the variations among the second (PHU), third (HYB), fourth (GUA), and fifth (DLT) rows from the northern hemisphere (red curves) and ninth (API) row from the southern hemisphere (blue curve) is observed. This set of magnetometer stations is located between 78^o and 188^o E geomagnetic longitude (called set-1 magnetometers in this study). These stations exhibit sharp and well-distinguished H-component depressions up to -200 nT or lesser during supersubstorm events. The minimum depressions of the H-component at all these stations are found to be simultaneous during each event. The other type of the H-component variations is found in the northern hemisphere (red curve) and is given in the first (KOU) row and southern hemisphere (blue curves) in the sixth (HUA), seventh (ASC) and eighth (SHE) rows of Figure 4.7. These stations are located between the geomagnetic longitudes of 284^o and 354^o E (called set-2 magnetometers in this study) and show multiple local depressions. The depressions over these stations show multiple bay-like gradual decrements around the global minimum and are not so well-distinguished in comparison to the sharp signatures from the set-1 magnetometers noted above. It is noteworthy that KOU being located in the northern hemisphere (red curve) belongs to set-2 magnetometers (where all other sites are from the southern hemisphere) and API is located in the southern hemisphere (blue) belongs to set-1 magnetometers (where all other sites are from the northern hemisphere). A clear local noon-dependent pattern is observed as a causative mechanism behind the stark difference in H-component variations between the set-1 and set-2 magnetometers. This proves the local time and longitude dependence of the H-component perturbations in low latitudes.

During the successive events of 2017-SSS1 and 2017-SSS2, it is observed that the magnitude of the minimum depression during the first supersubstorm (2017-SSS1) is found to be more than that of the second one (2017-SSS2) recorded by the magnetometers at KOU (first row), GUA (fourth row), and HUA (sixth row) stations as given in Figure 4.7. On the contrary, the magnitude of the minimum depression during 2017-SSS1 is found to be less than 2017-SSS2 at HYB (third row), DLT (fifth row) ASC (seventh row), and SHE (eighth row) stations. Intriguingly, the observations show no depression during 2017-SSS2 at API (ninth row) and almost equal depression during both the events of 2017 at PHU (second row) station. For the 2011 event, the minimum depressions are found to be between the evening and the night-time sector (peaking at ~2200 LT at GUA, at ~1800 LT at HYB, and at 1930 LT at PHU) for the set-1 magnetometers. On the other hand, minimum depressions are found to occur around the noon or afternoon sector in the case of the set-2 magnetometers. For the 2012 event, the set-1

magnetometers exhibited the minimum depressions between afternoon and evening, and the set-2 magnetometers during the morning and noon intervals. For the 2017-SSS1 (2017-SS2) event, the depressions are observed during the morning-noon (night) interval for the set-1 magnetometers and the night (afternoon-evening) interval for the set-2 magnetometers.

4.3.4 Response of D-components during the supersubstorm period

The supersubstorms affect the ionospheric currents at all latitudes and the effect of FACs generated during these events can be observed over the high-altitude auroral current system. All these variations are well-reflected in the variations of the D-component as well. The magnitude of the D-component varies according to local time and latitude and shows different patterns of behaviors with respect to those of the H-component (Rastogi et al., 2001). The D-component variations from the co-latitude range of 15^o-$70^o$are observed from 60 stations, but results from only 4 stations (LER, UPS, NUR from the northern hemisphere and PAF from the southern hemisphere) located between 55^o and 70^o are shown in Figure 4.8 for brevity. Similarly, out of 9 stations located between co-latitudes of 0^o and 15^o, the results from 4 magnetometers (HYB, GUA from the northern hemisphere and HUA, ASC from the southern hemisphere) are only shown. The most important signature discernible from Figure 4.8 is that the D-component does not attain a global minimum when the H-component (Figures 4.5 to 4.7), SML, and SYM-H (Figure 4.2) attain drastic decrement. Rather in some cases, positive undulations in the D-component are observed when the H-components show extreme fall, which relates to the latitude of the station and associated current systems during the supersubstorm.

A north-south hemispheric asymmetry corresponding to the high latitude magnetometers is found in the D-component but with a lesser magnitude than in the H-component. Alike the variations in the H-component, the high latitude D-component shown in the top and bottom rows of Figure 4.8 (a, k, u, j, t, d1) variations show a similar pattern only for latitudes higher than ~75^o within a particular hemisphere. A completely different pattern of the phase variations in the D-component is observed for the stations located between the latitudes of 70^o-75^o e.g. the variations over HRN (northern) and MAW (southern) stations.

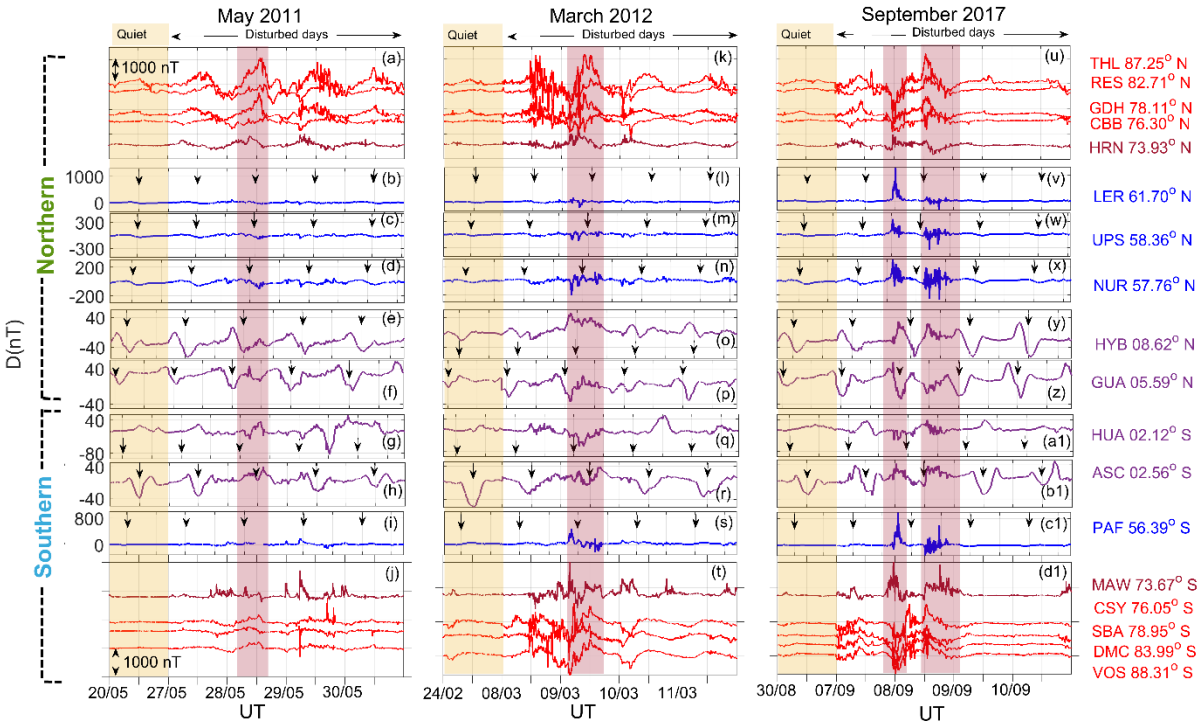

Figure 4.8: Observations of the D-component from a particular station are given in each row respectively in the columnar panels for the events of 2011, 2012, and 2017 from left to right. The vertical arrangement of panels is made to display the variations from pole-to-pole following a notation for hemispheres given on the left. The station code names with geomagnetic latitudes are given at the right of each row. The curves in red, blue, and violet respectively refer to the high latitude, the sub-auroral/mid-latitude, and, the low-latitude stations. All panels are plotted against UT, whereas, the axis tick marks in each panel correspond to local midnight and local noon with a black arrow depicting the local noon time at the respective station. The tick marks given on the bottom abscissa depict 0000 UT and 1200 UT for reference to all the panels.

The variations from 55^{o}-70^{o} co-latitudes show a deep depression followed by a steep identical enhancement during the supersubstorm periods shaded by brown boxes in Figure 4.8. Interestingly, during the 2011 and the 2012 supersubstorms, the mid-latitude phase reversals are only observed over the PAF station from the southern hemisphere which is like the H-component phase reversals from both hemispheres. During the 2017-SSS1, the phase reversal of the D-component is observed, much like the H-component variations. The very interesting fact is that global maxima (minima) in the D-component is found in contrast to global minima (maxima) in the H-component during the 2017-SSS1 (2017-SSS2) event over the mid-latitudes.

In context to the low latitude variations (0^o and 15^o co-latitudes), consecutive undulations with many local maxima and minima and no signature of global minimum during the supersubstorm period are observed over almost all the stations. In contrast to the H-component variations, no common or specific pattern in the variations in the D-component from any of the stations is observed. Most importantly, in most cases, drastic enhancements are observed during the supersubstorm period indicating an increase in the eastward geomagnetic field. The D-component perturbations are found to vary significantly from one station to another, which is possibly due to large longitude differences and a varying presence of the local currents and electric fields. Eventually, it implicates a highly variable, and local time-dependent nature of the low-latitude ionosphere. A detailed response with a specified magnitude of the D-component variations for four days covering each of the events is provided in the supporting information as SI-6 in Appendix B.

4.3.5 Signatures of the GIC during supersubstorms

The variations of geomagnetically induced currents (GICs) can be represented based on the variations of the dB/dt, the time derivative of the total intensity of the geomagnetic field variations at the ground. The variations of latitudinal peak maximum and minimum values of dB/dt (Figure 4.9) are obtained by using 1-minute sampled H-component observations from globally-spread 45 stations of the INTERMAGNET network.

It is found that the perturbations in the dB/dt are almost negligible within the latitude band of 5^o-55^o latitudes in both hemispheres during all the supersubstorm events. Whereas, a minor amplification of the dB/dt over the dip equatorial region is observed. The equatorial enhancement in the GIC during geomagnetic storms and impulsive events has been known (see Ngwira et al. 2013; Carter et al. 2016 and references therein) under the effect of the equatorial electrojet. However, the sudden huge amplification of the dB/dt noted over the auroral and sub-auroral stations (with latitudes higher than ~55^o) in both hemispheres needs to be seen under the effect of the different current systems. The maximum dB/dt values are measured during 2011, 2012, and 2017 events respectively at CMO (315.34 nT/min, 65.38^o N), SOD (349.35 nT/min, 63.95^o N), and LYC (868.83 nT/min, 62.54^o N) in the northern hemisphere and, at CSY (626.72 nT/min, 76.05^o S), MCQ (279.59 nT/min and 59.66^o S), MAW (486.52 nT/min, 73.07^o S) in the southern hemisphere. The stations located between 55^o-80^o latitudes record the peak value of the dB/dt (~900 nT/min) compared to the stations closer to the respective geomagnetic poles.

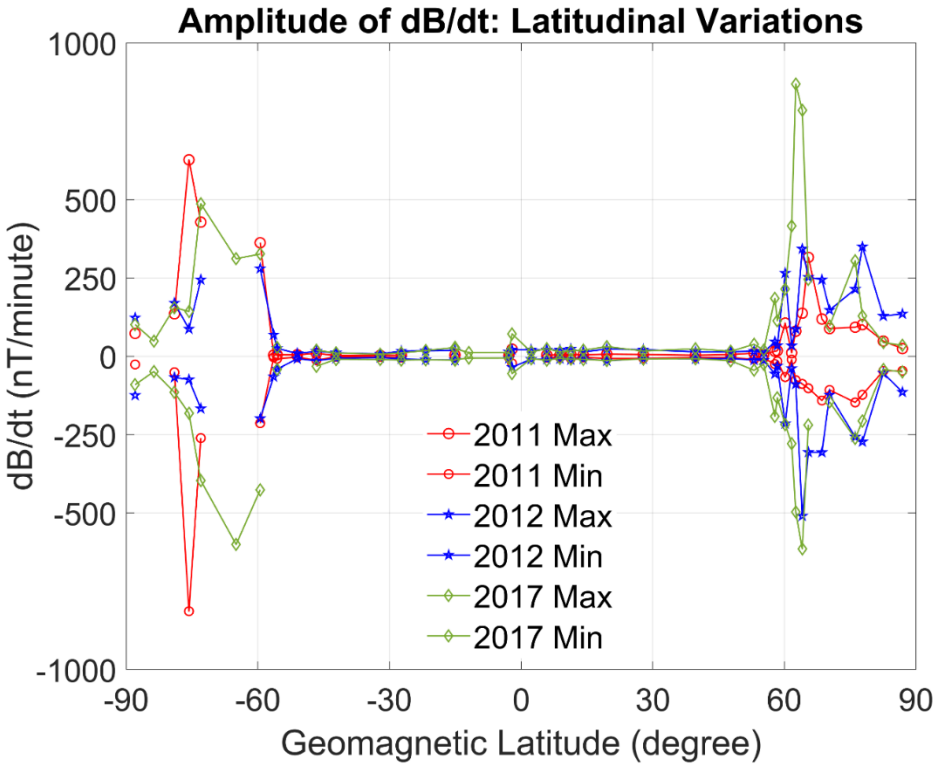

Figure 4.9. The maximum and minimum dB/dt values as observed over 44 magnetometer stations are given according to the geomagnetic latitude of the stations. The peak values corresponding to the supersubstorm event of 2011, 2012, and 2017 are given by red, blue, and green markers, respectively.

The variations show a clear north-south asymmetry in the peak deviations during each event and among the events. Further, the diurnal variations of the dB/dt over different stations at different latitudes show very intriguing and interesting patterns beyond the duration of the supersubstorms as shown in Figure 4.10. Although the variations from 40 magnetometer stations are analyzed, the observations from only 5 stations are shown in Figure 4.10 for brevity, which represents very unusual and unique characteristics.

It is observed from Figure 4.10 that for the 2011 event, all of the multiple peaks of the dB/dt fluctuations occur outside the period of the supersubstorm event. Almost similar kinds of signatures are found in the case of the 2012 event. However, for the 2017 event, most of the enhancements are found to occur during the supersubstorm period, whereas, a few cases of outside occurrences are also observed.

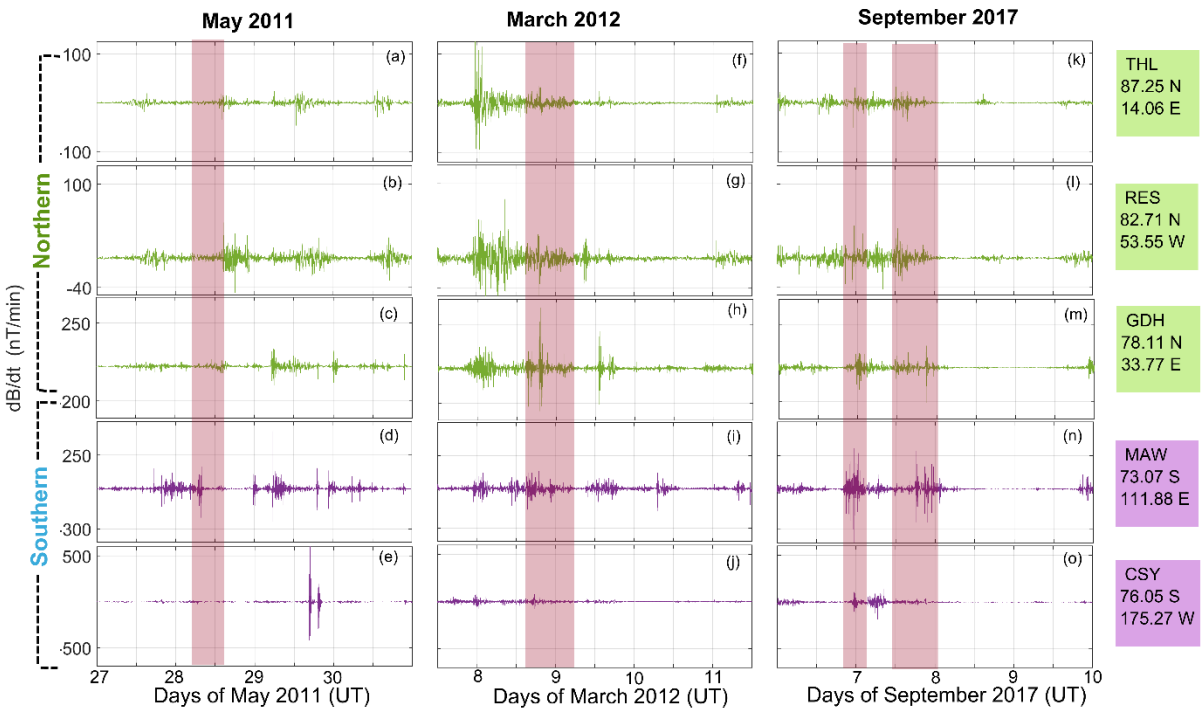

Figure 4.10. The variations in the dB/dt for four days surrounding the supersubstorm period are given in columnar panels from left to right, respectively for the 2011, 2012, and 2017 events. The top three rows show variations from the northern hemisphere and the bottom two rows from the southern hemisphere for the respective stations.

The dB/dt variations for the above-mentioned four-day period of events from all over the globe are examined. It is found that the high-latitude stations show prominent signatures of large fluctuations even outside the supersubstorm periods. A similar result for the peak dB/dt variations is shown in Figure 4.9. This result corroborates the fact of the non-uniformity of the GIC threat over the high latitude regions. The anomalous and inhomogeneous variations of the dB/dt are discussed in a section below in light of the latitude-longitude variations in the field-aligned currents and their relationship with the total variations in the H-component.

4.3 Discussion

The solar cycle 24 exhibited only four supersubstorms during three space weather events compared to the higher number of supersubstorms during solar cycles 21 to 23 (Hajra et al. 2022). The implications of the supersubstorm events in terms of their geomagnetic response are also very interesting, as their characteristics are very unusual and unique.

First, the results on the impact of the storm sudden commencement (SSC) on the H-component during the moderate geomagnetic storms of March 2012 and September 2017 are

given (in Figure 4.3). The SSC is found to exhibit a latitude-dependent short-lived signature (preliminary impulse) followed by the main impulse (MI) (Sastri et al. 1993). The short-lived signature is found to be of three distinct types namely: a step-like PPI in the latitude band of 0^o-45^o, a Gaussian-kind of PPI in the latitude band 45^o-65^o, and, a PRI in the latitude band 65^o-90^o. Within the band of 0^o-45^o latitudes, the low latitude step-like sudden rise of the H-component is possibly produced from the Chapman-Ferraro current which originates at the sudden shock impinged on the magnetopause (Yamada et al. 1997; Fujita 2019 and references therein). This shock traverses longitudinally as a compressional hydromagnetic wave across the magnetospheric cross-section and enhances the geomagnetic field (Araki 1977). It is noteworthy to mention that the impact of this sudden shock or the resultant Chapman-Ferraro current at the magnetopause is simultaneous on the geomagnetic field at the low latitudes on the earth's ionosphere and is observed as the step-like PPI in the present study (Figure 4.3). On the contrary, the high latitude preliminary reverse impulse (PRI) is produced due to the dusk-to-dawn electric field (of the DP_{PI} origin) at high altitudes in the magnetosphere and transmitted tailward in the magnetosphere. This field propagates as a transverse hydromagnetic wave along the geomagnetic lines of force down to the high-latitude ionosphere (Yamada et al. 1997) and eventually produces FACs. Hence, the advent of the high-latitude FACs may happen after some time of the advent of the Chapman Ferraro current (at the magnetopause) which can produce a finite delay in the occurrence of the PRI with respect to the step-like PPI. Nevertheless, the high latitude FACs subsequently generate a twin vortex type two-cell DP (disturbance polar) current system known as DP2; composed of the ionospheric Hall and Pedersen currents (Kikuchi et al. 1996). Over the mid-latitudes, the poleward progression of the enhancement in the H-component due to the Chapman Ferraro current (step-like positive impulse) is modulated by the gradual expansion of the high-latitude DP2 current cell, causing a subsequent decrement in the H-component (a negative impulse) ultimately creating the Gaussian-kind of PPI. This is observed as the second signature of the SSC vastly in the latitude band of 45^o-65^o in both hemispheres (Figure 4.3). Later, the magnetospheric convection at high latitudes produces a global dawn-to-dusk convection electric field giving rise to the relatively longer-term enhancement in the H-component called a main impulse (MI) (Yamada et al., 1997; Fujita 2019 and references therein). The MI is observed in the low and mid-latitudes after the occurrence of the PPI (Figure 4.3). Intriguingly, a completely different signature of sustained decrement after PRI is observed over polar stations in the northern (Thule) and southern (Vostok) hemispheres during the 2012 event as shown in Figure 4.3. At a high latitude station near the pole, we surmise that the flow of strong FAC and a subsequently higher magnitude of Hall-

current dominates the impact of the global magnetospheric convection, causing the above-mentioned negative main impulse after the PRI over there.

However, it is significant to note that even within a given latitude band as mentioned above, different shapes of the PPI, PRI, and MI are observed at different local times in response to the SSC, which requires further exploration of the underlying mechanisms. Recently, Piersanti and Villante (2016) have reported a latitude-specific response and explained the magnetospheric and ionospheric contributions using model simulations. So, an analysis is performed considering the possible current systems that could arise in the magnetosphere-ionosphere system during different periods and eventually produce the net variations in the H-component during a geomagnetic event. A complex interplay of the global magnetosphere-ionosphere current circuit is found to produce perturbations in the net H-component (ΔH) at any given latitude and local time. The ΔH can be expressed in terms of the perturbations due to the Chapman-Ferraro currents (ΔH_{CF}), FACs or the Birkland currents (ΔH_{FAC}), ring currents (ΔH_R), partial ring currents (ΔH_{PR}), polar ionospheric currents such as DP0, DP1, and DP2 (ΔH_{DP0}, ΔH_{DP1}, and ΔH_{DP2}), cusp current DPY due to substantial IMF-B_y (ΔH_{DPY}), equatorial electrojets (EEJ) (ΔH_{EEJ}) and counter electrojets (CEJ) (ΔH_{CEJ}), etc. (Kikuchi et al. 2001; Amory-Mazaudier et al. 2017). Following the studies by Cole (1966), Kamide and Fukushima (1971), Le Huy and Amory-Mazaudier (2005), Nava et al. (2016), Amory-Mazaudier et al. (2017), the global disturbance amplitude can be expressed as the sum of all the above terms with two additional terms of disturbance dynamo (ΔH_{Dynamo} in the ionosphere) and tail current (ΔH_T in the magnetosphere). The ionospheric disturbance dynamo (ΔH_{Dynamo}), which is generally delayed (towards the equatorward latitudes (Fejer et al. 2017) with respect to the advent of other currents and fields, also play a significant role. Eventually, the net disturbance can be expressed as:

$$\Delta H=\Delta H_{CF}+\Delta H_T+\Delta H_{FAC}+\Delta H_R+\Delta H_{PR}+\Delta H_{DP0}+\Delta H_{DP1}+\Delta H_{DP2}+\Delta H_{DPY}+\Delta H_{EEJ}+\Delta H_{CEJ}+\Delta H_{Dynamo}$$

To further corroborate our results on the impact of the SSC on the global H-component variations, the results from one of the possibly largest supersubstorms in the space age, which occurred on 21 January 2005 (with minimum SML=-4035 nT) are analyzed. It can be designated as an example of an isolated supersubstorm following Tsurutani et al. (2015) because the SML index during this event uniquely reached its minimum during the time of the SSC (and note in the vicinity of the main phase) of the associated geomagnetic storm. In the context of the results from the present study, wherein, the supersubstorms are associated with an ongoing geomagnetic storm, it is significant to compare the H-component variations during

the supersubstorm of 21 January 2005. The global H-component variations (from 29 magnetometer stations) from 21 January 2005 are corrected using quiet days of observations during 6-8 January 2005.

A sharp depression in the SML index at ~1738 UT (Figure 4.11a) corresponds to a signature of SSC in SYM-H at ~1709 UT (Figure 4.11b) followed by the start of the main phase of the geomagnetic storm at ~1920 UT (Figure 4.11b). A sharp positive step-like excursion of the H-component can be seen at ~1713 UT (Figure 4.11c) from the stations located between a latitude band of 0^o-55^o, which conforms to the occurrence of the SSC. However, at the time of SSC, the mid-latitude reversal of phase of the H-component occurs poleward from ~55^o, which gets enhanced in the latitude band of 58^o-63^o during the supersubstorm period between ~1713 and 1820 UT. While the largest perturbations are seen over the high latitude stations, the results of Figure 4.11 substantiate that during extreme events like supersubstorms, the reversal of the phase in the H-component occurs with the poleward boundary of ~55^o in both hemispheres. Our results as given in Figure 4.6 show a similar signature of reversals which has already been explained as a result of the composite effect of the currents produced at the time of SSC.

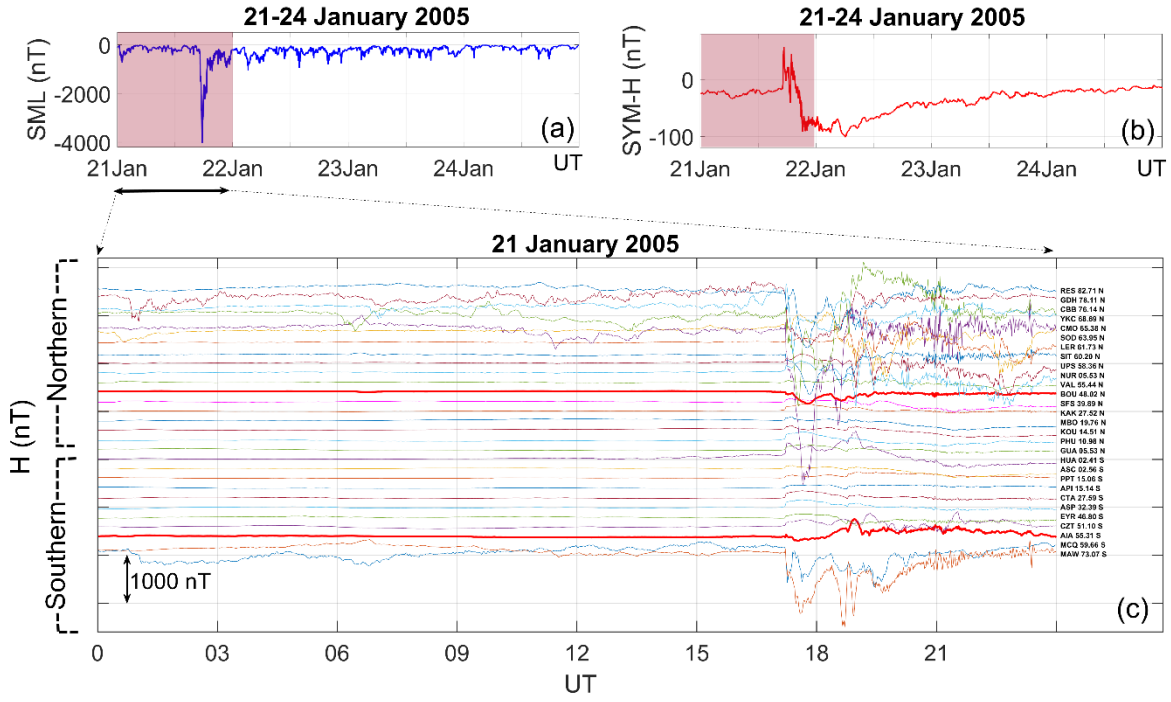

Figure 4.11. Panels (a) and (b) receptively give the variations in the SML and SYM-H indices during 21-24 January 2005. Brown-shaded regions in these panels highlight observations on 21 January 2005 which are blown out in panel (c), which gives the variations in the H-component as observed by 29 stations from the northern and southern hemispheres. The station

code with geomagnetic latitude for each curve in panel (c) is given on the right side and two heavy red curves depict the poleward beginning of the phase reversal in the H-component variations.

The multiple peaks and depressions over the high-latitude stations as shown in Figure 4.5 are possible because of the formation of the FACs and the associated DP currents, which are absent over the mid and low latitudes. The inter-hemispheric (north-south) asymmetry observed at high latitudes in the case of the 2011 event can be attributed to the seasonal (winter versus summer) effect. The growth and decay rates of the plasma in the southern hemisphere could be grossly different due to the nightside (substorm current wedge) compared with the northern hemisphere (dayside) (Milan et al. 2017) during the 2011 event. The phase changes over HRN and MAW stations compared to other polar stations (Figure 4.5) are found to be remarkably different. The curling auroral electrojet currents can induce depressions (enhancements) of varying magnitude depending upon the location being equatorward (poleward) from the respective center of the concentric DP2 vortices, which provides a plausible explanation of the observed changes.

In addition, the large instantaneous positive reversals observed during all the supersubstorm events between 56^{o} and 63^{o} latitudes (as shown in Figure 4.6) can be explained through a complex interplay of many competing factors, which act simultaneously. During these extreme substorm events, the generation of many complex systems like the magnetospheric currents and their manifestations, DP currents their equatorial manifestations, the auroral and sub–auroral joule heating and the corresponding dynamo, the Hadley cell between the pole and the equator due to thermospheric storm winds, etc. happen (Ganushkina et al. 2018; Ebihara 2019) and the complex interplay eventually lead to some unique kind of signatures depending on the local time and latitude. The ionosphere over the latitude band of 56^{o}-63^{o} also connects to the low latitude boundary layer (LLBL), which separates the inner and outer magnetospheric regions. In addition, there could be ionospheric equivalent currents related to the bursty-bulk-flows (Keith and Heikkila, 2020) that could produce fluctuations in the H-component of the geomagnetic field. Hence, it is highly probable that a composite effect of all the above-mentioned currents in this latitude band has resulted in a unique and characteristic geomagnetic response. Ebihara (2019) has performed simulations that have reproduced various processes and their signatures during the substorm occurrences. Considering their involved analysis of the coupling processes and their manifestation in the

magnetosphere-ionosphere system, the effect of supersubstorms on the global H-component variations needs further investigation.

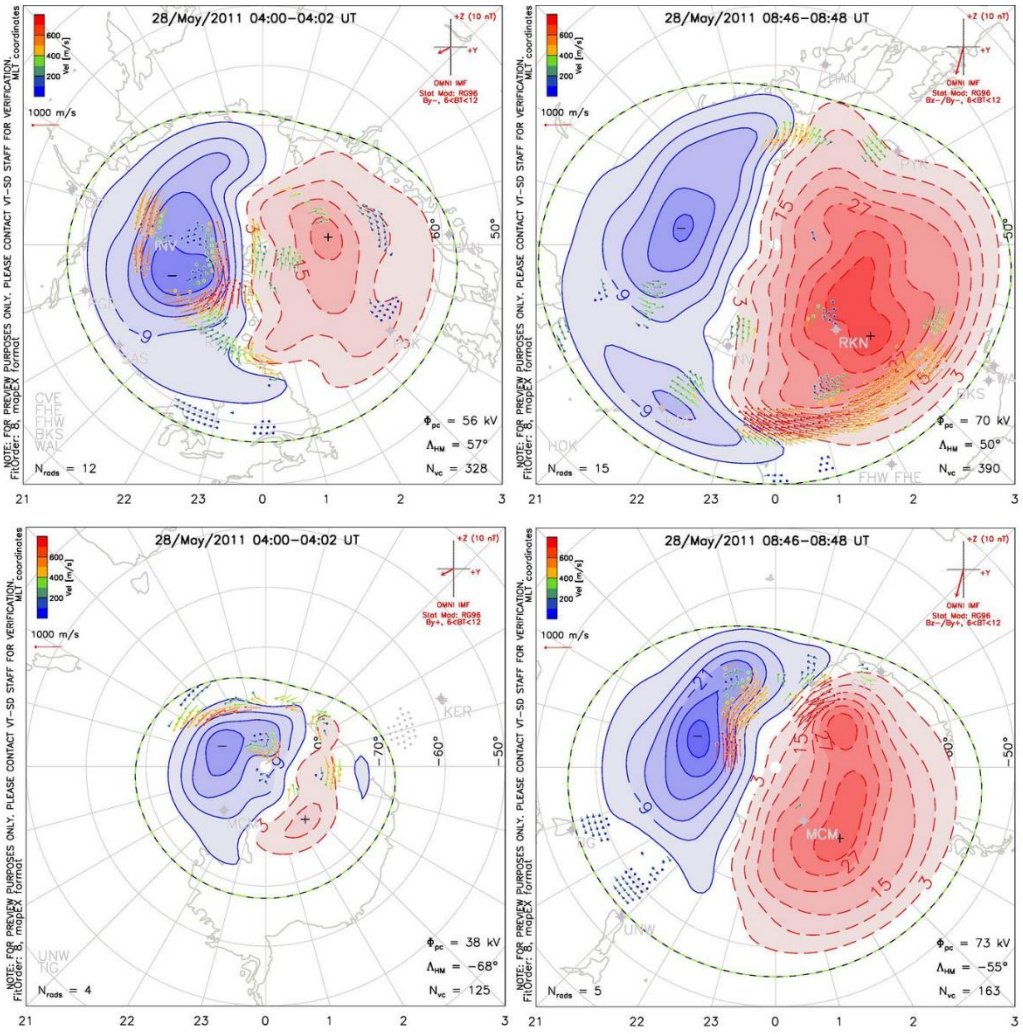

Figure 4.12. The latitudinal and longitudinal extensions of the DP2 current system as observed by SuperDARN radars during the 2011 event are presented. The variations in the DP2 just before the start of the expansion phase are given in the left panels and at the peak of the main phase in the right panels respectively, for the northern (upper panels) and southern (lower panels) hemispheres. Various label and notations have their usual meanings according to Cousins et al. (2013).

To substantiate this unique result and to strengthen the above qualitative explanation, the high latitude convection maps produced using the SuperDARN radars (Cousins et al. 2013) are used. Figure 4.12 provides a time-specific latitude-longitudinal map of the DP2 current

system associated with the time interval of the large positive enhancement in the H-complement in the latitude band of 56^o-63^o (Figure 4.6). For brevity, the observations from SuperDARN radars are shown in Figure 4.12 for the supersubstorm event of May 2011. The SuperDARN convection maps with a cadence of 10 minutes for all the supersubstorm durations are provided in the supporting information as SI-5 in Appendix B. The maps can also be viewed at the website of SuperDARN through "https://kauai.ccmc.gsfc.nasa.gov/instantrun/superdarn/" by selecting the date and time.

Figure 4.12 shows that the dominant cell of the DP2 current system (depicted by deep red or blue colors in the map), in general, extends up to ~75^o or at most ~70^o just before the expansion phase of the supersubstorm (which can be considered as the quiet time) in both the hemispheres. However, at the peak of the supersubstorm, the cell extends equatorward up to ~55^o and a series of the convection and velocity maps (given in SI-5) show that the latitude band of ~55^o-65^o marks the equatorward boundary of the DP2 current system. It is found that during these supersubstorm events, the equatorward expansion of the FACs happens which pervades up to the mid-latitude (~55^o) in both hemispheres. We have noted at the beginning of this section that at the same time, a poleward expansion of the effect of the compressional hydromagnetic wave and the resulting Chapman Ferraro current also happen. Thus, the resultant latitudinal signature is a composite effect of all these ionospheric and magnetospheric currents (Ganushkina et al. 2018; Ebihara 2019 and references therein) observed at different time intervals as observed in the H-component perturbations in all the cases.

The main phase of the geomagnetic storms begins with the formation of the ring current and the partial ring current in the inner magnetosphere (at about 5 R_E to 7 R_E) which produces two major different sets of depressions (Figure 4.7) in the H-component over low latitudes. With the subsequent decay in the ring current and partial ring current during the recovery phase (Gonzalez et al. 1994), the H-component perturbations revert to their quiet time signatures. The H-component variations in the close vicinity of the dip equator are also affected by the equatorial electrojet (EEJ) and are highly dependent upon the local time and the phase of the storm (Peymirat et al. 2000; Amory-Mazaudier et al. 2017; Dashora et al. 2019). Our results show that Huancayo (HUA) and Ascension Island (ASC) stations being very close to the dip equator, suffer from the largest variations (Figure 4.7) compared to other stations within the low latitude region. The longitudinal differences in the H-component responses (e.g. 2017 event) conform to the dominance of the local time effects in the resultant variations. The intensity of the low-latitude ionospheric currents depends upon an anisotropic distribution of the ionospheric conductivity and the electron density during the events. The equatorial and low

latitude ionosphere show large longitudinal differences owing to various factors like the UT start time of the storm and the difference in the topology of the geomagnetic field around the globe (Greer et al. 2017). Hajra et al. (2022) have recently performed a detailed analysis of the solar wind-magnetosphere-ionosphere coupling processes during the supersubstorm events (an extension of which is presented in this study). So, we understand that both the coupling scenario and the patterns in the H-component observations pose serious challenges to quantifying and understanding the interdependence of the competing factors and underlying mechanisms. Further investigations are needful in this context.

The perturbations in the D-component of the geomagnetic field are shown in the context of the impact of SSC (Figure 4.4) and the impact of the supersubstorms (Figure 4.8). Previous studies have shown that during an SSC event, a combination of ionospheric and field-aligned currents dominate the perturbations in the D-component (Kamide et al., 1981; Villante and Peirsanti, 2009 and references therein). Also, a latitudinal dependence of contributions from the magnetopause current (low to mid-latitudes) and Hall current (high latitudes) contributes majorly to the perturbations in the H-component. Using a chain of geomagnetic observatories, the latitudinal variations in the H, Y, and Z components of the geomagnetic field during SSC events are investigated by Rastogi (1999) and Rastogi et al. (2001). They found that the amplitude of the SSC in the H-component increases with decreasing latitude, while it shows a weak latitudinal dependence in the Y- and Z-components, which again show a strong-day-night asymmetry. Villante and Piersanti (2011) have studied the effect of sudden impulse events using simultaneous records from the geosynchronous satellites GOES 8 and GOES 11, as well as from the ground-based magnetometers located in Italy and Antarctica. They have established a global nature of SSC that affects the entire magnetosphere-ionosphere system with a delay in the onset time at different locations mostly owing to the solar wind-speed, and direction associated with varying strength and duration of the IMF-Bz.

The results of the present study on the effect of SSC on the D-component for the 2012 and 2017 events are shown in Figure 4.4, which depicts a weak latitudinal pattern. Positive and negative Gaussian-type patterns in the D-component over most of the stations resemble respectively eastward and westward geomagnetic perturbations. An ionospheric contribution to the D-component follows from increments/decrements in the storm time electric fields, which produce currents in a specific distribution of ionospheric conductivities and hence greatly depend upon the local time (longitude) (Rastogi 1999; Villante and Piersanti, 2011). Piersanti and Villante (2016) have estimated the individual contributions to the total current over a given latitude range and deciphered the contribution of the FACs and ionospheric

currents in response to the PI and MI during different geomagnetic storms. They have used the TS04 (Tsyganenko and Sitnov, 2005) model to estimate different magnetospheric currents and obtained the sum of the Chapman–Ferraro current and the tail current (as the DL field components) as the best representation of the magnetospheric response to the sudden impulse. Through this analysis, they estimated the ground component of the DL field along both the H and the D components. The residual DP fields are determined by subtracting the estimated DL_H and DL_D fields from ground magnetic observations (e.g. see Figure 39 of Piersanti et al. 2017). It is planned to carry out such an extensive analysis in the present study but this shall be part of a future paper. However, in this connection, our results indicate specifically that due to the presence of the DP2 type of polarization vortices over the high-latitudes, a rapid change in the Hall currents might have propagated equatorward, which is observed as Gaussian-like features in the D-component (Kikuchi et al. 2022 and references therein). Also notably, during the 2017 SSC event, larger amplitudes of the D-component perturbations over the low and mid-latitudes are observed in comparison to the 2012 event. So, we surmise that this result also provides a clue on how the amplitude of the SSC may relate to the amplitude of perturbations in the D-component.

In context to the supersubstorm duration, the present study finds that the perturbations in the D-components show different patterns compared to the H-component, with negligible day-night effect (Figure 4.8). A north-south hemispheric asymmetry in D-component variations is also observed along a latitude-specific pattern. In contrast to the H-component perturbations, the mid-latitude stations do not show sudden jumps and reversals in phase during supersubstorms. Notably, some similarities in the D and H component variations are also observed with respect to the amplitude and phase over high-latitude stations. The low-latitude stations exhibit irregular behavior without significant latitudinal or longitudinal effects. However, the amplitude of the perturbation in the D-component from individual stations shows a local time effect. Overall, the study highlights the complex and highly variable nature of ionospheric currents and their response to supersubstorms. In this context, Piersanti et al. (2020) have shown the direct impact of abrupt shifts in the direction of the IMF on the H and D components of the geomagnetic field at different latitudes. Similarly, Adhikari et al. (2017) have shown an explicit positive correlation of the FACs on the east-west (D) geomagnetic component at high latitudes and also a strong negative correlation with the H component over the auroral oval region. These works of literature find that the magnetic field fluctuations during substorms and magnetic storms exhibit a multifractal behavior, which indicates that the underlying physical processes are complex and nonlinear.

Following the results and analyses from the present study it is found that the relationship between the D-component and the H-component is complex and depends on many factors, including the location and time of day. In general, variations in the D-component tend to be more localized (due to ionospheric contribution) and smaller in magnitude than variations in the H-component, which can be affected by large-scale disturbances in the magnetosphere. During times of geomagnetic disturbances, especially during a supersubstorm, the D-component and the H-component may both show significant variations, but the patterns of variation may be different. Several cases are found in this study where the D-component shows positive undulations while the H-component shows a drastic fall. Overall, the D-component and the H-component are both important for understanding the behavior of the Earth's magnetic field, and their variations can provide insight into the underlying physical processes that drive geomagnetic activity. However, more and more case studies and relevant analyses are required to better understand the dynamics of the Earth's magnetosphere-ionosphere system and improve space weather forecasting.

We have also presented the variations in the dB/dt to depict the effect of the GICs and their latitudinal variations. Many previous studies have reported failures of electrical equipment at a given threshold value of the dB⁄dt (Kappenman, 2005; Gaunt and Coetzee, 2007; Kataoka and Ngwira, 2016). Even during the most intense storm of the solar cycle 24, the St. Patrick's Day storm of 17 March 2015, wherein the SYM-H dropped to -222 nT, the maximum dB⁄dt varied between 350-700 nT/min over different latitudes (Kozyreva et al., 2018). So, considering that the present study is concerned with moderate geomagnetic storms which are associated with supersubstorm events, our results of the peak dB⁄dt levels at ~900 nT/min over LYC (64.6^{o}N, 18.8^{o}E) station during the 2017 event and over CSY (-66.28^{o}N, 110.53^{o}E) station during the 2011 event are significant. Also, Dimmock et al. (2019) have shown a large impact of the GIC in the Gas pipelines during the same event in September 2017. Especially, a hemispheric asymmetry observed during the May 2011 event (Figure 4.9) in the occurrence of the peak dB/dt over comparative poleward latitudes (around 70^{o}-80^{o} S) is significant. Because of the local winter seasonal background with a large possibility of disparity in the magnetotail location and auroral onset location of the supersubstorm, a large impulsive response over a station could be possible. This fact is further strengthened by our results (Figure 4.10) which show that the respective peaks of the dB⁄dt recorded at different latitudes do not occur simultaneously, and sometimes they differ by a day or more and occasionally they occur much after the supersubstorm periods. While more investigations are required, this could be a plausible explanation for the observed asymmetry observed in the

present study. Therefore, the results of this study also bear importance towards the space weather impacts, which are likely to be a significant factor in power stability and other technological problems (Clilverd et al. 2018) during the supersubstorms.

4.4 Summary and conclusion

The solar cycle 24 has exhibited only four supersubstorms associated with three geomagnetic events during May 2011, March 2012, and September 2017. Detailed analyses of the geomagnetic responses of these events are performed using the H-component observations from the global network of magnetometer stations. The H-component variations are classified according to the observed latitude band-specific patterns in both hemispheres. A summary of the salient features of the new findings from this study is given below.

1. Response of the sudden storm commencement during the 2012 and 2017 events is found to produce three different types of latitudinal signatures (a) step-like preliminary positive impulse (PPI) followed by main impulse (MI) in the co-latitude band of 0^o-45^o (b) a Gaussian-kind of PPI followed by MI in the band of 45^o-65^o and, (c) a preliminary reverse impulse (PRI) followed by MI between 65^o-90^o.
2. A sequential impact of the hydromagnetic longitudinal shock wave and the FACs (and their manifestations as DP2 currents) associated with the SSC and the global magnetospheric convection is observed as the above-mentioned three different types of net responses in the H-component variations.
3. A strong north-south asymmetry in high latitude H-component variations is observed during the supersubstorms, which is attributed to the seasonal dependence of the growth and decay of ionospheric currents respectively in the summer and winter hemispheres.
4. A remarkable observation from the co-latitude band of ~55^o-65^o is found which shows a complete reversal of phase (i.e. global positive peak) of the H-component when the maximum depression from close-by latitude bands is observed along with peak depression in the SYM-H, SML, and AE indices. This response implicates a complex temporal composite of supersubstorm-associated magnetospheric processes, the magnetosphere-ionosphere coupling, and the associated currents in the magnetosphere-ionosphere system to produce a latitude-specific signature during each supersubstorm event. Such a phase reversal in a particular latitude band during supersubstorms is possibly being reported for the first time.

5. The low latitudes are found to respond in two completely different longitudinally dependent sets of signatures in the H-component depressions which align with local noon and midnight. The first set (longitude sector of 78^{o}-188^{o}E) shows sharp and steep, well-distinguished, simultaneous depressions, whereas, the second set (longitude sector of 284^{o}-354^{o} E) shows multiple, gradual, local depressions which are not so well-distinguished. Such drastic longitudinal differences (day versus night effect) during the main phases (due to the effect of ΔH_{DP2}) as well as during recovery phases (due to the effect of the ΔH_{Dynamo}) depict a dominant local time-dependent control of the perturbation electric fields over low latitudes.
6. Unlike the H-component, the variations in the D-component do not exhibit any specific latitudinal pattern owing to a complex and non-linear signature of the underlying ionospheric processes. Positive and negative Gaussian-like features in the D-component at the time of sudden commencements may represent the propagation of the ionospheric disturbances from mid-to-low latitudes.
7. A north-south asymmetry in the variations of the D-component during the supersubstorm periods is noted, however, the amplitude of such perturbations is found smaller than the ones observed in the H-component during the same intervals. The mid-latitude reversal as well as the local time-specific pattern in the low latitudes is found to be absent in the D-component variations during the supersubstorm periods.
8. The GIC threat represented by the dB/dt shows peaks during the supersubstorms with the highest magnitude (~900 nT/min) observed in the latitude band of 60^{o}-75^{o} and secondary peaks over the dip equatorial regions.
9. Remarkably, the peak occurrences of dB/dt are not simultaneous and are also prominently found after the supersubstorm periods over the mid and high latitudes. These results indicate the susceptibility of a global GIC threat beyond the supersubstorm periods, which require further investigations.

Thus, in Chapters 3 and 4, we conducted thorough and robust analyses to examine the significant effects of Supersubstorms during solar cycle 24 on the interrelated systems of solar wind-magnetosphere-ionosphere and their large-scale coupling. In the next chapter, we will focus on analyzing specific coupling processes at the kinetic scale. **The work carried out in this Chapter has been published as a research article by Hajra et al. (2023a) in Space Weather Journal.**

CHAPTER 5

SW-M Coupling at the Kinetic Electron Scales During a Geomagnetic Storm

"An unseen electrical generator, more powerful than any man-made generator, exists in space near Earth."

-John G. Lyon

5.1 Introduction:

The geomagnetic storms and substorms are the manifestation of solar wind-magnetosphere-ionosphere coupling and energy transfer. The coupling processes such as magnetic reconnection (Dungey, 1961; Yamada et al. 2010; Gonzalez and Parker, 2016), viscous interaction (Axford and Hines 1961; Tsurutani and Gonzalez 1995); cross-field diffusion (Tsurutani et al. 1981; Khotyaintsev et al., 2019) and the pressure fluctuation of the solar wind (Song and Russel 1994) play a significant role during the storms. Magnetic reconnection is one of the dominant mechanisms by which the interaction between the solar wind and the magnetosphere of the Earth happens (Torbert et al. 2018). Though it begins with processes at very small ion and electron kinetic scales in a region characterized by X-line, it can influence large scales processes (Fu et al. 2015a, 2015b; Hesse and Cassak, 2020). The dayside reconnection happens at the magnetopause, whereas the nightside reconnection happens in the magnetotail (Baumjohann and Treumann 2012; Petrukovich et al. 2014; Torbert et al. 2018). For the nightside reconnection and transfer, the plasma sheet boundary layer (PSBL) which is the region between the plasma sheet and the tail lobe, is considered to be an important region. During these dayside and nightside coupling processes, a huge amount of mass, momentum, and energy are transported to the magnetosphere-ionosphere system from the reconnection site (Chen et al. 2008; Burch and Phan 2016; Fu et al. 2016, 2019). These generate a complex interplay of currents and electric fields in different parts of the magnetosphere and ionosphere which eventually generate large-scale magnetic field perturbations and change the dynamics of the magnetosphere-ionosphere system (Amory-Mazaudier et al. 2017, Ganushkina et al. 2018; Hajra et al. 2023). The transfer of energy from the reconnection regions to the ionosphere is supported by the field-aligned currents (FACs) (Cheng et al. 2016; Chen et al. 2019) and the electric fields (Burch et al. 2016). This may also exhibit energetic particle precipitation and Kinetic Alfven waves. Since, FACs play a significant role in the solar wind-magnetosphere-ionosphere coupling processes (Milan et al., 2017; Carter et al. 2018 and references therein), the understanding of the origin and the carriers of FAC and their relation with different geomagnetic processes during storms and substorms is important. Also, to understand the energy dynamics of the reconnection regions, it is important to estimate the power (rate of change of energy) transfer. The power can be estimated by the multiplication of vector fields representing current and total electric field contributions to the generalized Ohm's law (Burch et al 2016). Thus, the two most important and variable quantities, the FACs and the electric fields must be estimated for understanding the kinetics of the coupling and its effects on the other connected regions in the solar-wind-magnetosphere-ionosphere system.

The accurate characterization of events and components of both ideal and non-ideal electric fields during the flow of a significant amount of FACs requires precise measurements that can only be obtained through the strategic deployment of multiple magnetospheric satellites. It is significant to note that the Cluster and THEMIS have been providing these measurements at larger scales (ranging between about 200-10000 km and second to a minute) (Angelopoulos et al. 2008; Haaland et al. 2019; Escoubet et al. 2021), whereas, the MMS (magnetospheric multi-scale) mission covers the electron diffusion region (EDR) in kinetic electron scale (≤ 10 km and ≤0.01 sec) in both the magnetopause and magnetotail regions (Burch et al. 2016; Torbert et al. 2018). These missions have provided a wealth of knowledge including discoveries in the the domain of physics of space weather (Luhr et al. 2017). Specifically, during the first phase of the MMS mission, it made several EDR crossings between March 2015 and December 2016. Thus, the MMS measurements in this phase have facilitated many path-breaking investigations on the reconnection processes (Torbert et al. 2016; Anderson et al. 2016; Burch and Phan 2016; Hesse et al. 2016; Torbert et al. 2018; Webster et al., 2018). However, it is found that so far, only a few studies have explored some of the phenomena like the dipolarization events (Fu et al. 2019, 2021; Zhao et al. 2019; Yu et al. 2022) and reconnection processes using MMS observations during geomagnetic storms (Reiff et al. 2016, Baker et al. 2016; Matsui et al. 2016; Le et al. 2016). We examined data sets from the above-mentioned satellite missions to study different geomagnetic storms in the post-MMS era and thus identified a possibility of having simultaneous measurements from the magnetopause, the magnetotail, and outside regions.

One important task in reconnection studies is tracing the EDR crossings of the spacecrafts. During magnetic reconnection in space plasma, the electrons can be significantly deviated from the expected Larmor orbits, resulting in non-gyrotropic motion (Genestreti et al., 2018). This motion can lead to the appearance of agyrotropy in the pressure tensor, which describes the distribution of particles in plasma and their pressure on the surrounding environment (Scudder et al., 2012, 2015; Che et al., 2018). Accurately quantifying the degree of agyrotropy in pressure tensor is crucial for tracing the Electron Diffusion Region (EDR) during magnetic reconnection. Various methods for measuring agyrotropy have been proposed, including anisotropy and eigenvalue analysis of the pressure tensor. Previous studies in the literature have proposed several measures like $\sqrt{Q}$, D_{ng}, $\frac{A\phi_e}{2}$ and $AG^{\frac{1}{3}}$ to detect probable EDRs (Scudder et al., 2012, 2015; Aunai et al., 2013; Che et al., 2018). Especially, $AG^{\frac{1}{3}}$ traces the EDR and

separatrices in both the Harris and force-free current sheets (Che et al., 2018).In our preliminary analysis of a geomagnetic storm between 31 December 2015 and 1 January 2016, we found that different spacecraft were so uniquely positioned that there could be crossings leading to the study of probable reconnection regions in the magnetosphere. Hence, this study aims to make a detailed and comparative analysis by using simultaneous observations from a unique spacing of MMS, Cluster, and THEMIS spacecraft during the above geomagnetic storm. It is found that particularly, during the main phase of this storm (lasting for about 12 hours), the MMS and the Cluster spacecraft have crossed the magnetopause twice and once, respectively (according to the T89 model). These spacecrafts have provided the needed measurements to investigate the regions where probably magnetic reconnection happened. Also, the THEMIS-A spacecraft remained in the magnetotail and the THEMIS-C remained in the lunar orbit outside the magnetosphere during the main phase of the storm. This unique configuration of spacecraft provided a rare opportunity to investigate the differences and similarities between these two regions. A review of existing literature on the dynamics and energetics of the reconnection in magnetopause and magnetotail regions is performed and the storm time observations from the magnetopause and magnetotail regions covering both the small and large spatio-temporal scales (Wang et al. 2020) are investigated. We have analyzed various plasma and field parameters and used our findings to illustrate a comparative picture of the magnetopause and magnetotail. Finally, we also examined the propagation of the storm through various parts of the magnetosphere to provide a more comprehensive understanding of the event. The primary objective of our study is to identify the primary carriers of the field-aligned currents (FACs), as well as the various ideal and non-ideal terms of the electric field in both the magnetopause and magnetotail regions. Section 2 details the methods we employed to calculate the currents and electric fields, as well as the in-situ instruments we used to estimate the plasma (kinetic properties like velocity, temperature, and pressure), and the field (electric and magnetic) characteristics. The results and the associated key findings of our study are presented in section 3. We will then provide a brief discussion of these results and conclude in sections 4 and 5. A summary of this study is provided at the end.

5.2 Observations and methods

Multi-satellite observations are utilized for a period from 31 December 2015 to 1 January 2016 with an emphasis on short-duration events of satellite crossings at magnetopause and magnetotail during the main phase of the storm. Extensive efforts have been made in the previous studies to obtain the 2-dimensional or 3-dimensional visualization of the

magnetospheric structures in the plasma kinetic and field parameters from one or more spacecraft (Dunlop et al., 2002; Dunlop et al., 2021). To achieve the aimed objective, measurements from MMS, Cluster, and THEMIS missions are analyzed. Particularly, the MMS mission provides unprecedented high-resolution observations at the kinetic electron and ion scales. The following Table 5.1 gives satellite-parameter pairs from different satellites and refers to a lead study that has described the method of estimation of the parameter from the instrument onboard.

Table 5.1: instruments on-board satellites providing different plasma and field parameters

Satellite	Electric field	Magnetic field	Ion parameters	Electron parameters
MMS	EDP (L- 2016)	FGM (T-2016)	FPI (P-2016)	FPI (P-2016)
Cluster	EFW (E-2001)	FGM (E-2001)	CIS (Re-1997)	PEACE (Ri-1997)
THEMIS-A, C	EFI (B-2008)	FGM (A-2008)	ESA (M-2008)	ESA (M-2008)

Extensions of the acronyms used are [EDI: Electron drift instrument; EFW: Electric field and waves; EFI: Electron field instrument; FGM: Fluxgate magnetometer; FPI: Fast plasma investigation; CIS: Cluster ion spectrometry; PEACE: Plasma electron and current experiment; ESA: Electrostatic analyzer] and [L-2016: Lindqvist et al. 2016; T-2016: Torbert et al. 2016; P-2016: Pollock et al. 2016; E-2001:Escoubet et al 2001; Re-1997: Reme et al. 1997; Ri-1997: Riedler et al. 1997; B-2008: Bonnell et al. 2008; A-2008: Auster et al. 2008; M-2008: McFadden et al 2008].

The following subsections provide details of the different measurements and derivation methods to estimate FACs and other field parameters.

5.2.1 Estimation of field-aligned currents

The FACs can be calculated using the Curlometer method (Dunlop et al., 2002) and the plasma method (Cheng et al. 2016). Considering some limitations of the Curlometer method (Dunlop et al., 2021), the FACs from the MMS and the Cluster observations (Fu et al., 2012) are estimated from both methods. However, FACs from the THEMIS-C observations can only be estimated by the plasma method due availability of measurement from a single spacecraft. It shall be noted that both the MMS and the Cluster missions have an array of 4 satellites, configured in a tetrahedron flying formation in their respective orbits. The Curlometer method uses the geometry of the face of the tetrahedron to apply Ampere's law and derives the current density normal to the face (see Dunlop et al., 2021 and references therein). This technique has

been widely used in many prior studies using both the Cluster and the MMS observations (Shi et al. 2010; Phan et al. 2016; Cheng et al. 2016; Nakamura et al. 2018) to calculate the FACs. To calculate the FACs, both the Curlometer (equation 12 of Chapter 2) and plasma methods (equation 13 of Chapter 2) are used and compared. See details in Chapter 2.5.

Since the sample rate of different instruments on a spacecraft is different, one needs to average data with higher rates to match the data with lower rates. For MMS, the sample rate of the magnetic field measured by FGM is ~12.5 Hz and that of ion and electron parameters measured by FPI in Fast survey mode is ~ 0.22 Hz (4.5-sec sample rate). The MMS data in the burst mode for this event was not available. Also, the data sets from other spacecrafts are available at different sample rates, even slower than the Fast data from the FPI of MMS. Hence, the FACs estimated using the Curlometer method are averaged to have the same time base as that obtained from the fast-mode plasma data from FPI. However, for THEMIS, the sample rates of the magnetic field obtained from FGM and electron parameters obtained from ESA are the same i.e. ~0.346 Hz. For ion parameters obtained from ESA, the frequency is very small i.e. ~0.01083 Hz. Hence for THEMIS, too, while calculating FAC, FGM, and ESA (electron) parameters are averaged to have the same time base as that obtained from the fast mode plasma data from ESA (ion). But, for Cluster, the sample rates of the field and plasma (both ion and electron) parameters are the same (~0.235 Hz).

5.2.2 Estimation of electric field components and power

The estimation of ideal, non-ideal electric field components and power is performed using equations 14-17 of Chapter 2.5.2.2. (See Chapter 2.5 for details).

5.2.3 Spacecraft orbits in geospace

The respective locations of the satellites are obtained from the space physics data facility of NASA (National Aviation and Space Administration) at 'https://sscweb.gsfc.nasa.gov/cgi-bin/Locator_graphics.cgi' and given in Figure 5.1. Figure 5.1(a) illustrates the trajectory of MMS-1, Cluster-4, THEMIS-A, and THEMIS-C for a month from 5 December 2015 to 5 January 2016. The period for the MMS-1, Cluster-4 and, THEMIS-A to complete one revolution around the earth is found to be ~26 hours, 54.31 hours and, 31.2 hours, respectively. The time interval between 2300 UT on 31 December 2015 and 1300 UT on 1 January 2016 is considered separately (termed as 'storm-time' in the figure) and highlighted with different colors in the respective orbits. During the geomagnetic storm, the MMS and Cluster satellites were on the sunward side and hence faced solar wind plasma

pressure, whereas, THEMIS-A was on the anti-sunward side and THEMIS-C was on the axis parallel to the dawn-dusk line.

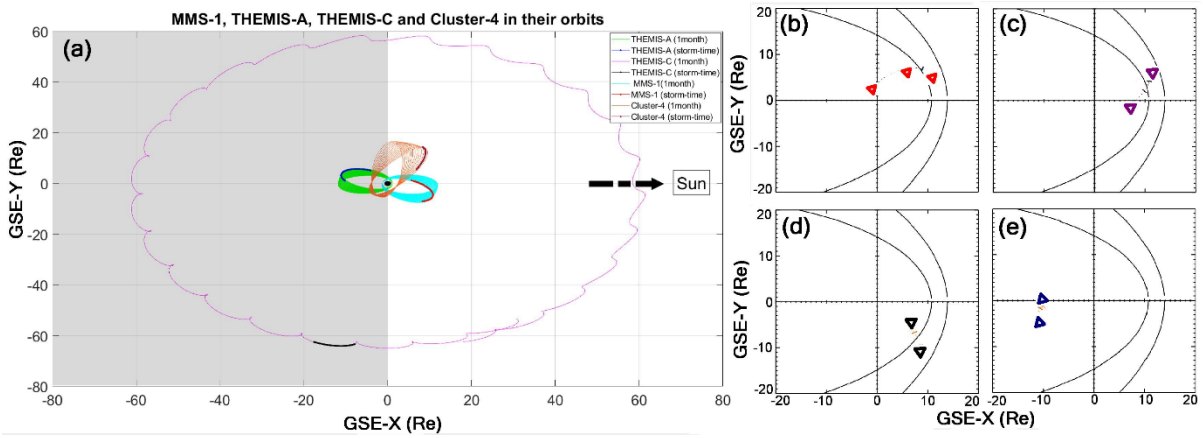

Figure 5.1. (a) Orbits of the MMS-1, Cluster-4, THEMIS-C, and THEMIS-A are shown for a month from 5 December 2015 to 5 January 2016 as given in the legend. The arcs of the orbits during the storm from 23:00 UT on 31 December 2015 to 13:00 UT on 1 January 2016 are highlighted by thick lines. Earth (black sphere) is located at the center of the GSE reference frame. The Sun is located towards positive abscissa as indicated by an arrow. The respective magnetopause crossing of the MMS-1 is given in (b) and (c) and of the Cluster in (d). The orbital locations of THEMIS-A in the magnetotail are given in (e). Two black parabolic curves in panels (b-e) show the location of the bow shock and magnetopause which cross the equatorial plane in an anti-sunward direction.

The crossings of the magnetopause (Figure 5.1 b-d) and magnetotail (Figure 5.1e) are deduced by the NASA-SSC web data set, which uses the IGRF (International Geomagnetic Reference Field) (Alken et al., 2021) and Tsyganenko-89C (Tsyganenko et al. 1989) models for this purpose. The crossings are assumed to be in the vicinity of the probable reconnection regions. Our analysis (in a later section) shows that these regions bear some inferential, circumstantial characteristics of the reconnection sites. It is found that during the main phase of the storm period, the magnetopause crossings of the MMS happened at 2321 UT on 31 December 2015 and at 0740 UT on 1 January 2016. The Cluster spacecraft met the dayside magnetopause at 1152 UT on 1 January 2016. THEMIS-A crossed the PSBL in nightside magnetotail during 1126 UT-1217 UT on 1 January 2016 and possibly the spacecraft has encountered PSBL. The identification of the PSBL region can be done through plasma beta value, which remains between 0.01 and 1 in PSBL (Chen et al. 2019 and reference therein;

Baumjohann et al., 1988; Cheng et al., 2016; Walsh et al., 2011). Also, the PSBL typically has a clear signature such as the sudden density drop or sudden change of magnetic fields, and can be identified with circumstantial evidence. In a nutshell, during the storm time, the MMS and the Cluster are found in the dayside magnetosphere; the THEMIS-A is found in the nightside magnetotail, and THEMIS-C is found in the night side in the lunar orbit i.e. in the interplanetary space.

5.3. Results

It is interesting to note that this paper possibly for the first time reports the magnetospheric observations during the geomagnetic storm of 31 December 2015-1 January 2016. So, a quantitative analysis of the solar wind parameters, the plasma energetics at the magnetopause and magnetotail, ideal and non-ideal electric fields, carriers of FACs, and other parameters is performed. The variations of the different parameters in the inner magnetosphere, magnetosheath, and plasma sheet are presented for some selective intervals during the storm. Additionally, both the large and small (kinetic electron and ion scale MMS data) scale observations are used whenever available from the respective satellites for a region of interest. The following subsections provide the main results of this study divided into different crossings of the satellites with magnetopause and magnetotail during the storm.

5.3.1 Solar wind conditions and geomagnetic perturbations

The observations of the solar wind from ACE (advanced composition explorer) located at L1-point are provided through OMNIWeb at a cadence of 1 min (see Papitashvili & King, 2020). This data set also provides geomagnetic indices like SYM-H (Iyemori and Rao 1996), the PC (polar cap) indices (Troshichev, 2006), and the AE (auroral electrojet) index (Nose et al. 2015). A sudden impulse is simultaneously observed in solar wind velocity, temperature, ram pressure, and density at 0100 UT (vertical dashed line in Fig. 2). A short-lived sudden rise in the z-component of the interplanetary magnetic field (IMF-Bz) is observed at the same time. However, the IMF-Bz fluctuates between north and south during 0100-1040 UT, and the high-density (15 to 27 cm^{-3}), high temperature ($1x10^5$ to 4×10^5K) plasma parcels are observed to impinge at a velocity of about 430 to 460 km/s. As a result, a simultaneous rise in the PCN index, AE, and the epsilon parameter (Hajra et al., 2022) is observed during ~0740-1040 UT. The IMF-Bz then remains southward between ~1050-1410 UT with a simultaneous dip in the SYM-H index termed as the first sub-main phase of the geomagnetic storm; associated with a larger rise in AE, PCN index, and the epsilon parameter. The SYM-H index

shows a shallow recovery during ~1410-1850 UT which is under the effect of the northward excursions in the IMF-Bz in this interval. The second sub-main phase is found to begin at ~1900 UT (dip in the SYM-H index) associated with a sudden southward turning of IMF-Bz on 31 December 2015. But, intriguingly the ram pressure, temperature, and density of the solar wind plasma are found to decrease to very low levels during this interval.

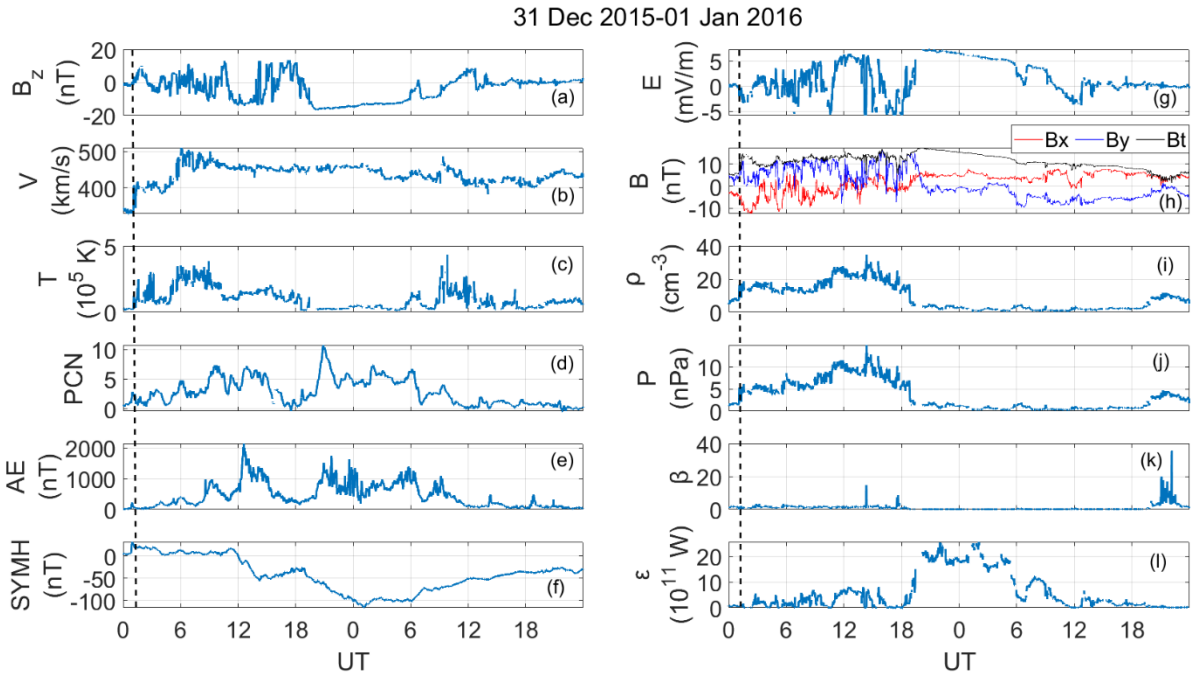

Figure 5.2. Panels (a), (b), (c), (g), (h), (i), and (j) show variations in the solar wind plasma parameters IMF-Bz, speed (V), temperature (T), electric field (E), magnetic field (B), plasma density (ρ) and ram pressure (P). Panels (d), (e), and (f) show PCN, AE, and SYM-H indices respectively on 31 December 2015 and 1 January 2016. Panel (k) depicts plasma beta (β) and panel (l) gives the epsilon parameter (ϵ).

The SYM-H index drops to the minimum value of ~113 nT at about ~0118 UT on 1 January 2016 and begins to gradually recover thereafter. However, the IMF-Bz remains southward till 1000 UT on 1 January 2016, albeit, a short duration northward excursion is seen between 06-07 UT, which is also reflected as a faster rise in the SYM-H index. The AE and PCN indices show larger and intermittent peaks between ~1900 UT on 31 December 2015 and 0600 UT on 1 January 2016. The two sub-phases of the main phase of the storm are well reflected in the variations of the epsilon parameter (coupling parameter). We find a sudden large increase in the epsilon parameter from ~1800 UT indicating a huge entry of solar energy inside the earth's magnetosphere, which sustained up to ~1100 UT on 1 January 2016. The

coupling strengthened in the above-mentioned interval because the IMF-Bz is found to remain southward for ~15 hours till ~1005 UT on 1 January 2016. The long-lasting southward IMF-Bz (even when the SYM-H index shows a recovery) is not very common to observe and has sources either in the magnetic cloud associated with the coronal mass ejection or the Alfven waves (Zhang and Moldwin 2014).

The plasma beta value is found to vary at low levels (less than ~3) throughout the storm, indicating the dominance of plasma pressure ($P_{plasma} = nk_BT$) over magnetic pressure ($P_{mag} = \frac{B^2}{2\mu}$), except for a few spikes. The epsilon parameter representing the probable energy input in the magnetosphere per unit of time raises to 5×10^6 watts during the main phase of the storm. So, the storm is found to be an intense storm with two sub-main phases, a stable long-duration southward IMF-Bz during both the main and recovery phases, and a relatively long recovery phase unlinked with IMF-Bz.

5.3.2 MMS-magnetopause encounter at 2310-2330 UT on 31 December 2015

The MMS is found to be located in the dayside magnetosheath during the first few hours of 31 December 2015 according to the Tsyganenko-89C and IGRF models. The MMS spacecraft then arrived at the magnetosphere after crossing the magnetopause, before the storm at ~0801 UT, and then completed a revolution passing subsequently through the dayside plasmasphere, nightside plasmasphere, dayside plasmasphere, dayside magnetosphere, and dayside magnetosheath on 31 December. The observed features from the MMS show some distinctive recognizable patterns during a few events in most of the plasma and field properties and also in the energy spectrograms. Two such events are selected considering a 20-minute interval of the MMS flight each. During the main phase of the storm, the MMS moved from the magnetosphere to the magnetosheath at 2318 UT and a possible MMS-magnetopause encounter is estimated at ~2321 UT on 31 December 2015 as referred from the above-mentioned data set and models.

To validate this, and to trace whether MMS has encountered a reconnection EDR, different measures of agyrotropy are estimated. The burst data set from FGM, EDP, and FPI of MMS are used to construct the pressure tensor. Then, different measures of agyrotropy of pressure tensor are estimated to deduce the agyrotropy in the motion of the electrons during the magnetopause crossing.

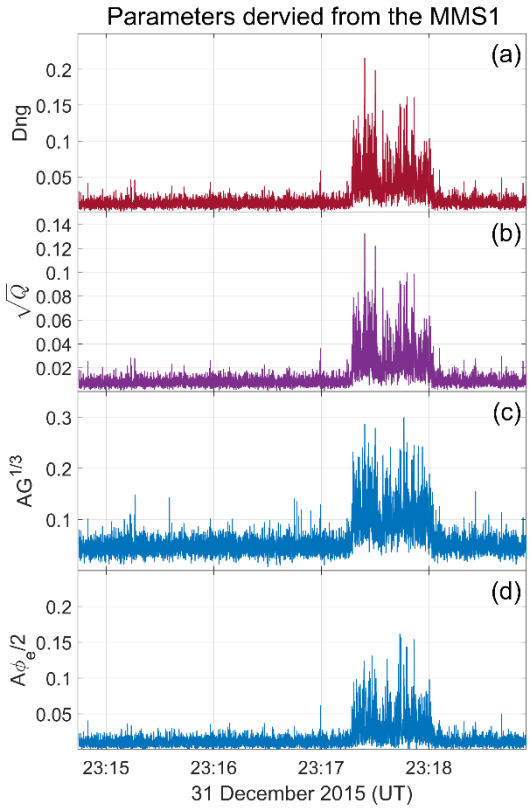

Figure 5.3: Variations of different parameters derived using observations from the MMS1 spacecraft during 23:14:45-23:18:55 on 31 December 2015. Panels show (a) D_{ng}, (b) $\sqrt{Q}$, (c) $AG^{\frac{1}{3}}$ and (d) $\frac{A\phi_e}{2}$ from top to bottom, respectively. Similar variations are noted in the case of MMS-2, 3, and 4, but are not shown here for brevity.

Figure 5.3 shows a sudden surge in all of the four parameters- D_{ng}, $\sqrt{Q}$, $AG^{\frac{1}{3}}$, and $\frac{A\phi_e}{2}$ at around 23:17:15 UT, which continues for ~49 seconds to revert to their previous values at 23:18:04 UT. The deviation of D_{ng} from the normal value (Figure 5.3a) implies aberration from the local, energetically equivalent, gyrotropic distribution. This eventually indicates the non-gyrotropy associated with the 3-D distribution, pointing to a possible encounter of MMS with an EDR (Aunai et al., 2013). In addition, the value of $\sqrt{Q}$ (Figure 5.3b) becomes ~ 0.1 several times, which indicates the presence of electron agyrotropies in that region (Genestreti et al., 2018). The variations of $\sqrt{Q}$ between 23:17:15 UT and 23:18:04 UT directly imply that MMS spacecrafts probably encountered a reconnection EDR (Swisdak, 2016). $AG^{\frac{1}{3}}$ and $\frac{A\phi_e}{2}$, which are constructed from the field-aligned transformation of the electron pressure tensor (Che et al., 2018), abruptly diverge from their typical value indicating MMS possibly come across an EDR. Based on the variations observed in all four parameters, it can be inferred that MMS

probably encountered a reconnection event with an outflow jet between 23:17:15- 23:18:04 on 31 December 2015.

A sudden spike in all of the kinetic parameters of the plasma is observed at 2318 UT (see Figure 5.4) lasting for about 3 minutes before the estimated MMS-magnetopause crossing at ~2321 UT. Since the observations from the four MMS satellites (probes) are found to be almost similar, we use the observations from the MMS-1. Figure 5.4 shows an obvious double-toothed rise in the ambient magnetic and electric fields, the velocity of electron and ion jets, and the parallel and perpendicular temperatures as observed during 2317-2318 UT. All three components of the magnetic field (B_x, B_y, and B_z) experience positive spikes with considerable magnitude during the encounter (Figure 5.4a). However, the y-component of the ambient electric field (E_y) shows a relatively larger excursion demonstrating the arrival of the solar wind plasma in the magnetosphere. The other two components, the E_x and E_z show negative perturbations.

A significant earthward flow of both the ions and electrons is observed during this interval depicted by the x-component of the respective velocities (red curves in 4c and 4d). A significant peak in both the parallel and perpendicular components of the ion and electron temperatures is observed (Figures 5.4e and 5.4f), respectively. Despite traversing through a possible reconnection region, all the values of temperatures are of low magnitude which is very intriguing. Interestingly, a gradual decrease in the ion and electron density is observed during the encounter (Figure 5.4g), whereas, the plasma beta value shows a typical positive spike during this encounter (Figure 5.4h). The plasma beta value ranges from 0.01-0.06, which indicates magnetic pressure is about two orders more than the plasma pressure inside the region. The very low plasma beta value indicates that the magnetic field is much stronger than the thermal pressure of the plasma. This also suggests that the magnetic field is the primary factor influencing the movement and behaviour of the plasma in this area. This very low value of plasma beta also indicates that MMS1 might have encountered a magnetic reconnection region. This is because magnetic reconnection involves the conversion of magnetic energy into kinetic energy of the plasma, and for this to occur efficiently, the magnetic field must be strong compared to the thermal pressure of the plasma. The right panels of Figure 5.4 demonstrate the energy-flux spectrogram of the electrons and ions during this 20-minute interval. The energy flux spectrogram presented here is a two-dimensional plot that shows the energy of charged particles on the y-axis and time on the x-axis. The colour of each pixel represents the flux of particles with a certain energy during a specific time interval. To get a detailed picture of the energy distribution of charged particles in the plasma, the energy flux spectrogram is plotted.

In the context of the energy flux spectrograms presented here, the term "flux" refers to the number of particles passing through a unit area per unit time. The flux of charged particles can be measured at different energies, and the energy flux spectrogram eventually provides a plot of the flux of particles as a function of their energy and time.

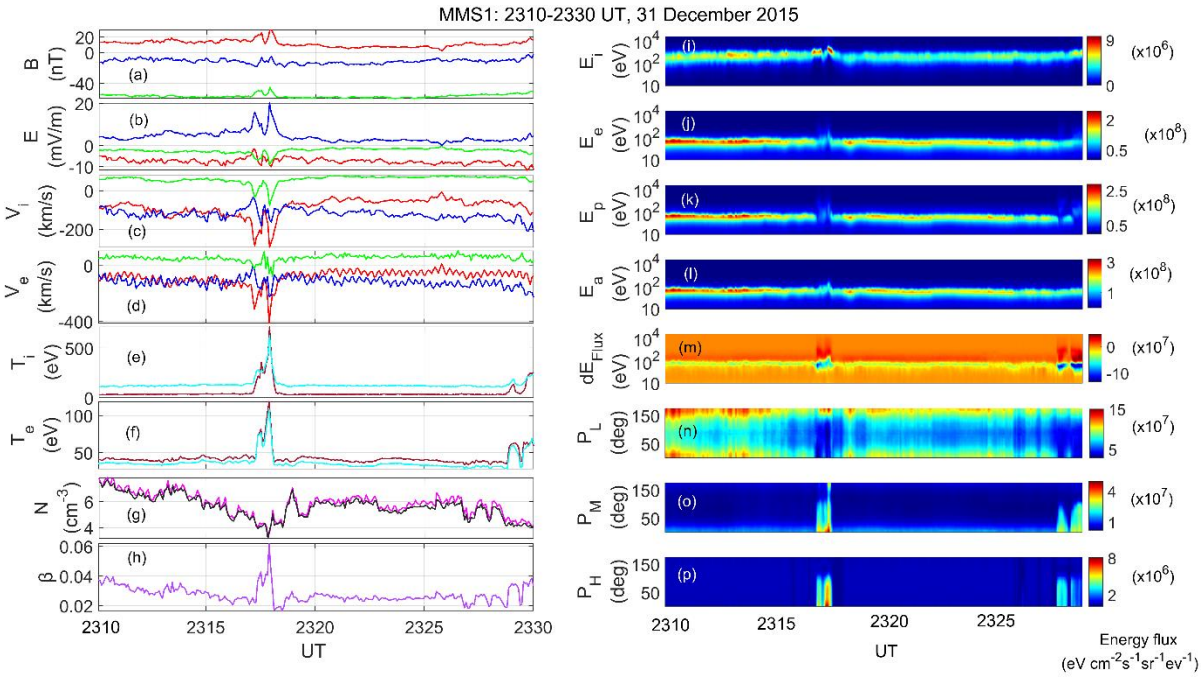

Figure 5.4. Variations in the different ambient measurements from the MMS-1 spacecraft are given for a 20-minute duration between 2310-2330 UT on 31 December 2015. Left panels a-d show the variations in the ambient magnetic field (B), electric field (E), the bulk velocity of ions (V_i), and bulk velocity of electrons (V_e) with the x, y, and z components in red, blue and green, respectively. Panels e-f show the parallel (brown curve) and perpendicular (sky blue curve) components of the ion and electron temperatures (T_i and T_e), respectively. Panel g shows the ion (magenta) and electron (black) density of the plasma (N) and panel h shows plasma beta (β). Right panels give the energy-time spectrogram of different components. Panels i-m show the spectrograms for ions (E_i) (omnidirectional), electrons (E_e) (omnidirectional), parallel electrons (E_p), anti-parallel electrons (E_a), and net energy flux (dE_{FLUX}), respectively. Panels n-p show the pitch angle distribution of the energy flux for the low-energy electrons (P_L), mid-energy electrons (P_M), and high-energy electrons (P_H), respectively.

The omnidirectional energy spectrums (Figures 5.4i and 5.4j) show that the flux (eV cm^{-2} s^{-1} sr^{-1} eV^{-1}) of the ions and electrons respectively remains in the order of 10^6 and 10^8.

Hence, it can be inferred that the electron population is more abundant than the ion population. Eventually, electrons are the main carriers of the current during this period, which corroborates the findings of Cheng et al. (2016) and Chen et al. (2019). The energy flux of the electrons for the parallel (E_p) and antiparallel (E_a) and the difference ($dE_{FLUX}=E_p-E_a$) are respectively given in Figures 5.4k-5.4m. The difference between the two fluxes yields a net flux along the field line (Nakamura et al., 2016; Varsani et al., 2017) and in this context, the dE_{Flux} is found to be mostly negative during the interval of ~2317-2318 UT; which demonstrates that the antiparallel electrons carry most of the current during this ~1-minute interval. The pitch angle distributions of the electrons with low (0-0.2 keV), mid (0.2-2 keV), and high (2-30 keV) energies at pitch-angle bins of 6 degrees are given in Figures 5.4n- 5.4p. The magnitude of current carried by the low-energy electrons is mostly found to remain lower at pitch angles between ~40^o-130^o, which decrease further during the ~2315-2318 UT and after ~2325 UT. However, a reverse response is observed for the current carried by the mid and high-energy electrons, which show a very sharp peak during ~2317-2318 UT at almost all pitch angles. Comparing the absolute values of the energy flux among the three types of electron populations, it is obvious that the low-energy electrons (most possibly the thermal electrons) still dominate the constitution of total current during this event, while they show a decrement noted above.

It shall also be noted, however, that the energy flux enhancement associated with the mid and high-energy electrons corresponds to a decrement in the low-energy electrons. So, the former contributes considerably to the electron population only during the event corresponding to MMS-magnetopause encounter with a transfer of energy from low to high values. In a nutshell, it can be inferred from our analysis that the mid-to-high energy electron populations form a significant earthward flow anti-parallel to the magnetic field and become major carriers of currents during this small period (~few seconds up to one minute).

The inferential and circumstantial signatures detailed above suggest a high probability of crossing a reconnection EDR by the MMS. Especially, the MMS observations during ~2315-2318 UT exhibit certainty of a reconnection event with an outflow jet. The components of the electric field contributing to the generalized Ohm's law are shown in Figure 5.5 (a-e). The components of the electric field terms exhibit similar double-toothed excursions for about a minute during 2317-2318 UT in E_h and E_a as observed in the ambient electric field E in Figure 5.4. On the contrary, the E_v and E_p exhibit positive excursions in the X and Z directions and negative excursions in the Y direction. However, eventually, the resultant electric field (E_t) shows negative excursion in X and Z components and positive excursion in Y-component

which is possibly due to the dominant contribution from ambient electric field E and the Hall term, E_h. In almost all cases, multiple saw-toothed spikes in the curves are observed.

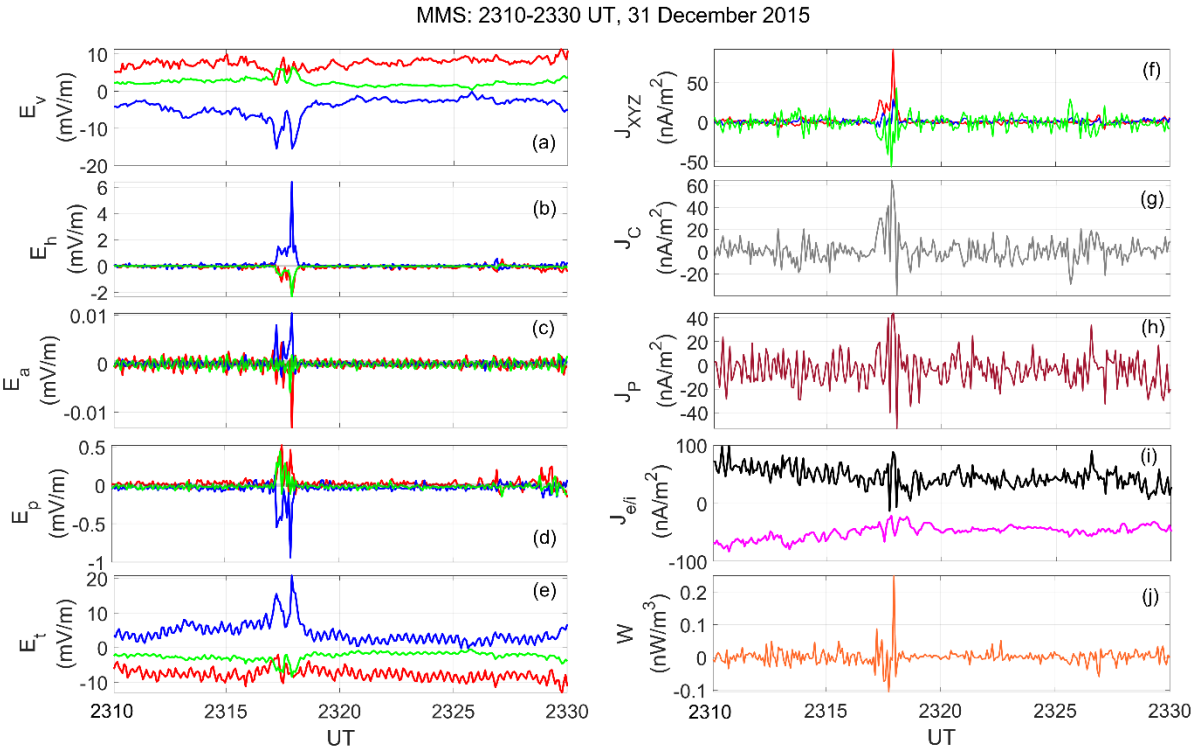

Figure 5.5. Variations in the estimated electric field and current components from the MMS-1 spacecraft are given for a 20-minute duration between 2310-2330 UT on 31 December 2015. Panels (a), (b), (c), (d), and (e) give variations of the second term of the ideal (E_v), Hall (E_h), inertial (E_a), pressure gradient (E_p) and total electric field (E_t), respectively. The X, Y, and Z components are shown respectively by red, blue, and green curves. Panel (f) shows components of total current, and panels (g) and (h) provide variations in the FAC estimated by the Curlometer method, and by the plasma method, respectively. Panel (i) gives variations in the FAC carried by electrons (black) and ions (magenta) from the Curlometer method and panel (j) provides power (W), representing the amount of electromagnetic energy density converted into plasma energy density.

Among the non-ideal terms of the electric field, the Hall electric field (E_h, Figure 5.5b) exhibits significant enhancement with higher amplitude compared to the low amplitude increase in the inertial (E_a, Figure 5.5c) and pressure divergence (E_p, Figure 5.5d) terms. It is to be noted that the Hall electric field is known to exhibit a substantial magnitude at the ion inertial scale, not solely within the confines of the reconnection diffusion region. Even at ion-scale structures like the depolarization front, the Hall electric field has been observed to be remarkably high (Fu et al. 2012). However, the variations of different parameters presented in

Figure 5.3 indicate that MMS possibly encounters a reconnection event and not a dipolarization front. We have also determined the uncertainties in the non-ideal terms that may arise due to photoelectron emissions and large Debye radius in the magnetosphere. However, the uncertainties associated with the Hall, inertial, and Pressure divergence terms are found to be minimal and comparable in this case.

Figure 5.5f shows a positive current toward the X and Y-directions and a negative current toward the Z-direction. Multiple peaks showing the presence of multiple layers (or filaments if we consider 3-D) of FACs are observed (Figure 5.5g and Figure 5.5h) during 2317-2318 UT (Phan et al., 2016; Chen et al. 2019). Specifically, three current layers (or filaments if we consider 3-D) in the same direction followed by a current layer in the reverse direction are noted. The FACs obtained by the Curlometer method (panel g) and plasma (or local) method (panel h) agree well with each other, which suggests that the current densities estimated are reliable and precise. Panel (i) shows that both the electrons and ions contribute significantly to the total FAC but in opposite magnitude. Panel (j) demonstrates a significant and sharp rise of the power that delineates a significant volume of electromagnetic energy converted into kinetic energy of plasma during the time. The sudden enhancements of all the parameters exemplify that MMS probably crossed or approached a magnetic reconnection region during the period under observation.

5.3.3 MMS-magnetopause encounter at 0735- 0755 UT on 1 January 2016

After the above encounter with the magnetopause, the MMS is found to remain in the dayside magnetosheath region for about 10 hours according to the T89 model estimates by NASA-SSC table as referred to in Section 2. In this interval, the MMS is found to again cross the magnetopause at 0741 UT on 1 January 2016. Then it travels through the dayside magnetosphere, nightside plasmasphere, dayside plasmasphere, dayside magnetosphere, and then dayside magnetosheath consecutively on 1 January 2016. Thus, the 20-minute interval between 0735-0755 UT on 1 January 2016 is analyzed as the second encounter case in this paper. It was possible that during this interval, the spacecraft stayed in the boundary layer for some time, and the magnetopause could have moved back and forth to some degree. Estimation of different measures of agyrotropy (similar to what is presented in Figure 5.3) to trace a possible encounter of reconnection EDR was not possible in this case because ‘brst’ data from the FGM, EDP, and FPI of the MMS were not available during the stipulated time. Hence, for this case, we try to draw some inferential and circumstantial observations and associated pieces

of evidence to trace whether the spacecraft has passed through a possible reconnection region. However, it is important to note that these observational pieces of evidence may not be sufficient to provide convincing proof that the spacecraft has traversed through a reconnection region.

The recovery phase of this storm initiated at ~ 0113 UT, however, similar perturbations in the kinetic parameters of plasma and the field parameters are observed after ~0745 UT during this crossing. However, the magnitude of the ambient electric field remains lower (~5 mV/m of the Y-component) in comparison to (~20 mV/m) at the first encounter. Conversely, a drastic rise in the Z-component of the electron velocity up to ~1500 km/s in comparison to ~200 km/s during the first encounter and drastic enhancement of the electron and ion temperature up to ~5000 eV in comparison to only ~600 eV during the first crossing, are observed.

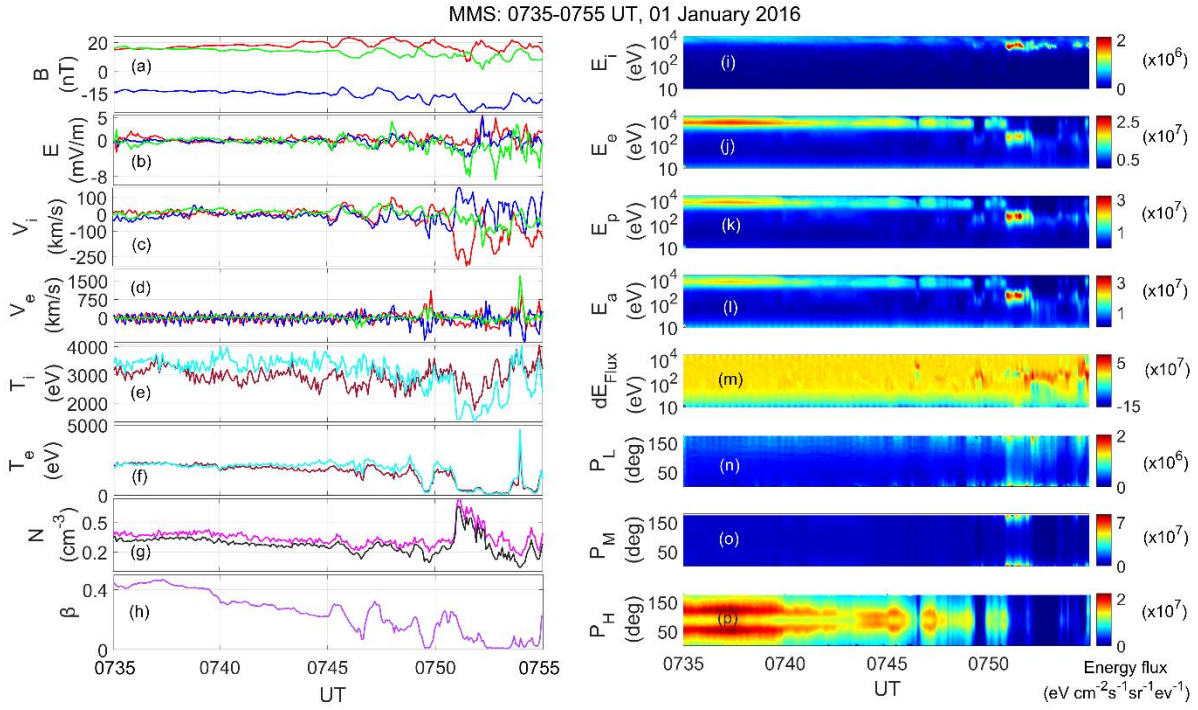

Figure 5.6. Same as Figure 5.4, but for the 20-minute duration between 0735-0755 UT on 1 January 2016, referred to here as the second encounter.

Interestingly, plasma density during the encounter is found to be low at ~0.5 cm^{-3}, which is one order smaller than that during the first encounter (~8 cm^{-1}). The Plasma Beta value is higher (~0.4) compared to the first encounter (0.06). Thus, though plasma density decreases, a dominance of plasma pressure over magnetic pressure is seen with the evolution of the storm in a very intriguing way. From the energy-time spectrograms of ion (Figures 5.6i) and electron (Figures 5.6j), the ion and electron flux are respectively found to be of the order of 10^6 and 10^7.

The difference flux (dE_{Flux}) shows enhancement corresponding to about 10^3 eV during 0748-0755 UT (Figure 5.6m), which indicates the dominance of the parallel electron current, but a decrement at smaller values of dE_{Flux} shows the contribution of anti-parallel electrons, as well. The associated pitch angle distribution shows mild enhancement in the flux at higher and lower angles in the low and mid-energy electron populations (Figure 5.6 n-p).

In contrast to the previous case (section 3.2), the high-energy electron population shows a dual-band structure corresponding to pitch angles of 20^o-70^o and 100^o-130^o. Thus, the high-energy electrons are found to be the main carriers of the FACs before the encounter but low and mid-energy electrons dominate during the encounter.

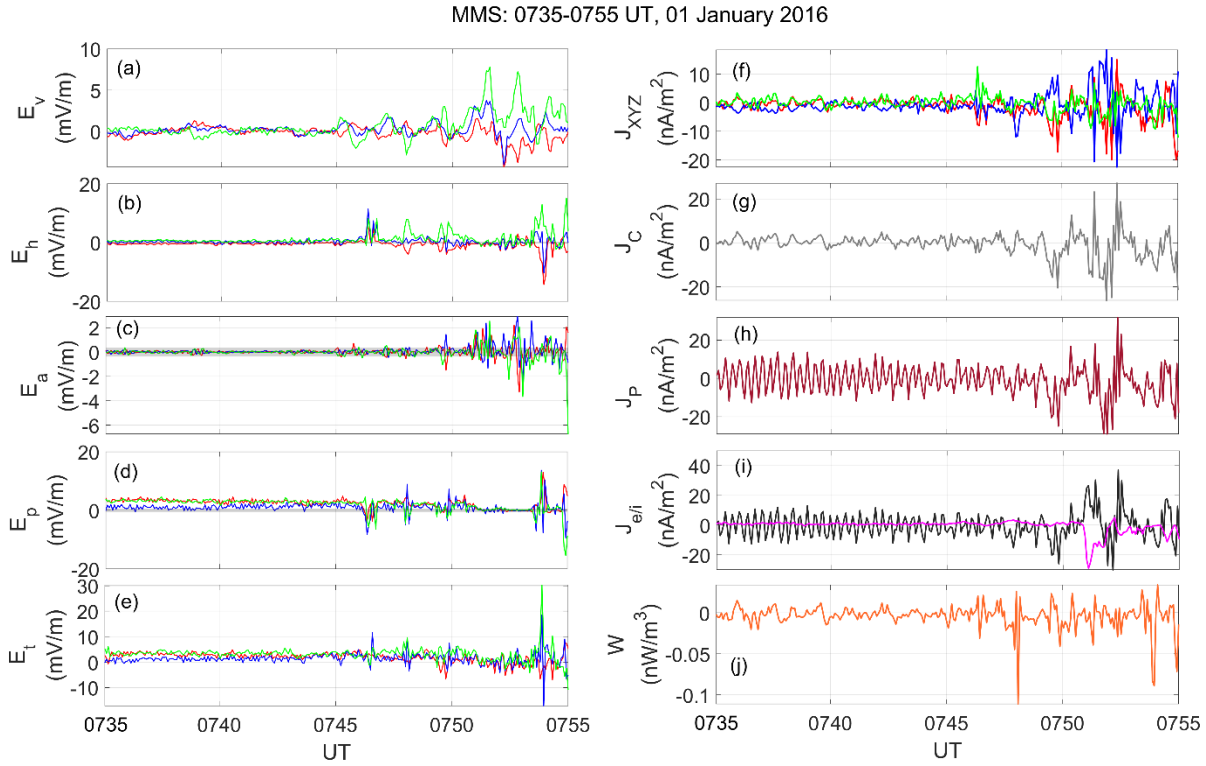

Figure 5.7. Same as figure 5.5 but for the 20-minute duration between 0735-0755 UT on 1 January 2016, referred to here as the second encounter.

Hence, in comparison to the first encounter (in the main phase), it is found that the flux of ions and electrons is almost one order less during the second encounter (in the recovery phase). In addition, before the encounters, low-energy electrons constituted most of the electron population during the first case (section 3.2) in comparison to the high-energy electrons during the second case (section 3.3). It is observed that although the magnitude of the inertial electric field remains moderate (1–2 mV/m), the large Hall electric field (1–20 mV/m) and electron

pressure gradient electric field (1–20 mV/m) provide the main contribution to the generalized Ohm's law at the neutral sheet during this event (in the recovery phase).

Hence a large dominance of electric field generated from electron-parameter variations is observed. This is a direct indication of the dominance of electron physics in a probable electron diffusion region. It is commonly understood that electron physics becomes the predominant factor after ions decouple from the magnetic field inside these kinds of specific current sheet regions (Macek et al. 2019a). Also, unlike in the previous case (section 3.2), similarity in variations in different terms of the ideal and non-ideal electric field is not observed. However, though the uncertainties associated with the Hall, inertial and Pressure divergence terms are found to be minimal and comparable (Figure 5.7b-d). In addition, unlike in the previous case (section 3.2), only electrons are found to be the main carriers of the currents (Figure 5.7i).

Multiple current layers (or current filaments if we consider 3-D) with different directions of FACs are found to flow during and after the crossing. Alike the previous case, FACs estimated from the Curlometer method and plasma (or local) method agree well which corroborates the authenticity of the respective calculations. Intriguingly, the power dissipated often attains a negative value, which indicates the magnetic energy, which is converted into kinetic energy during the encounter, is absorbed by the system rather than being released.

5.3.4 Cluster-magnetopause encounter at 1145- 1205 UT on 1 January 2016

The Cluster constellation is found to move from the dayside magnetosheath and enter the dayside magnetosphere at ~1149 UT on 1 January 2016 (Figure 5.1). The constellation is found to cross the magnetopause at ~1152 UT and enter the dayside magnetosphere thereafter until it moves to the nightside magnetosphere at 1931 UT on the same day. We have considered a 20-minute interval between 1145-1205 UT on 1 January 2016 considering the magnetopause crossing of the Cluster during the recovery phase of the storm.

Figure 5.8 shows the observations during this interval from the Cluster-4 spacecraft. The velocities (Figures 5.8a and 5.8b) and temperatures (Figures 5.8c and 5.8d) of both the ions (V_i, T_i) and electrons (V_e, T_e) show low-magnitude variations. The magnitude of the z-component of velocity is found higher than the other two components and the y-component shows a spike-like enhancement at ~1152UT.

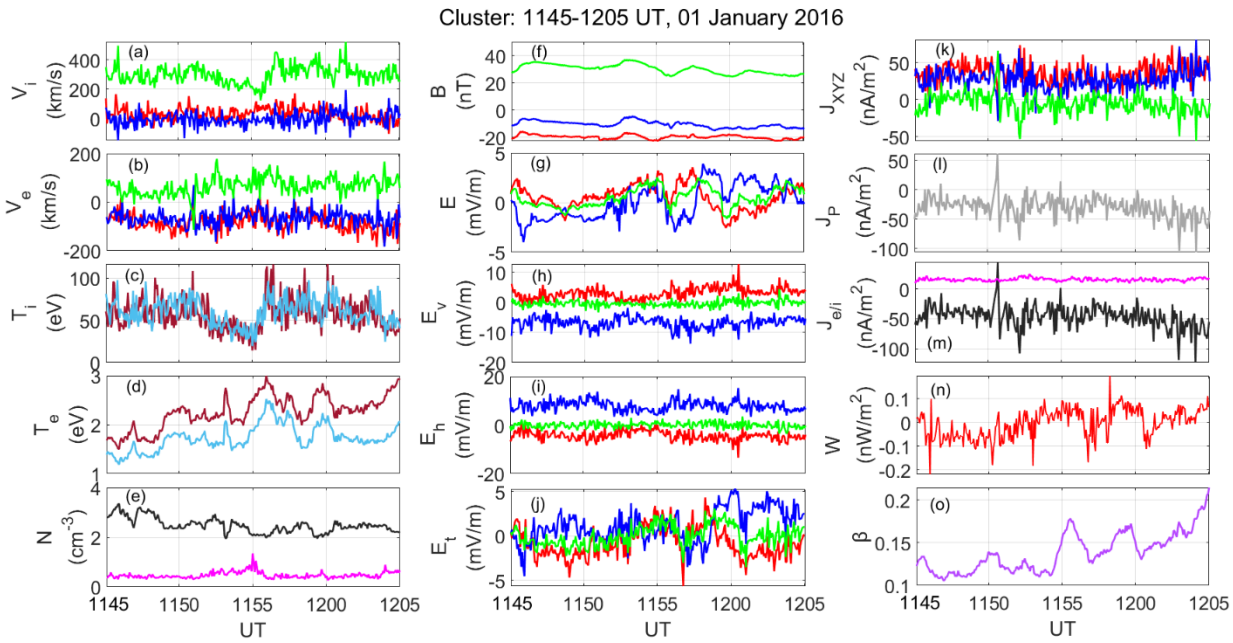

Figure 5.8. Variations in the different measurements and estimations from the Cluster-4 spacecraft are given for the 20-minute duration between 1145-1205 UT on 1 January 2016. Panels a and b exhibit variations in the bulk velocity of ions (V_i) and bulk velocity of electrons (V_e) with the x, y, and z components in red, blue, and green, respectively. Panels c and d show the parallel (brown curve) and perpendicular (sky blue curve) components of the ion and electron temperatures (T_i and T_e), respectively. Panel e shows the ion (magenta) and electron (black) density of the plasma (N). Panels (f)-(j) give variations of the ambient magnetic field (B), first (E) and second term (E_v) of the ideal electric field, Hall electric field (E_h), and total electric field (E_t), respectively with the x, y, and z components. Panel (k) shows components of the total current flowing in the region; panels l and m give variations in the total FAC estimated by the plasma method and FAC carried by electrons (black) and ions (magenta) respectively. Panel (n) provides power (W) and panel h shows plasma beta (β).

A gradual decrement in ion temperatures is observed during ~1152-1156 UT but the electron temperatures show successive increments and decrements. A significant difference in the electron (higher) and ion (lower) density (Figure 5.8e) is found during the 20 minutes, but a small rise in ion density is seen at ~1155 UT, which is after the crossing. At 1152 UT (during the Cluster-magnetopause encounter), a negligible kink in all the components of the magnetic field (Figure 5.8f) and the ambient electric field (Figure 5.8g) are observed. The contribution of the Hall electric field (Figure 5.8i) to the total electric field is found relatively higher. A single layer (filament if we consider 3-D) sheet of FAC (Figure 5.8l) is observed as an upsurge at ~1151 UT which is only seen in the electron current density parallel to the magnetic field

(Figure 5.8m). Plasma beta value (Figure 5.8o) is found to bear a similar variation as seen in the electron temperature. Overall, we do not observe a significant sudden change either in the magnitude or in the direction of the magnetic and electric fields, current density, or the velocity components during ~1145-1205 UT. Though a single layer (filament) FAC is observed during the crossing, the variations in other parameters do not affirm that the spacecraft encountered a reconnection region inside an EDR (or IDR) or a reconnection event. Interestingly, the episodic variations in the ion and electron temperature are found to reflect in the total electric field, power, and plasma beta variations.

5.3.5 THEMIS-A approach of the magnetotail at 1110 - 1130 UT on 1 January 2016

THEMIS-A is found to move in the region of the nightside magnetosphere from the early hours of 31 December 2015. Then, it crosses the plasma-sheath at 0147 UT, stays therein for 14 hours, and again enters the nightside magnetosphere. Then again, it traverses through the regions of the nightside plasmasphere, dayside plasmasphere, nightside plasmasphere, and nightside magnetosphere in succession to enter the plasma-sheath region, eventually. During the revolution in its orbit, the largest distance it passes away from the magnetopause is ~14.96 R_E during 1125 UT-1217 UT. The spacecraft is then found to move in the plasma-sheath during the interval of 0148 UT-1542 UT.

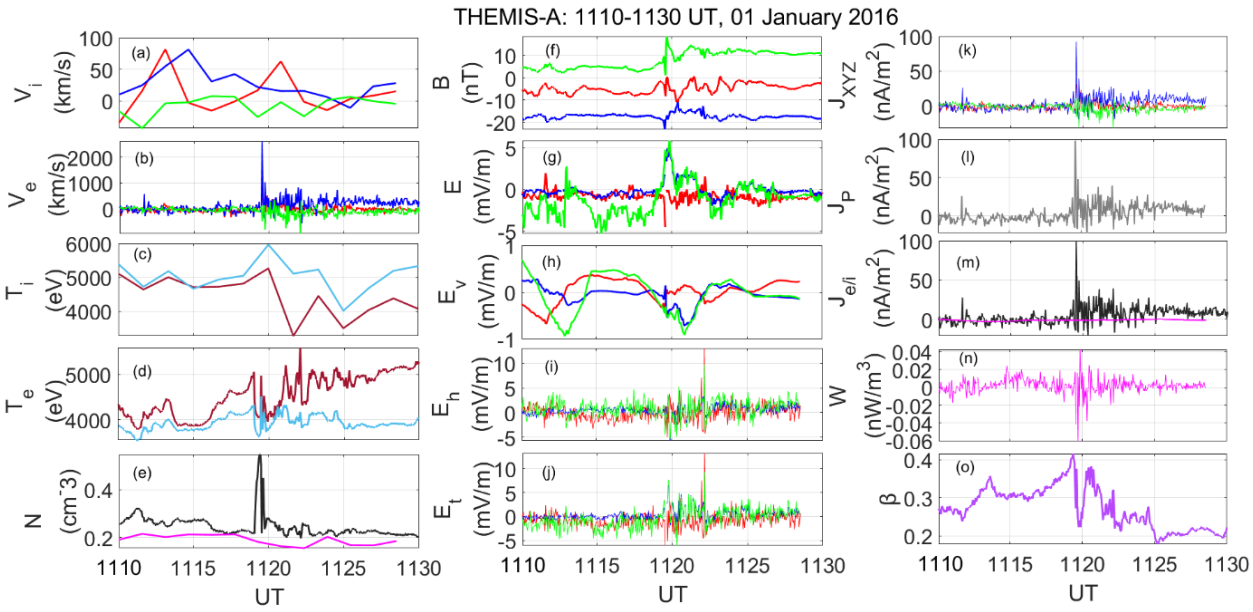

Figure 5.9. Same as figure 5.8 but for THEMIS-A spacecraft and the 20-minute duration between 1110-1130 UT on 1 January 2016.

After that, it traverses through the nightside magnetosphere, nightside plasmasphere, dayside plasmasphere, nightside plasmasphere, and nightside magnetosphere until the end of 1 January 2016. We consider 20 minutes during 1110 UT-1130 UT during which THEMIS-A was in the magnetotail during the recovery phase of the storm. During this period, the value of plasma ß of the region was ~0.2-0.4, which indicates the spacecraft might have encountered a PSBL. In many of the previous literature, which discussed magnetic reconnection in PSBL, the PSBL region has been identified by the condition $0.01 \leq ß \leq 1$ (Ueno et al., 2002; Cheng et al., 2016). Whereas, the presence of the spacecraft in the lobe region is given by the condition $ß < 0.01$, and in the plasmasheet is given by the condition $ß > 1$ (Ueno et al., 2002). On the contrary, the variations of Bx and Bz (Figure 5.9f) indicate that the spacecraft may not encounter the PSBL during this period. The value of Bx suddenly drops to ~0 nT, which indicates that the spacecraft was around the magnetotail current sheet center. The continuous decrease of plasma beta may be because of a current sheet disturbance. In addition, the sharp increase of Bz indicates a signature of a probable dipolarization front (Fu et al., 2012).

A sudden enhancement is observed at ~1119 UT in most of the plasma and field parameters, which is found to sustain for ~1 minute. A very sharp rise in electron velocity (figure 5.9b) up to ~2600 km/s at 1119 UT is seen which is found to be in contrast with the variations (at about one order less) in ion velocity (figure 5.9a). However, very high ion (figure 5.9c) and electron (figure 5.9d) temperatures are observed throughout the 20-minute interval. Electron density (black curve in figure 5.9e) exhibits a sharp rise at 1119 UT, against a flat variation in ion density (magenta curve in figure 5.9e). However, the ion density shows an average pattern due to a lesser sample rate, so the difference between ion and electron density variations shall not be surprising. Both the ambient magnetic field (figure 5.8f) and electric field (figure 5.9g) show a spike at 1119 UT. Among the electric field terms, the Hall electric field (figure 5.9i) is found to contribute the most to the total electric field in the magnetotail. However, the peak in Hall electric field is found to be at ~1922 UT, 3 minutes later than the sudden surge in all the parameters of both the magnetic and electric field. A single-layer FAC (figure 5.9i) is observed at 1119 UT followed by several smaller peaks for about 4 minutes. FAC density is contributed mostly by the electrons (figure 5.9m). The plasma energy (W, Figure 5.9n) also shows a spike at ~1119 UT but is found to be about one order lesser in magnitude than that during the previous three cases. The plasma beta (figure 5.9o) value remained in the range of ~0.2-0.4, which indicates plasma pressure was mostly 20-40% of the magnetic pressure. Intriguingly, a large depression in plasma beta is found at 1119 UT

indicating a significant fall in plasma pressure and enhancement of magnetic pressure. However, many of these signatures mentioned above indicate a possible encounter with a reconnection event in the PSBL.

5.3.6 Simultaneous observations from the MMS-1, Cluster-4, THEMIS-C, and THEMIS-A (2300 UT on 31 December 2015 - 0700 UT on 1 January 2016)

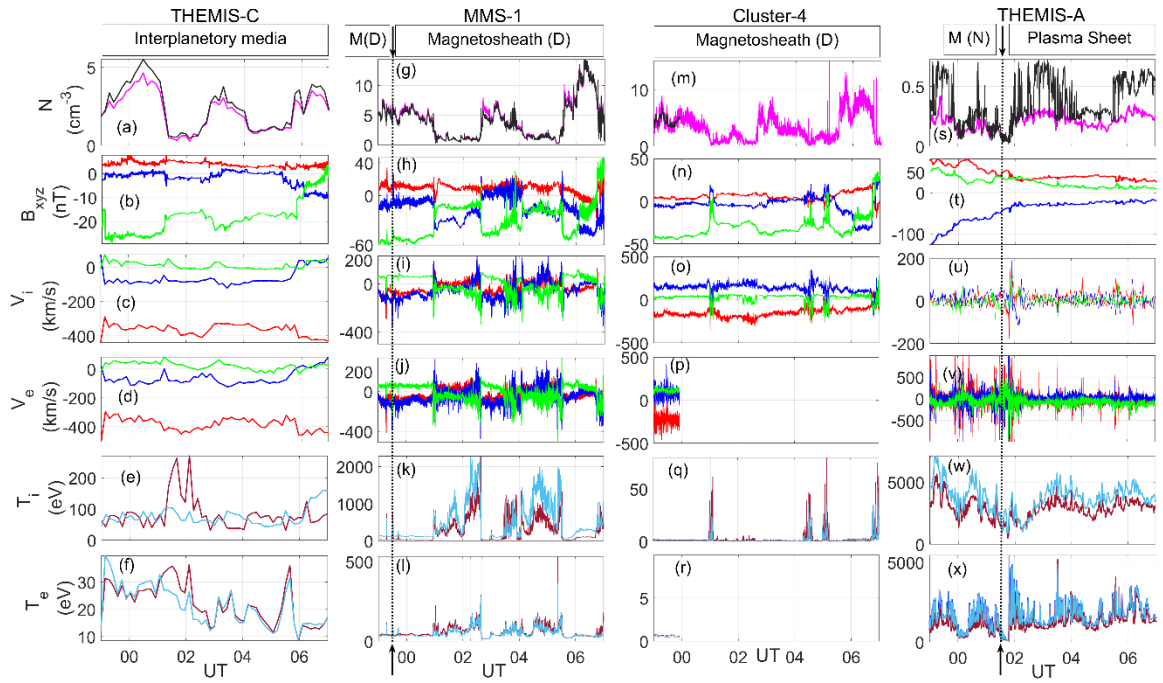

Figure 5.10. The columnar panels show the variations in the different ambient measurements, respectively from the THEMIS-C, MMS-1, Cluster-4, and THEMIS-A spacecraft for the 8-hour duration between 2300 UT on 31 December 2015 and 0700 UT on 1 January 2016. Top panels (a, g, m, and s) show variations in ion (magenta) and electron (black) density (N). The panels in the second (b, h, n, and t), third (c, i, o, and u), and fourth (d, j, p, and v) rows from the top show magnetic field (B), ion velocity (V_i) and electron velocity (V_e) respectively with the x, y, and z components in red, blue and green. The fifth (e, k, q, and w) and sixth (f, l, r, and x) rows represent ion temperature (T_i) and electron temperature (T_e) with parallel (brown) and perpendicular (sky blue) components. The specific regions in the geospace traversed by respective satellites are marked on top of the columns, where, M(D/N) denotes magnetosphere (day/night).

As noted in section 2 above, it is difficult to find simultaneous availability of observations from different spacecraft but we found a time window, which represents

simultaneous observations from different parts of the magnetosphere and the interplanetary medium. This interval corresponds to 8 hours of the main and the recovery phase of the storm between 2300 UT on 31 December 2015 and 0700 UT and 1 January 2016. The THEMIS-C is found in the lunar orbit in the interplanetary media, MMS-1 in the dayside magnetosphere (mostly in the sun-earth plane), Cluster-4 in the dayside magnetosphere (out of the sun-earth plane), and THEMIS-A in the earth's magnetotail during this interval.

Remarkably, the variations in the plasma densities measured by all four spacecrafts show simultaneous rise and fall, wherein, the densities from the MMS-1 and Cluster-4 are found at an almost similar magnitude and higher level than the rest two (Figure 5.10a, g, m, and s). The lowest densities are observed (almost one order less) in the magnetotail by THEMIS-A with a higher density of the electrons than that of ions compared to similar densities of both in the other regions in the magnetosheath and interplanetary media. The magnetic field profiles (figure 5.10b, h, n, and t) show noticeable dissimilarities in terms of the spatial variations while traveling from the interplanetary media to different regions of the magnetosphere. In this context, it shall be noted that the magnetic field topology (3-D magnetospheric configuration at large) could have remained constant over many hours during 00-08 UT (see Figure 5.2), but the magnetic field intensity varied at different locations differently. An enhancement in the magnitude of the magnetic field in the magnetotail indicates the dominance of magnetic properties over the kinetic properties of the plasma in this region. A drastic increase in the velocity of the ions and electrons (third and fourth rows of Figure 5.10) is noticed in the magnetotail (THEMIS-A) with a major difference among different regions. However, the variations in the electron and ion velocities are found to match across the individual spacecrafts in the respective regions as observed by the THEMIS-C and MMS-1. Remarkably, very high electron and ion temperatures (both parallel and perpendicular) in the magnetotail are observed compared to the other regions. The temperature is linked with the energetics of the plasma, so, it can be speculated that the energy per particle is higher in the magnetotail than in the dayside regions (Torbert et al. 2018).

The variations in the energy flux, electric field, current density, and power during the 8-hour interval are given in Figure 5.11. The observations from the Cluster spacecraft are not shown in this figure due to the non-availability of the electron properties. The first and second rows from the top of Figure 5.11 show the ion and electron energy-time spectrograms.

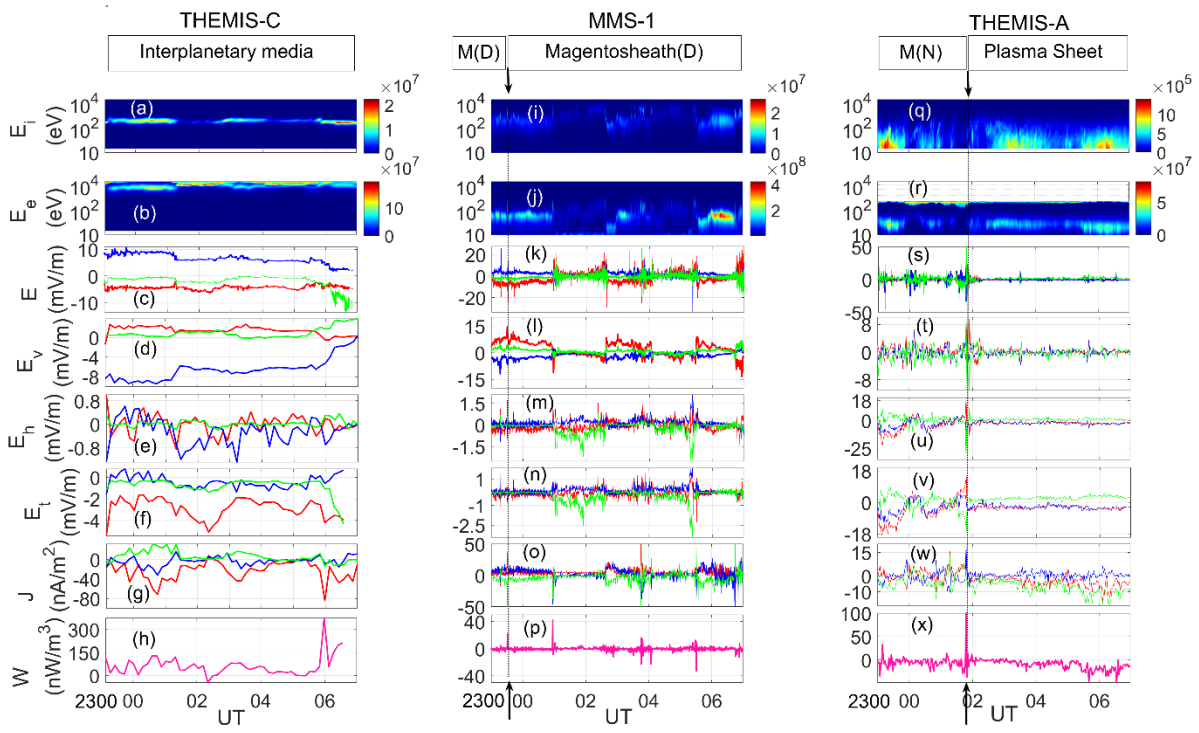

Figure 5.11. Rows from the top show the variations in the energy flux (top two rows), electric field terms (the third to sixth row from the top), current density, and power estimated, respectively. The columnar panels respectively show observations from THEMIS-C, MMS-1, and THEMIS-A spacecraft for the 8-hour duration. The rest of the annotations and symbols are the same as given in Figure -5.4, Figure 5.5, and Figure 5.10.

The ionic flux in the magnetotail observed by THEMIS-A is found to be significantly lower (in the order of 10^5) than from THEMIS-C and MMS-1 (in the order of 10^7). The estimated total electric field (sixth row from top) represents the sum of the classical (third row from top), reference frame (fourth row from top), and Hall (fifth row from top) terms of the electric field. The amplitude of the total electric field (sixth row from top) is more in the magnetotail observed by THEMIS-A (third columnar panel).

In this region, while the ideal electric field terms (E and E_v) are almost comparable (Figures 5.11s and 5.11t), the Hall term (Figure 5.11u) is found to dominantly contribute to the total electric field, unlike in other regions. The observations at ~0150 UT on 1 January 2016 from THEMIS-A show sudden distinct spikes in the ideal, Hall, and total electric field, current density, and power. The orbit of THEMIS-A shows a changeover from the region of the nightside magnetosphere to the plasma sheet at this time and resembles the variations. Also, notably, the recovery phase began at ~0113 UT, but the IMF-Bz was still stably southward in the above period. However, the magnitude of the current density from THEMIS-C (in the lunar

orbit in interplanetary space) is found to be the highest of all (second row from the bottom). In addition to this, the power is also found higher in the lunar orbit compared to that in the magnetosphere (bottom row). Interestingly, another observation of a sudden spike in different parameters at ~2317 UT from the MMS-1 is observed, which also is found to be associated with orbit crossing from the dayside magnetosphere to the dayside magnetosheath.

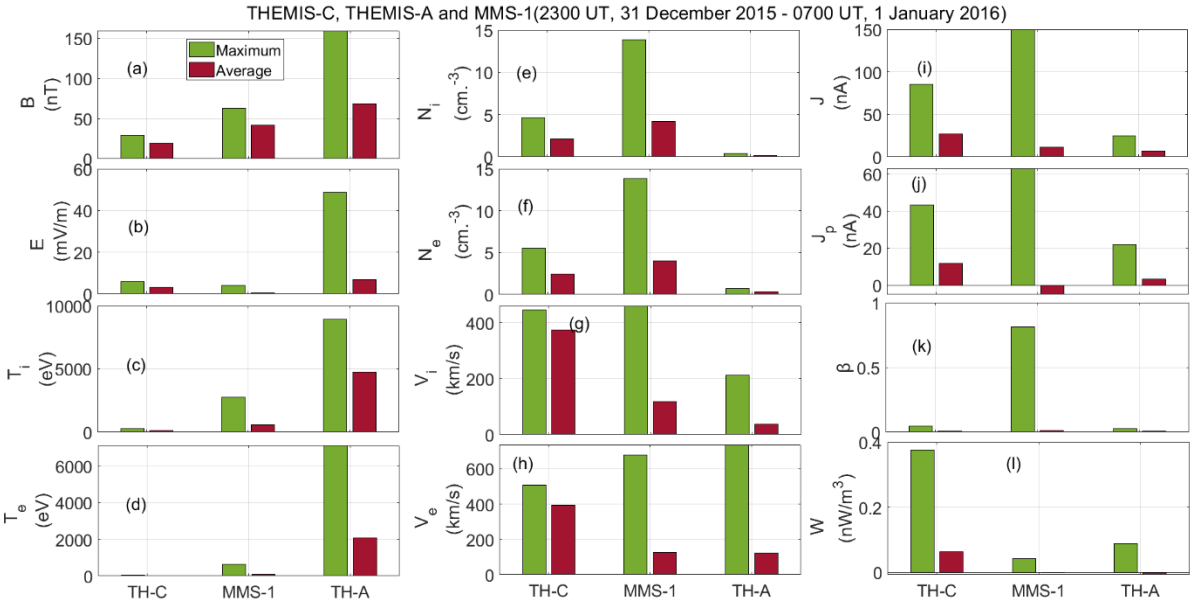

Figure 5.12. Same as figure 5.10 but for the maximum (green) and average (violet) values of observations from the THEMIS-C, MMS-1, and THEMIS-A spacecraft. The variations in maximum and average values of net magnetic field (B), ambient electric field (E), ion temperature (T_i), electron temperature (T_e) (in the left column); ion density (Ni), electron density (Ne), ion velocity (V_i), electron velocity (V_e) (in the middle column); and current density (J), current density by plasma method (J_p), plasma beta (β), and power (W) (in the right column), respectively.

A more comprehensive comparison of the observations from the three spacecraft (THEMIS-C, MMS-1, and THEMIS-A) during the 8-hour interval is illustrated in Figure 5.12. The maximum and average values of the magnetic field (Figure 5.12a) are found higher in the magnetotail (THEMIS-A) followed by that in the magnetopause in the sun-earth line (MMS-1) and that in the interplanetary media (THEMIS-C), respectively. The average value of the electric field (Figure 5.12b) is found higher in the magnetotail (THEMIS-A), than in the interplanetary media (THEMIS-C) and magnetopause (MMS-1). The magnetotail also hosts the highest magnitude of the electron and ion temperatures (Figures 5.11c and 5.11d). On the

contrary, both the ion and electron density show a peak in the magnetopause (MMS-1), followed by the interplanetary media (THEMIS-C) and the magnetotail (THEMIS-A) in the maximum as well as average values. The average values of both the ion velocity (Figure 5.12g) and electron velocity (Figure 5.12h) show a decreasing pattern from the interplanetary media (THEMIS-C) to the magnetopause (MMS-1) and the magnetotail (THEMIS-A), which differ from the maximum values in each of the cases. While the maximum values of the total current density (Figure 5.12i) and the FAC (Figure 5.12j) are found to be the highest in the magnetopause (MMS-1), the average value of the FAC is found negative in this region. On the contrary, the maximum power (Figure 5.12l) is found more in the interplanetary media (THEMIS-C) but the average power in the magnetotail shows a negative value.

In a nutshell, we can infer that the magnetotail hosts higher magnitudes of magnetic and electric fields and plasma temperatures; but the magnetopause region shows high values of the plasma density and velocity, the current density, and the plasma beta. Further, in the earth's magnetotail, a magnetic dominance over the kinetic properties of the plasma is observed in contrast to the magnetopause.

5.4. Discussion

Magnetic reconnection bears great significance in coupling processes around many celestial bodies and is associated with large-scale astrophysical phenomena like X-ray flares in pulsar wind nebulae, active galactic nuclei jets, edge of the heliosphere, fusion in laboratory experiments; and solar coronal mass ejections, flares, prominence eruptions, coronal jets; and other planetary magnetospheres (Hesse and Cassak, 2020). Detailed investigations on the magnetic reconnections and associated variations at the X-lines in the magnetopause and magnetotail regions have been reported in the literature by Hones (1984), Lee and Fu (1986), Hesse and Schindler (1988), Lyon (2000), Phan et al. (2006), Drake et al. (2006), Yamada et al. (2010). Recent studies on magnetic reconnection have mostly used the Cluster and MMS observations like Cheng et al. (2016), Burch et al. (2016), Torbert et al. (2016), Fu et al. (2018), Chen et al, (2019), and Macek et. al (2019a, 2019b). In this study, the characteristics of the field and kinetic parameters of plasma near and at the current sheets are investigated during the geomagnetic storm of 31 December 2015 to 1 January 2016 using multi-satellite observations. We consider the magnetopause and PSBL encounters of the MMS, Cluster, and THEMIS spacecraft by using the NASA-SSC data set which is based upon the spacecraft orbit, Tsyganenko-89C and IGRF models (https://sscweb.gsfc.nasa.gov). The results from the study

establish a probable reconnection region or the approach to EDR or IDR in some cases which is characterized by large fluctuations in the electron and ion velocity, field variations and reversals, drastic temperature rise, and changes in plasma density. Our results shown in Figure 5.3 on the agyrotropic terms indicate a strong possibility of a reconnection event with an outflow jet between 23:17:15- 23:18:04 on 31 December 2015. However, these results do not provide a piece of conclusive evidence regarding the crossing of an EDR. The sudden spikes in these terms could also have originated in conditions of the spacecraft crossing a reconnection separatrix region where additional influences such as the electron diamagnetic drift (Egedal et al., 2016) and the lower-hybrid wave fluctuations localized along the separatrices (Roytershteyn et al. 2012) set in. Nevertheless, by considering both the in-situ observations made by spacecrafts and the fluctuations in the agyrotropic terms, it can be inferred that spacecrafts have encountered reconnection events characterized by robust outflow jets. We find the enhancements in all these parameters happen ~3-4 minutes before or later than the estimated time of crossings.

The simultaneous observations are used to estimate the FAC density from the plasma (local method) and the Curlometer methods. The previous studies, in general, have shown the two estimations of the FAC to be very different most of the time (Cheng et al. 2016). The primary reason could be the use of local measurement in the plasma method (as it is based on the observations entirely made by a single spacecraft through the local method) in contrast to the Curlometer method (as it is based on the observations entirely made by a multiple spacecrafts), wherein the calculations are done at the center of the spacecraft tetrahedron, globally contributed by the currents in different locations (Marchaudon et al., 2009, Cheng et al. 2016). Additionally, such a difference could emerge because of the temporally varying separation between the individual spacecraft, which is a general source of error in the Curlometer method. However, the plasma method can also be erroneous owing to partial measurements out of the full energy range of the ions (Frank 1981; Asano et al. 2004; Cheng et al. 2016). Hence, the present study becomes significant in providing comparable FAC results from the two methods (see Figures 5.5g-h and Figures 5.7g-h) using high-resolution coordinated observation from MMS. Significantly, the FACs estimated from the Curlometer method and plasma (or local) method agree well which corroborates the authenticity of the respective calculations and becomes a main highlight of the present study.

The results (Figure 5.4 and Figure 5.6) show that the electrons moving anti-parallel to the magnetic field are the major carriers of the FACs when the MMS encounters the possible

reconnection sites. Before and after the crossings (respective magnetopause or PSBL crossings of the spacecraft), the minimal amount of FAC flowing through the sites is mostly carried by low energy (0-0.2 keV) electrons. Whereas, during the encounter, the electron population generally shifts towards the mid (0.2-2 keV) and high energy (2-30 keV) range (Figure 5.4 and Figure 5.6). In addition, the pitch angle distribution of the electrons shows a dominant contribution from the parallel (~0^o) and anti-parallel (~180^o) electrons to the total FAC density. Chen et al. (2019) have studied three distinct cases of layered FACs in the PSBL during the non-storm period using high-resolution observations from the MMS and found that electrons are the main carriers, while the contribution of ions cannot be neglected. They also inferred a dominant contribution from the 'thermal' electron population against the negligible contribution of cold and 'superthermal' electrons. Using the Cluster observations, Cheng et al. (2016) reported an event in PSBL on 14 September 2004 during the recovery phase of a substorm. They have inferred that the earthward FACs are mainly carried by the dominant tailward motion of electrons hailing from energy levels of ~0.5 to 26 keV with large field-aligned bulk speed. Our study corroborates the results from the previous studies regarding the dominant carriers of the FACs during the main phase of the geomagnetic storm. However, the magnitude of FAC density (20-100 nA/m^2) as observed in the present study is much higher than that reported in the above-mentioned papers (5-30 nA/m^2). The contribution of the ions to total FAC is found negligible in the magnetotail (observed by THEMIS-A, Figure 5.9), in comparison to higher values in the magnetopause (observed by MMS-1, Figures 5.5 and 5.7). Wright et al. (2002) have attributed the origin of the electrons carrying intense FACs to a general generator region located some distance away, whereas, the ions probably have their origin from the ionosphere through the ion-outflow process (Cheng et al. 2016). Notably, the average current flow is found to be the highest from the THEMIS-C when the spacecraft was close to the lunar orbit in interplanetary space (Figure 5.11).

Chen et al. (2019) have found that the omnidirectional ion and electron energy flux varies in the order of ~10^5 (ion flux) and ~10^7 (electron flux) during the FAC flows during the non-storm period. However, in our study (Figures 5.4 and 5.6), an order of magnitude larger values are observed at ~10^6 (ion flux) and ~10^8 (electron flux) during the main phase of the geomagnetic storm. In addition, the difference flux (dE_{Flux}) during non-storm time is of the order ~10^6 (Chen et al, 2019) which is of the order ~10^7 in the present study. This is probably due to the higher magnitudes of FAC flow during the geomagnetic storm in the present case.

The ideal (ambient and reference frame-dependent) and non-ideal (Hall, inertial, and pressure-gradient) terms of the total electric field during all of the encounters of MMS-1, Cluster-4, and THEMIS-A are presented in this study. The Hall term of the electric field is found to contribute the most to the total electric field (Figures 5.5, 5.7, 5.8, and 5.9). Macek et al. (2019a) have reported that in addition to the ideal electric fields, the Hall and inertial electric fields of large magnitude (1-2 mV/m) may be responsible for fast reconnection in the ion diffusion region. In the case of the fast reconnections presented here, we find a huge contribution of the Hall electric field of the magnitude of ~6 mV/m during the main phase (Figure 5.5) and 20 mV/m during the recovery phase (Figure 5.7). However, Macek et al. (2019a) have figured out that during approaches to EDR, the pressure-gradient term becomes the main contributor with as large as 20-200 mV/m magnitude. On the contrary, we find a negligible contribution from the pressure gradient term during the main phase (Figure 5.5) but a remarkable contribution during the recovery phase (Figure 5.7). In addition, an enhancement in most of the parameters is found in the magnetotail during the encounters (Figure 5.9).

A comparative analysis of the characteristics of different regions, considering the different field and kinetic parameters and energetics of the plasma, is also performed in the present study. Significant intensification in the plasma and field parameters is observed by MMS-1 during the crossings with the magnetopause in the main phase (Figures 5.4 and 5.5) and the recovery phase (Figures 5.6 and 5.7), which indicates a possible magnetic reconnection. On the contrary, Cluster-4 observed almost no significant enhancements in the parameters except a single layer FAC while crossing the magnetopause during the recovery phase (Figure 5.8). The magnitude of the velocity of the ions and electrons observed by the MMS-1 is found much larger than that by Cluster-4 (mostly during the recovery phase). Even no sudden change in the directions in the x, y, and z-components of the field parameters or velocity is observed by Cluster-4. In addition, higher levels of the electron and ion temperature (both parallel and perpendicular) are observed by MMS-1 compared to Cluster-4. The recovery phase begins at about 01 UT but the IMF-Bz remains southward until ~10 UT (Figure 5.2). Thus, the 20-minute duration of the MMS-1 (Cluster-4) crossing the magnetopause corresponds to the southward (northward) orientation of the IMF-Bz.

The results of this study bring out some interesting relationships between different kinetic parameters of the plasma. The magnetosphere has several specific regions with specific plasma densities and temperatures, wherein, the plasma density is contributed by the solar wind and terrestrial ionospheric outflow (Cheng et al. 2016). The ion velocity is found almost at similar

levels (200-300 km/s) from all the satellite observations in this study. The electron velocity and the ion/electron temperatures are found at almost one order less during the MMS-magnetopause first encounter (Figure 5.4) when compared to the second encounter (Figure 5.6). However, the plasma density during the first crossing (Figure 5.4) is almost one order higher than that during the second encounter (Figure 5.6). A similar pattern between the variations of the velocity/temperature and the plasma density is observed while comparing Cluster-4 (magnetopause) and THEMIS-A (magnetotail) encounters (Figures 5.8 and 5.9). Therefore, it is found that during different encounters at the magnetopause and magnetotail, the plasma density is found at lower (higher) levels when the levels of the velocity/temperature are higher (lower). While comparing the average velocity of the ions and electrons during the 8-hour interval (Figure 5.12) during the main and the recovery phase of the storm, the highest magnitude is observed by THEMIS-C in the lunar orbit in the interplanetary space, followed by MMS-1 in the magnetopause, and by THEMIS-A in the magnetotail. However, the observations in the interplanetary media (THEMIS-C in lunar orbit) show the maximum magnitude of the current density and the power.

Some interesting and intriguing features of the plasma obtained from this study establish evidence of two-reconnection regions near earth-space i.e. the magnetopause and magnetotail are unique in terms of hosting the plasma kinetic and field properties. The results of this geomagnetic storm corroborate the results of previous studies (Torbert et al. 2018). Especially, the magnetotail is found to be highly dynamic in context to higher plasma (parallel and perpendicular) temperatures, and higher levels of electric and magnetic fields, despite the presence of the least magnitude of plasma density and FACs among the different encounters. In addition, the average and maximum values of the magnetic field are found at a higher level compared to plasma beta values in this region (Figure 5.12), leading to a dominance of magnetic over the kinetic properties of the plasma. Basically, plasma beta also reflects the balance between the thermal activity of electrons and ions, as described by kinetic theory, and the influence of magnetic fields. In other words, plasma beta indicates the extent to which the disordering effect of thermal motion competes with the ordering effect of magnetic fields in a plasma system.

The magnetotail observations (THEMIS-A) exhibit lesser plasma density at higher temperatures (Figure 5.10), which results in a higher order of energy per particle in the magnetotail with respect to the magnetopause. In addition, the magnetotail hosts lesser energy flux (~one order) compared to other regions (Figure 5.11) mostly because of very low plasma

density. The average power associated with plasma in the magnetotail and the magnetopause is comparable, but both the total current density and FAC are more in magnetopause. But during the spacecraft encounters with probable EDR, the power is found one order more in magnetopause compared to that in the magnetotail (Figures 5.5, 5.7, 5.8, and 5.9). In addition, the results of Figure 5.3 on the electron agyrotropy and the divergence of electron pressure tensor carry evidence indicating that the MMS1 spacecraft possibly encountered the EDR in dayside during 2317-2320 UT. These results match with a previous study by Genestreti et al. (2018). However, such an encounter from magnetotail could not be established in the present study from the available THEMIS data set. So, we can only infer from the present study that the higher plasma density as well as plasma beta in the magnetopause, depict a dominance of the kinetic properties of the plasma, which is in contrast to the dominance of magnetic properties in the magnetotail (noted above).

Our results show higher plasma density at the magnetopause than in the interplanetary media (Figure 5.12) which is likely due to the compression across the shock. In addition, lower values of the plasma beta show the dominance of magnetic pressure over the plasma pressure (Figure 5.4) during the first encounter of MMS-1 with the magnetopause during the main phase of the storm. However, during the recovery phase (Figure 5.6), as the magnetic pressure slowly decreases and plasma pressure slowly increases in the magnetopause, the plasma beta grows. As the main phase evolves, more and more plasma entry happens through the magnetopause, and plasma pressure starts increasing. Here, notably, the plasma entry is favourably supported by the longer-than-normal extension (into the recovery phase) in the southward IMF-Bz (Figure 5.2). These results show dynamic, anomalous, and inhomogeneous interactions of the interplanetary plasma with different parts of the magnetosphere during different phases of the storms.

Several previous studies have provided various reasons behind these intriguing differences in coupling among different parts of the Earth's magnetosphere. Keiling et al. (2005) have found that sometimes, the observed FAC in the tail lobe and PSBL regions in the earth's magnetotail can also be due to the superimposition of the Alfvén waves, especially during geomagnetic storms and substorms. In addition, these waves may also have an impact on particle velocity and acceleration (Cheng et al. 2016). Torbert et al. (2018) have explored the MMS observations of the reconnection in the EDR and explained the day and night-side differences in the processes that convert the magnetic energy. Burch et al. (2016) have found that there exists higher asymmetry in the regions of "X" type reconnection and electron flow

stagnation point at the magnetopause region (Burch and Phan 2016; Genestreti et al 2017; Cassak and Shay 2007) but, these two regions are found to be coincident in the magnetotail with symmetric inflow conditions (Torbert et al. 2018). Notably, the amount of magnetic energy per particle in the magnetotail is comparable to that of the solar corona and much other space and laboratory plasma, where magnetic reconnection also occurs (Torbert et al. 2018). Lyon (2000) summarized this with 'an unseen electrical generator, more powerful than any man-made generator, exists in space near Earth'. It is important to say that this generator is capable of producing as much as hundreds of billions of watts of power every day. The present study provides some unique dynamic characteristics of the magnetosphere and the reconnection regions inside it (the magnetopause and magnetotail). The results are very interesting and entrancing and warrant further investigations for the growth of our understanding of space weather.

5.5. Summary and conclusions

Coordinated observations of the MMS, Cluster, and THEMIS spacecraft during a geomagnetic storm of 31 December 2015-1 January 2016 are used to understand the short-scale variations at probable reconnection regions in near earth-space. A conclusive summary of the salient features and new findings is provided below.

1. The FACs observed at the magnetopause are found to be predominantly carried by electrons moving anti-parallel to the magnetic field, particularly in the magnetotail region. The day-night difference in FAC density is possibly enhanced during the main phase of the geomagnetic storm.
2. Significantly, the FACs estimated from the Curlometer method and plasma (or local) method agree well which corroborates the authenticity of the respective calculations and becomes a main highlight of the present study in contrast to some previous studies which showed major differences.
3. Mostly, fewer low energy (0-0.2 keV) electrons are found to carry a low magnitude of FAC density away from the reconnection region. However, during reconnections, the majority of the electron population is found to shift towards the mid (0.2-2 keV) and high-energy (2-30 keV) range. In comparison to the previous studies, our results show higher levels (~one order more) of ion and electron energy flux.
4. The kinetic electron-scale observations provided by the MMS prove that the non-ideal terms of the electric field bear higher significance and relevance during magnetic

reconnection. Especially, the Hall electric field is found to be the major contributor to the total electric field during magnetic reconnection when compared to the higher contribution by the pressure-gradient term reported earlier. In the case of the geomagnetic storm, our results indicate the growing significance of the pressure divergence term during later phases of the storm.

5. Longer duration (8-hour) continuous observations show a dominance of magnetic (kinetic) properties compared to kinetic (magnetic) properties in the magnetotail (magnetopause). Also, respective variations in the magnitude of plasma beta represent the varying magnitude of the magnetic and plasma pressure, as the storm progresses.
6. The signatures of power representing electromagnetic energy density being converted into plasma density show that only during the magnetopause and PSBL encounters, a large conversion of electromagnetic energy to particle energy happens in the magnetopause, whereas, such conversion is very common and usual in the magnetotail during the rest of the times. Drastic sudden changes are observed at the crossovers between different regions.
7. In context to the magnetopause-magnetotail, the results establish largely anomalous plasma characteristics (inside the magnetosphere) during the geomagnetic storm. The highly dynamic character of the magnetotail is established by observation of higher levels of the electric and magnetic field, ion, and electron temperature, and simultaneous lower levels of plasma density, energy flux, and FACs. On the contrary, the magnitude of FAC, total current, and plasma density are found to be the highest in the magnetopause.
8. It is found that during different encounters at the magnetopause and magnetotail, the plasma density is found at lower (higher) levels when the levels of the velocity/temperature are higher (lower). Thus, an indirect/inverse common relationship between the plasma density and temperature/electron velocity is derived.

Thus, it can be inferred that the coupling processes at the kinetic scale are inherently intricate and fascinating in the realm of space weather research, thus constituting a significant and active topic in this domain. **The work presented in this chapter is published as a research article by Hajra et al. (2023b).**

CHAPTER 6

Summary and Future Directions

"Somewhere, something incredible is waiting to be known."

— Carl Sagan

6. Summary of the thesis

The motivation behind space research encompasses a blend of both scientific exploration and practical benefits of the civilization. For many decades, scientists have been intrigued by the dynamic and intricate nature of the solar wind-magnetosphere-ionosphere system and associated coupling mechanisms which govern the flow of mass, energy, and momentum. During extreme events like solar and geomagnetic disturbed periods, extreme events such as geomagnetic storms and substorms happen, and they can have detrimental effects on sensitive and delicate technological systems, including satellite communication and navigation signals, ground-based power grids, and satellites. This field of study is dynamically evolving within the realm of science due to the continuously changing nature of solar wind, the earth's magnetosphere, and the ionosphere. Moreover, there are ongoing debates and discussions within the scientific community regarding the sequence of events that occur during geomagnetic storms and substorms and the associated coupling between the magnetosphere and ionosphere. Although large-scale processes in the solar wind-magnetosphere-ionosphere system are mostly -well-understood, numerous small-scale processes remain undiscovered. With the launch of diverse magnetospheric and ionospheric satellites by space agencies from various countries, new opportunities have arisen to investigate these unresolved questions.

This thesis aims to comprehensively explore several facets of the solar wind drivers, coupling mechanisms at both large and small scales in the solar-wind-magnetosphere-ionosphere system, energy transfer and partitioning, ionospheric variabilities, and geomagnetic responses during extreme events. To achieve this, the thesis focuses on analysing data from four supersubstorms of solar cycle 24 and the 31 December 2015 geomagnetic storm, using multiple satellite and instrument datasets, estimations, and established methodologies.

Chapter 1 serves as an introductory section, contextualizing the study and providing a comprehensive overview of the relevant literature. Chapter 2 details the data sources, instruments, and observations utilized throughout the study, establishing the groundwork for the ensuing analyses. Chapters 3 and 4 undertake a rigorous examination of four supersubstorms of solar cycle 24. Specifically, Chapter 3 scrutinizes large-scale coupling processes and energy flow in the solar wind-magnetosphere-ionosphere system, while Chapter 4 focuses on geomagnetic responses and a few magnetosphere-ionosphere coupling processes during the supersubstorms. Chapter 5 provides results and analyses pertaining to kinetic scale coupling processes, based on in-situ observations from three magnetospheric satellites during a geomagnetic storm on December 31, 2015.

Therefore, this thesis offers a few major findings that can make contributions to the areas of solar wind-magnetosphere-ionosphere coupling study and associated existing knowledge. A concise summary of these new findings and the corresponding conjectures they engender are provided in the subsequent section.

6.1 Summary of new findings

1. The solar cycle 24 was the weakest in the space age in terms of the occurrence and average intensity of supersubstorms. It is found that Extreme space weather events are caused by multiple hits of magnetic clouds, which are associated with fast-moving background plasma (FAST) and shock waves most of the time, leading to the occurrence of multi-phase storms and substorms. The results on the solar wind-magnetosphere-ionosphere coupling efficiencies and ratios reveal that only a small fraction (~3%) of the solar kinetic energy enters the earth's magnetosphere and around 55-60% of the input energy dissipates in the form of the sinks. A significant portion of the 'left-over' energy is accreted inside the magnetosphere, which is augmented and re-energized by various intra-magnetospheric processes and plasma instabilities in the post-substorm period. This conjecture is validated by a comparative analysis of the energy partitioning between shorter and longer time intervals, which reveal that for shorter intervals like period of substorms and supersubstorms, the magnetospheric input energy (derived from the Epsilon parameter) dominates over the energy dissipated, whereas, for the longer durations, the energy dissipated surpasses. The variability of input energy in the magnetosphere-ionosphere system, despite high levels of solar kinetic energy, underscores the crucial role played by solar wind-magnetosphere coupling in the energy dynamics of the magnetosphere.

   The results of the studies conducted signify the control of coupling on the transmission, conversion, and dissipation in the solar wind-magnetosphere-ionosphere system, and the coupling mechanisms are not simplistic but depend on various factors. The dissipation through Joule heating is the dominant energy sink in shorter intervals, whereas, the dissipation through auroral precipitation takes over for longer periods. It is found that the dissipation through the ring current remains always at the lowest levels, whereas, ~79-91% of the energy is dissipated through ionospheric energy sinks during the supersubstorm periods. Individually, the Joule heating (ring current) sink gains more (less) percentage in the recovery phase with respect to the expansion phase.

Through the examination of 101 substorms with varying intensities, it has been determined that as the intensity of a substorm increases, a greater proportion of the energy is dissipated through ionospheric energy sinks. Within these sinks, the rate of increase for Joule heating is greater than that of other major energy sinks. This indicates that the response of the earth's magnetosphere varies according to the intensity of the substorm over a specific period. Our findings indicate that as the intensity of substorms increases, a smaller proportion of energy is dissipated through magnetospheric energy sinks such as the ring current, while a larger share is directed towards ionospheric energy sinks. Additionally, the variation in input efficiency with substorm intensities suggests that fully isolated supersubstorms may occur very infrequently.

2. The responses of the SSC in both the 2012 and 2017 events display three distinct latitudinal signatures. These include (a) a step-like PPI followed by the MI between 0° and 45° latitude, (b) a PPI with a Gaussian shape followed by MI between 45° and 65° latitude, and (c) a PRI followed by MI between 65° and 90° latitude. A sequential impact of the hydromagnetic longitudinal shock wave and the FACs (and their manifestations as DP2 currents) associated with the SSC and the global magnetospheric convection is observed as the above-mentioned three different types of net responses in the H-component variations.

During supersubstorms, a significant north-south asymmetry is observed in the H-component variations at high latitudes, which is attributed to the seasonal differences in the growth and decay of ionospheric currents, with the summer and winter hemispheres exhibiting contrasting behaviours. An intriguing observation has been made in the co-latitude band ranging from approximately 55° to 65°, which reveals a complete reversal of phase, characterized by a global positive peak in the H-component, which occurs concurrently with the maximum depression in nearby latitude bands and peak depression in the SYM-H, SML, and AE indices. This suggests that each supersubstorm event involves a complex temporal composite of magnetospheric processes, magnetosphere-ionosphere coupling, and associated currents in the magnetosphere-ionosphere system. Furthermore, the composite effect generates a latitude-specific signature during the event. The H-component depressions at low latitudes exhibit two distinct sets of longitudinally dependent signatures, which can be attributed to local noon and midnight.

In contrast to the H-component, the variations in the D-component do not display any discernible latitudinal pattern during the SSC. Intriguing positive undulations in the D-component are observed when the H-components fall. In addition, the D-components vary significantly from one station to another. This lack of a clear pattern can be attributed to the

complex and non-linear nature of the underlying ionospheric processes. During supersubstorm periods, a north-south asymmetry in the variations of the D-component is observed. However, the amplitude of these perturbations is smaller than those observed in the H-component during the same intervals. Furthermore, the mid-latitude reversal and local time-specific pattern observed in the low latitudes are not present in the variations of the D-component during supersubstorm periods. In addition, intriguingly no global minimum during the supersubstorm, and highly variable, and local time-dependent low-latitude signatures are observed.

During supersubstorms, the GIC severity, as indicated by the dB/dt, exhibits peaks that reach their highest magnitudes of ~900 nT/min in the latitude range of 60°-75°. Additionally, secondary peaks are observed in the dip equatorial regions. Interestingly, the peaks of dB/dt over different magnetometer stations do not occur simultaneously during the supersubstorm periods and are also observed prominently after these periods over the mid and high latitudes. These findings suggest the possibility of a global threat of GICs beyond the supersubstorm periods, which warrants further investigation.

3. The coordinated observations of the MMS, Cluster, and THEMIS spacecraft during a geomagnetic storm of 31 December 2015-1 January 2016 are used to understand the short-scale variations at probable reconnection regions in near earth-space. Electrons moving anti-parallel to the magnetic field are found to be the main carriers in the magnetopause and the magnetotail region. A clear shift of electron flux of low energy (0-0.2 keV) to the mid (0.2-2 keV) and high-energy (2-30 keV) range during the reconnection is observed. In comparison to many of the previous studies, our results show higher levels (~one order more) of ion and electron energy flux. The kinetic electron-scale observations provided by the MMS prove that the non-ideal terms of the electric field bear higher significance and relevance during magnetic reconnection. Especially, the Hall electric field is found to be the major contributor to the total electric field during magnetic reconnection. Longer duration continuous observations show a dominance of magnetic (kinetic) properties compared to kinetic (magnetic) properties in the magnetotail (magnetopause). Drastic sudden changes are observed at the crossovers between different regions. In context to the magnetopause-magnetotail, the results establish largely anomalous plasma characteristics (inside the magnetosphere) during the geomagnetic storm. The highly dynamic character of the magnetotail is established by observation of higher levels of the electric and magnetic field, ion, and electron temperature, and simultaneous lower levels of plasma density, energy flux,

and FACs. On the contrary, the magnitude of FAC, total current, and plasma density are found to be the highest in the magnetopause. In a nutshell, magnetotail is proved to be a region of very low plasma density, and energy flux; however, energy per particle is higher with respect to magnetopause, which makes the magnetotail a very dynamic region for space weather studies.

6.2 Future scope

The possibilities for research in the field of SW-M-I coupling are endless. Especially, with the launch of several satellite missions in different parts of the magnetosphere and interplanetary space in the recent past and near future (for example the Aditya L1 by ISRO in 2025), the possibility to investigate and explore different intricate phenomena in the SW-M-I system has been enhanced several fold. Numerous compelling questions remain unanswered, and ongoing debates and discussions persist within the scientific community on several issues. In the following discussion, we outline some potential and feasible future research areas that can effectively address a few of the unresolved issues. These research scopes are intended to build upon and extend the work and studies presented in this thesis, ensuring a continued exploration of the subject matter.

1. After having a vivid analysis of the SW-M-I coupling, the immediate task from the view of coupling aspects is the investigation of the high latitude- low latitude coupling during these extreme events. It is a feasible task to integrate satellite and ground-based observations of ionospheric plasma irregularities with measurements of geomagnetic activity to study the evolution of ionospheric storms. In addition, combining the measurements of ionospheric plasma convection and total electron content (TEC) (from GNSS, ionosonde, etc.) with ground-based magnetometer observations may lead to understanding the magnetosphere-ionosphere coupling and high latitude-low latitude coupling better during extreme events, especially substorms.
2. To understand the complex response of the magnetosphere-ionosphere system during solar transient forcing (especially in the case of the SSC), an analysis of the D-component variations is essential to decipher the ionospheric contribution to the total current. The ‘TS04’ (Tsyganenko and Sitnov, 2005) and ‘Piersanti and Villante’ models (Piersanti and Villante., 2016) can be incorporated into the magnetometer observations during SSCs to

evaluate the ionospheric current vortices in both hemispheres and segregate the magnetospheric and the ionospheric contributions to the SSC.

3. Magnetic reconnection occurs over a wide range of spatial and temporal scales, and many complex processes that interact with it, such as turbulence and waves. A bigger set of EDR crossing events may be taken up to understand the kinetic scale coupling processes and these large-scale interactions better during magnetic reconnection.
4. A large dataset encompassing the solar cycles 23 and 24 could be investigated to study the impacts of space weather on the power grid and develop mitigation strategies to minimize the damage caused by GICs. In addition, a task to investigate the effects of ionospheric scintillation on GPS signals and develop algorithms to improve the accuracy of GPS positioning during ionospheric storms can also be taken up.

The above-mentioned scopes are based on four basic factors of any investigation, namely, multi-instrument observations and integration of multiple datasets, conducting simulations and development of new models, investigation of more extreme events, and, exploration of the impacts of these events on technology.

Appendix A

Summary table for the validation of the occurrence of the supersubstorms and their energetics

This appendix provides supplementary material in continuation of Chapter 3, wherein the observations and results on the sources, coupling, and energy distribution in the SW-M-I system during the four supersubstorms of solar cycle 24 are presented. The study basically carries out the details of the solar wind drivers, energy coupling, flow, and distribution during the events on 28 May 2011, 9 March 2012, and 7-8 September 2017.

This appendix contains a figure and a table that entail detailed information on the occurrence of the supersubstorms and the associated results on the energy partitioning presented in Chapter 3. The contents are presented sequentially below as supporting information (SI) 1-2.

SI-1. DMSP SSUSI observations during the four supersubstorms

SI-2. A table containing different energy estimations for different short and long periods

SI-3 A figure depicting the variations in ring current following eleven different static and dynamic models during the supersubstorm events

SI-1. Observations from DMSP-SSUSI during the four supersubstorms occurred on 28 May 2011, 9 March 2012, and 7-8 September 2017

Each row designates the auroral evolution observed from the top of the poles by DMSP-SSUSI satellites during each supersubstorm event. In each row, the leftmost and rightmost columns designate the quiet period just before and after the event respectively. The second and third columns in each row show the auroral evolution of each hemisphere due to the large inflow of solar plasma during the peak hours of the supersubstorm events. The exact time when the snapshots are taken and the corresponding DMSP satellite which covered the respective pass is depicted in each cell. To validate/cross-check the large inflow of solar energy into the magnetosphere-ionosphere system during the aforementioned time periods, global longitudinal coverage using DMSP-SSUSI UV observations is taken.

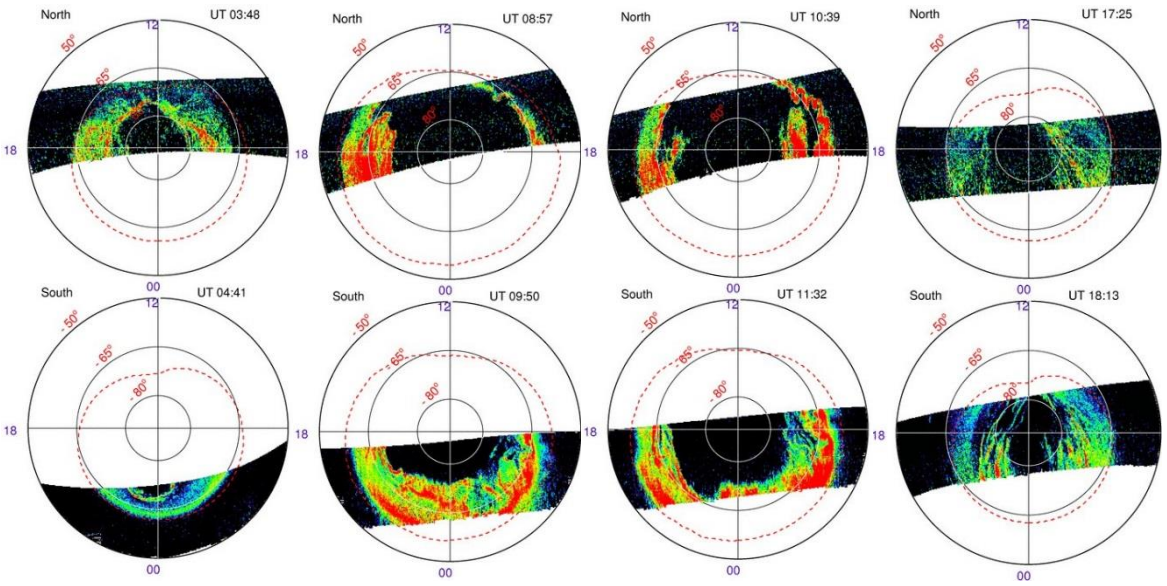

28 May 2011: North- 0348 UT South- 0441 UT DMSP-F16	28 May 2011: North- 0857 UT South- 0950 UT DMSPF-16	28 May 2011: North- 1039 UT South- 1132 UT DMSP-F16	28 May 2011: North- 1725 UT South- 1813 UT DMSP-F16

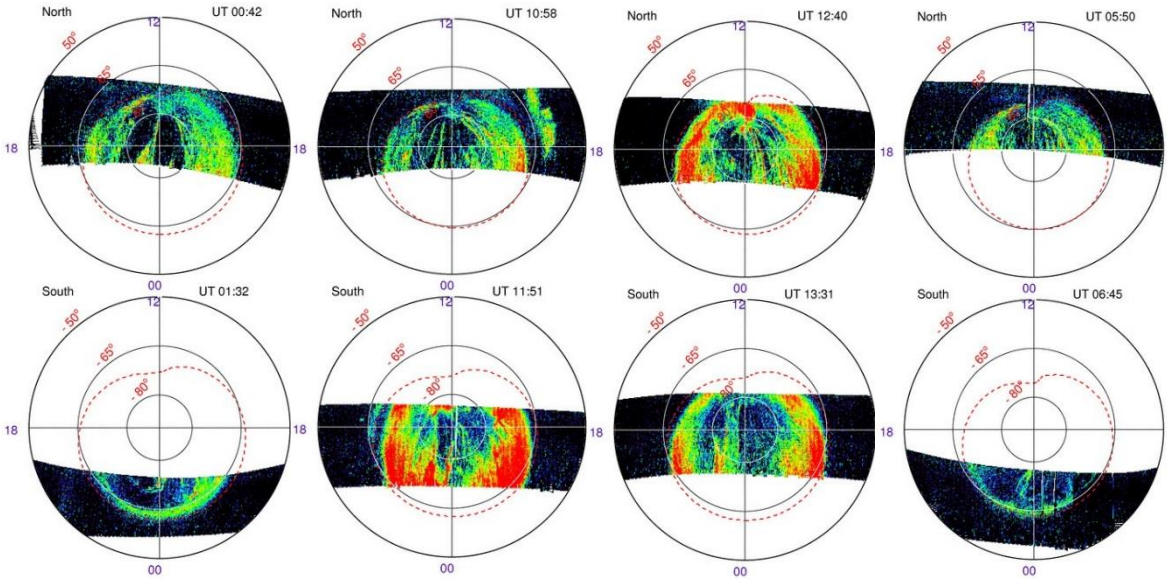

8 March 2012: North- 0042 UT South- 0132 UT DMSP-F16	8 March 2012: North- 1058 UT South- 1151 UT DMSP-F16	8 March 2012: North- 1240 UT South- 1331 UT DMSP-F16	9 March 2012: North- 0348 UT South- 0441 UT DMSP-F16

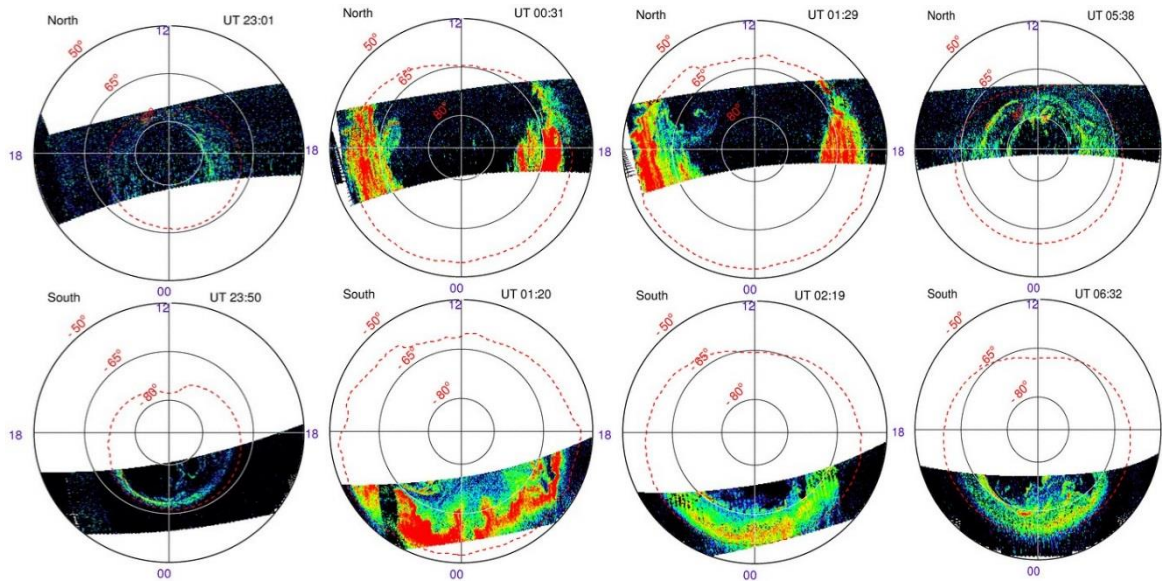

7 September 2017: North- 2301 UT South- 2350 UT DMSPF-18	8 September 2017: North- 0031 UT South- 0120 UT DMSP-F18	8 September 2017: North- 0129 UT South- 0219 UT DMSP-F17	8 September 2017: North- 0538 UT South- 0632 UT DMSP-F18

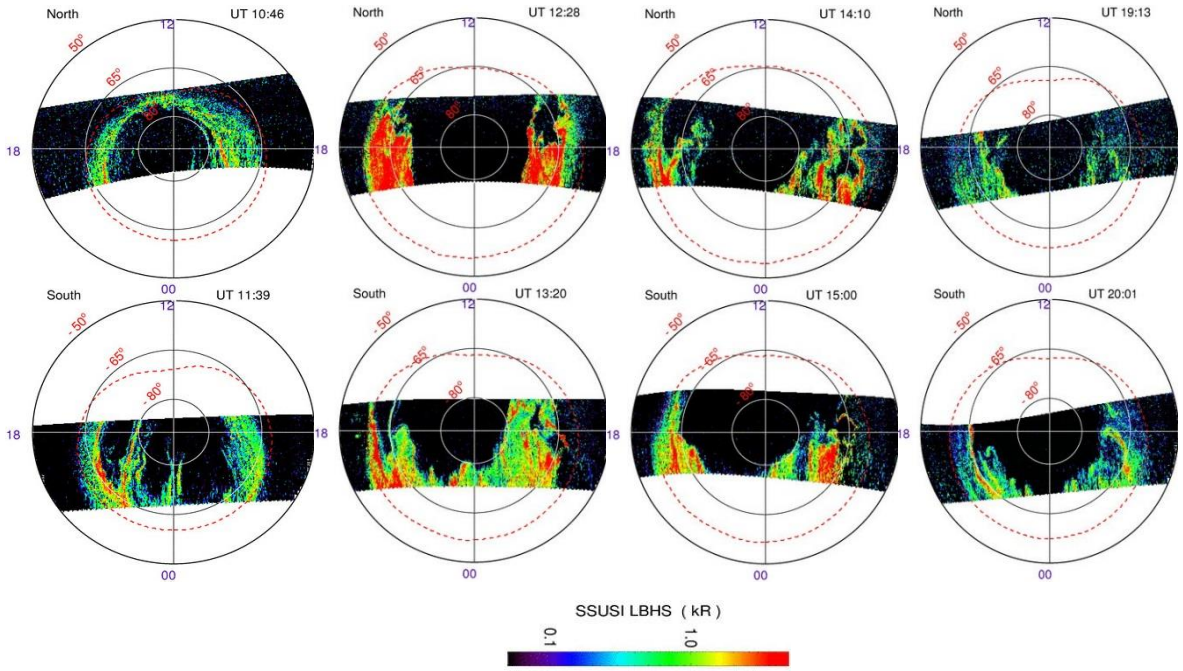

8 September 2017: North- 1046 UT South- 1139 UT DMSP-F18	8 September 2017: North- 1228 UT South- 1320 UT DMSP-F18	8 September 2017: North- 1410 UT South- 1500 UT DMSP-F18	8 September 2017: North- 1913 UT South- 2001 UT DMSP-F18

Observations from the top of the poles show perturbations centered around the Midnight sector and indicate longitudinal differences in the incoming energy fluxes. Supersubstorm events are basically designated by large depressions in SML indices. These large perturbations in H-components during those specific time periods are validated by the auroral evolution due to the huge inflow of solar wind energy which is clearly depicted in the observations from DMSP SSUSI.

SI-2: Table containing different energy estimations for different short and long periods. The columns from left provide the concerned duration to obtain an average, available solar energy (E_{sw}), magnetospheric input energy (E_{ε}), total dissipated energy (E_t), and the energy dissipated over the three major sinks (E_j, E_r, E_a), the corresponding coupling efficiencies are given by e1, e2, and e3, respectively. The estimates are given as averages for different types of short and long periods.

Event	Year	E_{sw} (10^{16} J)	E_{ε} (10^{16} J)	E_r (10^{16} J)	E_j (10^{16} J)	E_a (10^{16} J)	E_t (10^{16} J)	e1 (%)	e2 (%)	e3 (%)
Substorm	average	78.98	0.27	0.07	0.29	0.18	0.52	0.34	192.6	14.89
Storm	average	168.15	4.25	1.44	2.42	1.22	5.08	2.53	119.5	39.56
Supersubstorm period	2011	58.88	1.80	0.11	0.68	0.54	1.33	3.05	73.95	9.04
	2012	145.15	7.19	0.50	2.47	1.25	4.21	4.95	58.56	13.35
	2017-SSS1	149.82	5.96	0.38	1.13	0.73	2.25	3.98	37.71	20.60
	2017-SSS2	227.20	2.61	0.33	0.96	0.74	2.03	1.15	77.94	19.57
4 days	2011	611.18	6.41	0.86	5.29	3.68	9.80			
	2012	954.25	15.29	1.63	7.03	4.60	13.33			
	2017	740.93	11.25	1.44	3.64	3.05	8.13			
1 month	2011	3.69×10^3	23.68	4.29	14.30	20.22	38.81			
	2012	3.58×10^3	34.47	5.57	18.64	20.56	44.77			
	2017	4.74×10^3	25.07	5.48	14.91	21.74	42.13			
1 year	2011	3.43×10^4	230.36	45.53	115.01	167.02	327.56			
	2012	3.51×10^4	329.84	51.63	160.53	194.08	406.24			
	2017	5.07×10^4	222.21	49.76	141.08	141.08	402.07			

Above table is an elaborate version of Table 3.1 of Chapter 3. Here, in addition to Table 3.1, the estimations of energy parameters in each column are given separately for each supersubstorm, and for longer periods like 4 days and 1 month.

SI-3: Estimates of ring current during the three supersubstorm events following eleven static and dynamic models and estimations of the decay time (τ).

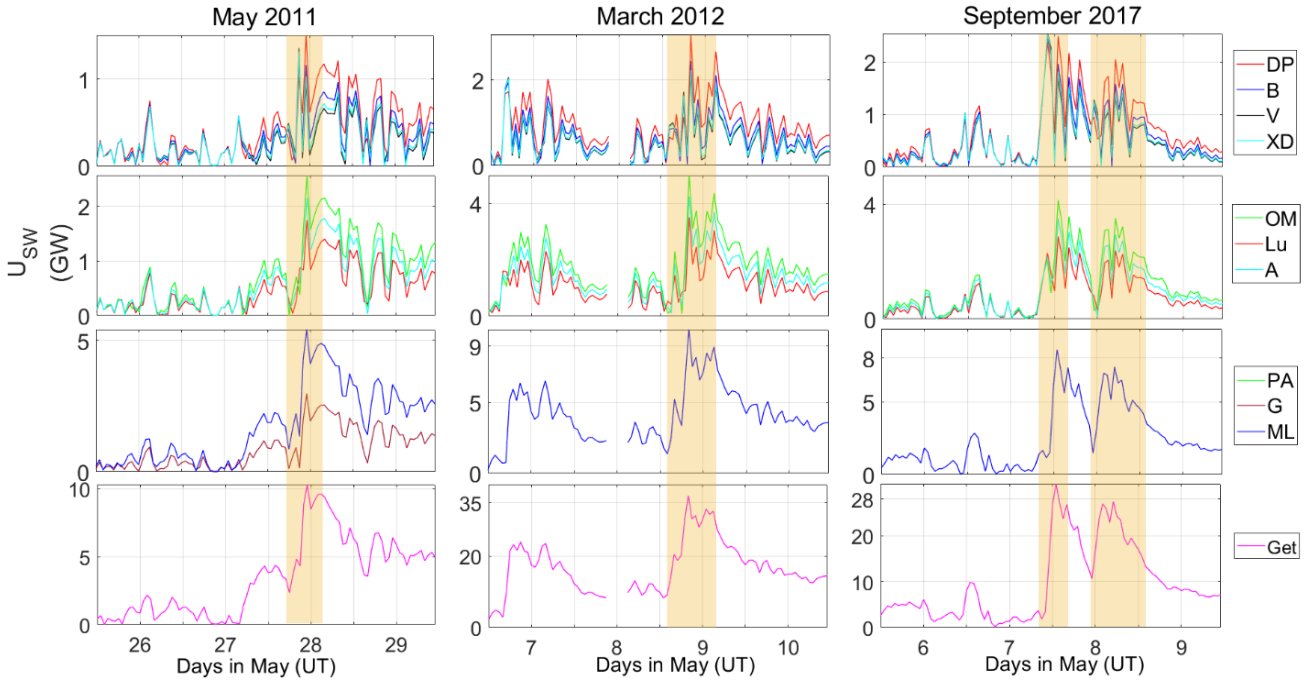

The above figure depicts variations of ring current following eleven different estimates (with reference to Table 2.3 given in Chapter 2). All the curves show almost identical phase variations, whereas, they show significant variations in amplitude. The estimates having similar magnitude are stacked in the same panels and hence four rows of curves are plotted. The first row depicts the variations of ring current following the estimates of Davis and Parthasarathy, Burton et al., Valdivia et al., and Xu and Du. The second row shows the variations of ring current following the models of O'Brien and McPherron, Lu et al., and Akasofu. The third row depicts the variations of ring current following Perrault and Akasofu, Gonzalez, and MacMahon, and Llop-Romero which almost coincide with each other. The bottommost row shows variations of ring current following Gonzalez et al. It is notable to mention that the model followed by O'Brien and McPherron is a dynamic model which is followed mostly in the community, and the same is followed to estimate ring current in Chapter 3.

Appendix B

Summary table for the Global H and D component observations

This appendix provides supplementary material in continuation of Chapter 4, wherein the observations and results on global geomagnetic responses during the four supersubstorms of solar cycle 24 are presented. The study basically carries out the responses of H and D components of the global magnetic field and the geomagnetically induced currents during the events on 28 May 2011, 9 March 2012, and 7-8 September 2017.

This appendix contains a table and five figures that entail detailed information on various results presented in Chapter 4. The contents are presented sequentially below as supporting information (SI) 1-7-

SI-1. Table of locations of the magnetometer stations used in the present study

SI-2. H-component observations during the SSC

SI-3. H-component observations from the latitude band of 70^{o} -90^{o}

SI-4. H-component observations from the latitude band of 15^{o} -70^{o}

SI-5. SuperDARN convection maps at the minimum SML epochs

SI-6. D-Component observations during the main phase of the supersubstorms

SI-7. SuperMAG polar maps of ground magnetometer H-component vectors

SI-1. The following table gives the locations of the INTERMAGNET magnetometer stations used in the study presented in Chapter 4 (Figure 2.4). The geographic coordinates of each station are given along with the difference between local time and GMT in terms of lead/lag. The magnetometer stations with their respective geographic lat-lon and geomagnetic lat-lon during 2011, 2012, and 2017 with exact time epochs of the advent of SSC are given in Table 1 below.

Table SI-1. List of all the INTERMAGNET stations used for the study presented in Chapter 4

Station name	Geographical coordinates (Lat, Long)	LT (GMT±)	LT 2012 (UT-	LT 2017 (UT-	Geomagnetic coordinates (Lat, Long)		
					2011	2012	2017

			11:04)	23:45)			
NORTHERN HEMISPHERE							
Dalat (DLT)	11.94, 108.48	+7	18:04	6:45	1.94N,179.25W	2.00N, 179.17W	2.29N, 178.90W
Guam (GUA)	13.59, 144.87	+10	21:04	9:45	5.53N, 143.84W	5.59N, 143.76W	5.85N, 143.48W
Hyderabad (HYB)	17.4, 78.6	+5:30	16:34	5:15	8.57N, 151.98E	8.62N, 152.05E	8.85N, 152.29E
Phuthuy (PHU)	21.03, 105.95	+7	18:04	6:45	10.98N,178.32E	11.04N,178.40E	11.33N,178.66E
Kourou (KOU)	5.21, 307.27	-3	8:04	20:45	14.51N, 20.15E	14.45N, 20.22E	14.17N, 20.47E
Mbour (MBO)	14.38, 343.03	0	11:04	23:45	19.76N, 57.86E	19.72N, 57.93E	19.53N, 58.11E
Kakioka (KAK)	36.23, 140.18	+9	20:04	8:45	27.52N,150.7W	27.58N,150.6W	27.85N,150.2W
San Fernando(SFS)	36.67, 354.06	-7	4:04	16:45	39.89N, 73.71E	39.86N, 73.74E	39.74N, 73.79E
Boulder (BOU)	40.14, 254.76	-6	5:04	17:45	48.02N,38.57W	47.98N,38.43W	47.79N, 37.93W
Hel (HLP)	54.603, 18.81	+1	12:04	0:45	53.06N,104.57E	53.06N,104.57E	53.09N,104.44E
Valentia (VAL)	51.93, 349.75	0	11:04	23:45	55.44N, 74.60E	55.41N, 74.60E	55.29N, 74.48E
Nurmijarvi (NUR)	60.51, 24.66	+2	13:04	1:45	57.75N,113.03E	57.76N,113.01E	57.83N,112.83E
Uppasala (UPS)	59.90, 17.353	+1	12:04	0:45	58.36N,106.13E	58.36N,106.11E	58.40N,105.91E
Sitka (SIT)	57.06, 224.67	-8	3:04	15:45	60.20N, 78.44W	60.20N, 78.25W	60.18N, 77.48W
Lerwick (LER)	60.13, 358.82	0	11:04	23:45	61.73N, 88.74E	61.71N, 88.71E	61.66N, 88.44E
Lycksele (LYC)	64.6, 18.8	+1	12:04	0:45	62.54N,110.77E	62.55N,110.74E	62.60N,110.45E
Sodankyla (SOD)	67.37, 26.63	+2	13:04	1:45	63.95N,119.37E	63.97N,119.33E	64.07N,119.03E
College (CMO)	64.87, 212.14	-8	3:04	15:45	65.38N, 97.04W	65.40N, 96.83W	65.47N, 95.95W
Yellowknife (YKC)	62.48, 245.51	-6	5:04	17:45	68.69N,59.15W	68.67N, 58.92W	68.56N, 57.97W
Deadhorse (DED)	70.36, 211.21	-8	3:04	15:45	70.16N,104.4W	70.19N,104.1W	70.30N,103.1W
Cambridge Bay (CBB)	69.12, 254.97	-6	5:04	17:45	76.30N, 54.93W	76.28N, 54.62W	76.14N, 53.30W
Godhavn (GDH)	69.25, 306.47	-2	9:04	21:45	78.11N, 33.77E	78.05N, 33.75E	77.78N, 33.45E
Hornsund (HRN)	77.00, 15.55	+1	12:04	0:45	73.93N, 125.1E	73.96N,125.1 E	74.08N,124.4 E
Resolute Bay (RES)	74.69, 265.11	-5	6:04	18:45	82.71N,53.55 W	82.68 N,53.03W	82.54N,50.80W
Thule (THL)	77.47, 290.77	-3	8:04	20:45	87.25N, 14.06E	87.19N, 14.11E	86.90N, 13.89E
SOUTHERN HEMISPHERE							
Huyankayo (HUA)	-12.05, 284.67	-5	6:04	18:45	2.41S, 2.63W	2.12S, 2.90W	2.06S, 2.98W
Ascension Island (ASC)	-7.95, 345.62	GMT	11:04	23:45	2.56 S, 57.14 E	2.60 S, 57.22 E	2.80 S, 57.50 E
Saint Helena (SHE)	-15.96, 354.25	+1	12:04	0:45	11.72S, 64.32E	11.76S, 64.41E	11.93S, 64.72E
Pamatai (PPT)	-17.57, 210.42	+10	21:04	9:45	15.03S, 74.48W	15.04S, 74.42W	15.07S, 74.23W
Apia (API)	-13.8, 188.22	+14	+1:04	13:45	15.14S, 96.96 W	15.11S, 96.90W	15.04S, 96.70W
Pilar (PIL)	-31.4, 296.12	-3	8:04	20:45	21.40S, 7.72E	21.46S, 7.79E	21.76S, 8.06E
Charters Tower (CTA)	-20.1, 146.3	+10	21:04	9:45	27.59S,138.59W	27.54S,138.53W	27.29S,138.34W

Alice Springs (ASP)	-23.77, 133.88	+9:30	20:34	9:15	32.45S,151.39W	32.39S,151.33W	32.11S,151.12W
Port Stanley (PST)	-51.7, 302.11	-4	7:04	19:30	41.85S, 11.99E	41.91S, 12.07E	42.2S, 12.35E
Eyrewell (EYR)	-43.47, 172.39	+13	+0:04	12:45	46.80S,105.98W	46.77S,105.96W	46.65S,105.98W
Port Alfred (CZT)	-46.43, 51.87	+2	13:04	1:45	51.11S, 114.27E	51.10S, 114.42E	51.02S, 115.04E
Argentine Islands (AIA)	-65.25, 295.75	+13	+0:04	12:45	55.25S, 5.93E	55.31S, 6.00E	55.60S, 6.24E
Port-aux-Francais (PAF)	-49.35, 70.26	+5	16:04	4:45	56.59S, 133.77E	56.55S, 133.93E	56.39S, 134.56E
Macquarie Island (MCQ)	-54.5, 158.95	+11	22:04	10:45	59.66S,115.78W	59.62S,115.79W	59.46S,115.93W
Neumayer Station III (VNA)	-70.68, 351.72	0	11:04	23:45	64.65S, 44.33E	64.71S, 44.48E	64.94S, 45.11E
Mawson (MAW)	-67.6, 62.88	+11	22:04	10:45	73.07S,111.88E	73.06S,112.16E	72.99S,113.36E
Casey Station (CSY)	-66.28, 110.53	+13	+0:04	12:45	76.05S,175.27W	75.99S,175.15W	75.69S,174.81W
Scott Base (SBA)	-77.85, 166.78	+13	+0:04	12:45	78.95S, 71.39W	78.95S, 71.62W	79.00S, 72.83W
Dome C (DMC)	-75.25, 124.17	+13	+0:04	12:45	83.99S,136.10W	83.94S,136.32W	83.70S,137.56W
Vostok (VOS)	-78.46, 106.84	+10	21:04	9:45	88.31S, 174.06E	88.25S, 174.78E	87.96S, 177.05E

Figure 2.4 of the thesis gives the locations of the magnetometer stations of the INTERMAGNET network. The geographic coordinates of each station are given along with the difference between local time and GMT in terms of lead/lag. The magnetometer stations with their respective geographic lat-lon and geomagnetic lat-lon during 2011, 2012, and 2017 with exact time epochs of the advent of SSC are given in Table SI-1.

Figure SI-2. The H-component observations from 41 INTERMAGNET stations during the SSC of the 2012 and 2017 events

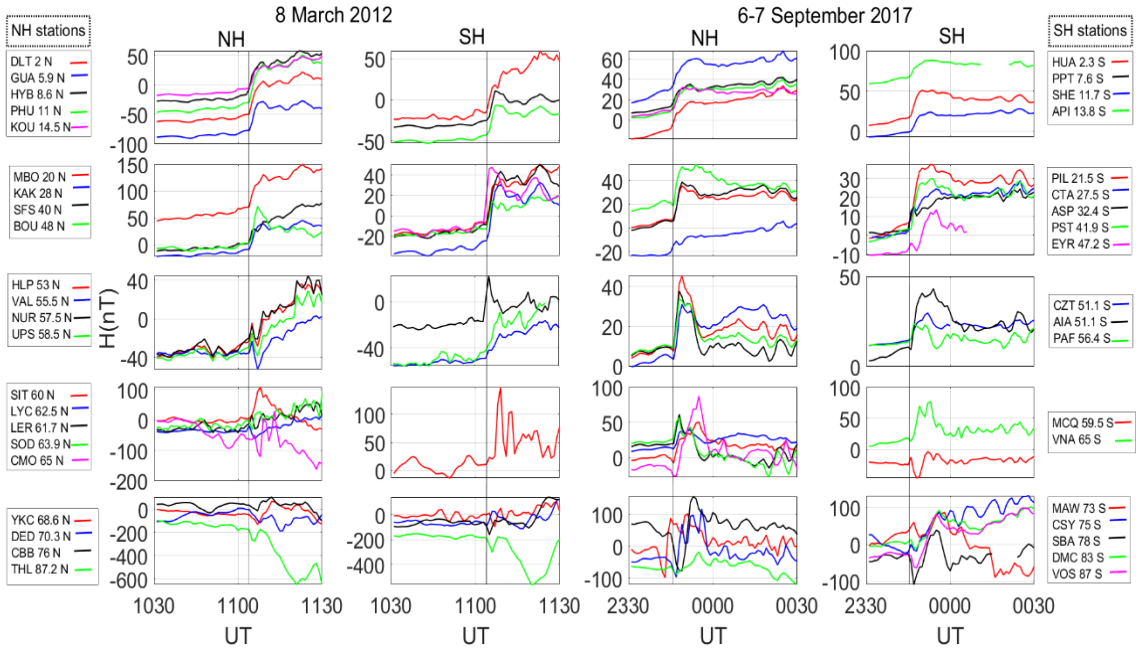

The above figure is an elaborate version of Figure 4.3 of Chapter 4 and explains the results of it in a vivid and elaborative way. It depicts the H-component perturbations of 41 magnetometer stations (in comparison to 29 magnetometers in the main manuscript) can be segregated into three distinct types of latitude-specific signatures in the latitude band of- 0º-45º, 45º-65º, and 65º-90º. This figure accommodates more stations and conforms to the similarity of the signatures in those specific latitude bands.

Figure SI-3. The H-component observations from 10 INTERMAGNET stations in the co-latitude band of 70º-90º during 4-days surrounding the supersubstorm events

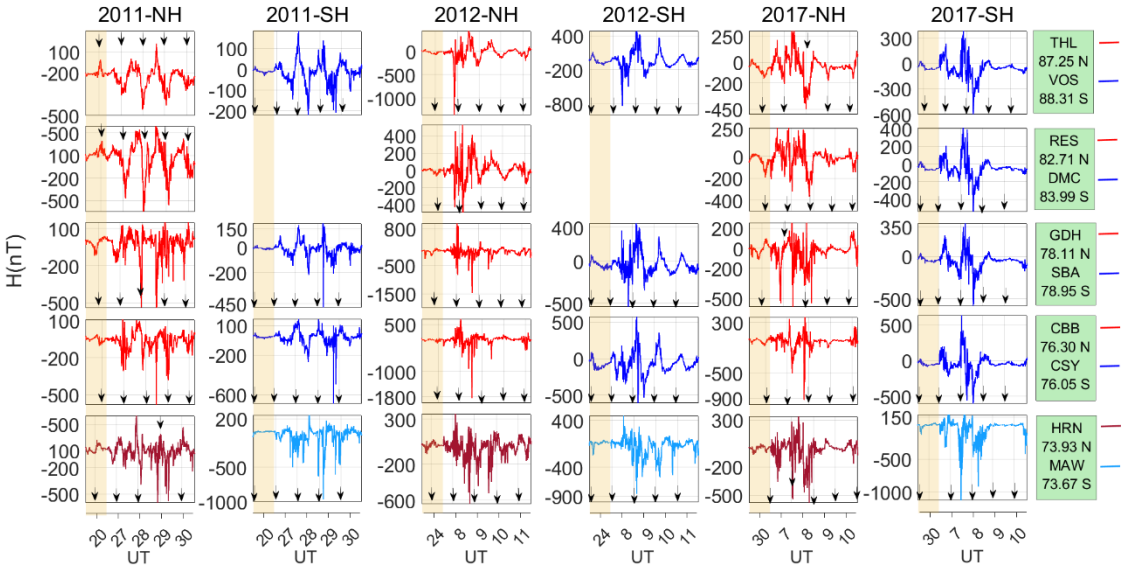

The above figure is a detailed version of Figure 4.5 of Chapter 4 and shows the individual H-component perturbations recorded in these stations in an elaborate way (in terms of both magnitude and phase). It shows the H-component perturbations recorded by the INTERMAGNET stations residing in the co-latitude band of 70o-90o separately during the four days surrounding the supersubstorm period.

SI-4. H-component observations from the latitude band of 15º -70º The H-component observations from 23 INTERMAGNET stations in the co-latitude band of 15º -70º during 4-days surrounding the supersubstorm events

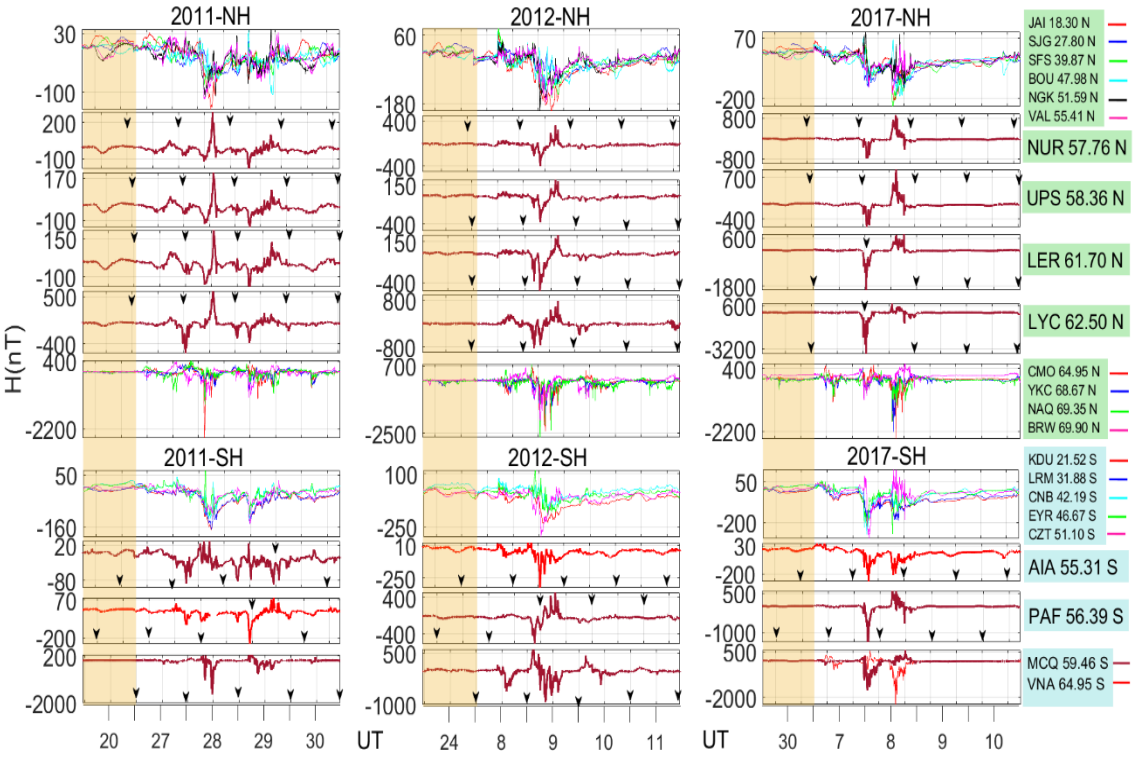

The above figure is an elaborate version of Figure 4.6 of the main manuscript. It shows the H-component perturbations recorded by the INTERMAGNET stations residing in the co-latitude band of 15o -70o separately during the four days surrounding the supersubstorm period. It is to be noted that this figure shows three distinct well-matched variations for bands of 63º-70º, 56º-63º, and 15º-55º for both hemispheres. This figure accommodates more stations (especially in the latitude band of 15º-55º and 63º-70º) and conforms to the similarity of the signatures in the specific latitude bands.

Figure SI-5. The latitudinal and longitudinal extensions of the DP2 current system as observed by the SUPERDARN radars during the 2012 and 2017 events

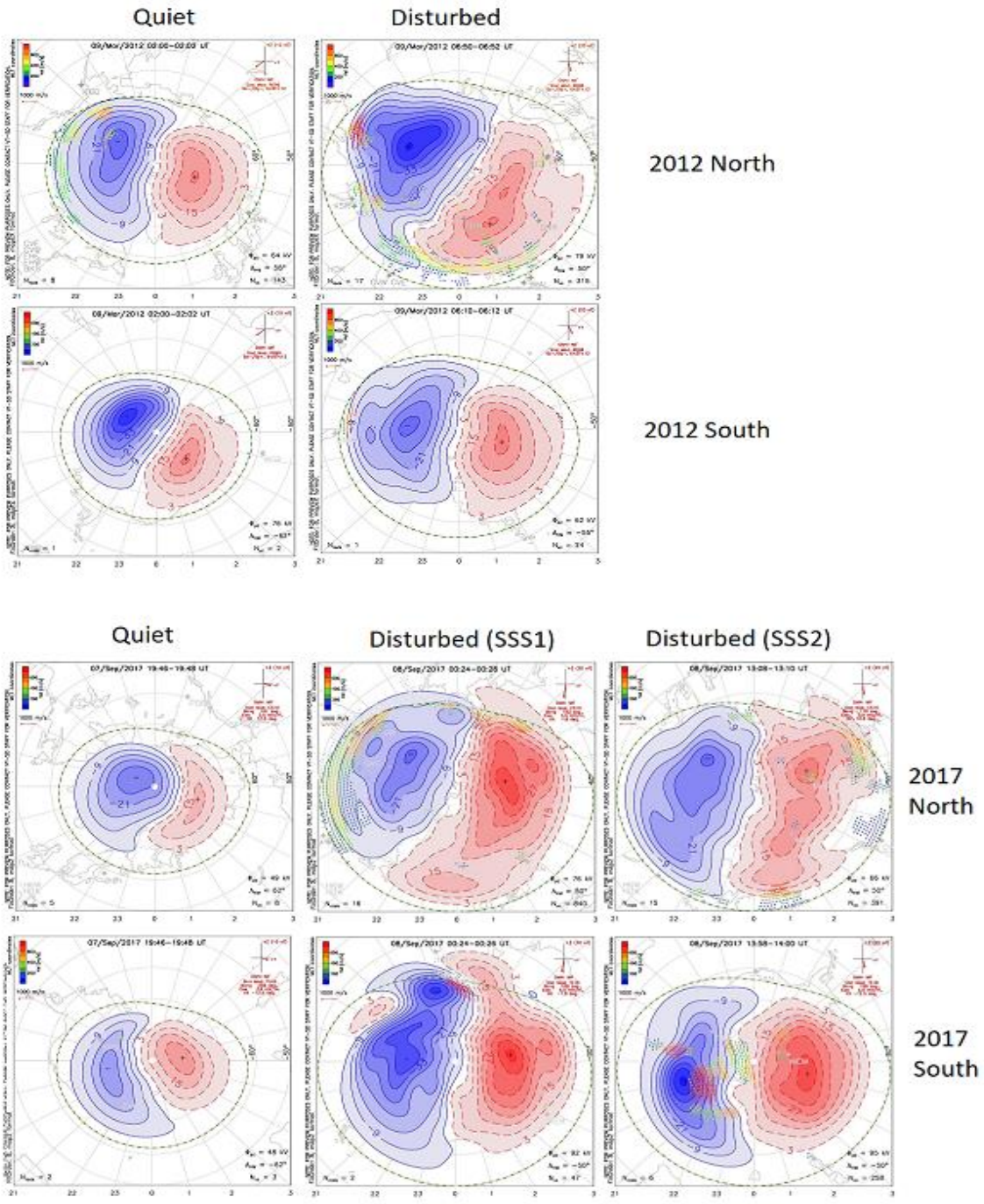

The variations in the DP2 just before the start of the expansion phase are given in the left panels and at the peak of the main phase in the right panels respectively, for the northern (upper panels) and southern (lower panels) hemispheres. Various label and notations have their usual meanings according to Cousins et al. (2013). The expansion of the concentric cells of the DP2 current system validates the hypothesis of equatorward extension of DP2 currents during the disturbed periods.

Figure SI-6. The D-component observations from 18 INTERMAGNET stations during 4-days surrounding the supersubstorm events

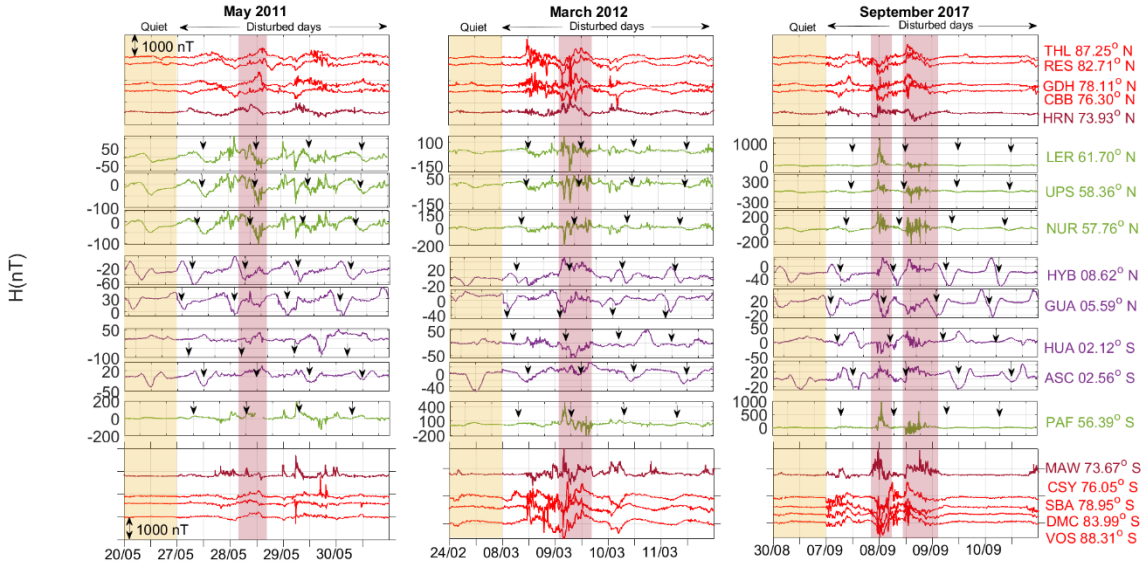

The above figure is an elaborate version of Figure 4.8 of the main manuscript. It shows the D-component perturbations recorded by the INTERMAGNET stations from the north pole to the south pole separately during the four days surrounding the supersubstorm period. It is to be noted that this figure separately shows the amplitudes in each panel and the normal phase variations. The red and brown curves represent the variations in D- component in the high latitudes, the blue curves in the mid-latitudes, and the violet curves in the low latitudes.

Appendix C

Summary table for the near earth space regions traversed by the satellites

This appendix provides supplementary material (SI) in continuation of Chapter 5, wherein the observations and results on small and large scale observations of plasma and field parameters from MMS, Cluster, and THEMIS during the 31 December 2015- 1 January geomagnetic storm are presented. The study also carries out estimations on important solar-wind-magnetosphere-ionosphere coupling phenomena like field-aligned currents, ideal and non-ideal electric fields, power loss, etc.

This appendix is in the form of a table, that entails the magnetospheric and near-earth space regions traversed by MMS1, Cluster-4, and THEMIS-A during 31 December 2015 and 1 January 2016. It also shows the distance of the respective spacecraft from the magnetopause. The columns represent-

1. Year
2. Day
3. Time
4. Distance from the Bow shock
5. Distance from the magnetopause
6. Magnetospheric regions

MMS1

Year	Day	Time	d_BS	d_M	Mag regions
2015	365	00:00:30	-3.62	0.27	D_Msheath
		08:00:30	-3.46	-0.12	D_Msheath
2015	365	08:01:30	-3.47	-0.13	D_Msphere
		14:18:30	-11.21	-7.38	D_Msphere
2015	365	14:19:30	-11.25	-7.42	D_Psphere
		15:08:30	-14.08	-10.04	D_Psphere
2015	365	15:09:30	-14.16	-10.12	N_Psphere
		16:27:30	-13.53	-9.09	N_Psphere

2015	365	16:28:30	-13.49	-9.04	D_Psphere
		16:42:30	-12.87	-8.38	D_Psphere
2015	365	16:43:30	-12.83	-8.33	D_Msphere
		23:17:30	-4.02	-0.03	D_Msphere
2015	365	23:18:30	-4.01	-0.02	D_Msheath
		23:21:30	-3.98	0.00	D_Msheath
		07:47:30	-3.47	-0.00	D_Msheath
		08:00:30	-3.47	-0.12	D_Msheath
2016	1	08:00:30	-3.47	-0.12	D_Msphere
		15:02:30	-14.13	-10.09	D_Psphere
2016	1	15:03:30	-14.20	-10.17	N_Psphere
		16:22:30	-13.49	-9.04	N_Psphere
2016	1	16:23:30	-13.45	-8.99	D_Psphere
		16:35:30	-12.93	-8.42	D_Psphere
2016	1	16:36:30	-12.89	-8.37	D_Msphere
		23:12:30	-4.05	-0.03	D_Msphere
2016	1	23:13:30	-4.04	-0.02	D_Msheath
		23:59:30	-3.60	0.34	D_Msheath

CLUSTER

Year	Day	Time	d_BS	d_M	Mag regions
2015	365	00:00:30	-11.80	-4.17	N_Msphere
2015	365	05:32:30	-7.62	0.17	N_Msphere
2015	365	05:33:30	-7.61	0.19	N_Msheath
2015	365	05:41:30	-7.52	0.27	N_Msheath
2015	365	05:42:30	-7.51	0.28	D_Msheath
2016	1	11:48:30	-5.06	0.05	D_Msheath
2016	1	11:49:30	-5.07	0.04	D_Msphere
2016	1	11:52:30	-5.10	0.00	D_Msphere
2016	1	19:30:30	-12.59	-7.37	D_Msphere
2016	1	19:31:30	-12.62	-7.39	N_Msphere
2016	1	23:59:30	-16.20	-9.99	N_Msphere

THEMIS-A

Year	Day	Time	d_BS	d_M	Mag regions
2015	365	00:00:00	-18.32	-11.21	N_Msphere
2015	365	01:46:00	-19.90	-12.08	N_Msphere
2015	365	01:47:00	-19.92	-12.09	Plasma_Sh

2015	365	15:45:00	-20.74	-13.97	Plasma_Sh
2015	365	15:46:00	-20.72	-13.97	N_Msphere
2015	365	18:43:00	-16.59	-11.47	N_Msphere
2015	365	18:44:00	-16.56	-11.45	N_Psphere
2015	365	19:49:00	-13.97	-10.05	N_Psphere
2015	365	19:50:00	-13.92	-10.03	D_Psphere
2015	365	20:49:00	-13.98	-9.61	D_Psphere
2015	365	20:50:00	-14.01	-9.62	N_Psphere
2016	1	01:47:00	-19.83	-11.97	N_Msphere
2016	1	01:48:00	-19.84	-11.98	Plasma_Sh
2016	1	15:42:00	-20.78	-14.02	Plasma_Sh
2016	1	15:43:00	-20.76	-14.01	N_Msphere
2016	1	18:39:00	-16.66	-11.53	N_Msphere
2016	1	18:40:00	-16.62	-11.51	N_Psphere
2016	1	19:46:00	-13.96	-10.06	N_Psphere
2016	1	19:47:00	-13.91	-10.04	D_Psphere
2016	1	20:46:00	-13.97	-9.59	D_Psphere
2016	1	20:47:00	-14.00	-9.59	N_Psphere
2016	1	21:32:00	-15.25	-9.86	N_Psphere
2016	1	21:33:00	-15.28	-9.87	N_Msphere
2016	1	23:59:00	-18.19	-11.02	N_Msphere

References

Abdu, M. A. (1997). Major phenomena of the equatorial ionosphere-thermosphere system under disturbed conditions. Journal of Atmospheric and Solar-Terrestrial Physics, 59(13), 1505–1519. doi:10.1016/s1364-6826(96)00152-6

Adhikari, B., Baruwal, P., & Chapagain, N. P. (2017). Analysis of supersubstorm events with reference to polar cap potential and polar cap index. Earth and Space Science, 4(1), 2–15. https://doi.org/10.1002/2016EA000217

Adhikari, B., Dahal, S., & Chapagain, N. P. (2017). Study of field-aligned current (FAC), interplanetary electric field component (Ey), interplanetary magnetic field component (Bz), and northward (x) and eastward (y) components of geomagnetic field during supersubstorm. Earth and Space Science, 4(5), 257–274. https://doi.org/10.1002/2017EA000258

Adhikari, B., Dahal, S., Sapkota, N., Baruwal, P., Bhattarai, B., Khanal, K., & Chapagain, N. P. (2018). Field-aligned current and polar cap potential and geomagnetic disturbances: A review of cross-correlation analysis. Earth and Space Science, 5, 440–455. https://doi.org/10.1029/2018EA000392

Adhikari, B., Kaphle, B., Adhikari, N. et al. Analysis of cosmic ray, solar wind energies, components of Earth's magnetic field, and ionospheric total electron content during solar superstorm of November 18–22, 2003. SN Appl. Sci. 1, 453 (2019). https://doi.org/10.1007/s42452-019-0474-8

Ahn, B. H., Akasofu, S. I., & Kamide, Y. (1983). The Joule heat production rate and the particle energy injection rate as a function of the geomagnetic indices AE and AL. Journal of Geophysical Research, 88(A8), 6275–6287. https://doi.org/10.1029/ja088ia08p06275

Ahn, B. H., Kroehl, H. W., Kamide, Y., & Gorney, D. J. (1989). Estimation of ionospheric electrodynamic parameters using ionospheric conductance deduced from bremsstrahlung X ray image data. Journal of Geophysical Research, 94(A3), 2565–2586. https://doi.org/10.1029/JA094iA03p02565

Akasofu, S. I. (1964). The development of the auroral substorm. Planetary and Space Science, 12(4), 273–282. https://doi.org/10.1016/0032-0633(64)90151-5

Akasofu, S. I. (1981). Energy coupling between the solar wind and the magnetosphere. Space Science Reviews, 28, 121-190.

Akasofu, S. I. (1981). Prediction of development of geomagnetic storms using the solar wind-magnetosphere energy coupling function ϵ. Planetary and Space Science, 29(11), 1151–1158. https://doi.org/10.1016/0032-0633(81)90121-5

Akasofu, S. I. (2017). Auroral substorms: Search for processes causing the expansion phase in terms of the electric current approach. Space Science Reviews, 212, 341-381.

Akasofu, S. I. (Ed.). (2012). Physics of magnetospheric substorms (Vol. 47). Springer Science & Business Media.

Akasofu, S.I., Sun, W. and Ahn, B.H. (2003). Comments on Some Long-Standing Problems in Storm/Substorm Studies. In Disturbances in Geospace: The Storm-Substorm Relationship (eds A.S. Sharma, Y. Kamide and G.S. Lakhina). https://doi.org/10.1029/142GM20

Akasofu, S.I., (2004) Several `Controversial' Issues on Substorms. Space Science Reviews 113, 1–40. https://doi.org/10.1023/B:SPAC.0000042938.57710.fb

Alken, P., Thébault, E., Beggan, C.D. et al. ((2021). International Geomagnetic Reference Field: the thirteenth generation. Earth Planets Space. 73, 49. https://doi.org/10.1186/s40623-020-01288-x.

Altschuler, M. D., Trotter, D. E., & Orrall, F. Q. (1972). Coronal holes. Solar Physics, 26, 354-365.

Amory-Mazaudier, C., Bolaji, O. S., & Doumbia, V. (2017). On the historical origins of the CEJ, DP2, and Ddyn current systems and their roles in the predictions of ionospheric responses to geomagnetic storms at equatorial latitudes. Journal of Geophysical Research: Space Physics, 122(7), 7827–7833. https://doi.org/10.1002/2017JA024132

Anderson, B. J., Korth, H.,Waters, C. L., Green, D. L.,Merkin, V. G., Barnes, R. J., & Dyrud, L. P. (2014). Development of large-scale Birkeland currents determined from the Active Magnetosphere and Planetary Electrodynamics Response Experiment. Geophysical Research Letters, 41, 3017–3025. https:doi.org/10.1002/2014GL059941

Anderson, B. J., Russell, C. T., Strangeway, R. J., Plaschke, F., Magnes, W., Fisher, D., Korth, H., Merkin, G.V, Barnes, R. J, Waters, C. L, Cohen, I. J., Westlake, J.H., Mauk, B. H., Leinweber, H.K., Greshman, D.J., Giles, B. L., Le, G., Torbert, R. B., Burch, J. L. (2016). Electrodynamic context of magnetopause dynamics observed by magnetospheric multiscale. Geophysical Research Letters, 43, 5988–5996. https://doi.org/10.1002/2016GL069577

Anderson, B. J., Russell, C. T., Strangeway, R. J., Plaschke, F., Magnes, W., Fisher, D., Korth, H., Merkin, G.V, Barnes, R. J, Waters, C. L, Cohen, I. J., Westlake, J.H., Mauk, B. H., Leinweber, H.K., Greshman, D.J., Giles, B. L., Le, G., Torbert, R. B., Burch, J. L. (2016). Electrodynamic context of magnetopause dynamics observed by magnetospheric multiscale. Geophysical Research Letters, 43, 5988–5996. https://doi.org/10.1002/2016GL069577

Angelopoulos, V., Sibeck, D., Carlson, C. W., McFadden, J. P., Larson, D., Lin, R. P., ... & Sigwarth, J. (2008). First results from the THEMIS mission. Space Sci. Rev., 141(1), 453-476. DOI 10.1007/s11214-008-9378-4

Antia, H. M., A. Bhatnagar and P. Ulmschneider (eds.). (2003). Lectures on Solar Physics, Series: Lecture Notes in Physics 619, Springer-Verlag Berlin Heidelberg. ISBN: 9783540015284,9783540369639

Araki, T. (1977). Global structure of geomagnetic sudden commencements. Planetary and Space Science, 25(4), 373–384. https://doi.org/10.1016/0032-0633(77)90053-8

Araki, T. (1994). A physical model of the geomagnetic sudden commencement. Geophysical Monograph-American Geophysical Union, 81, 183.

Araki, T., & Shinbori, A. (2016). Relationship between solar wind dynamic pressure and amplitude of geomagnetic sudden commencement (SC). Earth Planets and Space, 68(1), 1–7. https://doi.org/10.1186/s40623-016-0444-y

Asano, Y., T. Mukai, M. Hoshino, Y. Saito, H. Hayakawa, and T. Nagai (2004), Current sheet structure around the near-Earth neutral line observed by Geotail, J. Geophys. Res., 109, A02212, doi: 10.1029/2003JA010114.

Asplund, M., Grevesse, N., Sauval, A. J., & Scott, P. (2009). The chemical composition of the Sun. Annual review of astronomy and astrophysics, 47, 481-522.

Aunai, N., Hesse, M., & Kuznetsova, M. (2013). Electron nongyrotropy in the context of collisionless magnetic reconnection. Physics of Plasmas, 20(9), 092903. doi:10.1063/1.4820953 \

Auster, H. U., et al. (2008), The THEMIS fluxgate magnetometer, Space Sci. Rev., 141, 235–264. DOI 10.1007/s11214-008-9365-9

Axford, W. I. (1962). The interaction between the solar wind and the Earth's magnetosphere. Journal of Geophysical Research, 67, 3791 3796.

Axford, W. I. (1964). Viscous interaction between the solar wind and the earth's magnetosphere. Planetary and Space Science, 12(1), 45-53.

Axford, W. I., & Hines, C. O. (1961). A unifying theory of high-latitude geophysical phenomena and geomagnetic storms. Canadian Journal of Physics, 39(10), 1433-1464. https://doi.org/10.1139/p61-172

Baker, D. N. (1996). Solar wind-magnetosphere drivers of space weather. Journal of Atmospheric and Terrestrial Physics, 58(14), 1509–1526. https://doi.org/10.1016/0021-9169(96)00006-2

Baker, D. N. (1998). What is space weather?. Advances in Space Research, 22(1), 7-16.

Baker, D. N., Jaynes, A. N., Turner, D. L., Nakamura, R., Schmid, D., Mauk, B. H., Cohen, I. J. , Fennell, J. F., Blake, J. B. , Strangeway, R. J., Russell, C. T., Torbert, R. B., Dorelli, J. C. , Gershman, D. J., Giles, B. L. and Burch J. L. (2016). A telescopic and microscopic examination of acceleration in the June 2015 geomagnetic storm:

Magnetospheric Multiscale and Van Allen Probes study of substorm particle injection, Geophys. Res. Lett., 43, 6051– 6059, doi:10.1002/2016GL069643.

Baker, D. N., Pulkkinen, T. I., Angelopoulos, V., Baumjohann, W., & McPherron, R. L. (1996). Neutral line model of substorms: Past results and present view. Journal of Geophysical Research, 101(A6), 12975–13010. https://doi.org/10.1029/95JA03753

Baker, D. N., Pulkkinen, T. I., Hesse, M., & McPherron, R. L. (1997). A quantitative assessment of energy storage and release in the Earth's magnetotail. Journal of Geophysical Research, 102(A4), 7159–7168. https://doi.org/10.1029/96JA03961

Balan, N., & Bailey, G. J. (1995). Equatorial plasma fountain and its effects: Possibility of an additional layer. Journal of Geophysical Research, 100(A11), 21421– 21432. https://doi.org/10.1029/95JA01555

Balan, N., Liu, L., & Le, H. (2018). A brief review of equatorial ionization anomaly and ionospheric irregularities. Earth and Planetary Physics, 2(4), 257-275.

Balogh, A., Gosling, J. T., Jokipii, J., Kallenbach, R., & Kunow, H. (Eds.). (1999). Corotating interaction regions (Vol. 7). Springer Science & Business Media.

Bartels, J., Heck, N. H., & Johnston, H. F. (1939). The three-hour-range index measuring geomagnetic activity. Journal of Geophysical Research, 44(4), 411. doi:10.1029/te044i004p00411

Baumjohann, W. (1982). Ionospheric and field-aligned current systems in the auroral zone: a concise review. Advances in Space Research, 2(10), 55–62. doi:10.1016/0273-1177(82)90363-5

Baumjohann, W. (2002), Modes of convection in the magnetotail, Phys. Plasmas, 9(9), 3665– 3667, doi:10.1063/1.1499116.

Baumjohann, W., & Kamide, Y. (1984). Hemispherical Joule heating and the AE indices. Journal of Geophysical Research, 89(A1), 383–388. https://doi.org/10.1029/JA089iA01p00383

Baumjohann, W., & Treumann, R. A. (2012). Basic space plasma physics. Imperial College Press, ISBN: 978-1-84816-894-7. DOI:10.1142/P850.

Baumjohann, W., Paschmann, G., Sckopke, N., Cattell, C. A., & Carlson, C. W. (1988). Average ion moments in the plasma sheet boundary layer. Journal of Geophysical Research, 93(A10), 11507. doi: 10.1029/ja093ia10p11507

Bauske R. and Prolss, G. W. (1997). Modelling the ionospheric response to travelling atmospheric disturbances, J. Geophys. Res., 102, 14555–14562. https://doi.org/10.1029/97JA00941.

Belehaki, A., Mavromickalaki, H., Sarafopoulos, D. V., & Sarris, E. T. (1995). Energy dissipation during a small substorm. Annales Geophysicae, 13(5), 494–504. https://doi.org/10.1007/s00585-995-0494-0

Berchem, J., & Russell, C. T. (1982). The thickness of the magnetopause current layer: ISEE 1 and 2 observations. Journal of Geophysical Research: Space Physics, 87(A4), 2108-2114.

Biskamp, D. (1996). Magnetic reconnection in plasmas. Astrophysics and Space Science, 242, 165-207.

Biswas A, Karak BB, Cameron R (2022) Toroidal flux loss due to flux emergence explains why solar cycles rise differently but decay in a similar way. Phys Rev Lett 129(24):241102. https://doi.org/10.1103/PhysRevLett.129.241102

Bonnell, J. W., Mozer, F. S., Delory, G. T., Hull, A. J., Ergun, R. E., Cully, C. M., … Harvey, P. R. (2008). The Electric Field Instrument (EFI) for THEMIS. Space Science Reviews, 141(1-4), 303–341. doi: 10.1007/s11214-008-9469-2

Borovsky, J. E. (2008). The rudiments of a theory of solar wind/magnetosphere coupling derived from first principles. Journal of Geophysical Research, 113(A8), A08228. https://doi.org/10.1029/2007JA012646

Borovsky, J. E. (2021). Is our understanding of solar-wind/magnetosphere coupling satisfactory?. Frontiers in Astronomy and Space Sciences, 8, 634073.

Borovsky, J. E. (2021). Is our understanding of solar-wind/magnetosphere coupling satisfactory?. Frontiers in Astronomy and Space Sciences, 8, 634073. doi.org/10.3389/fspas.2021.634073

Boström, R. (1964), A model of the auroral electrojets, J. Geophys. Res., 69(23), 4983– 4999, doi:10.1029/JZ069i023p04983.

Boteler D. H. and Pirjola R. J., "Modelling geomagnetically induced currents produced by realistic and uniform electric fields," in IEEE Transactions on Power Delivery, vol. 13, no. 4, pp. 1303-1308, Oct. 1998, doi: 10.1109/61.714500.

Boyle, C. B., Reiff, P. H., & Hairston, M. R. (1997). Empirical polar cap potentials. Journal of Geophysical Research, 102(A1), 111–125. https://doi.org/10.1029/96JA01742

Britannica, The Editors of Encyclopaedia. "solar flare". Encyclopedia Britannica, 9 Mar. 2023, https://www.britannica.com/science/solar-flare. Accessed 24 March 2023.

Buonsanto, M. J. (1999). Ionospheric storms—A review. Space Science Reviews, 88(3-4), 563-601. https://doi.org/10.1023/A:1005107532631.

Burch, J. L. (2016). A telescopic and microscopic examination of acceleration in the June 2015 geomagnetic storm: Magnetospheric Multiscale and Van Allen Probes study of substorm particle injection. Geophysical Research Letters, 43(12), 6051-6059. https://doi.org/10.1002/2016GL069643

Burch, J. L., & Phan, T. D. (2016). Magnetic reconnection at the dayside magnetopause: Advances with MMS. Geophysical Research Letters, 43(16), 8327-8338. https://doi.org/10.1002/2016GL069787

Burch, J. L., Moore, T. E., Torbert, R. B., & Giles, B. (2016). Magnetospheric multiscale overview and science objectives. Space Science Reviews, 199(1), 5-21. DOI 10.1007/s11214-015-0164-9

Burlaga, L.F, Magnetic Clouds, in Physics of the Inner Heliosphere, Schwenn, R. and Marsch, E., Eds., New York: Springer, 1991, vol. 2, p. 1. 38.

Burlaga, L.F., Sittler, E., Mariani, F., and Schwenn, R., Magnetic Loop behind an Interplanetary Shock: Voyager, Helios, and IMP 8 Observations, J. Geophys. Res., 1981, vol. 86, p. 6673. 34.

Burton, R. K., McPherron, R. L., & Russell, C. T. (1975). An empirical relationship between interplanetary conditions and Dst. Journal of Geophysical Research, 80(31), 4204–4214. https://doi.org/10.1029/JA080i031p04204

Campbell, W. H., (2003). Introduction to Geomagnetic Fields. Cambridge University Press

Cane, H. V., Richardson, I. G., & St. Cyr, O. C. (2000). Coronal mass ejections, interplanetary ejecta and geomagnetic storms. Geophysical Research Letters, 27(21), 3591–3594. doi:10.1029/2000gl000111

Cane, H.V. and Richardson, I.G., What Caused the Large Geomagnetic Storm of November 1978?, J. Geophys. Res., 1997, vol. 102, no. A8, p. 17445.

Cao, X., Halekas, J. S., Chu, F., Kistler, M., Poppe, A. R., & Glassmeier, K. H. (2020). Plasma convection in the terrestrial magnetotail lobes measured near the Moon's orbit. Geophysical Research Letters, 47(20), e2020GL090217.

Carpenter, D. L., & Park, C. G. (1973). On what ionospheric workers should know about the plasmapause-plasmasphere. Reviews of Geophysics, 11(1), 133-154.

Carter, B. A., Yizengaw, E., Pradipta, R., Halford, A. J., Norman, R., & Zhang, K. (2015). Interplanetary shocks and the resulting geomagnetically induced currents at the equator. Geophysical Research Letters, 42(16), 6554–6559. https://doi.org/10.1002/2015GL065060

Carter, B. A., Yizengaw, E., Pradipta, R., Weygand, J. M., Piersanti, M., Pulkkinen, A., et al. (2016). Geomagnetically induced currents around the world during the 17 March 2015 storm. J. Geophys. Res.- Space Physics, 121(10), 10496–10507. https://doi.org/10.1002/2016JA023344

Carter, J. A., Milan, S. E., Fogg, A. R., Paxton, L. J., & Anderson, B. J. (2018). The association of high- latitude dayside aurora with NBZ field- aligned currents. Journal of Geophysical Research: Space Physics, 123(5), 3637-3645. https://doi.org/10.1029/2017JA025082

Cassak, P. A., & Shay, M. A. (2007). Scaling of asymmetric magnetic reconnection: General theory and collisional simulations. Physics of Plasmas, 14(10), 102114. doi:10.1063/1.2795630

Chapman, S., and Ferraro, V. C. A. (1933), A new theory of magnetic storms, Terr. Magn. Atmos. Electr., 38(2), 79– 96, doi:10.1029/TE038i002p00079.

Chapmann, S., & Ferraro, V. C. A. (1931). A new theory of magnetic storms, 1, the initial phase. J. Geophys. Res, 36, 77.

Che, H., Schiff, C., Le, G., Dorelli, J. C., Giles, B. L., & Moore, T. E. (2018). Quantifying the effect of non-Larmor motion of electrons on the pressure tensor. Physics of Plasmas, 25(3), 032101. doi:10.1063/1.5016853

Chen, C. J. (2011). Physics of solar energy. John Wiley & Sons.

Chen, L. J., Bessho, N., Lefebvre, B., Vaith, H., Fazakerley, A., Bhattacharjee, A., ... & Torbert, R. (2008). Evidence of an extended electron current sheet and its neighboring magnetic island during magnetotail reconnection. Journal of Geophysical Research: Space Physics, 113(A12). https://doi.org/10.1029/2008JA013385

Chen, Y., Wu, M., Wang, G., Schmid, D., Zhang, T., Nakamura, R., ... & Russell, C. T. (2019). Carriers of the field- aligned currents in the plasma sheet boundary layer: An MMS multicase study. Journal of Geophysical Research: Space Physics, 124(4), 2873-2886. https://doi.org/10.1029/2018JA026216

Cheng, Z. W., Zhang, J. C., Shi, J. K., Kistler, L. M., Dunlop, M., Dandouras, I., & Fazakerley, A. (2016). The particle carriers of field- aligned currents in the Earth's magnetotail during a substorm. Journal of Geophysical Research: Space Physics, 121(4), 3058-3068. https://doi.org/10.1002/2015JA022071

Chi, P. J., Russell, C. T., Raeder, J., Zesta, E., Yumoto, K., Kawano, H., et al. (2001). Propagation of the preliminary reverse impulse of sudden commencements to low latitudes. Journal of Geophysical Research, 106(A9), 18857–18864. https://doi.org/10.1029/2001ja900071

Chisham, G., Lester, M., Milan, S., Freeman, M., Bristow, W., Grocott, A., & Walker, A. (2007). A decade of the super dual auroral radar network (superdarn): Scientific achievements, new techniques and future directions. Surveys in Geophysics, 28(1), 33–109.https://doi. org/10.1007/s10712-007-9017-8.

Clilverd, M. A., Rodger, C. J., Brundell, J. B., Dalzell, M., Martin, I., Mac Manus, D. H., et al. (2018). Long-lasting geomagnetically induced currents and harmonic distortion observed in New Zealand during the 7–8 September 2017 disturbed period. Space Weather, 16(6), 704–717. https://doi.org/10.1029/2018SW001822

Cole, K. D. (1962). Joule heating of the upper atmosphere. Australian Journal of Physics, 15(2), 223–235. https://doi.org/10.1029/2018SW001956

Cole, K. D. (1966). Magnetic storms and associated phenomena. Space Science Reviews, 5(6), 699–770. https://doi.org/10.1007/BF00173103

Cole, K. D. (1971). Electrodynamic heating and movement of the thermosphere. Planetary and Space Science, 19(1), 59–75. https://doi.org/10.1016/0032-0633(71)90067-5

Coster, A. J., Erickson, P. J., & Lanzerotti, L. J. (Eds.). (2021). Space Physics and Aeronomy, Space Weather Effects and Applications (Vol. 5). John Wiley & Sons.

Courtillot, V., & Le Mouel, J. L. (1988). Time variations of the Earth's magnetic field: From daily to secular. Annual Review of Earth and Planetary Sciences, 16(1), 389-476.

Cousins, E. D. P., Matsuo, T., & Richmond, A. D. (2013). SuperDARN assimilative mapping. Journal of Geophysical Research: Space Physics, 118(12), 7954–7962. https://doi.org/10.1002/2013JA019321

Cowley F.R.S. and W.H. Stenley (2015). Dungey's Reconnection Model of the Earth's Magnetosphere: The First 40 Years. In: Cowley FRS, S., Southwood, D., Mitton, S. (eds) Magnetospheric Plasma Physics: The Impact of

Jim Dungey's Research. Astrophysics and Space Science Proceedings, vol 41. Springer, Cham. https://doi.org/10.1007/978-3-319-18359-6_1

Cowley, S. W. H. (2000). Magnetosphere-ionosphere interactions: A tutorial review. Geophysical Monograph Series, 91–106. doi:10.1029/gm118p0091

Cowley, S.W.H. and Southwood, D.J. (1980), Some properties of a steady-state geomagnetic tail. Geophys. Res. Lett., 7: 833-836. https://doi.org/10.1029/GL007i010p00833

Cox, A., Doell, R.R; Long period variations of the geomagnetic field. Bulletin of the Seismological Society of America (1964); 54 (6B): 2243–2270. doi: https://doi.org/10.1785/BSSA05406B2243

Cranmer, S. R. (2009). Coronal holes. Living Reviews in Solar Physics, 6, 1-66.

Cranmer, S.R. Coronal Holes. Living Rev. Sol. Phys. 6, 3 (2009). https://doi.org/10.12942/lrsp-2009-3

Cummings, W. D., & Dessler, A. J. (1967). Field- aligned currents in the magnetosphere. Journal of geophysical research, 72(3), 1007-1013.

Cummings, W. D., and Dessler, A. J. (1967), Field-aligned currents in the magnetosphere, J. Geophys. Res., 72(3), 1007–1013, doi:10.1029/JZ072i003p01007.

Curto JJ, 2020. Geomagnetic solar flare effects: a review. J. Space Weather Space Clim. 2020, 10, 27, https://doi.org/10.1051/swsc/2020027

D'Amicis R, Telloni D and Bruno R (2020) The Effect of Solar-Wind Turbulence on Magnetospheric Activity. Front. Phys. 8:604857. doi: 10.3389/fphy.2020.604857

Dandouras, I. (2021). Ion outflow and escape in the terrestrial magnetosphere: Cluster advances. Journal of Geophysical Research: Space Physics, 126, e2021JA029753. https://doi.org/10.1029/2021JA029753.

Dashora, N., Sharma, S., Dabas, R. S., Alex, S., & Pandey, R. (2009). Large enhancements in low latitude total electron content during 15 May 2005 geomagnetic storm in Indian zone. Annales Geophysicae, 27(5), 1803–1820. doi:10.5194/angeo-27-1803-2009

Dashora, N., Suresh, S., & Niranjan, K. (2019). Interhemispheric asymmetry in response of low-latitude ionosphere to perturbation electric fields in the main phase of geomagnetic storms. Journal of Geophysical Research: Space Physics, 124(8), 7256–7282. https://doi.org/10.1029/2019JA026671

Davis, T. N., & Sugiura, M. (1966). Auroral electrojet activity index AE and its universal time variations. Journal of Geophysical Research, 71(3), 785–801. https://doi.org/10.1029/JZ071i003p00785

De Forest, S. E., & McIlwain, C. E. (1971). Plasma clouds in the magnetosphere. Journal of Geophysical Research, 76(16), 3587-3611.

Despirak, I. V., Kleimenova, N. G., Gromova, L. I., Gromov, S. V., & Malysheva, L. M. (2020). Supersubstorms during storms of September 7–8, 2017. Geomagnetism and Aeronomy, 60(3), 292–300. https://doi.org/10.1134/S0016793220030044

Despirak, I. V., Lyubchich, A. A., & Kleimenova, N. G. (2019). Supersubstorms and conditions in the solar wind. Geomagnetism and Aeronomy, 59(2), 170–176. https://doi.org/10.1134/S0016793219020075

Despirak, I. V., Lyubchich, A. A., Kleimenova, N. G., Gromova, L. I., Gromov, S. V., & Malysheva, L. M. (2021). Longitude geomagnetic effects of the supersubstorms during the magnetic storm of March 9, 2012. Bulletin of the Russian Academy of Sciences: Physics, 85(3), 246–251. https://doi.org/10.3103/s1062873821030096

Dessler, A. J. (1961). The stability of the interface between the solar wind and the geomagnetic field. Journal of Geophysical Research, 66(10), 3587–3590. https://doi.org/10.1029/JZ066i010p03587

Dimmock, A. P., Rosenqvist, L., Hall, J. O., Viljanen, A., Yordanova, E., Honkonen, I., et al. (2019). The GIC and geomagnetic response over Fennoscandia to the 7–8 September 2017 geomagnetic storm. Space Weather, 17(7), 989–1010. https://doi.org/10.1029/2018sw002132

Drake, J. F., Swisdak, M., Che, H., & Shay, M. A. (2006). Electron acceleration from contracting magnetic islands during reconnection. Nature, 443(7111), 553–556. doi: 10.1038/nature05116

Dungey, J. W. (1961). Interplanetary magnetic field and the auroral zones. Physical Review Letters, 6(2), 47. doi:10.1103/physrevlett.6.47

Dunlop, M. W., Balogh, A., Glassmeier, K. H., & Robert, P. (2002). Four- point Cluster application of magnetic field analysis tools: The Curlometer. Journal of Geophysical Research: Space Physics, 107(A11), SMP-23. https://doi.org/10.1029/2001JA005088

Dunlop, M. W., Dong, X. C., Wang, T. Y., Eastwood, J. P., Robert, P., Haaland, S., ... & De Keyser, J. (2021). Curlometer technique and applications. Journal of Geophysical Research: Space Physics, 126(11), e2021JA029538. https://doi.org/10.1029/2021JA029538

Eastman, T. E., Frank, L. A., Peterson, W. K., & Lennartsson, W. (1984). The plasma sheet boundary layer. Journal of Geophysical Research: Space Physics, 89(A3), 1553-1572.

Eastman, T. E., Hones Jr, E. W., Bame, S. J., & Asbridge, J. R. (1976). The magnetospheric boundary layer: Site of plasma, momentum and energy transfer from the magnetosheath into the magnetosphere. Geophysical research letters, 3(11), 685-688.

Eastwood, J. P., Hietala, H., Toth, G., Phan, T. D., & Fujimoto, M. (2014). What Controls the Structure and Dynamics of Earth's Magnetosphere? Space Science Reviews, 188(1-4), 251–286. doi:10.1007/s11214-014-0050-x

Ebihara, Y. (2019). Simulation study of near-Earth space disturbances: 2. Auroral substorms. Prog. Earth Planet Science, 6(1), 24. https://doi.org/10.1186/s40645-019-0273-2

Ebihara, Y., & Tanaka, T. (2022). Where is Region 1 field-aligned current generated? Journal of Geophysical Research: Space Physics, 127, e2021JA029991. https://doi.org/10.1029/2021JA029991

Echer, E., Gonzalez, W. D., Tsurutani, B. T., & Gonzalez, A. L. C. (2008). Interplanetary conditions causing intense geomagnetic storms ($Dst \leq -100$ nT) during solar cycle 23 (1996–2006). Journal of Geophysical Research, 113(A5), A05221. https://doi.org/10.1029/2007JA012744

Edwards, T. R., Weimer, D. R., Olsen, N., Lühr, H., Tobiska, W. K., & Anderson, B. J. (2020). A third generation field-aligned current model. Journal of Geophysical Research: Space Physics, 125. e2019JA027249 https://doi.org/10.1029/2019JA027249

Egedal J, Le A, Daughton W, Wetherton B, Cassak PA, Chen LJ, Lavraud B, Torbert RB, Dorelli J, Gershman DJ, Avanov LA (2016). Spacecraft Observations and Analytic Theory of Crescent-Shaped Electron Distributions in Asymmetric Magnetic Reconnection. Phys Rev Lett. 117(18):185101. doi: 10.1103/PhysRevLett.117.185101.

Elsasser, W. M. (1939). On the origin of the earth's magnetic field. Physical Review, 55(5), 489.

Escoubet, C. P., Fehringer, M., & Goldstein, M. (2001). Introduction the Cluster mission. In Ann. Geophys., 19, 10/12, 1197-1200. https://doi.org/10.5194/angeo-19-1197-2001

Escoubet, C. P., Masson, A., Laakso, H., Goldstein, M. L., Dimbylow, T., Bogdanova, Y. V., ... & Taylor, M. G. G. T. (2021). Cluster after 20 years of operations: Science highlights and technical challenges. https://doi.org/10.1029/2021JA029474

Evans, D. S., Maynard, N. C., Trøim, J., Jacobsen, T., & Egeland, A. (1977). Auroral vector electric field and particle comparisons, 2, Electrodynamics of an arc. Journal of Geophysical Research, 82(16), 2235–2249. https://doi.org/10.1029/JA082i016p02235

Fairfield, D. H. (1971). Average and unusual locations of the Earth's magnetopause and bow shock. Journal of Geophysical Research, 76(28), 6700-6716.

Fairfield, D. H., Baumjohann, W., Paschmann, G., Lühr, H., & Sibeck, D. G. (1990). Upstream pressure variations associated with the bow shock and their effects on the magnetosphere. Journal of Geophysical Research: Space Physics, 95(A4), 3773-3786.

Farris, M. H., & Russell, C. T. (1994). Determining the standoff distance of the bow shock: Mach number dependence and use of models. Journal of Geophysical Research, 99(A9), 17681. doi:10.1029/94ja01020

Fedrizzi, M., Fuller- Rowell, T. J., Codrescu, M., Maruyama, N., & Khalsa, H. (2008). Sources of F- region height changes during geomagnetic storms at mid- latitudes. In P. M. Kintner, Jr., A. J. Coster, T. J. Fuller-Rowell, A. J. Mannucci, M. Mendillo, & R. Heelis (Eds.), Midlatitude ionospheric dynamics and disturbances, Geophysical Monograph Series (Vol. 181, pp. 247–258). Washington, DC: American Geophysical Union. https://doi.org/10.1029/181GM22

Fejer, B. G., Blanc, M., & Richmond, A. D. (2017). Post-storm middle and low-latitude ionospheric electric fields effects. Space Science Reviews, 206(1–4), 407–429. https://doi.org/10.1007/s11214-016-0320-x

Feldman, U., Landi, E., and Schwadron, N. A. (2005), On the sources of fast and slow solar wind, J. Geophys. Res., 110, A07109, doi:10.1029/2004JA010918.

Feldstein, Y. I., Grafe, A., Gromova, L. I., and Popov, V. A. (1997), Auroral electrojets during geomagnetic storms, J. Geophys. Res., 102 (A7), 14223– 14235, doi:10.1029/97JA00577.

Feldstein, Y. I., Popov, V. A., Cumnock, J. A., Prigancova, A., Blomberg, L. G., Kozyra, J. U., ... & Levitin, A. E. (2006). Auroral electrojets and boundaries of plasma domains in the magnetosphere during magnetically disturbed intervals. Ann. Geophys. 24(8): 2243-2276. https://doi.org/10.5194/angeo-24-2243-2006

Feynman, J., and Ruzmaikin, A. (2014), The Centennial Gleissberg Cycle and its association with extended minima, J. Geophys. Res. Space Physics, 119, 6027– 6041, doi:10.1002/2013JA019478.

Forbes, J. M. (1981). The equatorial electrojet. Reviews of Geophysics, 19(3), 469-504.

Forbes, J. M., & Lindzen, R. S. (1976). Atmospheric solar tides and their electrodynamic effects—I. The global Sq current system. Journal of Atmospheric and Terrestrial Physics, 38(9-10), 897-910. doi.org/10.1016/0021-9169(76)90073-8

Forbes, J. M., Palo, S. E., & Zhang, X. (2000). Variability of the ionosphere. Journal of Atmospheric and Solar-Terrestrial Physics, 62(8), 685-693.

Forbes, J.M, Lindzen, R.S. (1976). Atmospheric solar tides and their electrodynamic effects—I. The global Sq current system, Journal of Atmospheric and Terrestrial Physics, 38 (9–10), 897-910, https://doi.org/10.1016/0021-9169(76)90073-8.

Frank, L. A. (1967), On the extraterrestrial ring current during geomagnetic storms, J. Geophys. Res., 72(15), 3753–3767, doi:10.1029/JZ072i015p03753.

Frank, L. A. (1971). Plasma in the earth's polar magnetosphere. Journal of Geophysical Research, 76(22), 5202-5219.

Frank, L. A., L. McPherron, R. J. DeCoster, B. G. Burek, K. L. Ackerson, and C. T. Russell (1981), Field-aligned currents in the Earth’s magnetotail, J. Geophys. Res., 86, 687–700, doi: 10.1029/JA086iA02p00687.

Frühauff, D., & Glassmeier, K.-H. (2017). The plasma sheet as natural symmetry plane for dipolarization fronts in the Earth's magnetotail. Journal of Geophysical Research: Space Physics, 122, 11,373– 11,388. https://doi.org/10.1002/2017JA024682

Fu, H. S., Cao, J. B., Cao, D., Wang, Z., Vaivads, A., Khotyaintsev, Y. V., et al. (2019). Evidence of magnetic nulls in electron diffusion region. Geophysical Research Letters, 46, 48– 54. https://doi.org/10.1029/2018GL080449

Fu, H. S., Cao, J. B., Vaivads, A., Khotyaintsev, Y. V., Andre, M., Dunlop, M., … Eriksson, E. (2016). Identifying magnetic reconnection events using the FOTE method. Journal of Geophysical Research: Space Physics, 121(2), 1263–1272. doi:10.1002/2015ja021701

Fu, H. S., Khotyaintsev, Y. V., Vaivads, A., André, M., and Huang, S. Y. (2012), Electric structure of dipolarization front at sub-proton scale, Geophys. Res. Lett., 39, L06105, doi:10.1029/2012GL051274.

Fu, H. S., Khotyaintsev, Y. V., Vaivads, A., André, M., and Huang, S. Y. (2012), Electric structure of dipolarization front at sub-proton scale, Geophys. Res. Lett., 39, L06105, doi:10.1029/2012GL051274.

Fu, H. S., Khotyaintsev, Y. V., Vaivads, A., André, M., and Huang, S. Y. (2012), Occurrence rate of earthward-propagating dipolarization fronts, Geophys. Res. Lett., 39, L10101, doi:10.1029/2012GL051784.

Fu, H. S., Vaivads, A., Khotyaintsev, Y. V., André, M., Cao, J. B., Olshevsky, V., … Retinò, A. (2017). Intermittent energy dissipation by turbulent reconnection. Geophysical Research Letters, 44(1), 37–43. doi:10.1002/2016gl071787

Fu, H. S., Vaivads, A., Khotyaintsev, Y. V., André, M., Cao, J. B., Olshevsky, V., Eastwood, J. P., and Retinò, A. (2017), Intermittent energy dissipation by turbulent reconnection, Geophys. Res. Lett., 44, 37– 43, doi:10.1002/2016GL071787.

Fu, H. S., Vaivads, A., Khotyaintsev, Y. V., Olshevsky, V., André, M., Cao, J. B., … Lapenta, G. (2015). How to find magnetic nulls and reconstruct field topology with MMS data? Journal of Geophysical Research: Space Physics, 120(5), 3758–3782. doi:10.1002/2015ja021082

Fu, H. S., Xu, Y., Vaivads, A., & Khotyaintsev, Y. V. (2019). Super-efficient Electron Acceleration by an Isolated Magnetic Reconnection. The Astrophysical Journal, 870(2), L22. doi:10.3847/2041-8213/aafa75

Fu, H. S., Zhao, M. J., Yu, Y., & Wang, Z. (2020). A new theory for energetic electron generation behind dipolarization front. Geophysical Research Letters. doi:10.1029/2019gl086790

Fu, W. D., Fu, H. S., Cao, J. B., Yu, Y., Chen, Z. Z., & Xu, Y. (2022). Formation of rolling-pin distribution of suprathermal electrons behind dipolarization fronts. Journal of Geophysical Research: Space Physics, 127, e2021JA029642. https://doi.org/10.1029/2021JA029642

Fujita, S. (2019). Response of the magnetosphere–ionosphere system to sudden changes in solar wind dynamic pressure. Reviews of Modern Plasma Physics, 3(1), 2. https://doi.org/10.1007/s41614-019-0025-1

Fukushima, N., & Kamide, Y. (1973). Partial ring current models for worldwide geomagnetic disturbances. Reviews of Geophysics, 11(4), 795-853.

Ganushkina, N. Y., Liemohn, M. W., & Dubyagin, S. (2018). Current systems in the Earth's magnetosphere. Reviews of Geophysics, 56(2), 309–332. https://doi.org/10.1002/2017RG000590

Ganushkina, N. Y., Liemohn, M. W., Dubyagin, S., Daglis, I. A., Dandouras, I., De Zeeuw, D. L., … Amariutei, O. (2015). Defining and resolving current systems in geospace. Annales Geophysicae, 33(11), 1369–1402. doi:10.5194/angeo-33-1369-2015

Ganushkina, N. Y., Liemohn, M. W., Kubyshkina, M. V., Ilie, R., & Singer, H. J. (2010, January). Distortions of the magnetic field by storm-time current systems in Earth's magnetosphere. In Annales Geophysicae (Vol. 28, No. 1, pp. 123-140). Copernicus GmbH.

Garcia, A., & Mouradian, Z. (1998). The Gleissberg cycle of minima. Solar Physics, 180, 495-498.

Gaunt, C. T., & Coetzee, G. (2007). Transformer failures in regions incorrectly considered to have low GIC-risk, 2007. In IEEE lausanne power tech (pp. 807–812). IEEE. https://doi.org/10.1109/PCT.2007.4538419

Genestreti, K. J., Burch, J. L., Cassak, P. A., Torbert, R. B., Ergun, R. E.,Varsani, A.,...Allen, R. C. (2017).The effect of a guide field on local energy conversion during asymmetric magnetic reconnection: MMS observations. Journal of Geophysical Research: Space Physics, 122, 11, 342–11,353. https://doi.org/10.1002/2017JA024247

Genestreti, K. J., Varsani, A., Burch, J. L., Cassak, P. A., Torbert, R. B., Nakamura, R., et al. (2018). MMS observation of asymmetric reconnection supported by 3-D electron pressure divergence. Journal of Geophysical Research: Space Physics, 123, 1806– 1821. https://doi.org/10.1002/2017JA025019

Gjerloev, J. W. (2009), A Global Ground-Based Magnetometer Initiative, EOS, 90, 230-231, doi:10.1029/2009EO270002.

Gjerloev, J. W. (2012), The SuperMAG data processing technique, J. Geophys. Res., 117, A09213, doi:10.1029/2012JA017683.

Gold, T. (1959). Motions in the magnetosphere of the Earth. Journal of Geophysical Research, 64(9), 1219-1224.

Goldstein, J. (2006). Plasmasphere response: Tutorial and review of recent imaging results. Space Science Reviews, 124, 203-216.

Gonzalez, W. D. (1993). Ring current evolution during intense magnetic storms. In Paper presented at Magnetic Storm/Substorm Relationship Workshop. National Geophysical Data Center.

Gonzalez, W. D., Joselyn, J. A., Kamide, Y., Kroehl, H. W., Rostoker, G., Tsurutani, B. T., & Vasyliunas, V. M. (1994). What is a geomagnetic storm? Journal of Geophysical Research, 99(A4), 5771–5792. https://doi.org/10.1029/93JA02867

Gonzalez, W., & Parker, E. (2016). Magnetic Reconnection-Concepts and applications. Springer Cham, ISBN: 978-3-319-26432-5. https://doi.org/10.1007/978-3-319-26432-5

Gopalswamy N, Lara A, Lepping RP, Kaiser ML, Berdichevsky D, Cyr OCS (2000) Interplanetary acceleration of coronal mass ejections. Geophys Res Lett 27(2): 145–148. https://doi.org/10.1029/1999GL003639

Gopalswamy, N. History and development of coronal mass ejections as a key player in solar terrestrial relationship. Geosci. Lett. 3, 8 (2016). https://doi.org/10.1186/s40562-016-0039-2

Gopalswamy, N., Akiyama, S., Yashiro, S., Xie, H., Mäkelä, P., and Michalek, G. (2014), Anomalous expansion of coronal mass ejections during solar cycle 24 and its space weather implications, Geophys. Res. Lett., 41, 2673–2680, doi:10.1002/2014GL059858.

Gopalswamy, N., Hanaoka, Y., Kosugi, T., Lepping, R. P., Steinberg, J. T., Plunkett, S., et al. (1998). On the relationship between coronal mass ejections and magnetic clouds. Geophys. Res. Lett. 25, 2485–2488. doi: 10.1029/98GL50757

Gopalswamy, N., Tsurutani, B. & Yan, Y. Short-term variability of the Sun-Earth system: an overview of progress made during the CAWSES-II period. Prog. in Earth and Planet. Sci. 2, 13 (2015). https://doi.org/10.1186/s40645-015-0043-8

Gosling, J. T., Asbridge, J. R., Bame, S. J., Feldman, W. C., & Zwickl, R. D. (1980). Observations of large fluxes of He+ in the solar wind following an interplanetary shock. Journal of Geophysical Research, 85(A7), 3431–3434. https://doi.org/10.1029/JA085iA07p03431

Gosling, J. T., Bame, S. J., McComas, D. J., & Phillips, J. L. (1990). Coronal mass ejections and large geomagnetic storms. Geophysical Research Letters, 17(7), 901–904. doi:10.1029/gl017i007p00901

Green, J. C., and M. G. Kivelson (2004), Relativistic electrons in the outer radiation belt: Differentiating between acceleration mechanisms, J. Geophys. Res., 109, A03213, doi:10.1029/2003JA010153.

Green, L. M., Török, T., Vršnak, B., Manchester, W., & Veronig, A. (2018). The Origin, Early Evolution and Predictability of Solar Eruptions. Space Science Reviews, 214(1). doi:10.1007/s11214-017-0462-5

Greenwald, R. A., Baker, K. B., Dudeney, J. R., Pinnock, M., Jones, T. B., Thomas, E. C., & Yamagishi, H. (1995). Darn/superdarn. Space Science Reviews, 71(1), 761–796. https://doi.org/10.1007/BF00751350.

Greenwald, R. A., Baker, K. B., Dudeney, J. R., Pinnock, M., Jones, T. B., Thomas, E. C., et al. (1995). DARN/SuperDARN. Space Science Reviews, 71(1–4), 761–796. https://doi.org/10.1007/BF00751350

Greer, K. R., Immel, T., & Ridley, A. (2017). On the variation in the ionospheric response to geomagnetic storms with time of onset. Journal of Geophysical Research: Space Physics, 122(4), 4512–4525. https://doi.org/10.1002/2016JA023457

Güdel, M. (2007). The Sun in time: activity and environment. Living Reviews in Solar Physics, 4, 1-137.

Guo, J., Feng, X., Emery, B. A., & Wang, Y. (2012). Efficiency of solar wind energy coupling to the ionosphere. Journal of Geophysical Research, 117(A7), A07303. https://doi.org/10.1029/2012JA017627

Gurnett, D. A., & Bhattacharjee, A. (2005). Introduction to plasma physics with space and laboratory applications. Cambridge, UK, Cambridge University Press. doi:10.1119/1.2201848

H. Che, C. Schiff, G. Le, J. C. Dorelli, B. L. Giles, T. E. Moore; Quantifying the effect of non-Larmor motion of electrons on the pressure tensor. Physics of Plasmas 1 March 2018; 25 (3): 032101. https://doi.org/10.1063/1.5016853

Haaland, S., Runov, A., Artemyev, A., & Angelopoulos, V. (2019). Characteristics of the flank magnetopause: THEMIS observations. Journal of Geophysical Research: Space Physics, 124(5), 3421-3435. https://doi.org/10.1029/2019JA026459

Hajra, R. (2021). Weakest solar cycle of the space age: A study on solar wind–magnetosphere energy coupling and geomagnetic activity. Solar Physics, 296(2), 1–10. https://doi.org/10.1007/s11207-021-01774-9

Hajra, R., & Tsurutani, B. T. (2018). Interplanetary shocks inducing magnetospheric supersubstorms (SML<− 2500 nT): Unusual auroral morphologies and energy flow. The Astrophysical Journal, 858(2), 123. https://doi.org/10.3847/1538-4357/aabaed

Hajra, R., Sunny, J.V. Corotating Interaction Regions during Solar Cycle 24: A Study on Characteristics and Geoeffectiveness. Sol Phys 297, 30 (2022). https://doi.org/10.1007/s11207-022-01962-1

Hajra, R., Tsurutani, B. T., Echer, E., Gonzalez, W. D., & Gjerloev, J. W. (2016). Supersubstorms (SML<− 2500 nT): Magnetic storm and solar cycle dependences. Journal of Geophysical Research: Space Physics, 121(8), 7805–7816. https://doi.org/10.1002/2015JA021835

Hajra, S., Dashora, N., and Ivan, J. S. (2022). On the sources, coupling and energetics during supersubstorms of the solar cycle 24. Journal of Geophysical Research: Space Physics, 127(10), e2022JA030604. https://doi.org/10.1029/2022JA030604

Hajra, S., Dashora, N., and Ivan, J. S. (2023a). Global observations of the short term disturbances in the geomagnetic field and induced currents during the supersubstorms events of solar cycle 24. Space Weather, 21, e2022SW003355. https://doi.org/10.1029/2022SW003355

Hajra, S., Dashora, N., and Ivan, J. S. (2023b). On the multi-scale dynamics and energy flow near reconnection regions in the magnetopause and magnetotail using the MMS, Cluster and THEMIS observations during the geomagnetic storm of 31 December 2015, Adv. Space Res., ISSN 0273-1177, https://doi.org/10.1016/j.asr.2023.06.025.

Hanslmeier, A. (2010). The sun and space weather (Vol. 18, p. 233). Berlin, Heidelberg: Springer Berlin Heidelberg.

Haraguchi, K., Kawano, H., Yumoto, K., Ohtani, S., Higuchi, T., & Ueno, G. (2004). Ionospheric conductivity dependence of dayside region- 0, 1, and 2 field- aligned current systems: Statistical study with DMSP- F7. Annales Geophysicae, 22(8), 2775–2783. https://doi.org/10.5194/angeo- 22- 2775- 2004

Hasegawa, A., Sato, T. (1979). Generation of Field Aligned Current During Substorm. In: Akasofu, SI. (eds) Dynamics of the Magnetosphere. Astrophysics and Space Science Library, vol 78. Springer, Dordrecht. https://doi.org/10.1007/978-94-009-9519-2_28

Heber, B., Sanderson, T. R., & Zhang, M. (1999). Corotating interaction regions. Advances in Space Research, 23(3), 567-579.

Heikkila, W.J. (1990). Magnetic reconnection, merging, and viscous interaction in the magnetosphere. Space Sci Rev 53, 1–44. https://doi.org/10.1007/BF00217427

Hesse, M., & Cassak, P. A. (2020). Magnetic reconnection in the space sciences: Past, present, and future. Journal of Geophysical Research: Space Physics, 125(2), e2018JA025935. https://doi.org/10.1029/2018JA025935

Hesse, M., & Schindler, K. (1988). A theoretical foundation of general magnetic reconnection. Journal of Geophysical Research, 93(A6), 5559. Doi: 10.1029/ja093ia06p05559

Hesse, M., Neukirch, T., Schindler, K., Kuznetsova, M. and Zenitani S. (2011). The Diffusion Region in Collisionless Magnetic Reconnection. Space Sci Rev 160, 3–23 https://doi.org/10.1007/s11214-010-9740-1

Hesse, M., Y.-H. Liu, L.-J. Chen, N. Bessho, M. Kuznetsova, J. Birn, and J. L. Burch (2016), On the electron diffusion region in asymmetric reconnection with a guide magnetic field, Geophys. Res. Lett., 43, 2359–2364, doi: 10.1002/2016GL068373.

Hill, T. W. (1974). Origin of the plasma sheet. Reviews of Geophysics, 12(3), 379-388.

Hocke, K., & Schlegel, K. (1996). A review of atmospheric gravity waves and travelling ionospheric disturbances: 1982–1995. Ann. Geophys. 14(9): 917. https://doi.org/10.1007/s00585-996-0917-6

Hoeksema, J. T., Wilcox, J. M., & Scherrer, P. H. (1983). The structure of the heliospheric current sheet: 1978–1982. Journal of Geophysical Research: Space Physics, 88(A12), 9910-9918.

Hoffman, R. A., Gjerloev, J. W., Frank, L. A., & Sigwarth, J. W. (2010). Are there optical differences between storm-time substorms and isolated substorms?. Ann. Geophys., 28(5)- 1183-1198.

Holzer, R. E., and Slavin, J. A. (1979), A correlative study of magnetic flux transfer in the magnetosphere, J. Geophys. Res., 84(A6), 2573–2578, doi:10.1029/JA084iA06p02573.

Hones, E. W. (1979). Transient phenomena in the magnetotail and their relation to substorms. Space Science Reviews, 23(3). doi:10.1007/bf00172247

Hones, E. W. (1984). Magnetic reconnection in space and laboratory plasmas. Eos, Transactions American Geophysical Union, 65(18), 340. doi: 10.1029/eo065i018p00340

Howard, T. (2011). Coronal mass ejections: An introduction (Vol. 376). Springer Science & Business Media.

Ieda, A., Machida, S., Mukai, T., Saito, Y., Yamamoto, T., Nishida, A., et al. (1998). Statistical analysis of the plasmoid evolution with Geotail observations. Journal of Geophysical Research, 103(A3), 4453–4465.https://doi.org/10.1029/97JA03240

Iijima, T. (2000). Field-aligned currents in geospace: Substance and significance. Magnetospheric Current Systems, Geophys. Monogr. Ser, 118, 107-129.

Iijima, T., & Potemra, T. A. (1976a). The amplitude distribution of field- aligned currents at northern high latitudes observed by Triad. Journal of Geophysical Research, 81(13), 2165–2174. https://doi.org/10.1029/JA081i013p02165

Iijima, T., & Potemra, T. A. (1976b). Field- aligned currents in the dayside cusp observed by Triad. Journal of Geophysical Research, 81(34), 5971–5979. https://doi.org/10.1029/JA081i034p05971

Iijima, T., & Potemra, T. A. (1978). Large- scale characteristics of field- aligned currents associated with substorms. Journal of Geophysical Research, 83(A2), 599–615. https://doi.org/10.1029/JA083iA02p00599

Iijima, T., & Potemra, T. A. (1982). The relationship between interplanetary quantities and Birkeland current densities. Geophysical Research Letters, 4, 442–445. https://doi.org/10.1029/gl009i004p00442

Iyemori, T. (1990). Storm-time magnetospheric currents inferred from mid-latitude geomagnetic field variations. Journal of Geomagnetism and Geoelectricity, 42(11), 1249–1265. https://doi.org/10.5636/jgg.42.1249

Iyemori, T., and Rao, D.R.K. (1996). Decay of the Dst field of geomagnetic disturbance after substorm onset and its implication to storm-substorm relation. Ann. Geophys. 14: 608–618. https://doi.org/10.1007/s00585-996-0608-3

Iyemori, T., M. Takeda, M. Nose, Y. Odagi and H. Toh (2010). Mid-latitude Geomagnetic Indices ASY and SYM for 2009 (Provisional), Internal Report of Data Analysis Center for Geomagnetism and Space Magnetism, Kyoto University, Japan. Get PDF (404.3KB)

Iyemori, T., Rao, D.R.K. (1996) Decay of the Dst field of geomagnetic disturbance after substorm onset and its implication to storm-substorm relation. Annales Geophysicae. 14, 608–618 https://doi.org/10.1007/s00585-996-0608-3

J. D. Scudder1, R. D. Holdaway1, W. S. Daughton2, H. Karimabadi3, V. Roytershteyn3, C. T. Russell4, and J. Y. Lopez1 https://doi.org/10.1103/PhysRevLett.108.225005

Jin, M., Manchester, W. B., Holst, B. van der, Sokolov, I., Tóth, G., Vourlidas, A., … Gombosi, T. I. (2017). Chromosphere to 1 au simulation of the 2011 March 7th event: A comprehensive study of coronal mass ejection propagation. The Astrophysical Journal, 834(2), 172. doi:10.3847/1538-4357/834/2/172

Johnson, E. A., Murphy, T., & Torreson, O. W. (1948). Pre- history of the Earth's magnetic field. Terrestrial Magnetism and Atmospheric Electricity, 53(4), 349-372.

Johnson, R. G. (1979), Energetic ion composition in the Earth's magnetosphere, Rev. Geophys., 17(4), 696– 705, doi:10.1029/RG017i004p00696.

Käki, S., Viljanen, A., Juusola, L., & Kauristie, K. (2022). Spatio-temporal development of large-scale auroral electrojet currents relative to substorm onsets. Annales Geophysicae, 40(1), 107–119. https://doi.org/10.5194/angeo-40-107-2022

Kamide, Y. (1992). Is substorm occurrence a necessary condition for a magnetic storm?. Journal of geomagnetism and geoelectricity, 44(2), 109-117. https://doi.org/10.5636/jgg.44.109

Kamide, Y., & Akasofu, S. I. (1983). Notes on the auroral electrojet indices. Reviews of Geophysics, 21(7), 1647–1656. https://doi.org/10.1029/RG021i007p01647

Kamide, Y., & Baumjohann, W. (2012). Magnetosphere-ionosphere coupling (Vol. 23). Springer Science & Business Media.

Kamide, Y., & Fukushima, N. (1971). Analysis of magnetic storms with DR indices for equatorial ring-current field. Radio Science, 6(2), 277–278. https://doi.org/10.1029/rs006i002p00277

Kamide, Y., & Joselyn, J. A. (1991). Toward a standardized definition of geomagnetic sudden impulses and storm sudden commencements. Eos, Transactions American Geophysical Union, 72(28), 300. https://doi.org/10.1029/90EO20231

Kamide, Y., & Rostoker, G. (2004). What is the physical meaning of the AE index? Eos, Transactions American Geophysical Union, 85(19), 188. doi:10.1029/2004eo190010

Kamide, Y., Baumjohann, W., Daglis, I. A., Gonzalez, W. D., Grande, M., Joselyn, J. A., ... & Vasyliunas, V. M. (1998). Current understanding of magnetic storms: Storm- substorm relationships. Journal of Geophysical Research: Space Physics, 103(A8), 17705-17728.

Kamide, Y., Richmond, A. D., & Matsushita, S. (1981). Estimation of ionospheric electric fields, ionospheric currents, and field-aligned currents from ground magnetic records. Journal of Geophysical Research, 86(A2), 801–813. https://doi.org/10.1029/JA086iA02p00801

Kamide, Y., Yokoyama, N., Gonzalez, W., Tsurutani, B. T., Daglis, I. A., Brekke, A., & Masuda, S. (1998). Two-step development of geomagnetic storms. Journal of Geophysical Research, 103(A4), 6917–6921. https://doi.org/10.1029/97JA03337

Kan, J. R., & Lee, L. C. (1979). Energy coupling function and solar wind-magnetosphere dynamo. Geophysical Research Letters, 6(7), 577–580. https://doi.org/10.1029/gl006i007p00577

Kappenman, J. G. (2003). Storm sudden commencement events and the associated geomagnetically induced current risks to ground-based systems at low-latitude and midlatitude locations. Space Weather, 1(3). https://doi.org/10.1029/2003SW000009

Kappenman, J. G. (2005). An overview of the impulsive geomagnetic field disturbances and power grid impacts associated with the violent Sun-Earth connection events of 29–31 October 2003 and a comparative evaluation with other contemporary storms. Space Weather, 3(8). https://doi.org/10.1029/2004sw000128

Karimabadi, H., Daughton, W., and Scudder, J. (2007), Multi-scale structure of the electron diffusion region, Geophys. Res. Lett., 34, L13104, doi:10.1029/2007GL030306.

Kataoka, R., & Ngwira, C. (2016). Extreme geomagnetically induced currents. Progress in Earth and Planetary Science, 3(1), 1–7. https://doi.org/10.1186/s40645-016-0101-x

Keika, K., Kasahara, S., Yokota, S., Hoshino, M., Seki, K., Amano, T., et al. (2022). Preferential energization of lower-charge-state heavier ions in the near-Earth magnetotail. Journal of Geophysical Research: Space Physics, 127(1), e2021JA029786. https://doi.org/10.1029/2021JA029786

Keika, K., Kasahara, S., Yokota, S., Hoshino, M., Seki, K., Nosé, M., et al. (2018). Ion energies dominating energy density in the inner magnetosphere: Spatial distributions and composition, observed by Arase/MEP-i. Geophysical Research Letters, 45(22), 12153–12162. https://doi.org/10.1029/2018GL080047

Keika, K., Kistler, L. M., & Brandt, P. C. (2013). Energization of O+ ions in the Earth's inner magnetosphere and the effects on ring current buildup: A review of previous observations and possible mechanisms. Journal of geophysical Research: Space Physics, 118(7), 4441–4464. https://doi.org/10.1002/jgra.50371

Keika, K., Seki, K., Nosé, M., Machida, S., Miyoshi, Y., Lanzerotti, L. J., et al. (2016). Storm time impulsive enhancements of energetic oxygen due to adiabatic acceleration of pre-existing warm oxygen in the inner magnetosphere. Journal of Geophysical Research: Space Physics, 121(8), 7739–7752. https://doi.org/10.1002/2016JA022384

Keika, K., Seki, K., Nosé, M., Miyoshi, Y., Lanzerotti, L. J., Mitchell, D. G., et al. (2018). Three-step buildup of the 17 March 2015 storm ring current: Implication for the cause of the unexpected storm intensification. Journal of Geophysical Research: Space Physics, 123(1), 414–428. https://doi.org/10.1002/2017JA024462

Keiling, A., et al. (2006), Energy-dispersed ions in the plasma sheet boundary layer and associated phenomena: Ion heating, electron acceleration, Alfvén waves, broadband waves, perpendicular electric field spikes, and auroral emissions, Ann. Geophys., 24, 2685–2707, doi: 10.5194/angeo-24-2685-2006.

Keiling, A., Ramos, C., Vu, N., Angelopoulos, V., & Nosé, M. (2022). Statistical properties and proposed source mechanism of recurrent substorm activity with one-hour periodicity. Journal of Geophysical Research: Space Physics, 127(3), e2021JA030064. https://doi.org/10.1029/2021JA030064

Keith, W. and W. Heikkila (2020), Earth's Magnetosphere: Formed by the Low Latitude Boundary Layer (Second Edition). Elsevier Inc. ISBN 978-0-12-818160-7. https://doi.org/10.1016/C2017-0-04309-4

Kelley, M. C. (2009). The Earth's ionosphere: Plasma physics and electrodynamics. Academic press.

Kelley, M. C., Fejer, B. G., & Gonzales, C. A. (1979). An explanation for anomalous equatorial ionospheric electric fields associated with a northward turning of the interplanetary magnetic field. Geophysical Research Letters, 6(4), 301-304.

Kepko, L., McPherron, R. L., Amm, O., Apatenkov, S., Baumjohann, W., Birn, J., ... & Sergeev, V. (2015). Substorm current wedge revisited. Space Science Reviews, 190, 1-46.

Kepko, L., McPherron, R. L., Amm, O., Apatenkov, S., Baumjohann, W., Birn, J., … Sergeev, V. (2014). Substorm Current Wedge Revisited. Space Science Reviews, 190(1-4), 1–46. doi:10.1007/s11214-014-0124-9

Kerridge, D. J. (2001). "INTERMAGNET: Worldwide near-real-time geomagnetic observatory data" (PDF). Proc. ESA Space Weather Workshop, ESTEC, Noordwijk, the Netherlands

Khotyaintsev, Y. V., Graham, D. B., Norgren, C., & Vaivads, A. (2019). Collisionless magnetic reconnection and waves: Progress review. Frontiers in Astronomy and Space Sciences, 6, 70. https://doi.org/10.3389/fspas.2019.00070

Kikuchi, T., & Araki, T. (1979). Transient response of uniform ionosphere and preliminary reverse impulse of geomagnetic storm sudden commencement. Journal of Atmospheric and Terrestrial Physics, 41(9), 917–925. https://doi.org/10.1016/0021-9169(79)90093-X

Kikuchi, T., Araki, T., Hashimoto, K. K., Ebihara, Y., Tanaka, T., Nishimura, Y., et al. (2022). Instantaneous achievement of the hall and pedersen–cowling current circuits in northern and southern hemispheres during the

geomagnetic sudden commencement on 12 May 2021. Frontiers in Astronomy and Space Sciences, 9, 879314. https://doi.org/10.3389/fspas

Kikuchi, T., Hashimoto, K. K., & Nozaki, K. (2008). Penetration of magnetospheric electric fields to the equator during a geomagnetic storm. Journal of Geophysical Research: Space Physics, 113(A6), n/a–n/a. doi:10.1029/2007ja012628

Kikuchi, T., Lühr, H., Kitamura, T., Saka, O., & Schlegel, K. (1996). Direct penetration of the polar electric field to the equator during a DP 2 event as detected by the auroral and equatorial magnetometer chains and the EISCAT radar. Journal of Geophysical Research, 101(A8), 17161–17173. https://doi.org/10.1029/96JA01299

Kikuchi, T., Pinnock, M., Rodger, A., Lühr, H., Kitamura, T., Tachihara, H., ... & Ruohoniemi, M. (2000). Global evolution of a substorm-associated DP2 current system observed by SuperDARN and magnetometers. Advances in Space Research, 26(1), 121-124.

Kikuchi, T., Tsunomura, S., Hashimoto, K., & Nozaki, K. (2001). Field-aligned current effects on mid latitude geomagnetic sudden commencements. Journal of Geophysical Research, 106(A8), 15555–15565. https://doi.org/10.1029/2001JA900030

Kilpua, Emilia & Balogh, Andre & von Steiger, Rudolf & Liu, Y.. (2017). Geoeffective Properties of Solar Transients and Stream Interaction Regions. Space Science Reviews. 212. 10.1007/s11214-017-0411-3.

King, J. H., & Papitashvili, N. E. (2005). Solar wind spatial scales in and comparisons of hourly Wind and ACE plasma and magnetic field data. Journal of Geophysical Research, 110, A02104. https://doi.org/10.1029/2004JA010649

Kivelson, M. G., & Russell, C. T. (Eds.). (1995). Introduction to space physics. Cambridge university press.

Klein, L.W. and Burlaga, L.F., Interplanetary Magnetic Clouds at 1 AU, J. Geophys. Res., 1983, vol. 87, p. 613. 35.

Knipp, D. J., Tobiska, W. K., & Emery, B. A. (2004). Direct and indirect thermospheric heating sources for solar cycles 21–23. Solar Physics, 224(1), 495–505. https://doi.org/10.1007/s11207-005-6393-4

Koskinen, H. (2011). Physics of space storms: From the solar surface to the Earth. Springer Science & Business Media. Chichester, UK.

Koskinen, H. E. J., Baker, D. N., Balogh, A., Gombosi, T., Veronig, A., & von Steiger, R. (2017). Achievements and Challenges in the Science of Space Weather. Space Science Reviews, 212(3-4), 1137–1157. doi:10.1007/s11214-017-0390-4

Koskinen, H. E., & Tanskanen, E. I. (2002). Magnetospheric energy budget and the epsilon parameter. Journal of Geophysical Research, 107(A11), SMP-42. https://doi.org/10.1029/2002JA009283

Kozyra, J. U., & Liemohn, M. W. (2003). Ring current energy input and decay. Magnetospheric Imaging—the Image Prime Mission, 105-131.

Kozyreva, O. V., Pilipenko, V. A., Belakhovsky, V. B., & Sakharov, Y. A. (2018). Ground geomagnetic field and GIC response to March 17, 2015, storm. Earth Planets and Space, 70(1), 157. https://doi.org/10.1186/s40623-018-0933-2

Kusano, K. (2023), Solar-Terrestrial Environmental Prediction. Springer, Singapore. https://doi.org/10.1007/978-981-19-7765-7

Lakhina, G. S., & Tsurutani, B. T. (2016). Geomagnetic storms: historical perspective to modern view. Geoscience Letters, 3, 1-11.

Le Huy, M., & Amory-Mazaudier, C. (2005). Magnetic signature of the ionospheric disturbance dynamo at equatorial latitudes: "Ddyn". Journal of Geophysical Research, 110(A10), A10301. https://doi.org/10.1029/2004JA010578

Le, G., Lühr, H., Anderson, B. J., Strangeway, R. J., Russell, C. T., Singer, H., ... & Torbert, R. B. (2016). Magnetopause erosion during the 17 March 2015 magnetic storm: Combined field- aligned currents, auroral oval, and magnetopause observations. Geophysical Research Letters, 43(6), 2396-2404. https://doi.org/10.1002/2016GL068257

Le, G.; J. A. Slavin; R. J. Strangeway (2010). "Space Technology 5 observations of the imbalance of regions 1 and 2 field-aligned currents and its implication to the cross-polar cap Pedersen currents". J. Geophys. Res. 115 (A07202): A07202. Bibcode:2010JGRA..115.7202L. doi:10.1029/2009JA014979

Lee, L. C., & Fu, Z. F. (1986). Multiple X line reconnection: 1. A criterion for the transition from a single X line to a multiple X line reconnection. Journal of Geophysical Research: Space Physics, 91(A6), 6807-6815. doi: 10.1029/JA091iA06p06807 (1986).

Leer, E., Holzer, T. E., & Flå, T. (1982). Acceleration of the solar wind. Space Science Reviews, 33, 161-200.

Li, H., Wang, C., Xu, W. Y., & Kan, J. R. (2012). Characteristics of magnetospheric energetics during geomagnetic storms. Journal of Geophysical Research, 117(A4), A04225. https://doi.org/10.1029/2012JA017584

Li, W., & Hudson, M. K. (2019). Earth's Van Allen radiation belts: From discovery to the Van Allen Probes era. Journal of Geophysical Research: Space Physics, 124, 8319–8351. https://doi.org/10.1029/2018JA025940

Liemohn, M. W., Jazowski, M., Kozyra, J. U., Ganushkina, N., Thomsen, M. F., & Borovsky, J. E. (2010). CIR versus CME drivers of the ring current during intense magnetic storms. Proceedings of the Royal Society A: Mathematical, Physical and Engineering Sciences, 466(2123), 3305-3328. doi:10.1098/rspa.2010.0075

Lindqvist, P. A., Olsson, G., Torbert, R. B., King, B., Granoff, M., Rau, D., ... & Tucker, S. (2016). The spin-plane double probe electric field instrument for MMS. Space Science Reviews, 199(1), 137-165. doi:10.1007/s11214-014-0116-9

Liou, K., Newell, P. T., & Meng, C.-I. (2001). Seasonal effects on auroral particle acceleration and precipitation. Journal of Geophysical Research, 106(A4), 5531–5542. https://doi.org/10.1029/1999JA000391

Liou, K., Newell, P. T., Sibeck, D. G., Meng, C. I., Brittnacher, M., & Parks, G. (2001). Observation of IMF and seasonal effects in the location of auroral substorm onset. Journal of Geophysical Research, 106(A4), 5799–5810. https://doi.org/10.1029/2000JA003001

Liou, K., Newell, P. T., Zhang, Y. L., & Paxton, L. J. (2013). Statistical comparison of isolated and non-isolated auroral substorms. Journal of Geophysical Research: Space Physics, 118(5), 2466–2477. https://doi.org/10.1002/jgra.50218

Liu, E., Hu, H., Liu, J., Teng, X., & Qiao, L. (2019). Predicting SuperDARN cross polar cap potential by applying regression analysis and machine learning. Journal of Atmospheric and Solar-Terrestrial Physics, 193, 105057.

Lockwood, M. (2019). Does Adding Solar Wind Poynting Flux Improve the Optimum Solar Wind-Magnetosphere Coupling Function? Journal of Geophysical Research: Space Physics, 124(7), 5498–5515. doi:10.1029/2019ja026639

Lockwood, M., Owens, M. J., & Barnard, L. A. (2023). Universal time variations in the magnetosphere and the effect of CME arrival time: Analysis of the February 2022 event that led to the loss of Starlink satellites. Journal of Geophysical Research: Space Physics, 128, e2022JA031177. https://doi.org/10.1029/2022JA031177

Love, J. J., & Chulliat, A. (2013). An international network of magnetic observatories. Eos, Transactions, American Geophysical Union, 94(42), 373–374.https://doi.org/10.1002/2013eo420001

Lu, G., Baker, D. N., McPherron, R. L., Farrugia, C. J., Lummerzheim, D., Ruohoniemi, J. M., et al. (1998). Global energy deposition during the January 1997 magnetic cloud event. Journal of Geophysical Research, 103(A6), 11685–11694. https://doi.org/10.1029/98JA00897

Lu, G., Richmond, A. D., Emery, B. A., & Roble, R. G. (1995). Magnetosphere-ionosphere-thermosphere coupling: Effect of neutral winds on energy transfer and field-aligned current. Journal of Geophysical Research, 100(A10), 19643–19659. https://doi.org/10.1029/95JA00766

Lu, J. Y., Zhou, Y., Ma, X., Wang, M., Kabin, K., & Yuan, H. Z. (2019). Earth's bow shock: A new three-dimensional asymmetric model with dipole tilt effects. Journal of Geophysical Research: Space Physics, 124, 5396–5407. https://doi.org/10.1029/2018JA026144

Lu, Q., Fu, H., Wang, R. and Lu S. (2022). Collisionless magnetic reconnection in the magnetosphere, Chin. Phys. B, 31(8): 089401. Doi:10.1088/1674-1056/ac76ab

Lucek, E. A., Constantinescu, D., Goldstein, M. L., Pickett, J., Pincon, J. L., Sahraoui, F., ... & Walker, S. N. (2005). The magnetosheath. Space Science Reviews, 118, 95-152.

Lühr, H., Xiong, C., Olsen, N., & Le, G. (2017). Near-Earth magnetic field effects of large-scale magnetospheric currents. Space Science Reviews, 206(1), 521-545. doi:10.1007/s11214-016-0267-y

Lyon, J. G. (2000), The solar wind-magnetosphere-ionosphere system, Science, 288(5473), 1987–1991, doi: 10.1126/science.288.5473.1987

Lyons, L. R., Nishimura, Y., Liu, J., Bristow, W. A., Zou, Y., & Donovan, E. F. (2022). Verification of substorm onset from intruding flow channels with high-resolution SuperDARN radar flow maps. Journal of Geophysical Research: Space Physics, 127(8), e2022JA030723. https://doi.org/10.1029/2022JA030723

Lyons, L. R., Zou, Y., Nishimura, Y., Gallardo-Lacourt, B., Angelopulos, V., & Donovan, E. F. (2018). Storm time substorm onsets: Occurrence and flow channel triggering. Earth Planets and Space, 70(1), 81. https://doi.org/10.1186/s40623-018-0857-x

Macek, W. M., Silveira, M. V. D., Sibeck, D. G., Giles, B. L., & Burch, J. L. (2019a). Magnetospheric Multiscale Mission Observations of Reconnecting Electric Fields in the Magnetotail on Kinetic Scales. Geophysical Research Letters. doi: 10.1029/2019gl083782

Macek, W. M., Silveira, M. V. D., Sibeck, D. G., Giles, B. L., & Burch, J. L. (2019b). Mechanism of Reconnection on Kinetic Scales Based on Magnetospheric Multiscale Mission Observations. The Astrophysical Journal, 885(1), L26. doi:10.3847/2041-8213/ab4b5a

Mac-Mahon, R. M., & Gonzalez, W. D. (1997). Energetics during the main phase of geomagnetic superstorms. Journal of Geophysical Research, 102(A7), 14199–14207. https://doi.org/10.1029/97JA01151

Mac-Mahon, R. M., and Gonzalez, W. D. (1997), Energetics during the main phase of geomagnetic superstorms, J. Geophys. Res., 102(A7), 14199–14207, doi:10.1029/97JA01151.

Maltsev, Y. P., & Ostapenko, A. A. (2004). Azimuthally asymmetric ring current as a function of Dst and solar wind conditions. Annals of Geophysics, 22(8), 2989–2996. https://doi.org/10.5194/angeo-22-2989-2004

Mann, I. R., Ozeke, L. G., Murphy, K. R., Claudepierre, S. G., Turner, D. L., Baker, D. N., ... & Honary, F. (2016). Explaining the dynamics of the ultra-relativistic third Van Allen radiation belt. Nature Physics, 12(10), 978-983.

Marchaudon, A., Cerisier, J.-C., Dunlop, M. W., Pitout, F., Bosqued, J.-M., & Fazakerley, A. N. (2009). Shape, size, velocity and field-aligned currents of dayside plasma injections: a multi-altitude study. Annales Geophysicae, 27(3), 1251–1266. doi: 10.5194/angeo-27-1251-2009

Matsui, H., Erickson, P. J., Foster, J. C., Torbert, R. B., Argall, M. R., Anderson, B. J., ... & Turner, D. L. (2016). Dipolarization in the inner magnetosphere during a geomagnetic storm on 7 October 2015. Geophysical Research Letters, 43(18), 9397-9405. https://doi.org/10.1002/2016GL070677

Matsushita, S. (1962). On geomagnetic sudden commencements, sudden im-pulses, and storm durations. Journal of Geophysical Research, 67(10), 3753–3777. https://doi.org/10.1029/JZ067i010p03753

Matzka, J., Stolle, C., Yamazaki, Y., Bronkalla, O., & Morschhauser, A. (2021). The geomagnetic Kp index and derived indices of geomagnetic activity. Space Weather, 19(5), e2020SW002641.

McComas, D.J., Gosling, J.T., and Bame, S.J., A Test of Magnetic Field Draping Induced Bz Perturbations ahead of Fast Coronal Mass Ejecta, J. Geophys. Res., 1989, vol. 94, p. 1465.36.

McFadden, J. P., Carlson, C. W., Larson, D., Ludlam, M., Abiad, R., Elliott, B., … Angelopoulos, V. (2008). The THEMIS ESA Plasma Instrument and In-flight Calibration. Space Science Reviews, 141(1-4), 277–302. doi: 10.1007/s11214-008-9440-2

McIntosh, S.W., Leamon R. J., Egeland R. (2023) Deciphering solar magnetic activity: The (solar) hale cycle terminator of 2021. Frontiers in Astronomy and Space Sciences, 10. Doi:10.3389/fspas.2023.1050523.

McPherron, R. L. (2023). Substorm triggering by the solar wind. Journal of Geophysical Research: Space Physics, 128, e2022JA031147. https://doi.org/10.1029/2022JA031147

McPherron, R. L., Russell, C. T., and Aubry, M. P. (1973), Satellite studies of magnetospheric substorms on August 15, 1968: 9. Phenomenological model for substorms, J. Geophys. Res., 78(16), 3131–3149, doi:10.1029/JA078i016p03131.

McPherron, R.L. (1997). The Role of Substorms in the Generation of Magnetic Storms. In Magnetic Storms (eds B.T. Tsurutani, W.D. Gonzalez, Y. Kamide and J.K. Arballo). https://doi.org/10.1029/GM098p0131

Merka, J., and A. Szabo (2004), Bow shock's geometry at the magnetospheric flanks, J. Geophys. Res., 109, A12224, doi:10.1029/2004JA010567.

Merrill, R. T., & McElhinny, M. W. (1983). The Earth's magnetic field: Its history, origin and planetary perspective (Vol. 401). London: Academic Press.

Milan, S. E., Clausen, L. B. N., Coxon, J. C., Carter, J. A., Walach, M. T., Laundal, K., ... & Anderson, B. J. (2017). Overview of solar wind–magnetosphere–ionosphere–atmosphere coupling and the generation of magnetospheric currents. Space Science Reviews, 206(1), 547-573. doi: 10.1007/s11214-017-0333-0

Milan, S. E.; Provan, G.; Hubert, B. (2007). "Magnetic flux transport in the Dungey cycle: A survey of dayside and nightside reconnection rates". Journal of Geophysical Research: Space Physics. 112 (A1): n/a. Bibcode:2007JGRA..112.1209M. doi:10.1029/2006JA011642. hdl:2027.42/140049. ISSN 2156-2202.

Mitra, A. P. (1974). Ionospheric effects of solar flares (Vol. 46). Boston: Reidel.

Moldwin, Mark. "coronal mass ejection". Encyclopedia Britannica, 11 Feb. 2023, https://www.britannica.com/science/coronal-mass-ejection. Accessed 24 March 2023.

Moretto, T., Hesse, M., Kuznetsova, M., Rastätter, L., Vennerstrøm, S., & Tenfjord, P. (2021). How does the magnetosphere go to sleep?. Journal of Atmospheric and Solar-Terrestrial Physics, 220, 105626. doi.org/10.1016/j.jastp.2021.105626

Morley, S. K. (2020). Challenges and opportunities in magnetospheric space weather prediction. Space Weather, 18(3), e2018SW002108.

Morley, S. K., Rouillard, A. P., & Freeman, M. P. (2009). Recurrent substorm activity during the passage of a corotating interaction region. Journal of Atmospheric and Solar-Terrestrial Physics, 71(10–11), 1073–1081. https://doi.org/10.1016/j.jastp.2008.11.009

Mullan, D. J. (2010). Physics of the Sun: A first course. Taylor & Francis Group, LLC. McComas, D. J., M. Velli, W. S. Lewis, L. W. Acton, M. Balat-Pichelin, V. Bothmer, et al. (2007), Understanding coronal heating and solar wind acceleration: Case for in situ near-Sun measurements, Rev. Geophys., 45, RG1004, doi:10.1029/2006RG000195.

Nakamura, T. K. M., Genestreti, K. J., Liu, Y.-H., Nakamura, R., Teh, W.-L., Hasegawa, H., et al. (2018). Measurement of the magnetic reconnection rate in the Earth's magnetotail. Journal of Geophysical Research: Space Physics, 123, 9150–9168. https://doi.org/10.1029/2018JA025713

Nava, B., Rodríguez-Zuluaga, J., Alazo-Cuartas, K., Kashcheyev, A., Migoya-Orué, Y., Radicella, S. M., & Fleury, R. (2016). Middle-and low-latitude ionosphere response to 2015 St. Patrick's Day geomagnetic storm. Journal of Geophysical Research: Space Physics, 121(4), 3421–3438. https://doi.org/10.1002/2015JA022299

Newell, P. T., & Gjerloev, J. W. (2011a). Evaluation of SuperMAG auroral electrojet indices as indicators of substorms and auroral power. Journal of Geophysical Research, 116(A12), A12211. https://doi.org/10.1029/2011JA016779

Newell, P. T., & Gjerloev, J. W. (2011b). Substorm and magnetosphere characteristic scales inferred from the SuperMAG auroral electrojet indices. Journal of Geophysical Research, 116(A12), A12232. https://doi.org/10.1029/2011ja016936

Newell, P. T., & Liou, K. (2011). Solar wind driving and substorm triggering. Journal of Geophysical Research, 116(A3), 16. https://doi.org/10.1029/2010ja016139

Newell, P. T., Liou, K., & Wilson, G. R. (2009). Polar cap particle precipitation and aurora: Review and commentary. Journal of Atmospheric and Solar-Terrestrial Physics, 71(2), 199–215. https://doi.org/10.1016/j.jastp.2008.11.004

Newell, P. T., Sotirelis, T., Liou, K., Meng, C. I., & Rich, F. J. (2007). A nearly universal solar wind-magnetosphere coupling function inferred from 10 magnetospheric state variables. Journal of Geophysical Research, 112(A1), A01206. https://doi.org/10.1029/2006JA012015

Ngwira, C. M., Pulkkinen, A., Wilder, F. D., & Crowley, G. (2013). Extended study of extreme geoelectric field event scenarios for geomagnetically induced current applications. Space Weather, 11(3), 121–131. https://doi.org/10.1002/swe.20021

Nicolet, M., & Aikin, A. C. (1960). The formation of the D region of the ionosphere. Journal of Geophysical Research, 65(5), 1469-1483.

Nishida, A. (1966). The origin of fluctuation in the equatorial electrojet; a new type of geomagnetic variations. Ann. Geophys., 22, 478-484.

Nishida, A. (1968), Geomagnetic Dp 2 fluctuations and associated magnetospheric phenomena, J. Geophys. Res., 73(5), 1795– 1803, doi:10.1029/JA073i005p01795.

Nishida, A., & Kamide, Y. (1983). Magnetospheric processes preceding the onset of an isolated substorm: A case study of the March 31, 1978, substorm. Journal of Geophysical Research, 88(A9), 7005–7014. https://doi.org/10.1029/ja088ia09p07005

Nishimura, Y., Artemyev, A. V., Lyons, L. R., Gabrielse, C., Donovan, E. F., & Angelopoulos, V. (2022). Spaceground observations of dynamics of substorm onset beads. Journal of Geophysical Research: Space Physics, 127(2), e2021JA030004. https://doi.org/10.1029/2021JA030004

Nishimura, Y., Lyons, L. R., Gabrielse, C., Sivadas, N., Donovan, E. F., Varney, R. H., et al. (2020). Extreme magnetosphere-ionosphere-thermosphere responses to the 5 April 2010 supersubstorm. Journal of Geophysical Research: Space Physics, 125(4), e2019JA027654. https://doi.org/10.1029/2019JA027654

Nishitani, N., Ruohoniemi, J.M., Lester, M. et al. (2019). Review of the accomplishments of mid-latitude Super Dual Auroral Radar Network (SuperDARN) HF radars. Prog Earth Planet Sci 6, 27 https://doi.org/10.1186/s40645-019-0270-5.

Nose, M., Sugiura, M., Kamei, T., Iyemori, T., & Koyama, Y. (2015). Geomagnetic dst index. Geomagnetic Dst index.

Nose, M., T. Iyemori, M. Sugiura, T. Kamei (2015), Geomagnetic AE index, World Data Center for Geomagnetism, Kyoto, doi:10.17593/15031-54800

O'Brien, T. P., & McPherron, R. L. (2000). An empirical phase space analysis of ring current dynamics: Solar wind control of injection and decay. Journal of Geophysical Research, 105(A4), 7707–7719. https://doi.org/10.1029/1998JA000437

Ohtani, S., Motoba, T., Gjerloev, J. W., Frey, H. U., Mann, I. R., Chi, P. J., & Korth, H. (2022). New insights into the substorm initiation sequence from the spatio-temporal development of auroral electrojets. Journal of Geophysical Research: Space Physics, 127(6), e2021JA030114. https://doi.org/10.1029/2021JA030114

Oliveira, D. M., & Raeder, J. (2014). Impact angle control of interplanetary shock geoeffectiveness. Journal of Geophysical Research: Space Physics, 119(10), 8188–8201. https://doi.org/10.1002/2014JA020275

Oliveira, D. M., & Samsonov, A. A. (2018). Geoeffectiveness of interplanetary shocks controlled by impact angles: A review. Advances in Space Research, 61(1), 1–44. https://doi.org/10.1016/j.asr.2017.10.006

Olsen, N., Hulot, G., & Sabaka, T. J. (2010). Sources of the Geomagnetic Field and the Modern Data That EnableTheir Investigation. In Handbook of geomathematics.

Online ISBN:9781139165136. doi.org/10.1017/CBO9781139165136.

Onwumechikli, C. A. (1997), The Equatorial Electrojet. CRC Press, New York.

Onwumechikli, C. A. (2019). Equatorial electrojet. Routledge.

Orr, L., Chapman, S. C., Gjerloev, J. W., & Guo, W. (2021). Network community structure of substorms using SuperMAG magnetometers. Nature Communications, 12(1), 1842. https://doi.org/10.1038/s41467-021-22112-4

Østgaard, N., Germany, G., Stadsnes, J., & Vondrak, R. R. (2002). Energy analysis of substorms based on remote sensing techniques, solar wind measurements, and geomagnetic indices. Journal of Geophysical Research, 107(A9), 1233. https://doi.org/10.1029/2001JA002002

Østgaard, N., Tsyganenko, N. A., Mende, S. B., Frey, H. U., Immel, T. J., Fillingim, M., & Sigwarth, J. B. (2005). Observations and model predictions of substorm auroral asymmetries in the conjugate hemispheres. Geophysical Research Letters, 32(5), L05111. https://doi.org/10.1029/2004GL022166

Owens, Mathew & Forsyth, Robert. (2013). The Heliospheric Magnetic Field. Living Reviews in Solar Physics. 10. 5-. 10.12942/lrsp-2013-5.

Palmroth, M., Janhunen, P., Pulkkinen, T. I., Aksnes, A., Lu, G., Østgaard, N., et al. (2005). Assessment of ionospheric Joule heating by GUMICS-4 MHD simulation, AMIE, and satellite-based statistics: Towards a synthesis. Annals of Geophysics, 23(6), 2051–2068. https://doi.org/10.5194/angeo-23-2051-2005

Panovska, S., Korte, M., & Constable, C. G. (2019). One hundred thousand years of geomagnetic field evolution. Reviews of Geophysics, 57(4), 1289-1337.

Papitashvili, N. E., & King, J. H. (2020). OMNI 1-min Data Set [Dataset]. NASA Space Physics Data Facility. https://doi.org/10.48322/45bb-8792

Papitashvili, V. O., Christiansen, F., and Neubert, T., A new model of field-aligned currents derived from high-precision satellite magnetic field data, Geophys. Res. Lett., 29(14), doi:10.1029/2001GL014207, 2002.

Parker, E. N. (1965). Dynamical theory of the solar wind. Space Science Reviews, 4(5-6), 666-708.

Pedatella, N. M., Forbes, J. M., & Richmond, A. D. (2011). Seasonal and longitudinal variations of the solar quiet (Sq) current system during solar minimum determined by CHAMP satellite magnetic field observations. Journal of Geophysical Research: Space Physics, 116(A4).

Pedatella, N. M., Forbes, J. M., & Richmond, A. D. (2011). Seasonal and longitudinal variations of the solar quiet (Sq) current system during solar minimum determined by CHAMP satellite magnetic field observations. Journal of Geophysical Research: Space Physics, 116(A4), n/a–n/a. doi:10.1029/2010ja016289

Perreault, P., & Akasofu, S. I. (1978). A study of geomagnetic storms. Geophysical Journal International, 54(3), 547–573. https://doi.org/10.1111/j.1365-246X.1978.tb05494.x

Petrinec, S. M., and C. T. Russell (1993), An emprirical model of the size and shape of the near-Earth magnetotail, Geophys. Res. Lett., 20, 2695.

Petrinec, S. M., and C. T. Russell (1995), An examination of the effect of dipole tilt angle and cusp regions on the shape of the dayside magnetopause, J. Geophys. Res., 100, 9559– 9566.

Petrinec, S. M., and C. T. Russell (1996), Near-Earth magnetotail shape and size as determined from the magnetopause flaring angle, J. Geophys. Res., 101, 137–152.

Petrukovich, A., Artemyev, A., Vasko, I., Nakamura, R., & Zelenyi, L. (2015). Current sheets in the Earth magnetotail: Plasma and magnetic field structure with Cluster project observations. Space Science Reviews, 188(1), 311-337. doi: 10.1007/s11214-014-0126-7

Peymirat, C. (2002). Neutral wind influence on the electrodynamic coupling between the ionosphere and the magnetosphere. Journal of Geophysical Research, 107(A1). doi:10.1029/2001ja900106

Peymirat, C., Richmond, A. D., & Kobea, A. T. (2000). Electrodynamic coupling of high and low latitudes: Simulations of shielding/overshielding effects. Journal of Geophysical Research, 105(A10), 22991–23003. https://doi.org/10.1029/2000JA000057

Phan, T. D., et al. (2016), MMS observations of electron-scale filamentary currents in the reconnection exhaust and near the X line, Geophys. Res. Lett., 43, 6060– 6069, doi:10.1002/2016GL069212.

Phan, T. D., Gosling, J. T., Davis, M. S., Skoug, R. M., Øieroset, M., Lin, R. P., … Balogh, A. (2006). A magnetic reconnection X-line extending more than 390 Earth radii in the solar wind. Nature, 439(7073), 175–178. doi: 10.1038/nature04393

Piersanti, M., & Villante, U. (2016). On the discrimination between magnetospheric and ionospheric contributions on the ground manifestation of sudden impulses. Journal of Geophysical Research: Space Physics, 121(7), 6674–6691. https://doi.org/10.1002/2015JA021666

Piersanti, M., Alberti, T., Bemporad, A., Berrilli, F., Bruno, R., Capparelli, V., et al. (2017). Comprehensive analysis of the geoeffective solar event of 21 June 2015: Effects on the magnetosphere, plasmasphere, and ionosphere systems. Solar Physics, 292(11), 169. https://doi.org/10.1007/s11207-017-1186-0

Piersanti, M., De Michelis, P., Del Moro, D., Tozzi, R., Pezzopane, M., Consolini, G., et al. (2020). From the Sun to Earth: Effects of the 25 August 2018 geomagnetic storm. Annales Geophysicae, 38(3), 703–724. https://doi.org/10.5194/angeo-38-703-2020

Pirjola, R. (2000). Geomagnetically induced currents during magnetic storms. IEEE Transactions on Plasma Science, 28(6), 1867–1873. doi:10.1109/27.902215

Pollock, C., Moore, T., Jacques, A., Burch, J., Gliese, U., Saito, Y., ... & Zeuch, M. (2016). Fast plasma investigation for magnetospheric multiscale. Space Science Reviews, 199(1), 331-406. https://doi.org/10.1007/s11214-016-0245-4.

Pontin, D.I., Priest, E.R. (2022). Magnetic reconnection: MHD theory and modelling. Living Rev Sol Phys 19 (1). https://doi.org/10.1007/s41116-022-00032-9

Poppe, A. R., Samad, R., Halekas, J. S., Sarantos, M., Delory, G. T., Farrell, W. M., ... & McFadden, J. P. (2012). ARTEMIS observations of lunar pick- up ions in the terrestrial magnetotail lobes. Geophysical Research Letters, 39(17).

Poudel, P., Simkhada, S., Adhikari, B., Sharma, D., & Nakarmi, J. J. (2019). Variation of Solar Wind Parameters along with the understanding of Energy Dynamics within the Magnetospheric System during Geomagnetic Disturbances. Earth and Space Science. doi:10.1029/2018ea000495

Priest and Forbes (2007) Magnetic reconnection, Cambridge University Press.

PRIEST AND WOOD, 1991, BOOK ADVANCES IN solar magnetohydrodynamcis.

Pulkkinen, A., Bernabeu, E., Eichner, J., Beggan, C. and Thomson, A. W. P. (2012), Generation of 100-year geomagnetically induced current scenarios, Space Weather, 10, S04003, doi:10.1029/2011SW000750.

Pulkkinen, A., Bernabeu, E., Eichner, J., Viljanen, A., & Ngwira, C. (2015). Regional-scale high-latitude extreme geoelectric fields pertaining to geomagnetically induced currents. Earth, Planets and Space, 67(1). doi:10.1186/s40623-015-0255-6

Pulkkinen, A., Bernabeu, E., Thomson, A., Viljanen, A., Pirjola, R., Boteler, D., … MacAlester, M. (2017). Geomagnetically induced currents: Science, engineering, and applications readiness. Space Weather, 15(7), 828–856. doi:10.1002/2016sw001501

Rao, U. R. (2001). Vikram Sarabhai, the scientist. Resonance, 6(12), 10-18.

Rasson, J. L. (2007). "Observatories, Intermagnet". In Gubbins, D.; Herrero-Bervera, E. (eds.). Encyclopedia of Geomagnetism and Paleomagnetism. Springer, Dordrecht. doi:10.1007/978-1-4020-4423-6_227

Rastätter, L., Shim, J. S., Kuznetsova, M. M., Kilcommons, L. M., Knipp, D. J., Codrescu, M., et al. (2016). GEM-CEDAR challenge: Poynting flux at DMSP and modeled Joule heat. Space Weather, 14(2), 113–135. https://doi.org/10.1002/2015SW001238

Rastogi, R. G. (1993). Longitudinal variation of sudden commencement of geomagnetic storm at equatorial stations. Journal of Geophysical Research, 98(A9), 15411–15416. https://doi.org/10.1029/92ja02971

Rastogi, R. G. (1999). Signatures of storm sudden commencements in geomagnetic H, Y and Z fields at Indian observatories during 1958±1992. Annales Geophysicae, 17(11), 1426–1438. https://doi.org/10.1007/s00585-999-1426-1

Rastogi, R. G. (2005). Magnetic storm effects in H and D components of the geomagnetic field at low and middle latitudes. Journal of Atmospheric and Solar-Terrestrial Physics, 67(7), 665–675. https://doi.org/10.1016/j.jastp.2004.11.002

Rastogi, R. G., & Stenning, R. J. (2002). On the eastward geomagnetic field variations at the equatorial stations. Indian Journal of Radio and Space Physics, 31, 67–74.

Rastogi, R. G., Pathan, B. M., Rao, D. R. K., Sastry, T. S., & Sastri, J. H. (2001). On latitudinal profile of storm sudden commencement in H, Y and Z at Indian geomagnetic observatory chain. Earth Planets and Space, 53(2), 121–127. https://doi.org/10.1186/BF03352369

Reddy, C. A. (1989). The equatorial electrojet. Pure and Applied Geophysics, 131, 485-508.

Reddy, C. A., Somayajulu, V. V., & Devasia, C. V. (1979). Global scale electrodynamic coupling of the auroral and equatorial dynamo regions. Journal of Atmospheric and Terrestrial Physics, 41(2), 189–201. https://doi.org/10.1016/0021-9169(79)90012-6

Rees, M. H. (1975). Magnetospheric substorm energy dissipation in the atmosphere. Planetary and Space Science, 23(12), 1589–1596. https://doi.org/10.1016/0032-0633(75)90086-0

Rees, M. H. (1989). Physics and chemistry of the upper atmosphere. Cambridge University Press. Cambridge, UK.

Reiff, P. H., Daou, A. G., Sazykin, S. Y., Nakamura, R., Hairston, M. R., Coffey, V., ... & Genestreti, K. J. (2016). Multispacecraft observations and modeling of the 22/23 June 2015 geomagnetic storm. Geophysical Research Letters, 43(14), 7311-7318. https://doi.org/10.1002/2016GL069154

Reiff, P. H., Spiro, R. W., & Hill, T. W. (1981). Dependence of polar cap potential drop on interplanetary parameters. Journal of Geophysical Research, 86(A9), 7639–7648. https://doi.org/10.1029/JA086iA09p07639

Reme, H., Bosqued, J. M., Sauvaud, J. A., Cros, A., Dandouras, J., Aoustin, C., ... & Balsiger, H. (1997). The Cluster ion spectrometry (CIS) experiment. The Cluster and Phoenix Missions, 303-350. doi: 10.1023/A: 1004929816409

Richardson, I. & Cane, Hilary. (2011). Galactic Cosmic Ray Intensity Response to Interplanetary Coronal Mass Ejections/Magnetic Clouds in 1995 – 2009. Solar Physics. 270. 609-627. 10.1007/s11207-011-9774-x.

Richardson, I. G. (2018). Solar wind stream interaction regions throughout the heliosphere. Living reviews in solar physics, 15(1), 1.

Richardson, I. G., and Cane, H. V. (2012). Near-earth solar wind flows and related geomagnetic activity during more than four solar cycles (1963–2011). J. Space Weather Space Clim. 2. doi: 10.1051/swsc/2012003

Richardson, I.G., Cane, H.V., and Cliver, E.W. (2002), Sources of Geomagnetic Activity during Nearly Three Solar Cycles, J. Geophys. Res., 107 (8). doi: 10.1029/2001JA000504.

Richmond, A. D. (2003). Long-lasting disturbances in the equatorial ionospheric electric field simulated with a coupled magnetosphere-ionosphere-thermosphere model. Journal of Geophysical Research, 108(A3). doi:10.1029/2002ja009758

Richmond, A. D. (2010). On the ionospheric application of Poynting's theorem. Journal of Geophysical Research, 115(A10), A10311. https://doi.org/10.1029/2010ja015768

Richmond, A. D., Kamide, Y., Akasofu, S. I., Alcaydé, D., Blanc, M., De la Beaujardière, O., et al. (1990). Global measures of ionospheric electrodynamic activity inferred from combined incoherent scatter radar and ground magnetometer observations. Journal of Geophysical Research, 95(A2), 1061–1071. https://doi.org/10.1029/ja095ia02p01061

Ridley, A. J. (2005). A new formulation for the ionospheric cross polar cap potential including saturation effects. Annales Geophysicae, 23(11), 3533–3547. doi:10.5194/angeo-23-3533-2005

Ridley, A. J., & Liemohn, M. W. (2002). A model-derived storm time asymmetric ring current driven electric field description. Journal of Geophysical Research: Space Physics, 107(A8), SMP 2–1–SMP 2–12. doi:10.1029/2001ja000051

Riedler, W., Torkar, K., Rudenauer, F., Fehringer, M., Pedersen, A., ¨Schmidt, R., Grard, R. J. L., Arends, H., Narheim, B. T., Troim, J., Torbert, R., Olsen, R. C., Whipple, E., Goldstein, R., Valavanoglou, N., and Zhao, H.: Active spacecraft potential control, Space Sci. Rev., 79, 271, 1997.

Riedler, W., Torkar, K., Rudenauer, F., Fehringer, M., Pedersen, A., ¨Schmidt, R., Grard, R. J. L., Arends, H., Narheim, B. T., Troim, J., Torbert, R., Olsen, R. C., Whipple, E., Goldstein, R., Valavanoglou, N., and Zhao, H.: Active spacecraft potential control, Space Sci. Rev., 79, 271, 1997.

Rishbeth, H., & Garriott, O. K. (1969). Introduction to ionospheric physics. Introduction to ionospheric physics.

Rodger, A. S., Wells, G. D., Moffett, R. J., & Bailey, G. J. (2001). The variability of Joule heating, and its effects on the ionosphere and thermosphere. Annals of Geophysics, 19(7), 773–781. https://doi.org/10.5194/angeo-19-773-2001

Rossi, B., & Olbert, S. (1970). Introduction to the physics of space. New York: McGraw-Hill

Rostoker, G., Akasofu, S. I., Foster, J. C., Greenwald, R. A., Kamide, Y., Kawasaki, K., et al. (1980). Magnetospheric substorms-Definition and signatures. Journal of Geophysical Research, 85(A4), 1663–1668. https://doi.org/10.1029/JA085iA04p01663

Rostoker, G., Friedrich, E. and Dobbs, M. (1997). Physics of Magnetic Storms. In Magnetic Storms (eds B.T. Tsurutani, W.D. Gonzalez, Y. Kamide and J.K. Arballo). https://doi.org/10.1029/GM098p0149

Roytershteyn, V., Daughton, W., Karimabadi, H., & Mozer, F. S. (2012). Influence of the lower-hybrid drift instability on magnetic reconnection in asymmetric configurations. Physical review letters, 108(18), 185001. https://doi.org/10.1103/PhysRevLett.108.185001.

Runov, A., Angelopoulos, V., Zhou, X.-Z., Zhang, X.-J., Li, S., Plaschke, F., and Bonnell, J. (2011), A THEMIS multicase study of dipolarization fronts in the magnetotail plasma sheet, J. Geophys. Res., 116, A05216, doi:10.1029/2010JA016316.

Russell, C. T. (1972). The configuration of the magnetosphere. In Critical problems of magnetospheric physics (p. 1).

Russell, C. T. (2000). The polar cusp. Advances in Space Research, 25(7-8), 1413-1424.

Russell, C. T., & McPherron, R. L. (1973). Semiannual variation of geomagnetic activity. Journal of Geophysical Research, 78(1), 92–108. https://doi.org/10.1029/JA078i001p00092

Russell, C. T., & McPherron, R. L. (1973). The magnetotail and substorms. Space Science Reviews, 15(2-3), 205-266.

Ruyters, G., Braun, M., & Stang, K. M. (2021). Breakthroughs in Space Life Science Research: From Apollo 16 to the ISS. Springer Nature.

Sandholt, P. E., Farrugia, C. J., & Denig, W. F. (2014). M–I coupling across the auroral oval at dusk and midnight: Repetitive substorm activity driven by interplanetary coronal mass ejections (CMEs). Annals of Geophysics, 32(4), 333–351. https://doi.org/10.5194/angeo-32-333-2014

Sarris, T. E. (2019). Understanding the ionosphere thermosphere response to solar and magnetospheric drivers: status, challenges and open issues. Philosophical Transactions of the Royal Society A: Mathematical, Physical and Engineering Sciences, 377(2148), 20180101. doi:10.1098/rsta.2018.0101

Sastri, J. H., Jyoti, N., Somayajulu, V. V., Chandra, H., & Devasia, C. V. (2000). Ionospheric storm of early November 1993 in the Indian equatorial region. Journal of Geophysical Research, 105(A8), 18443–18455. https://doi.org/10.1029/1999JA000372

Sastri, J. H., Rao, J. V., & Ramesh, K. B. (1993). Penetration of polar electric fields to the nightside dip equator at times of geomagnetic sudden commencements. Journal of Geophysical Research, 98(A10), 17517–17523. https://doi.org/10.1029/93JA00418

Schrijver, C. J., & Beer, J. (2014). Space weather from explosions on the Sun: How bad could it be? Eos, Transactions American Geophysical Union, 95(24), 201–202. https://doi.org/10.1002/2014EO240001

Schulz M. (1995). Planetary Magnetospheres, Earth, Moon and Planets, 67:161-173.

Schulz, M. (1991). The magnetosphere. Geomagnetism.

Schunk, R. W., & Nagy, A. F. (1978). Electron temperatures in the F region of the ionosphere: Theory and observations. Reviews of Geophysics, 16(3), 355-399.

Schunk, R. W., & Nagy, A. F. (2000). Ionospheres: Physics, plasma physics, and chemistry, cambridge atmos. Space Sci. Ser, 59, 554.

Schuster, A., & Lamb, H. (1888). The Diurnal Variation of Terrestrial Magnetism. Proceedings of the Royal Society of London, 45(273-279), 481–486. doi:10.1098/rspl.1888.0119

Schwenn, R. (2006). Solar Wind Sources and Their Variations over the Solar Cycle, Space Sci. Rev., 124:51. doi: 10.1007/s11214-006-9099-5.

Schwenn, R. and Marsch, E. (Eds), Physics of Inner Heliosphere. I, Berlin–Heidelberg–New York: Springer, 1990, p. 99. 33.

Schwenn, R., Solar Wind Sources and Their Variations over the Solar Cycle, Space Sci. Rev., 2006, no. 124, p. 51. doi: 10.1007/s11214-006-9099-5. 32.

Sckopke, N., Paschmann, G., Haerendel, G., Sonnerup, B. Ö., Bame, S. J., Forbes, T. G., ... & Russell, C. T. (1981). Structure of the low- latitude boundary layer. Journal of Geophysical Research: Space Physics, 86(A4), 2099-2110.

Scudder, J. D., Holdaway, R. D., Daughton, W. S., Karimabadi, H., Roytershteyn, V., Russell, C. T., and Lopez, J. Y. (2012). First Resolved Observations of the Demagnetized Electron-Diffusion Region of an Astrophysical Magnetic-Reconnection Site. Phys. Rev. Lett. 22 (108): 225005. doi/10.1103/PhysRevLett.108.225005.

Seki, K., Nagy, A., Jackman, C. M., Crary, F., Fontaine, D., Zarka, P., Wurz, P., Milillo, A., Slavin, J. A., Delcourt, D. C. and Wiltberger, M. (2015). "A Review of General Physical and Chemical Processes Related to Plasma Sources and Losses for Solar System Magnetospheres". Space Science Reviews. 192 (1–4): 27–89. doi:10.1007/s11214-015-0170-y. ISSN 0038-6308.

Sharma, A.S., Baker, D.N., Grande, M., Kamide, Y., Lakhina, G.S., McPherron, R.M., Reeves, G.D., Rostoker, G., Vondrak, R. and Zelenyiio, L. (2003). The Storm-Substorm Relationship: Current Understanding and Outlook. In Disturbances in Geospace: The Storm-Substorm Relationship (eds A.S. Sharma, Y. Kamide and G.S. Lakhina). https://doi.org/10.1029/142GM01

Shepherd, S. G. (2007). Polar cap potential saturation: Observations, theory, and modeling. Journal of Atmospheric and Solar-Terrestrial Physics, 69(3), 234–248. https://doi.org/10.1016/j.jastp.2006.07.022

Shepherd, S. G., (2007). Polar cap potential saturation: Observations, theory, and modeling, Journal of Atmospheric and Solar-Terrestrial Physics, 69(3):234-248. https://doi.org/10.1016/j.jastp.2006.07.022.

Shi, J. K., Cheng, Z. W., Zhang, T. L., Dunlop, M., Liu, Z. X., Torkar, K., … Shen, C. (2010). South-north asymmetry of field-aligned currents in the magnetotail observed by Cluster. Journal of Geophysical Research: Space Physics, 115(A7). doi: 10.1029/2009ja014446

Shi, J. K., Qureshi, M. N. S., Ma, S. Z., Xia, L. D., & Wang, J. S. (2007). The energy release of substorm and magnetic storm: Its present state and future improvements by KuaFu mission. Advances in Space Research, 40(12), 1842–1851. https://doi.org/10.1016/j.asr2007.02.024

Shinbori, A., Tsuji, Y., Kikuchi, T., Araki, T., & Watari, S. (2009). Magnetic latitude and local time dependence of the amplitude of geomagnetic sudden commencements. Journal of Geophysical Research, 114(A4), A04217. https://doi.org/10.1029/2008JA013871

Shue, J.-H., and Chao, J.-K. (2013), The role of enhanced thermal pressure in the earthward motion of the Earth's magnetopause, J. Geophys. Res. Space Physics, 118, 3017–3026, doi:10.1002/jgra.50290.

Shue, J.-H., Chao, J. K., Fu, H. C., Russell, C. T., Song, P., Khurana, K. K., and Singer, H. J. (1997), A new functional form to study the solar wind control of the magnetopause size and shape, J. Geophys. Res., 102(A5), 9497–9511, doi:10.1029/97JA00196.

Shue, J.-H., Song, P., Russell, C. T., Steinberg, J. T., Chao, J. K., Zastenker, G., et al. (1998). Magnetopause location under extreme solar wind conditions. Journal of Geophysical Research, 103(A8), 17691–17700. https://doi.org/10.1029/98JA01103

Sibeck, D. G., Lopez, R. E., and Roelof, E. C. (1991), Solar wind control of the magnetopause shape, location, and motion, J. Geophys. Res., 96(A4), 5489–5495, doi:10.1029/90JA02464.

Sibeck, D. G., R. E. Lopez, and E. C. Roelof (1991), Solar wind control of the magnetopause shape, location, and motion, J. Geophys. Res., 96,5489– 5495.

Singh, Ram. (2019). Coupling of the solar driven prolonged and transient processes to the equatorial and low latitude ionosphere. 10.13140/rg.2.2.29064.55041.

Siscoe, G. Big storms make little storms. Nature 390, 448–449 (1997). https://doi.org/10.1038/37239

Siscoe, G. L., & Petschek, H. E. (1997, February). On storm weakening during substorm expansion phase. In Annales Geophysicae (Vol. 15, No. 2, pp. 211-216). Berlin/Heidelberg: Springer-Verlag.

Siscoe, G. L., Lotko, W., & Sonnerup, B. U. (1991). A high-latitude, low-latitude boundary layer model of the convection current system. Journal of Geophysical Research, 96(A3), 3487–3495. https://doi.org/10.1029/90JA02362

Slavin, J. A., Smith, M. F., Mazur, E. L., Baker, D. N., Hones, E. W., Jr., Iyemori, T., & Greenstadt, E. W. (1993). ISEE 3 observations of traveling compression regions in the Earth's magnetotail. Journal of Geophysical Research, 98(A9), 15425–15446. https://doi.org/10.1029/93ja01467

Smith, E. J. (2001). The heliospheric current sheet. Journal of Geophysical Research: Space Physics, 106(A8), 15819-15831.

Solanki, S. K. (2003). Sunspots: An overview. Astronomy & Astrophysics Review, 11.

Song, P., Le, G., & Russell, C. T. (1994). Observational differences between flux transfer events and surface waves at the magnetopause. Journal of Geophysical Research: Space Physics, 99(A2), 2309-2320. https://doi.org/10.1029/93JA02852

Song, P., Singer, H. J., & Siscoe, G. L. (2001). Space weather. Geophysical Monograph Series, 125.

Sonnerup, B. Ö. (1980). Theory of the low-latitude boundary layer. Journal of Geophysical Research, 85(A5), 2017–2026. https://doi.org/10.1029/ja085ia05p02017

Sotirelis, T., H. Korth, S.-Y. Hsieh, Y. Zhang, D. Morrison and L. Paxton (2013), Empirical relationship between electron precipitation and far-ultraviolet auroral emissions from DMSP observations, J. Geophys. Res. Space Physics, 118, 1203–1209, doi:10.1002/jgra.50157

Spiro, R. W., Reiff, D. H., & Maher, J. L. J. (1982). Precipitating electron average flux and auroral zone conductance: An empirical model. Journal of Geophysical Research, 87(A10), 8215–8227. https://doi.org/10.1029/JA087iA10p08215

Spitzer, L. (1956). Physics of fully ionized gases. New York: Interscience Publishers.

Spreiter, J. R., & Alksne, A. Y. (1969). Effect of neutral sheet currents on the shape and magnetic field of the magnetosphere tail. Planetary and Space Science, 17(2), 233-246.

Spreiter, J. R., Summers, A. L., & Alksne, A. Y. (1966). Hydromagnetic flow around the magnetosphere. Planetary and Space Science, 14(3), 223-253.

Spreiter, J. R., Summers, A. L., & Alksne, A. Y. (1966). Hydromagnetic flow around the magnetosphere. Planetary and Space Science, 14(3), 223-253. doi.org/10.1016/0032-0633(66)90124-3

Srivastava, N., & Venkatakrishnan, P. (2004). Solar and interplanetary sources of major geomagnetic storms during 1996–2002. Journal of Geophysical Research: Space Physics, 109(A10).

Stewart, B. (1861). XXII. On the great magnetic disturbance which extended from August 28 to September 7, 1859, as recorded by photography at the Kew Observatory. Philosophical Transactions of the Royal Society of London, (151), 423-430.

Stix, M. (2004). The sun: an introduction. Springer Science & Business Media.

Subramanian P. and Vourlidas A, (2009). Driving currents for fluc rope coronal mass ejections. Astrophys. J. 693(1219), doi:10.1088/0004-637X/693/2/1219.

Sugiura, M. (1963). Hourly values of equatorial Dst for the IGY (No. NASA-TM-X-55238).

Sugiura, M., & Poros, D. J. (1971). Hourly values of equatorial Dst for the years 1957 to 1970. NASA, Goddard Space Flight Center.

Suresh, S., and N. Dashora (2016), Climatological response of Indian low-latitude ionosphere to geomagnetic storms, J. Geophys. Res.Space Physics, 121, 4880–4897,doi:10.1002/2015JA022004.

Svestka Z., B. V. Jackson, M. E. Machado (Eds) (1992). Eruptive Solar Flares, Proceedings of colloquium number 133 of international Astronomical union held at Iguazu, Argentina, 2-6 August 1991, Springer-Verlag, Germany. ISBN-3-540-55246-4.

Swaminathan, M.S. (2020) Vikram Sarabhai – A scientist's scientist, 118(8): 1183. doi: 10.18520/cs/v118/i8/1183.

Swisdak, M. (2016), Quantifying gyrotropy in magnetic reconnection, Geophys. Res. Lett., 43, 43– 49, doi:10.1002/2015GL066980.

Tamao, T. (1964). The structure of three-dimensional hydromagnetic waves in a uniform cold plasma. Journal of Geomagnetism and Geoelectricity, 16(1), 89–114. https://doi.org/10.5636/jgg.16.89

Tenfjord, P., & Østgaard, N. (2013). Energy transfer and flow in the solar wind-magnetosphere-ionosphere system: A new coupling function. Journal of Geophysical Research: Space Physics, 118(9), 5659–5672. https://doi.org/10.1002/jgra.50545

Tobiska, W. K. (2004). SOLAR2000 irradiances for climate change research, aeronomy and space system engineering. Advances in Space Research, 34(8), 1736-1746.

Torbert, R. B., Burch, J. L., Phan, T. D., Hesse, M., Argall, M. R., Shuster, J., ... & Saito, Y. (2018). Electron-scale dynamics of the diffusion region during symmetric magnetic reconnection in space. Science, 362(6421), 1391-1395. doi: 10.1126/science.aat2998

Torbert, R. B., Russell, C. T., Magnes, W., Ergun, R. E., Lindqvist, P. A., Le Contel, O., ... & Lappalainen, K. (2016). The FIELDS instrument suite on MMS: Scientific objectives, measurements, and data products. Space Science Reviews, 199(1), 105-135. DOI 10.1007/s11214-014-0109-8

Troshichev, O. A., & Janzhura, A. (2012). Space weather monitoring by ground-based means: PC index. Springer Verlag. https://doi.org/10.1007/978-3-642-16803-1

Troshichev, O., Janzhura, A., and Stauning, P. (2006), Unified PCN and PCS indices: Method of calculation, physical sense, and dependence on the IMF azimuthal and northward components, J. Geophys. Res., 111, A05208, doi:10.1029/2005JA011402.

Tsunomura, S. (1998). Characteristics of geomagnetic sudden commencement observed in middle and low latitudes. Earth Planets and Space, 50(9), 755–772. https://doi.org/10.1186/BF03352168

Tsurutani BT, Verkhoglyadova OP, Mannucci AJ, Lakhina GS, Li G, Zank GP. (2009). A brief review of "solar flare effects" on the ionosphere. Radio Sci 44: RS0A17. https://doi.org/10.1029/2008RS004029.

Tsurutani, B. T., & Gonzalez, W. D. (1995). The efficiency of "viscous interaction" between the solar wind and the magnetosphere during intense northward IMF events. Geophysical Research Letters, 22(6), 663–666. https://doi.org/10.1029/95GL00205

Tsurutani, B. T., & Meng, C. I. (1972). Interplanetary magnetic-field variations and substorm activity. Journal of Geophysical Research, 77(16), 2964–2970. https://doi.org/10.1029/JA077i016p02964

Tsurutani, B. T., & Rodriguez, P. (1981). Upstream waves and particles: An overview of ISEE results. Journal of Geophysical Research, 86(A6), 4317–4324. https://doi.org/10.1029/JA086iA06p04317

Tsurutani, B. T., E. J. Smith, R. M. Thorne, R. R. Anderson, D. A. Gurnett, G. K. Parks, C. S. Lin, and C. T. Russell (1981), Wave-particle interactions at the magnetopause: Contributions to the dayside aurora, Geophys. Res. Lett., 8, 183. https://doi.org/10.1029/GL008i002p00183

Tsurutani, B. T., Gonzalez, W. D., Gonzalez, A. L., Guarnieri, F. L., Gopalswamy, N., Grande, M., et al. (2006). Corotating solar wind streams and recurrent geomagnetic activity: A review. Journal of geophysical Research, 111(A7), A07S01. https://doi.org/10.1029/2005JA011273

Tsurutani, B. T., Hajra, R., Echer, E., & Gjerloev, J. W. (2015). Extremely intense (SML≤–2500 nT) substorms: Isolated events that are externally triggered? Annals of Geophysics, 33(5), 519–524. https://doi.org/10.5194/angeo-33-519-2015

Tsurutani, B. T., Lakhina, G. S., & Hajra, R. (2020). The physics of space weather/solar-terrestrial physics (STP): what we know now and what the current and future challenges are. Nonlinear Processes in Geophysics, 27(1), 75–119. doi:10.5194/npg-27-75-2020

Tsurutani, B. T., Lakhina, G. S., Verkhoglyadova, O. P., Gonzalez, W. D., Echer, E., & Guarnieri, F. L. (2011). A review of interplanetary discontinuities and their geomagnetic effects. Journal of Atmospheric and Solar-Terrestrial Physics, 73(1), 5–19. https://doi.org/10.1016/j.jastp.2010.04.001

Tsurutani, B.T., Gonsalez, W.D., Tang, E., et al., Origin of Interplanetary Southward Magnetic Fields Responsible for Major Magnetic Storms near the Solar Maximum (1978–1979), J. Geophys. Res., 1988, vol. 93, p. 8519.

Tsurutani, B.T., Gonzalez, W.D. & Kamide, Y. Magnetic storms. Surveys in Geophysics 18, 363–383 (1997). https://doi.org/10.1023/A:1006555215463

Tsurutani, Bruce & Gonzalez, Walter & Gonzalez, Alicia & Guarnieri, F. & Gopalswamy, Nat & Grande, M. & Kamide, Yohsuke & Kasahara, Yoshiya & Lu, Gang & Mann, Ian & McPherron, Robert & Soraas, Finn. (2006). Corotating solar wind streams and recurrent geomagnetic activity: A review. Journal of Geophysical Research. 111. 10.1029/2005JA011273.

Tsyganenko, N. A. (1989). A solution of the Chapman-Ferraro problem for an ellipsoidal magnetopause. Planetary and Space Science, 37(9), 1037–1046. doi: 10.1016/0032-0633(89)90076-7

Tsyganenko, N. A. (1995), Modeling the Earth's magnetospheric magnetic field confined within a realistic magnetopause, J. Geophys. Res., 100(A4), 5599–5612, doi:10.1029/94JA03193.

Tsyganenko, N. A., & Sitnov, M. I. (2005). Modeling the dynamics of the inner magnetosphere during strong geomagnetic storms. Journal of Geophysical Research, 110(A3), A03208. https://doi.org/10.1029/2004JA010798

Tu, C.-Y. (2005). Solar Wind Origin in Coronal Funnels. Science, 308(5721), 519–523. doi:10.1126/science.1109447

Turner, N. E., Baker, D. N., Pulkkinen, T. I., Roeder, J. L., Fennell, J. F., & Jordanova, V. K. (2001). Energy content in the storm time ring current. Journal of Geophysical Research, 106(A9), 19149–19156. https://doi.org/10.1029/2000JA003025

Turner, N. E., Cramer, W. D., Earles, S. K., & Emery, B. A. (2009). Geoefficiency and energy partitioning in CIR-driven and CME-driven storms. Journal of Atmospheric and Solar-Terrestrial Physics, 71(10–11), 1023–1031. https://doi.org/10.1016/j.jastp.2009.02.005

Ueno, G., Ohtani, S., Saito, Y., and Mukai, T., Field-aligned currents in the outermost plasma sheet boundary layer with Geotail observation, J. Geophys. Res., 107(A11), 1399, doi:10.1029/2002JA009367, 2002.

Usoskin, I. G. (2008). A History of Solar Activity over Millennia. Living Reviews in Solar Physics, 5. doi:10.12942/lrsp-2008-3

V. D. Albertson, J. M. Thorson and S. A. Miske, "The Effects of Geomagnetic Storms on Electrical Power Systems," in IEEE Transactions on Power Apparatus and Systems, vol. PAS-93, no. 4, pp. 1031-1044, July 1974, doi: 10.1109/TPAS.1974.294047.

V. D. Albertson, J. M. Thorson, R. E. Clayton and S. C. Tripathy, "Solar-Induced-Currents in Power Systems: Cause and Effects," in IEEE Transactions on Power Apparatus and Systems, vol. PAS-92, no. 2, pp. 471-477, March 1973, doi: 10.1109/TPAS.1973.293746.

Valdivia, J. A., Sharma, A. S., & Papadopoulos, K. (1996). Prediction of magnetic storms by nonlinear models. Geophysical Research Letters, 23(21), 2899–2902. https://doi.org/10.1029/96GL02828

Vanhamäki, H., Yoshikawa, A., Amm, O., & Fujii, R. (2012). Ionospheric Joule heating and Poynting flux in quasi-static approximation. Journal of Geophysical Research, 117(A8), A08327. https://doi.org/10.1029/2012JA017841

Venkatesh, K., Patra, A. K., & Reinisch, B. W. (2020). F3 layer characteristics revealed by the Jicamarca incoherent scatter radar: First results. Journal of Geophysical Research: Space Physics, 125, e2020JA028082. https://doi.org/10.1029/2020JA028082

Verkhoglyadova, O. P., Tsurutani, B. T., Mannucci, A. J., Mlynczak, M. G., Hunt, L. A., Paxton, L. J., & Komjathy, A. (2016). Solar wind driving of ionosphere-thermosphere responses in three storms near St. Patrick's Day in 2012, 2013, and 2015. Journal of Geophysical Research: Space Physics, 121(9), 8900–8923. https://doi.org/10.1002/2016JA022883

Vichare, G., Alex, S., & Lakhina, G. S. (2005). Some characteristics of intense geomagnetic storms and their energy budget. Journal of Geophysical Research, 110(A3), A03204. https://doi.org/10.1029/2004JA010418

Villante, U., & Piersanti, M. (2009). Analysis of geomagnetic sudden impulses at low latitudes. Journal of Geophysical Research, 114(A6), A06209. https://doi.org/10.1029/2008JA013920

Villante, U., & Piersanti, M. (2011). Sudden impulses at geosynchronous orbit and at ground. Journal of Atmospheric and Solar-Terrestrial Physics, 73(1), 61–76. https://doi.org/10.1016/j.jastp.2010.01.008

Villante, U., Francia, P., Vellante, M., Di Giuseppe, P., Nubile, A., & Piersanti, M. (2007). Long-period oscillations at discrete frequencies: A comparative analysis of ground, magnetospheric, and interplanetary observations. Journal of Geophysical Research, 112(A4), A04210. https://doi.org/10.1029/2006JA011896

Vorobjev, V. G., Yagodkina, O. I., & Zverev, V. L. (2016). Investigation of isolated substorms: Generation conditions and characteristics of different phases. Geomagnetism and Aeronomy, 56(6), 682–693. https://doi.org/10.1134/s0016793216060165

Vourlidas A, Patsourakos S, Savani NP (2019) Predicting the geoeffective properties of coronal mass ejections: current status, open issues and path forward. Philos Trans R Soc A Math Phys Eng Sci 377(2148):20180096 https://doi.org/10.1098/rsta.2018.0096

Wallace, J. M., & Hobbs, P. V. (2006). Atmospheric science: an introductory survey (Vol. 92). Elsevier.

Walsh, A. P., Owen, C. J., Fazakerley, A. N., Forsyth, C., & Dandouras, I. (2011). Average magnetotail electron and proton pitch angle distributions from Cluster PEACE and CIS observations. Geophysical Research Letters, 38(6), n/a–n/a. doi: 10.1029/2011gl046770

Wang Z., H. S. Fu, A. Vaivads, J. L. Burch, Y. Yu and J. B. Cao (2020). Monitoring the Spatio-temporal Evolution of a Reconnection X-line in Space, The Astrophys. J. Lett. 899(2): L34. https://dx.doi.org/10.3847/2041-8213/abad2c

Wang, B., Liu, T., Nishimura, Y., Zhang, H., Hartinger, M., Shi, X., et al. (2020). Global propagation of magnetospheric Pc5 ULF waves driven by foreshock transients. Journal of Geophysical Research: Space Physics, 125, e2020JA028411. https://doi.org/10.1029/2020JA028411

Wang, B., Nishimura, Y., Hietala, H., Shen, X. C., Shi, Q., Zhang, H., et al. (2018). Dayside magnetospheric and ionospheric responses to a foreshock transient on 25 June 2008: 2. 2-D evolution based on dayside auroral imaging. Journal of Geophysical Research: Space Physics, 123(8), 6347–6359. https://doi.org/10.1029/2017ja024846

Wang, H., Lühr, H., Ridley, A., Ritter, P., & Yu, Y. (2008). Storm time dynamics of auroral electrojets: CHAMP observation and the Space Weather Modeling Framework comparison. Ann. Geophys. 26(3):555-570. https://doi.org/10.5194/angeo-26-555-2008.

Watanabe, Takashi. (2009). WDC activities in Japan, 2008. Data Science Journal. 8. S102-S107. 10.2481/dsj.IGY-026.

Waters, C. L., Gjerloev, J. W., Dupont, M., & Barnes, R. J. (2015). Global maps of ground magnetometer data. Journal of Geophysical Research: Space Physics, 120(11), 9651–9660. https://doi.org/10.1002/2015JA021596

Webster, J. M., Ergun, J. L., Reiff, P. H., Daou, A. G., Genestreti, K. J., Graham, D. B., et al. (2018). Magnetospheric Multiscale dayside reconnection electron diffusion region events. Journal of Geophysical Research: Space Physics, 123, 4858–4878. https://doi.org/10.1029/2018JA025245

Webster, J. M., Ergun, J. L., Reiff, P. H., Daou, A. G., Genestreti, K. J., Graham, D. B., et al. (2018). Magnetospheric Multiscale dayside reconnection electron diffusion region events. Journal of Geophysical Research: Space Physics, 123, 4858–4878. https://doi.org/10.1029/2018JA025245

Weimer, D. R. (2001). Maps of field-aligned currents as a function of the interplanetary magnetic field derived from Dynamic Explorer 2 data. Journal of Geophysical Research, 106, 12,889.

Weimer, D. R. (2005). Improved ionospheric electrodynamic models and application to calculating Joule heating rates. Journal of Geophysical Research, 110(A5), A05306. https://doi.org/10.1029/2004JA010884

Weiss, L. A., Reiff, P. H., Moses, J. J., Heelis, R. A., & Moore, D. B. (1992). Energy dissipation in substorms. In Substorms 1 (ESA SP-335, pp. 309–317). European Space Agency.

Wellenzohn, S., Nakamura, R., Nakamura, T. K. M., Varsani, A., Sergeev, V. A., Apatenkov, S. V., ... & Torbert, R. B. (2021). Remote sensing of magnetic reconnection in the magnetotail using in situ multipoint observations at the plasma sheet boundary layer. Journal of Geophysical Research: Space Physics, 126(1), e2020JA028917.

Wickwar, V. B., Baron, M. J., & Sears, R. D. (1975). Auroral energy input from energetic electrons and Joule heating at Chatanika. Journal of Geophysical Research, 80(31), 4364–4367. https://doi.org/10.1029/JA080i031p04364

Wolf, R.A., Freeman, J.W., Jr., Hausman, B.A., Spiro, R.W., Hilmer, R.V. and Lambour, R.L. (1997). Modeling Convection Effects in Magnetic Storms. In Magnetic Storms (eds B.T. Tsurutani, W.D. Gonzalez, Y. Kamide and J.K. Arballo). https://doi.org/10.1029/GM098p0161

World Data Center for Geomagnetism, Kyoto, M. Nose, T. Iyemori, M. Sugiura, T. Kamei (2015), Geomagnetic AE index, doi:10.17593/15031-54800,

World Data Center for Geomagnetism, Kyoto, M. Nose, T. Iyemori, M. Sugiura, T. Kamei (2015), Geomagnetic Dst index, doi:10.17593/14515-74000,

Wright, A. N., W. Allan, M. S. Ruderman, and R. C. Elphic (2002), The dynamics of current carriers in standing Alfvén waves: Parallel electric fields in the auroral acceleration region, J. Geophys. Res., 107(A7), 1120, doi: 10.1029/2001JA900168.

Xu, W. Y., & Du, A. M. (2010). Effect of the ring current decay rate on the energy state of the magnetosphere. Chinese Journal of Geophysics, 53(3), 329–338. https://doi.org/10.1002/cjg2.1501

Yamada, M., Kulsrud, R., & Ji, H. (2010). Magnetic reconnection. Reviews of modern physics, 82(1), 603. https://doi.org/10.1103/RevModPhys.82.603

Yamada, Y., Takeda, M., & Araki, T. (1997). Occurrence characteristics of the preliminary impulse of geomagnetic sudden commencement detected at middle and low latitudes. Journal of Geomagnetism and Geoelectricity, 49(8), 1001–1012. https://doi.org/10.5636/jgg.49.1001

Yamauchi, M. (2019). Terrestrial ion escape and relevant circulation in space. Ann. Geophys., 37, 1197–1222. https://doi.org/10.5194/angeo-37-1197-2019.

Yamazaki, Y., and Kosch, M. J. (2015), The equatorial electrojet during geomagnetic storms and substorms. J. Geophys. Res. Space Physics, 120, 2276– 2287. doi: 10.1002/2014JA020773.

Yamazaki, Y., Maute, A. Sq and EEJ—A Review on the Daily Variation of the Geomagnetic Field Caused by Ionospheric Dynamo Currents. Space Sci Rev 206, 299–405 (2017). https://doi.org/10.1007/s11214-016-0282-z

Yermolaev, Y. I., Nikolaeva, N. S., Lodkina, I. G., & Yermolaev, M. Y. (2009). Catalog of large-scale solar wind phenomena during 1976–2000. Cosmic Research, 47(2), 81–94. https://doi.org/10.1134/S0010952509020014

Yu, Y., Wang, Z., Fu, H. S., & Cao, J. B. (2022). Direct evidence of interchange instabilities at dipolarization fronts. *Journal of Geophysical Research: Space Physics*, 127, e2022JA030805. https://doi.org/10.1029/2022JA030805

Yue, C., Zong, Q. G., Zhang, H., Wang, Y. F., Yuan, C. J., Pu, Z. Y., et al. (2010). Geomagnetic activity triggered by interplanetary shocks. Journal of Geophysical Research, 115(A5), A00I05. https://doi.org/10.1029/2010JA015356

Zhang, J., et al. (2007), Solar and interplanetary sources of major geomagnetic storms (Dst ≤ −100 nT) during 1996–2005, J. Geophys. Res., 112, A10102, doi:10.1029/2007JA012321.

Zhang, J., Temmer, M., Gopalswamy, N. et al. Earth-affecting solar transients: a review of progresses in solar cycle 24. Prog Earth Planet Sci 8, 56 (2021). https://doi.org/10.1186/s40645-021-00426-7

Zhang, Y and Paxton, LJ (2008) An empirical Kp-dependent global auroral model based on TIMED/GUVI FUV data. J Atmos Sol Terr Phys 70:1231. https://doi.org/10.1016/j.jastp.2008.03.008.

Zhao, M. J., Fu, H. S., Liu, C. M., Chen, Z. Z., Xu, Y., Giles, B. L., & Burch, J. L. (2019). Energy range of electron rolling-pin distribution behind dipolarization front. Geophysical Research Letters. doi:10.1029/2019gl082100

Zhou S, Han D, Gokani S A, Selvakumaran R, Zhang Y. (2020). Throat aurora observed by DMSP/SSUSI in a global view. Science China Earth Sciences, 63: 891–898, https://doi.org/10.1007/s11430-019-9592-y

Zhou, X. Y., Strangeway, R. J., Anderson, P. C., Sibeck, D. G., Tsurutani, B. T., Haerendel, G., & Arballo, J. K. (2003). Shock aurora: FAST and DMSP observations. Journal of Geophysical Research, 108(A4), 8019. https://doi.org/10.1029/2002JA009701

Zhu, Q., Deng, Y., Richmond, A., & Maute, A. (2018). Small‐ scale and mesoscale variabilities in the electric field and particle precipitation and their impacts on Joule heating. Journal of Geophysical Research: Space Physics, 123(11), 9862-9872.

Zou, S., Ozturk, D., Varney, R., & Reimer, A. (2017). Effects of sudden commencement on the ionosphere: PFISR observations and global MHD simulation. Geophysical Research Letters, 44(7), 3047–3058. https://doi.org/10.1002/2017GL072678

Zurbuchen, T. H., & Richardson, I. G. (2006). In-Situ Solar Wind and Magnetic Field Signatures of Interplanetary Coronal Mass Ejections. Space Science Reviews, 123(1-3), 31–43. doi:10.1007/s11214-006-9010-4

Papers published in Peer-Reviewed International Journals:

1. Hajra, S., Dashora, N., & Ivan, J. S. (2022). On the sources, coupling, and energetics during supersubstorms of the solar cycle 24. **Journal of Geophysical Research: Space Physics**, 127, e2022JA030604. https://doi.org/10.1029/2022JA030604, AGU.

2. Hajra, S., Dashora, N., & Ivan, J. S. (2023). Global observations of the short-term disturbances in the geomagnetic field and induced currents during the supersubstorms events of solar cycle 24. **Space Weather**, 21, e2022SW003355. https://doi.org/10.1029/2022SW003355, AGU.

3. Hajra, S., Dashora, N., & Ivan, J. S. (2023). On the multi-scale dynamics and energy flow near reconnection regions in the magnetopause and magnetotail using the MMS, Cluster and THEMIS observations during the geomagnetic storm of 31 December 2015, **Advances in Space Research**, ISSN 0273-1177, https://doi.org/10.1016/j.asr.2023.06.025.COSPAR.

Presentations at International/ National Conferences:

International

(1) 42th **COSPAR** scientific assembly, **Athens, Greece**, 16 – 24 July 2022:
Sritam Hajra and Nirvikar Dashora, A synthetic analysis of the Supersubstorms of Solar Cycle 24: The sources, SMI coupling and impacts.

(2) Solar Terrestrial Physics Symposia (STP-15), Indian Institute of Geomagnetism (IIG), Alibag, India, 21-25 February 2022 (VIRTUAL)
Sritam Hajra and Nirvikar Dashora, The supersubstorms (SML ≤-2500 nT) of solar cycle 24: The sources, energy coupling and impacts on the solar wind-magnetosphere-ionosphere system

National

(3) 21th National Space Science Symposium (**NSSS-2022**), IISER, Kolkata, 29 Jan – 04 Feb 2022. (VIRTUAL)
Sritam Hajra and Nirvikar Dashora, The supersubstorms (SML ≤-2500 nT) of solar cycle 24: The sources, energy coupling and impacts on the solar wind-magnetosphere-ionosphere system

(4) Indian **Space Weather Conference**, **PRL, Ahmedabad**, India 11-12 January 2022 (VIRTUAL)
Sritam Hajra and Nirvikar Dashora, The supersubstorms (SML less than 2500 nT) of solar cycle 24: The sources, energy coupling and impacts on the solar wind-magnetosphere-ionosphere system

(5) URSI regional Conference On Radio Science (5th **URSI-RCRS**) **IIT Indore**, Indore, 1-4 December 2022.
Sritam Hajra and Nirvikar Dashora, Multi-scale analysis of the Magnetic reconnection events using multi-spacecraft observations during 31 December 2015 geomagnetic storm.

The End

"The end of a melody is not its goal: but nonetheless, had the melody not reached its end it would not have reached its goal either."

- Friedrich Nietzsche

(The Wanderer and His Shadow)